Role of Intracellular Lipid Binding Proteins in Xenobiotic and Retinoid Metabolism and Disposition

King Clyde Baluyot Yabut

A dissertation

submitted in partial fulfillment of the

requirements for the degree of

Doctor of Philosophy

University of Washington

2024

Reading Committee:

Nina Isoherranen, Chair

Kenneth Thummel

Allan Rettie

Program Authorized to Offer Degree:

Pharmaceutics

University of Washington

Abstract

Role of Intracellular Lipid Binding Proteins in Xenobiotic and Retinoid Metabolism and Disposition

King Clyde Baluyot Yabut

Chair of the Supervisory Committee:
Nina Isoherranen
Pharmaceutics

Intracellular lipid binding proteins (iLBPs) are a family of small (~15 kDa) β-barrel proteins that bind and solubilize diverse endogenous lipids essential for life. iLBPs serve as cytosolic carriers facilitating the uptake of endogenous ligands into cells and targeting ligands to cellular sites of action. Xenobiotics have also been shown to bind to iLBPs, however, whether iLBPs influence xenobiotic disposition is poorly understood. Retinoid binding proteins and fatty acid binding proteins comprise the family of iLBPs. Retinoid binding proteins have high specificity toward the essential vitamin, A, and its metabolites (retinoids) and have been shown to channel retinoids directly to metabolic enzymes. Cellular retinoic acid binding proteins (CRABP1 and CRABP2) specifically interact with the cytochrome P450 (CYP) 26 family of enzymes to regulate the metabolism of the active form of vitamin A, *all*-trans-retinoic acid (*at*RA). Liver fatty

acid binding protein (FABP1) is a highly expressed iLBP in the liver (0.7-1 mM) which is a major organ involved in the metabolic clearance of drugs. Yet, the role of FABP1 in the metabolism and disposition of drugs has not been defined, and it is unknown if FABP1 interacts with CYP enzymes in the liver to facilitate drug metabolism, similar to what has been observed for retinoid binding proteins. The overarching hypothesis for this thesis work was that CRABPs and FABPs facilitate the metabolism of their ligands via interactions with CYP enzymes in the liver. In this thesis work, I aimed to 1) define the interactions between CRABPs and CYP26A1, the major CYP26 enzyme in the liver, that influence the metabolism of *at*RA, 2) determine the binding affinities of drugs with FABP1 and the effect of FABP1 on the metabolism of diclofenac by CYP2C9 and 3) identify the major CYP enzymes responsible for the metabolism of Δ9-tetrahydrocannabinol (THC) and the effect of FABP1 on THC metabolism by these CYPs.

The results presented in this thesis show that CRABPs and FABP1 alter the metabolism of their ligands by CYP enzymes. In chapter 2, kinetic modeling suggested that both CRABPs interact directly with CYP26A1 to regulate *at*RA metabolism similar to previous reports with CYP26B1 and CYP26C1. Based on the kinetic modeling, apo-CRABPs inhibited *at*RA metabolism by CYP26A1 while holo-CRABPs directly delivered *at*RA to CYP26A1. The findings in chapter 2 propose a mechanism by which CRABPs can fine tune cellular *at*RA levels via their interactions with CYP26A1.

Similar to the findings in chapter 2, chapters 3 and 4 showed that FABP1 had a significant impact on the metabolism of drug ligands by several CYPs. The work in chapters 3 and 4 showed that a variety of drugs bound to FABP1 with binding affinities (K_ds) ranging from 0.3-20 µM and these drugs formed ternary complexes with the fluorescent probe, DAUDA, and FABP1. In chapter 3, FABP1 had a significant impact on the metabolism of diclofenac by CYP2C9, decreasing the k_{cat} of 4'-OH-diclofenac formation by ~50%. Chapter 4 showed similar effects of FABP1 with THC metabolism. Four major metabolites of THC were identified in human liver microsomes – 11-OH-THC and M1-M4 metabolites, and the major CYPs that contributed to the formation of these metabolites in HLMs were CYP2C9 (11-OH-THC), CYP2C19 (M3 and 11-OH-THC) and CYP3A4 (M2-M4). FABP1 altered the formation of these metabolites in an enzyme specific manner, altering both the K_m and k_{cat} of THC metabolite formation by these enzymes. Collectively, the data presented in this thesis suggest that iLBPs can modulate the metabolism of their ligands via interactions with CYP enzymes. Drugs are expected to be bound to FABP1 in the liver *in vivo* and the FABP1 may be a determinant of drug metabolism in the liver.

TABLE OF CONTENTS

LIST OF FIGURES

LIST OF TABLES

ACKNOWLEDGEMENTS

To my advisor, Nina, what a journey it has been to get this thesis to completion. Thank you for all your guidance throughout the years and the seemingly endless energy you put into my growth and development as a scientist. You taught me that pursuing my endeavors with a sense of passion and intensity will always lead to success. I will always treasure the lessons in science and life that you taught me, and I will always remember that all my problems can be solved with just a little bit of lab tape…

To my committee members: Ken, thank you for recruiting me to the department all those years ago. I am grateful for all your encouragement throughout graduate school and your guidance. I always enjoyed listening and soaking up the wealth of knowledge that you would teach about (even if it were just about birds). Allan, it was an enormous pleasure to have you on my committee. I always appreciated your thoughtful insight into the nooks and crannies of my thesis. Med Chem 527 was my favorite class in graduate school, and I thoroughly enjoyed learning P450 biochemistry from you. Abhi, I learned a lot of cool science from you that I never thought I would do. Thank you for all your guidance and patience, and for your contributions to my thesis work. It was a true pleasure to work with you.

To my parents Rose and Steve, I am eternally grateful for all your love and support. You taught me the meaning of hard work and persistence, and that has led me to the successes that I have today. To all my siblings, nieces and nephews, life would have been a lot more dull without you. Thank you all for your unending support. To my titos and titas, thank you for raising me when I was little. I would not be the same person without you. To my sensei Alex, thank you for all the bruises, face cuts, and bloody lips. Somewhere in there, I found the courage to undertake anything that came my way. To all my precious lab mates, the best parts of graduate school were with you. I will never forget you and the camaraderie we shared.

To MacKenzie, there is no one else I would have rather picked to go on this journey with. Thank you for always being by my side and for reminding me what is most important in life.

DEDICATION

To all the kids that may never have the opportunity that I had.

Chapter 1. INTRODUCTION

The work presented in this chapter was published in:

Drug Metabolism and Disposition 51(6): 700-717 (2023)

Co-author: Nina Isoherranen[a]

[a]*Department of Pharmaceutics, School of Pharmacy, University of Washington, Seattle, WA, United States*

1.1 PHYLOGENY OF INTRACELLULAR LIPID BINDING PROTEINS

Intracellular lipid binding proteins (iLBPs) are a family of ubiquitous proteins in animals that solubilize essential cellular lipids (Schaap et al., 2002; Storch and Corsico, 2008; Smathers and Petersen, 2011; Napoli, 2017). Together with avidins and lipocalins, iLBPs belong to the calycin superfamily of structurally related binding proteins. Despite low amino acid sequence homology (<10%), avidins, lipocalins and iLBPs share a common β-barrel structural fold that makes up their ligand binding cavity (Flower et al., 2000; Schaap et al., 2002; Smathers and Petersen, 2011). Avidins and lipocalins are found in both prokaryotic and eukaryotic organisms, but iLBPs are only present in vertebrate and invertebrate animals (Schaap et al., 2002). The ancestral iLBP gene evolved after animals diverged from plants and fungi, and individual isoforms arose through gene duplication and diversification (Schaap et al., 2002; Haunerland and Spener, 2004; Smathers and Petersen, 2011). The primary amino acid sequence identity for the 16 known human iLBPs ranges from 21% to 77% (Figure. 1.1A). Generally, the amino acid sequence identity for specific iLBPs across different species is greater than the sequence identity of all fatty acid binding proteins (FABPs) within the same species. For example, fatty acid binding protein 1 (FABP1) has > 60% amino acid sequence identity across 18 different species (Zhang et al., 2020), but the sequence identity of all FABPs in humans is as low as 21%.

The human iLBPs are divided into four subfamilies (Figure 1.1B) based on phylogenetic analysis and amino acid sequences (Schaap et al., 2002; Liu et al., 2008; Smathers and Petersen, 2011; Ragona et al., 2014). Subfamily I is comprised of the cellular retinol binding proteins (CRBPs) and cellular retinoic acid binding proteins (CRABPs). Subfamily II contains liver FABP (FABP1) and ileal FABP (FABP6, also called I-BABP). Intestinal FABP (FABP2) is the lone iLBP to make up subfamily III and heart (FABP3), adipocyte (FABP4), epidermal

(FABP5), brain (FABP7), myelin (FABP8), and testis (FABP9) FABPs, and FABP12 make up subfamily IV (Schaap et al., 2002; Smathers and Petersen, 2011). The FABPs were originally named after the organs from which they were cloned but have been later found to have broader expression.

The human iLBP genes are located in several different chromosomes (Table 1.1) and, like most iLBP genes in animals, have four exons with three introns (Schaap et al., 2002; Babin, 2009; Smathers and Petersen, 2011; Zhang et al., 2020). The second and third exons are conserved in nearly all FABP genes (Zhang et al., 2020). Phylogenetic studies suggest that FABP genes evolved from a common ancestor likely through tandem duplication (Babin, 2009; Zhang et al., 2020). FABP4, 5, 8, 9, and 12 form a gene cluster on the same chromosome in humans and several other mammals. Some of these FABP genes also form clusters in aves, amphibians, and reptiles. This supports the hypothesis that vertebrate FABP genes may have arisen through continuous tandem duplication from a common ancestor (Zhang et al., 2020).

The complete physiologic functions of iLBPs have yet to be defined, but iLBPs appear to facilitate the efficient uptake of endogenous lipids into tissues, acting as carriers to shuttle ligands through the cytosol and modulating rates of ligand metabolism (Kushlan et al., 1981; Luxon and Weisiger, 1993; Martin et al., 2003; Kaczocha et al., 2009; Yu et al., 2014; Gajda and Storch, 2015). Altered iLBP function and expression have been associated with dyslipidemia, metabolic syndrome, obesity, diabetes, atherosclerosis, and inflammation (Furuhashi and Hotamisligil, 2008; Atshaves et al., 2010; Peng et al., 2012; Wang et al., 2016; Furuhashi, 2019; Valizadeh et al., 2021). Several iLBP isoforms also bind xenobiotics (Chuang et al., 2008; Trevaskis et al., 2011; Velkov, 2013; Lee et al., 2015; Huang et al., 2018; Elmes et al., 2019). Based on their high and ubiquitous expression in tissues, iLPBs may be determinants of xenobiotic distribution and uptake into tissues. This review focuses on ligand binding to iLBPs, tissue expression of iLBPs, methods to determine ligand binding, and the biochemical roles of iLBPs as they relate to the potential of iLBPs to be determinants of drug disposition.

1.2 INTRACELLULAR LIPID BINDING PROTEIN STRUCTURES AND ENDOGENOUS LIGAND BINDING

1.2.1 *General Structure of iLBPs*

The tertiary structures of iLBPs are virtually superimposable and have two characteristic structural features, a β-barrel domain and helix-turn-helix motif (Figure. 1.2). Ten anti-parallel β-strands fold into two β-sheets to form the β-“clam-like” cavity of the iLBPs (Figure 1.2) (Furuhashi and Hotamisligil, 2008; Storch and McDermott, 2009; Ferrolino et al., 2013; Napoli, 2016). The two alpha-helices along with nearby loops form a portal region for ligand entry and egress into the interior binding cavity (Figure 1.2). The iLBPs have a characteristic fingerprint composed of three separate motifs termed FATTYACIDBP1-3 (Figure 1.1A). The G-x-W triplet in the first FATTYACIDBP1 motif is highly conserved between iLBP members (Figure 1.1A) and homologous with a similar motif in lipocalin family of binding proteins (Smathers and Petersen, 2011). FABP5 is unique in the iLBP family in that it is the only FABP known to form an intramolecular disulfide bond (C120-C127) (Hohoff et al., 1999). The dynamics of iLBP structures and consequences on ligand binding have been extensively studied, and several comprehensive reviews are available on this topic (Storch and McDermott, 2009; Atshaves et al., 2010; Smathers and Petersen, 2011; Ragona et al., 2014).

1.2.2 *iLBP Structure-Function Relationship in Ligand Binding*

Crystal structures and NMR solution structures of iLBPs show that ligands are stabilized within the binding cavity by ionic interactions, hydrogen bonding networks with water molecules, and interactions with hydrophobic regions (Kleywegt et al., 1994; Cai et al., 2012; Nossoni et al., 2014; Silvaroli et al., 2016). Hydrophobic interactions between the ligand and amino acid sidechains that line the iLBP binding cavity are important for ligand binding (Thumser et al., 1996). The residues identified as part of the hydrophobic interaction network are shown for representative iLBPs in Figure 1.3A. The importance of the hydrophobic interactions is also illustrated in the general observation that binding affinities with FABPs correlate with increasing hydrophobicity (Storch and Corsico, 2008; Smathers and Petersen, 2011). Ionic and hydrogen bonding interactions for ligand binding typically involve charged residues. The arginine residue in the FATTYACIDBP3 (Figure 1.1A) is highly conserved in the iLBPs that bind acidic ligands (R122 in FABP1, R126 in FABP3 and FABP4, R129 in FABP5 and R132 in CRABP2) and is located on the βJ strand of these proteins (Figure 1.3A). For CRBP1 that binds nonacidic ligands all-trans-retinol and all-trans-retinal, the Q128 appears to be the corresponding residue important for ligand binding (Silvaroli et al., 2016). For CRABP1 and CRABP2, the amino acids R132 and Y134 coordinate with the carboxylic acid of all-trans-retinoic acid (*at*RA) and R111 appears to coordinate with the carboxylic acid via an ordered water molecule (Figure 1.3C) (Kleywegt et al., 1994). Analogous amino acids in some FABPs also coordinate with the carboxylate of fatty acids bound to FABPs (Hanhoff et al., 2002; Smathers and Petersen, 2011). However, these residues are not essential for ligand binding in all iLBPs. Mutations of the conserved arginine in the βJ strand confer different effects on ligand binding depending on the iLBP isoform and the ligand in question. A single R132A or R132Q mutation completely abolishes binding of *at*RA to CRABP2 (Chen et al., 1995). Similarly, an R126Q mutation on the analogous residue in FABP4 reduces the binding affinity for cis-parinaric acid by >10-fold (Sha et al., 1993). In contrast, an R122Q mutation in FABP1 only moderately decreases fatty acid binding and increases binding of bulkier ligands (Thumser et al., 1996). Charged or polar residues in the βH strand also interact with hydroxy and carbonyl head groups (Figure 1.3A), except for subfamily II FABPs (FABP1 and FABP6), and likely contribute to ligand binding. The hydroxy group of all-trans-retinol interacts with Q108 in CRBP1 (Figure 1.3A) and Q109 in CRBP2. Ligands appear to interact with the conserved residue R111 in CRABPs (Figures 1.1A and 1.3A). In addition, ligands interact with R106 in FABP2, and this residue is also conserved in subfamily IV FABPs (Figures 1.1A and 1.3A).

The helix-turn-helix motif, in conjunction with nearby βC-βD and βE-βF loops, form the portal region of the iLBP that permits ligand entry and egress from the interior binding cavity (Figure 1.2) (Vaezeslami et al., 2006; Storch and Corsico, 2008; Silvaroli et al., 2016). Different hypotheses describe the extent of the dynamics and flexibility of the portal region. Early observations from NMR solution structures of FABP2 showed disorder and flexibility in the portal region leading to the “dynamic portal hypothesis” (Hodsdon and Cistola, 1997a,b). This hypothesis suggests that the disordered portal region in the apo-protein could undergo large structural fluctuations to permit ligand entry but shifts to an ordered closed state upon ligand binding. Processes that destabilize the helical cap, such as interactions with cationic membranes, would then shift the protein toward the disordered state and, hence, facilitate ligand release. Later studies with FABP1 supported this hypothesis and showed the apo- and holo-protein structures to have an open and closed “helix cap”, respectively (He et al., 2007). However, the dynamic portal hypothesis is not sufficient to reconcile observations that some FABPs have similar structures between ligand bound and unbound forms (Vaezeslami et al., 2006; Gillilan et al., 2007; Cai et al., 2012).

Internal protein dynamics may also have a major role in influencing ligand accessibility as major fluctuations in the portal region are not observed in structural studies with retinoid binding proteins and some FABPs (Vaezeslami et al., 2006; Cai et al., 2012; Ragona et al., 2014). In CRABP2, the portal appears large enough to allow entry of all-trans-retinoic acid (*at*RA) in both the apo- and holo-structures with little change in the overall protein backbone (Vaezeslami et al., 2006). However, the sidechain of R59 (Figure 1.3), which is located at the entry of the portal region (βC-βD loop) in the apo-protein, appears to rotate in the holo-protein to form stabilizing interactions with *at*RA (Figure 1.3). An analogous residue (F57) in FABP4 appears to have a similar function and supports the importance of sidechain dynamics in the internal binding cavity. Structural studies with FABP4 suggest that locking the internalized ligand in the holo-protein is controlled by the F57 sidechain on the βC-βD loop that rotates into the binding cavity in the holo-conformation (Gillilan et al., 2007) despite little conformational change between apo- and holo-proteins. Indeed, ligand binding kinetics with the fluorescent ligand 8-anilinonaphthalene-1-sulfonic acid (ANS) are faster in an FABP4 portal mutant (V32G, F57G, K58G), which has an enlarged portal region, than with wildtype (WT) FABP4 (Jenkins et al., 2002).

Solution NMR studies show that the backbone dynamics in the portal region in apo-proteins vary between iLBP isoforms. FABP6 has a relatively rigid portal region while FABP1, 3, and 4 portal regions are more flexible, and the FABP2 portal is virtually disordered (Ragona et al., 2014). However, in general the changes in the backbone dynamics of FABPs upon ligand binding are consistent with disordered to ordered stabilizing interactions.

1.3 ENDOGENOUS LIGAND BINDING IN ILBPS

The divergence of ligand specificity in iLBPs arises from nuanced differences in the β-barrel cavity and portal regions. Figure 1.4 shows representative structures of CRBP1, FABP1, FABP2, and FABP4 bound with their endogenous ligands illustrating general features of ligand binding with iLBPs. Historically protein fractionation, gel filtration, ion-exchange chromatography, and electrophoresis techniques were used to isolate and identify iLBPs in tissues and tissue homogenates, and bound ligands were identified from this isolated protein (Bashor et al., 1973; Ockner and Manning, 1974; Maatman et al., 1991; Veerkamp and Maatman, 1995). Subsequent characterization of ligand binding has been largely done with fluorescent probes or radiolabeled ligands in tissue homogenates or with purified recombinant iLBPs (MacDonald and Ong, 1987; Giguère et al., 1990; Nemecz et al., 1991; Sanquer and Gilchrest, 1994; Folli et al., 2001) and with x-ray crystallography and NMR (Kleywegt et al., 1994; LaLonde et al., 1994; Thompson et al., 1997; Hohoff et al., 1999).

The known endogenous ligands of iLBPs are summarized in Table 1.1. The retinoid binding proteins appear to be selective toward vitamin A and its metabolites while all FABPs bind long chain fatty acids (LCFAs) (Table 1.1). Some FABPs also bind a variety of other endogenous ligands (Table 1.1). It is important to note that the list of known ligands is limited to those ligands that have been explicitly tested for their binding and may not be comprehensive for all endogenous ligands. Several studies have explored synthetic derivatives of the endogenous ligands of FABPs (Wang et al., 2016; Floresta et al., 2017), but these synthetic derivatives are not discussed in this review. Additionally, the summary here includes binding data from species other than human proteins, as many ligand binding studies with iLBPs were done with rat, mouse, and bovine recombinant protein.

1.3.1 *Endogenous Ligands of Subfamily I*

Vitamin A (retinol) or its biologically important metabolites retinaldehyde and the pharmacologically active *at*RA bind the proteins in subfamily I with high affinity. Notably, all proteins in this subfamily are intracellular, in contrast to the lipocalin retinol binding protein 4 (RBP4), which is the circulating carrier for retinol. all-trans-retinol, all-trans-retinaldehyde, and their 13-cis and 9-cis isomers bind to CRBP1 (Figure 1.4A) and CRBP2 with nanomolar affinity. Yet, neither *at*RA nor its 13-cis and 9-cis-isomers bind to CRBPs (Kane et al., 2011; Napoli, 2016, 2017; Menozzi et al., 2017). all-trans-retinol binds to CRBP3 (Folli et al., 2001) and all-trans-retinol along with 13-cis and 9-cis retinol bind to CRBP4 (Vogel et al., 2001; Folli et al., 2002). Although CRBPs appear to be specific for retinol and retinal ligands, monoacylglycerols were also recently shown to bind to CRBPs (Lee et al., 2020). This suggests CRBPs and CRABPs may have broader ligand specificity than previously assumed. *at*RA and its isomers and metabolites bind specifically to CRABP1 and CRABP2 with *at*RA having higher binding affinity toward CRABP1 and CRABP2 (K_d = 0.4–39 nM) (Fiorella and Napoli, 1991; Fogh et al., 1993; Norris et al., 1994; Wang et al., 1997) than 9-cis-RA (K_d = 51–69 nM) (Norris et al., 1994) or 13-cis-RA (K_d = 156–238 nM) (Fiorella et al., 1993). Generally, *at*RA appears to bind slightly tighter to CRABP1 than CRABP2 (Fiorella et al., 1993; Dong et al., 1999; Yabut and Isoherranen, 2022). Retinol or retinal isomers do not bind to CRABP1 or CRABP2 (Fiorella and Napoli, 1991; Fiorella et al., 1993; Napoli, 2017).

1.3.2 *Endogenous Ligands of Subfamily II*

FABP1 and FABP6 make up subfamily II. Generally, bulky ligands in addition to LCFA bind to FABP1 and FABP6 (Smathers and Petersen, 2011). The binding pockets of FABP1 and

FABP6 are larger (≥639 and 460 Å3, respectively) (Lücke et al., 2000) than other FABPs that have solvent accessible binding pockets of approximately 230 to 330 Å3 (Smathers and Petersen, 2011). FABP1 and FABP6 can accommodate larger ligands found in the liver such as bile acids, cholesterol, bilirubin, and heme (Bernlohr et al., 1997; Smathers and Petersen, 2011). Other ligands of FABP1 include branched fatty acids, endocannabinoids, acyl-CoA, prostaglandins, and vitamin K (Khan and Sorof, 1990; Thumser and Wilton, 1996; Martin et al., 2003; Storch and Corsico, 2008; Atshaves et al., 2010; Smathers and Petersen, 2011). While fatty acid ligands appear to bind to all other FABPs in a 1:1 ratio, two fatty acids can bind to FABP1 simultaneously (Figure 1.4B) (Bernlohr et al., 1997; Thompson et al., 1997; Cai et al., 2012). FABP1 has a high-affinity fatty acid binding site (K_d = 4–60 nM) located deep within its interior cavity and a low affinity site (0.3–12 μM) closer in proximity to the alpha-helical domain and opening of the portal region (Figure 1.4B) (Atshaves et al., 2010; Smathers and Petersen, 2011; Cai et al., 2012). With larger ligands such as bile acids, this stoichiometry appears to be reduced (1:1) along with reduced binding affinities (K_d 4–50 μM) (Richieri et al., 1995). FABP6 is structurally similar to FABP1, but due to differences in interior amino acid side chains between the two proteins, preferential ligands of FABP6 include bile acids over LCFAs (Lücke et al., 2000). Due to the size of bile acids, only a single ligand is typically observed in the FABP6 binding cavity.

1.3.3 *Endogenous Ligands of Subfamily III*

FABP2 is the sole member of subfamily III. In contrast to the iLBPs in subfamily II, FABP2 has a small solvent accessible binding pocket (234 Å3) (Smathers and Petersen, 2011), and its preferential ligands include saturated LCFAs (Figure 1.4C) (Lowe et al., 1987; Richieri et al., 1994; Velkov et al., 2005; Smathers and Petersen, 2011). Measured fatty acid binding affinities with FABP2 range between 0.02 and 1.5 μM based on fluorescence displacement assays (Nemecz et al., 1991; Velkov et al., 2005, 2007).

1.3.4 *Endogenous Ligands of Subfamily IV*

The seven members of subfamily IV collectively bind diverse lipids. The size of the solvent accessible binding pockets of subfamily IV FABPs appear to be larger than subfamily III (FABP2) but smaller than subfamily II (FABP1 and FABP6). FABP3, 4 and 8 have 323, 310, and 330 Å3 binding pockets, respectively (Smathers and Petersen, 2011). Saturated and unsaturated fatty acids bind to FABP3 with nanomolar affinity, and oxygenated fatty acids (epoxyeicosatrienoic acid, hydroxyeicosatetraenoic acid, dihydroxyeicosatrienoic acid) bind to FABP3 with K_d values from 0.4 to 14 μM (Widstrom et al., 2001; Smathers and Petersen, 2011). FABP4 appears to be more ligand selective, and only LCFAs bind to FABP4 with nanomolar affinity (K_d = 22–196 nM) (Figure 1.4D) (Richieri et al., 1994; Gillilan et al., 2007; Storch and Corsico, 2008; Smathers and Petersen, 2011). However, other ligands such as *at*RA also bind to FABP4 but with a considerably lower binding affinity (K_d = 50 μM) (Matarese and Bernlohr, 1988; Veerkamp et al., 1999).

With FABP5, stearic acid and docosahexaenoic acid have nanomolar affinity to FABP5 (K_d = 0.17–0.29 and 0.16 μM, respectively) and oleic acid, lauric acid, and arachidonic acid binding affinity range from nanomolar to micromolar (K_d = 0.15–1.6, 2.5 and 0.12–1.7 μM, respectively) (Hohoff et al., 1999; Smathers and Petersen, 2011; Kaczocha et al., 2012; Pan et al., 2015; Lee et al., 2018). *at*RA has also been reported to bind to FABP5 in fluorescence displacement assays with ANS (K_d = 35 nM) (Schug et al., 2007). However, FABP5 did not to sequester *at*RA from metabolism by cytochrome P450 (CYP) enzymes, suggesting binding may not be as tight as suggested by the displacement assay (Yabut and Isoherranen, 2022). FABP7 prefers polyunsaturated fatty acids with longer chains (docosahexaenoic acid, eicosapentaenoic acid, arachidonic acid), and these fatty acids bind to FABP7 with affinities ranging from 27 to 250 nM (Smathers and Petersen, 2011).

In addition to the fatty acid ligands of FABPs, FABP3, FABP5, and FABP7 have also been shown to bind the endocannabinoids 2-archidonylglycerol and anandamide (AEA), and FABPs have been proposed to have a role in modulating endocannabinoid metabolism and signaling. 2-archidonylglycerol and AEA bind to FABP7 with higher affinity (K_d = 0.2 and 0.8 µM, respectively) than to FABP3 (K_d = 1.63 and 3.07 µM, respectively) and to FABP5 (K_d = 1.45 and 1.26 µM, respectively) (Kaczocha et al., 2012; Elmes et al., 2015). FABP8, 9, and 12 have not been extensively studied, and the binding of their endogenous ligands is not well characterized (Storch and Corsico, 2008; Smathers and Petersen, 2011).

1.4 TISSUE DISTRIBUTION AND EXPRESSION OF ILBPS

The tissue distribution of iLBPs is broad and expression patterns have been studied in several mammalian species including rat, mice, pig, and human (Paulussen et al., 1988, 1990; Gong et al., 1994; Sanquer and Gilchrest, 1994). However, species differences in tissue expression have not been comprehensively compared for all iLBPs. The following is a summary of the tissue expression of iLBPs in adult mammals determined using a combination of techniques including western and northern blot analysis, immunohistochemistry, enzyme-linked immunosorbent assay, reverse transcriptase-quantitative polymerase chain reaction, and binding assays with radiolabeled ligands. Some iLBPs are expressed in multiple tissues while others are expressed in specific tissues and cell types that may be indicative of specialized biologic functions (Storch and Corsico, 2008). The expression pattern of the FABPs is sometimes evident from the original name of the FABP, as FABPs were named after the tissues from where they were first identified. However, multiple FABPs are often expressed in the same tissues, and the expression patterns are typically broader than what is implied from the original names of the FABPs. Hence, early studies identifying FABPs in tissues often required confirming the specificity of antisera against multiple FABPs (Paulussen et al., 1990; Maatman et al., 1991; Gong et al., 1994).

Although the iLBPs are generally considered to be intracellular, FABP1, 2, 3, 4, and 5 have also been measured in plasma in humans (0.3–13 ng/mL) (Pelsers et al., 2003; Ishimura et al., 2013). Yet their concentrations are much lower than other circulating proteins such as albumin that bind fatty acids in plasma, and the importance of the circulating FABPs is unknown. FABP4 is the only isoform shown to be secreted from tissues (adipose) into circulation (Hotamisligil and Bernlohr, 2015; Shrestha et al., 2018; Villeneuve et al., 2018). For this review only CRABPs and those FABPs that xenobiotics have been shown to bind to are discussed, but the tissue expression for all iLBPs is summarized in Table 1.1.

CRABP1 protein is found in various tissues including liver, kidney, stomach, lymph, eye, and brain, but it is most abundant in skin and reproductive tissues (seminal vesicles, vas deferens, and testis) (Kato et al., 1985). CRABP2 protein expression appears to be limited to skin (Giguère et al., 1990).

FABP1, or liver FABP, is the major FABP in the liver and the intestine but is also found in the kidney, lung, pancreas, and stomach (Besnard et al., 2002; Pelsers et al., 2003; Gajda and Storch, 2015; Wang et al., 2015). FABP1 is most abundant in the liver and comprises 2% to 11% of all cytosolic protein in the liver (Wang et al., 2015; Schroeder et al., 2016). Expression of FABP1 in the liver is zonal, possibly indicating a unique role in specific areas of the liver (Bass et al., 1989). Peroxisome proliferators, female sex steroids, retinoids, and a diet high in fat increase the expression of FABP1 messenger RNA (mRNA) and protein in the liver (Poirier et al., 1997; Hung et al., 2003; Trevaskis et al., 2011; Velkov, 2013). Interestingly, FABP1 mRNA and protein expression are decreased after dexamethasone treatment, likely due to altered lipid metabolism and concentrations (Foucaud et al., 1998). In the gut, FABP1 mRNA is expressed throughout the length of the small intestines but is highest in the duodenum and jejunum (Agellon et al., 2002; Gajda and Storch, 2015). The expression pattern of FABP1 in the liver and intestines suggests FABP1 may also impact drug metabolism in the liver and drug absorption in the intestines. Additionally, FABP1 expression and function may have a role in metabolic disease progression as FABP1 polymorphisms in humans are associated with dyslipidemia, nonalcoholic fatty liver disease, and hepatocellular carcinoma (Peng et al., 2012; Schroeder et al., 2016; McKillop et al., 2019; Valizadeh et al., 2021). For example, the T94A mutation (allele frequency 26%–38%) in FABP1 alters FABP1 expression, ligand binding characteristics, protein structure and stability, and protein function (Schroeder et al., 2016). The T94A single nucleotide polymorphism is associated with elevated triglycerides, low-density lipoprotein cholesterol, and altered response to fenofibrate (Schroeder et al., 2016).

FABP2, also called intestinal FABP, is solely expressed in the gut, and its expression appears to be similar to FABP1 in rodent intestine but lower than FABP1 in human intestine. FABP2 mRNA is expressed throughout the length of the small intestine, and its expression is highest in the jejunum (Sacchettini et al., 1990; Gajda and Storch, 2015). Along with FABP1, FABP2 expression is highest in the villi of enterocytes, and it is not expressed in the crypt. FABP2 expression in enterocytes may be regulated by the gut peptide tyrosine tyrosine (Halldén and Aponte, 1997). FABP2 expression appears to be diffused throughout enterocytes but localized to the apical side in a fasted state (Alpers et al., 2000). Similar to FABP1, an A54T polymorphism in FABP2 appears to be associated with dyslipidemia, insulin resistance, obesity, and cardiovascular disease and may increase the risk of colorectal cancer (McKillop et al., 2019; Huang et al., 2022). FABP2 has been proposed as a potential biomarker for disruption of intestinal epithelial integrity as FABP2 is released to circulation when intestinal epithelium is compromised (Huang et al., 2022).

FABP3, or heart FABP, protein has been found in the heart, skeletal muscle, brain, kidney, liver, lung, spleen, and placenta (Paulussen et al., 1990). FABP3 is most abundant in the heart where its expression is nearly twofold greater than in skeletal muscle. Protein abundance in the kidney and brain is about half of that in the muscle and even less in the liver and placenta. FABP3 is also found to circulate at elevated levels in plasma in response to myocardial injury, presumably due to release from the heart. As such, it may be a potential biomarker for cardiovascular disease (Pelsers et al., 2005). In the kidney, FABP3 is found to be expressed in the distal and proximal convoluted tubules (Maatman et al., 1991), suggesting FABP3 could play a role in renal handling of drugs and xenobiotics.

FABP4, known as adipocyte FABP, is abundantly expressed in adipose tissue and is also the major FABP found in macrophages (Pelton et al., 1999; Furuhashi and Hotamisligil, 2008). FABP4 is the most abundant FABP in circulation (Ishimura et al., 2013) and is secreted from adipocytes via a membrane-bound pathway independent of the canonical endoplasmic reticulum-Golgi-plasma membrane secretion pathway (Villeneuve et al., 2018). Secreted FABP4 may serve as an adipokine, and lipolysis increases secretion of FABP4 from adipocytes (Furuhashi et al., 2015). Exogenous FABP4 influences hepatocyte glucose production, insulin secretion by pancreatic β cells, and cellular functions of cardiomyocytes and smooth muscle cells (Furuhashi et al., 2015). Indeed, circulating FABP4 levels are associated with the development of insulin resistance, diabetes, atherosclerosis, cardiac dysfunction, and inflammation (Furuhashi and Hotamisligil, 2008; Ishimura et al., 2013; Furuhashi et al., 2015; Saito et al., 2021). Reduced FABP4 appears to reduce the risk of metabolic and cardiovascular disease (Hotamisligil et al., 1996; Furuhashi and Hotamisligil, 2008; Furuhashi et al., 2015), and, hence, FABP4 has been explored as a potential therapeutic target (Floresta et al., 2017). Due to its small size, FABP4 found in circulation is subject to glomerular filtration, but it accumulates in the kidney via megalin-mediated reabsorption from the tubular lumen (Shrestha et al., 2018). Notably, circulating FABP4 levels also showed a sex difference with females having higher concentrations than males (Ishimura et al., 2013).

FABP5, epidermal FABP, is the major FABP found in the epidermis, but FABP5 tissue expression is broad and not restricted to the skin (Table 1.1). FABP5 mRNA along with FABP3 and FABP4 mRNAs are found in human brain endothelial cells (hCMEC/D3), and FABP5 protein appears to be more abundant than FABP3 and FABP4 in these cells (Lee et al., 2015). FABP7, brain FABP, is largely expressed in the brain and central nervous system but is also found in the skeletal muscle (Shimizu et al., 1997; Veerkamp and Zimmerman, 2001; Owada et al., 2006) with diurnal variation in its expression (Gerstner et al., 2008). FABP7 mRNA in the brain increases during light periods and declines in the dark period. This leads to an accumulation of FABP7 protein in dark periods and a decrease in protein in the light period. Yet the biologic role of this diurnal variation has not been defined.

1.5 XENOBIOTIC LIGANDS OF iLBPS AND METHODS TO CHARACTERIZE LIGAND BINDING

1.5.1 *Known Xenobiotic Ligands of iLBPs and Their Binding Characteristics*

The literature is rich with binding and structural studies of endogenous ligands of iLBPs, but binding of xenobiotics to iLBPs has not been as extensively studied. This is despite clear evidence of xenobiotics binding to iLBPs. For example, synthetic retinoid drugs [agonists of retinoic acid receptors (RAR) and retinoid X receptors] bind to retinoid binding proteins (Ferreira et al., 2020), but the clinical relevance of the binding is not known. Whether retinoid binding proteins bind other classes of therapeutic drugs has not been explored. The majority of xenobiotic binding studies with iLBPs have been done with FABPs, likely due to their broad ligand specificity and high expression in tissues relevant to drug disposition and pharmacological activity. Of the 10 FABPs, xenobiotics have been shown to bind to FABP1–5 and FABP7 in vitro (Table 1.2). Xenobiotic binding to FABP6, 8, 9, and 12 has not been reported to our knowledge.

Initial binding studies of lipophilic drugs to FABP1 and FABP2 were done to explore the potential of FABP1 and 2 to facilitate drug absorption into enterocytes (Velkov et al., 2005, 2007; Chuang et al., 2008). A broad range of therapeutic drugs such as nonsteroidal anti-inflammatory drugs, peroxisome proliferator-activated receptor (PPAR) agonists (fibrates and glitazones), and benzodiazapines were shown to bind to FABP1 and FABP2 (Table 1.2). Additionally, due to the high expression of FABP1 in the liver, the role of FABP1 binding as the rate-limiting step in hepatocyte uptake has been explored (Rowland et al., 2015). FABP3, 4, and 5 were found to be expressed in brain endothelial cell lines, and hence, the potential of drugs to bind to these FABPs at the blood-brain-barrier was evaluated (Lee et al., 2015). Similar drugs were shown to bind to FABP3, 4, and 5 as to FABP1 and FABP2. Xenobiotic cannabinoids Δ9-tetrahydrocannabinol and cannabidiol also bind to FABP1 and the brain FABPs, FABP3, 5, and 7 (Elmes et al., 2015, 2019; Huang et al., 2018). Due to its role in metabolic disease, FABP4 has become a potential therapeutic target, and a variety of inhibitor ligands have been developed and their binding to FABP4 characterized (Floresta et al., 2017).

FABP1 has been a focus of binding and structural studies with PPAR agonists (fibrates, glitazones, and synthetic agonists) to probe PPAR binding specificities as they relate to interactions with residues within the binding cavity of FABP1. Ester and carboxylic acid fibrates showed distinct differences in chemical shift perturbations (CSPs) within the FABP1 binding cavity in NMR studies (Chuang et al., 2009). Carboxylic acid fibrates showed significant CSPs with residues S39, R122, S124 in FABP1 that directly interact with the carboxylate of fatty acids while ester fibrates showed far less CSPs at these residues. Additionally, thermodynamic analysis showed that binding of carboxylic acid fibrates to the high affinity site of FABP1 was mainly driven by enthalpic interactions while ester fibrate binding had a much larger entropic component (Chuang et al., 2009). These data suggest that while ionic interactions play a role in the recognition and binding specificity of nonfatty acid ligands, they are not essential for ligand binding. Hydrophobic interactions are a large component of xenobiotic binding to FABP1.

The importance of hydrophobic interactions in ligand binding is evident in structural studies with FABP4 and (S)-ibuprofen (Figure 1.5A). (S)-ibuprofen binding to FABP4 is stabilized by both ionic and edge-to-face aromatic interactions with FABP4 sidechains (Figure 1.5, B and C) (González and Fisher, 2015). Similar to binding of endogenous ligands, internal protein dynamics also appear to play an important role in xenobiotic binding to FABPs. NMR solution structures of FABP1 with the synthetic PPAR agonist GW7647 bound (Figure 1.5D) demonstrate that significant sidechain conformational changes occur within the binding cavity of holo-FABP1 upon ligand binding. This is despite there being little change in the overall backbone structure with ligand binding (Patil et al., 2019). Knowledge of the structures and ligand binding characteristics of individual FABPs can aid in designing FABP isoform specific ligands. For example, the synthetical FABP4 ligand BMS309403 binds to FABP4 (Figure 1.5E) with a binding affinity of less than 2 nM but binds to FABP3 and FABP5 with >100-fold weaker affinity (Sulsky et al., 2007).

1.5.2 *Methods to Measure Ligand Binding with iLBPs*

Historically, measuring free ligand concentrations using separation techniques such as Lipidex-1000 (Glatz and Veerkamp, 1983; Vork et al., 1990) was used to determine ligand binding affinities to iLBPs that were isolated from tissue homogenates or recombinantly expressed and purified. However, as the concentration of free ligand is decreased via partitioning to Lipidex, these techniques generally disturb the equilibrium between ligand and iLBP, and the binding affinities are generally underestimated (apparent K_d > true K_d) using this technique (Kane and Bernlohr, 1996; Veerkamp et al., 1999). Most of the recent work to characterize xenobiotic binding to iLBPs has been done using in vitro spectrophotometric assays. The following is a brief description of the direct and indirect spectrophotometric approaches to determine xenobiotic equilibrium binding affinities along with potential caveats associated with these methods.

1.5.3 *Direct Binding Assays*

Binding affinities (K_d) of retinoids with retinoid binding proteins are typically determined via direct fluorescence titration assays. These monitor either the increase in retinoid fluorescence upon binding to the binding protein or the quenching of intrinsic protein fluorescence (from tryptophan or tyrosine) as a result of retinoid binding (Fiorella et al., 1993; Norris et al., 1994; Wang et al., 1997; Dong et al., 1999; Vogel et al., 2001; Folli et al., 2002; Yabut and Isoherranen, 2022). These methods work well for retinoid binding proteins such as CRBP1, CRABP1, and CRABP2, which have five or more fluorescent (tryptophan and tyrosine) amino acids in their primary sequence. The intrinsic fluorescence spectra of tryptophan and tyrosine (excitation peak 280–290 nm, emission peak 330–355 nm) and the fluorescence spectra of retinoids (excitation peak 348–360 nm and emission peak 450–480 nm) (MacDonald and Ong, 1987; Fiorella and Napoli, 1991; Dong et al., 1999; Herr et al., 1999; Folli et al., 2002) are amenable for monitoring binding via fluorescence resonance energy transfer from protein to retinoid ligands (Peterson and Rask, 1971).

Because retinoids bind to retinoid binding proteins tightly (nanomolar affinities), performing the fluorescence titrations under steady state assumptions can be challenging. Relatively low concentrations of protein (ideally subnanomolar) are necessary to obtain accurate K_d value estimates, and hence protein fluorescence signal and instrument (fluorimeter) sensitivity can become a limitation. Therefore, retinoid binding assays are often done with protein concentrations that are much greater than the estimated K_d values. This approach may lead to inaccuracies in K_d estimates. These inaccuracies may be compounded by the use of kinetic binding models that assume steady state and that ligand binding to the binding protein does not alter free ligand concentrations in solution ($[L]_{total} \approx [L]_{free}$). These experimental challenges likely partially explain the wide range of binding affinities reported in the literature (Norris et al., 1994; Napoli, 2016). The impact of protein concentrations and model fitting on the error in determination of the K_d values is illustrated in Figure 1.6. For an iLBP-ligand interaction with a true K_d of 10 nM, using 100 nM iLBP protein (10-fold >K_d) in the experiment can result in an error as high as fivefold when a simple binding model ($\% \, iLBP \, bound = \frac{\% \, iLBP \, Bound_{max} \times [L]}{K_d + [L]}$) is fit to the data (Figure 1.6B). The error becomes negligible when the quadratic binding equation ($\% \, iLBP \, bound = \% \, iLBP \, bound_{max} \frac{[P] + [L] + K_d - \sqrt{([P] + [L] + K_d)^2 - 4 \times [P] \times [L]}}{2 \times [P]}$) is fit to the data as it accounts for ligand depletion when the iLBP concentration ranges from 0.01 to 10 times the true K_d value (Figure 1.6B). However, caution should be used when using the quadratic binding equation for tight binding ligands as the dependence of K_d for the model fit becomes negligible when $[P] \gg K_d$, and hence, a K_d estimate may not be meaningful (Jarmoskaite et al., 2020). As such, even when the quadratic equation is used, the K_d values estimated should be assumed to be the upper limit of the true K_d value if the iLBP concentration in the assay exceeds the determined K_d value. Nevertheless, direct fluorescence titration assays have provided extensive information on the ligand binding characteristics and binding specificities of iLBPs.

1.5.4 *Fluorescence Displacement Assays*

Measuring direct protein fluorescence is not always feasible due to a lack of fluorescent amino acids or lack of fluorescence of the ligand. For example, FABP1 has no tryptophan residues and only one tyrosine residue, preventing the use of direct fluorescence measurements in evaluating ligand binding to FABP1. Hence, one approach for measuring direct ligand binding to FABP1 is to introduce tryptophan mutations to increase intrinsic protein fluorescence (Thumser and Wilton, 1994). However, such mutations may also affect ligand binding, and hence indirect fluorescence displacement assays are more commonly used.

Indirect measurements of ligand binding have been a common approach for estimating binding affinities for FABPs (Schug et al., 2007; Smathers and Petersen, 2011; Kaczocha et al., 2012;

Elmes et al., 2015, 2019; Huang et al., 2016, 2018; Schroeder et al., 2016). Fluorescence displacement assays using fluorescent probes such as ANS or fluorophore conjugated fatty acids such as 11-(dansylamino)undecanoic acid and nitrobenzoxadiazole-stearate are commonly used due to the low intrinsic fluorescence of FABPs and the lack of measurable fluorescence from fatty acid ligands upon FABP binding. In these assays, a fluorescent probe is first bound to the FABP at a predetermined concentration, and the shift in the fluorescence of the ligand upon protein binding is measured. The drug of interest is then titrated into the sample, and the decrease in the probe fluorescence due to probe displacement by the drug is measured. Because displacement of the probe is assumed to be a purely competitive interaction, inhibitory constants (K_i) are determined either from a direct fit of a competitive binding model to the fluorescence data or are calculated from IC_{50} values assuming competitive inhibition (Velkov et al., 2005; Chuang et al., 2008; Lee et al., 2015; Elmes et al., 2019). Interfering fluorescence at similar wavelengths as the probe from the ligand of interest should be considered in these assays as this may confound the binding data. For example, *at*RA has a similar fluorescence emission peak (475 nm) as the fluorescent probe ANS (480 nm) with excitation wavelengths at 350 and 380 nm, respectively (Fiorella et al., 1993; Huang et al., 2014; Vogler, 2015). This fluorescence overlap may affect the interpretation of ANS displacement data for *at*RA binding to FABPs.

For most FABPs the assumption of competitive binding is likely appropriate as only one ligand appears to bind at a time to FABPs (Figures 1.4 and 1.5). However, with FABP1, which can have multiple ligands bound to it simultaneously (Figure 1.4B), a simple competitive binding model may not be appropriate, and EC_{50} or IC_{50} values determined with ligand displacement assays with FABP1 should not be directly translated to K_d or K_i values. It is possible that a ligand can bind simultaneously with a fluorescent probe to the FABP1 or that the binding of one fluorescent probe molecule affects the binding affinity of the ligand tested that may bind to a second binding site.

Similar concerns may be relevant for FABP2, although endogenous ligands appear to bind to FABP2 with 1:1 stoichiometry, possibly due to the size of the ligands. In FABP2, ANS and ketorolac have been shown to bind to different binding sites based on fluorescence and isothermal titration calorimetry data (Patil et al., 2014). This suggests that the two ligands could also bind simultaneously. However, there is currently no structural evidence that two ligands bind to FABP2 simultaneously. In the case of FABP1 and FABP2, it is unclear whether it is possible for a ligand to bind to the second binding site without affecting the binding of the fluorescent ligand in the first, high affinity binding site. The probe fluorescence intensity or the wavelength maxima of the probe fluorescence may be allosterically affected by binding of a ligand at an additional binding site, or complete displacement of the fluorescent probe may only occur when all binding sites are occupied by the xenobiotic ligand. Hence, alternative kinetic binding models may be more appropriate than a purely competitive one.

Like the direct binding assays described here, limitations with fluorescence signal, instrument sensitivity, and protein and probe concentrations should be carefully considered with displacement assays. Figure 1.6C shows simulated fluorescence displacement assay where the true affinity for the probe (K_d) and test ligand (K_i) are the same (10 nM). Using an iLBP concentration of 100 nM (10-fold greater than the K_d) can result in a >10-fold error in the estimated K_i value, illustrating the potential confounding effects of experimental design on the data collected (Figure 1.6, C and D).

1.6 IMPACT OF iLBPS ON LIGAND DISTRIBUTION AND METABOLISM

One of the biologic functions of iLBPs is to serve as lipid carriers that bind, solubilize, and shuttle their ligands to relevant cellular compartments (Storch and Corsico, 2008; Storch and Thumser, 2010). iLBPs may simply bind their often unstable or toxic ligands to stabilize the ligand or prevent ligand interactions with nonspecific proteins in a cell. However, iLBPs have been shown to interact with phospholipid membranes, associate with cellular compartments such as mitochondria and lysosomes, and interact with different metabolic enzymes and nuclear receptors, suggesting more broad functions in a cell. Three different mechanisms for the impact of iLBPs on ligand disposition have been proposed (Figure 1.7) (Smith and Storch, 1999; Storch and Corsico, 2008). In the first model, the iLBPs release their ligands to solution (diffusional model). Alternatively, iLBPs may interact with the phospholipid membranes via direct protein-membrane interactions to accept their ligands from or release their ligands directly to the membrane (collisional model). Finally, iLBPs may participate in direct protein-protein interactions and channel their ligands directly to catalytic enzymes or transporters. Since FABPs are highly expressed in tissues relevant to xenobiotic disposition, it is likely that xenobiotics bind to FABPs in these tissues, and the three models of iLBP functions may also be relevant for xenobiotic disposition. The following sections summarize various studies on the impact of iLBPs on ligand distribution and metabolism and the possible mechanisms of ligand delivery.

1.6.1 *Impact of FABPs on Ligand Uptake into Tissues*

The role FABPs have in regulating the uptake and tissue distribution of their endogenous ligands has been studied for many FABPs to which xenobiotic ligands also bind. It is well established that FABP1 facilitates lipid uptake into the liver, and FABP1 expression in the liver correlates with uptake of fatty acids (Kushlan et al., 1981; Hung et al., 2003; Newberry et al., 2003). Induction of FABP1 expression by PPAR agonists in HepG2 cells resulted in increased rates of oleate uptake, while knocking down FABP1 expression significantly reduced rates of uptake (Wolfrum et al., 1999). Changes in uptake appear to also alter lipid metabolic products. FABP1-knockout mice have decreased rates of [H]3oleate uptake to the liver, which corresponds to decreased fatty acid β-oxidation and incorporation of [H]3oleate into triglycerides (Newberry et al., 2003). In rat perfused livers, higher expression of FABP1 in the liver correlated with greater palmitate clearance and higher retention of palmitate and its metabolites in the liver (Hung et al., 2003). Similarly, FABP5 and FABP7 that are expressed in the brain appear to enhance endocannabinoid uptake into cells and endocannabinoid metabolism. The cellular uptake of AEA and subsequent metabolism by fatty acid amide hydrolase was greater in N18TG2 (mouse neuroblastoma) and COS-7 cells transfected with FABP5 and FABP7 when compared to mock transfected cells while FABP3 had no effect (Kaczocha et al., 2009).

FABP2 appears to play a role in the cellular uptake and distribution of xenobiotic ligands in the gut, and many orally administered drugs bind to FABP2 (Table 1.2). The potential role of FABP2 in modulating apical and basolateral transport of drugs in the intestine was studied in the parallel artificial membrane permeability assays where an artificial phospholipid membrane separates donor and acceptor reservoirs (Velkov et al., 2007). These studies were designed to test the effect of FABP2 on the rates of diffusion across an artificial phospholipid membrane mimicking the apical membrane of enterocytes. For apical membrane permeability, drugs were added to the donor side, and physiological concentrations of FABP2 in the enterocytes (0.33 mM) were present on the acceptor side. The rates of drug uptake from the apical membrane were increased for drugs that bound to FABP2, with tighter binding drugs showing higher rates of uptake. This suggests FABP2 may facilitate drug absorption in the small intestine. In support of these findings, FABPs appear to also increase rates of drug uptake in perfused rat intestines. In rats, FABP1 and FABP2 mRNA expression in the gut increased approximately 1.5- to twofold by feeding a high-fat diet. Compared with control-fed rats, this higher expression of FABP1 and FABP2 correlated with nearly twofold higher rates of disappearance of ibuprofen (disappearance Papp 158 versus 97 × 106 cm/s) and midazolam (disappearance Papp 239 versus 143 × 106 cm/s) from intestinal perfusate and increased accumulation of the drugs in the intestinal tissue (Trevaskis et al., 2011). This suggests that FABPs may facilitate the uptake of these drugs into the enterocytes (Trevaskis et al., 2011). Interestingly, significantly less 4-hydroxy-midazolam was quantified in mesenteric blood in animals with elevated FABP, and the extraction ratio of midazolam by the intestine was decreased from 11% to 7% in rats with higher FABP1 expression compared with control-fed rats. This suggests that midazolam likely bound to FABP1 in the enterocytes, altering midazolam metabolism in the enterocytes (Trevaskis et al., 2011). Despite these findings, the contribution of FABPs to rate and extent of drug absorption has received relatively little attention.

The potential impact of FABP binding on drug distribution is clear from the high expression of FABPs in different tissues and the capacity of FABPs for drug binding in a variety of tissues throughout the body. Binding of numerous drugs that target the central nervous system to FABP3, FABP4, and FABP5, which are expressed in the brain, was proposed to impact the distribution of drugs across the blood-brain barrier (Lee et al., 2015). This process is similar to the regulation of endogenous docosahexaenoic acid concentrations in the brain by FABP5 (Pan et al., 2015, 2016). Current models (Utsey et al., 2020) for predicting tissue distribution of drugs and tissue partition coefficients (Kp values) do not account for specific protein binding sinks in tissues, and hence extensive FABP binding in any tissue is not considered when distribution kinetics are modeled. As physiologically based pharmacokinetic models of drug distribution become more mainstream, incorporation of FABP binding into tissue distribution models and considering FABP binding when rates of distribution are considered will become increasingly important.

1.6.2 *Ligand Delivery to Membranes*

It remains unclear whether the observed changes in lipid metabolism that correlate with FABP expression are simply because FABPs provide an intracellular reservoir to increase uptake of their ligands to cells and, hence, the availability of ligands to sites of metabolism (diffusional model, Figure 1.7A) or if FABPs deliver ligands via specific interactions to enzymes or to cellular membranes. The mechanism of ligand transfer from FABPs to model phospholipid membranes has been studied for FABPs 1–5 using fluorescent fatty acids as ligands (Storch and Thumser, 2000). The rates of ligand transfer from FABPs to phospholipid membranes could be measured via quenching of fluorescence upon fatty acid ligand incorporation into the phospholipid membrane. The rate of ligand transfer from FABP1 to acceptor membranes was not affected by the concentrations or composition of phospholipid. However, FABP1 transfer rates were substantially impacted by the ionic strength of the surrounding aqueous medium. These data suggest that FABP1 does not interact directly with phospholipid membranes and that ligand delivery to model membranes requires release of ligand into solution (Hsu and Storch, 1996).

In contrast, the transfer rates of FABPs 2–5 were proportional to phospholipid concentration in acceptor membranes and affected by membrane phospholipid composition (Kim and Storch, 1992; Wootan et al., 1993; Hsu and Storch, 1996; Storch and Thumser, 2000). FABP2 was shown to also accept fatty acids from donor membranes. Faster fatty acid transfer rates from donor membranes to FABP2 were observed with negatively charged membranes compared with zwitterionic membranes (Thumser and Storch, 2000). Taken together, these data suggest that FABPs 2–5 directly deliver their ligands to phospholipid membranes via ionic interactions. The structural basis for this interaction has been elucidated with mutagenesis studies with FABP2. These studies suggest that the alpha-helical domain in FABP2 is important for these interactions (Corsico et al., 1998; Falomir-Lockhart et al., 2006). The rate of fatty acid transfer from a helix-less FABP2 variant to phospholipid model membranes was unaffected by increasing phospholipid concentration compared with WT, suggesting the loss of the helices also eliminates the membrane interactions (Corsico et al., 1998). Additionally, WT FABP2 could outcompete cytochrome c interactions with anionic membranes, but this function was severely disrupted with the helix-less variant. These findings were corroborated with later mutational studies showing that charged lysine residues in the alpha-helical region are critical for efficient fatty acid transfer (Falomir-Lockhart et al., 2006). The significance of this protein-membrane interaction in vivo is unknown but may play a role in the uptake and targeting of ligands to specific cellular organelles (Hsu and Storch, 1996).

1.6.3 *Ligand Delivery by iLBPs to Enzymes and Receptors*

The role of iLBPs in delivering their ligands to metabolic enzymes or receptors via protein-protein interactions and substrate channeling has been most extensively studied with the retinoid binding proteins (Napoli, 2017). Possibly due to the reactivity and potential toxicity of retinoids, the retinoid binding proteins appear to modulate and direct retinoid metabolism and signaling via a network of protein-protein interactions. Extensive kinetic and metabolic studies have been conducted (Napoli, 2016, 2017) in rat and human intestinal and liver microsomes with holo-CRBPs. In these studies, despite the tight binding of the ligands with the CRBPs, the apparent K_m values for the total ligand are often significantly decreased or unaltered when the ligand is entirely bound to the CRBP in comparison with free ligand (Ong et al., 1987; Herr et al., 1999; Napoli, 2016, 2017). This kinetic data cannot be explained by the diffusional model (free drug hypothesis) and have been interpreted through protein-protein interactions between the CRBPs and retinoid metabolizing enzymes. Consistent with the protein-protein interaction model, apo-CRBP1 appears to also inhibit retinol esterification by lecithin retinol acyltransferase enzyme suggesting a function of the apo-CRBP1 in regulating metabolism even in the absence of its ligand. These data suggest that the ratio of apo- to holo-CRBP1 or the ratio of CRBP1 to its ligand may have an important role in regulating vitamin A homeostasis in the cell. This concept is illustrated via kinetic simulations in Figure 1.8. Yet these observations are limited to endogenous retinoids and their specified metabolic enzymes, and the importance to drug metabolism by major drug-metabolizing enzymes is unknown.

Protein-protein interactions between CRABPs and nuclear RARs have also been extensively studied (Dong et al., 1999; Budhu et al., 2001; Schug et al., 2007; Majumdar et al., 2011). Expression of CRABP2 but not CRABP1 in Cos7 cells enhances RAR transactivation (Dong et al., 1999), and the transfer rate of *at*RA from CRABP2 to RAR appears to be dependent on RAR acceptor concentration while transfer rates from CRABP1 are unaffected by changes in RAR concentration. Holo-CRABP2 also appears to translocate to the nucleus via a SUMOylation dependent mechanism to channel *at*RA directly to RAR (Majumdar et al., 2011). These findings demonstrate the potential role that iLBPs may have in cellular targeting of their ligands and delivery of their ligands to target receptors, and suggest that iLBP interaction may be protein specific.

The impact of the CRABPs on *at*RA hydroxylation has also been studied in rodent microsomes (Napoli et al., 1991; Fiorella and Napoli, 1994), with recombinant drug metabolizing CYPs, CYP3A4, and CYP2C8 and with the *at*RA hydroxylases CYP26A1, CYP26B1, and CYP26C1 (Nelson et al., 2016; Zhong et al., 2018; Yabut and Isoherranen, 2022). Recently holo-CRABP2 was also shown to be a substrate of CYP27C1, a retinoid desaturase in the skin (Glass and Guengerich, 2021). As expected from the tight binding of *at*RA to CRABP1 and CRABP2, CYP3A4 and CYP2C8 mediated metabolism of *at*RA was nearly completely abolished when *at*RA was bound to the CRABPs, consistent with the free drug hypothesis (Nelson et al., 2016; Yabut and Isoherranen, 2022). However, with the CYP26 enzymes, efficient *at*RA formation was observed also when *at*RA was completely bound to CRABPs. The apparent K_m values for holo-CRABPs were either unchanged or decreased when compared with free ligand in solution. Surprisingly the k_{cat} values for *at*RA hydroxylation were also significantly decreased in the presence of CRABPs for all three CYP26 enzymes. This suggests that apo-CRABPs inhibit CYP26 enzymes via a noncompetitive mechanism similar to the inhibition observed between CRBPs and lecithin retinol acyltransferase. The observed kinetics could be explained using a substrate channeling model incorporating direct protein-protein interactions between CYP26 and apo- and holo-CRABPs (Nelson et al., 2016; Yabut and Isoherranen, 2022).

The binding protein (CRBP, CRABP)-enzyme interactions may be critical modulators of ligand metabolism and vitamin A homeostasis in cells in a ligand concentration dependent manner, and the phenomenon may be important for other iLBPs as well. This hypothesis was explored via kinetic simulations of the effect of the binding protein-ligand ratio on the metabolic rates and ligand clearance in a cell (Figure 1.8). The simulations show how altered expression of the binding proteins will change ligand metabolism and concentrations through direct protein-protein interactions between the apo- and holo-binding protein and the metabolic enzyme. When substrate is in excess to the binding protein, the substrate is relatively freely metabolized (Figure 1.8, blue and green lines) allowing for homeostasis to be maintained. However, under circumstances of substrate deficiency when the binding protein is in excess to substrate, nearly all of the enzyme is bound by the apo-binding protein, severely inhibiting metabolism (Figure 1.8, red and purple lines).

In addition to the retinoid binding proteins, the FABPs have also been shown to directly interact with nuclear receptors and metabolic enzymes. Similar to holo-CRABP2 channeling *at*RA to RARs, FABP1, FABP4, and FABP5 have been shown to translocate to the nucleus upon ligand binding to enhance PPAR transactivation (Wolfrum et al., 2001; Tan et al., 2002; Schug et al., 2007; Hostetler et al., 2009; Velkov, 2013). Physical interactions between FABPs and PPARs have been demonstrated using biochemical and biophysical assays (coimmunoprecipitation, circular dichroism, fluorescence resonance energy transfer, and NMR). These studies suggest that FABP-PPAR interactions are protein specific. FABP1, FABP4, and FABP5 specifically activate and interact with PPARα, PPARγ, and PPARβ, respectively, and the extent of transactivation appears to be ligand dependent.

FABP4 and FABP5 have been shown to directly interact with hormone sensitive lipase (HSL) (Jenkins-Kruchten et al., 2003; Storch and Corsico, 2008; Storch and Thumser, 2010) to promote the liberation of free fatty acids from triglycerides in times of fatty acid scarcity. FABP4 and FABP5 showed ligand dependent interactions with HSL in isothermal titration calorimetry experiments and increased HSL catalytic activity by approximately twofold (Jenkins-Kruchten et al., 2003). Similarly, FABP1 has been shown to interact with carnitine palmitoyl transferase I (CPTI), a key mitochondrial enzyme for fatty acid β-oxidation (Hostetler et al., 2011). Significant deviation from the theoretical circular dichroism (CD) spectra of the C-terminal and active domain of CPTI was observed in the presence of FABP1. The affinity (K_d) between FABP1 and CPTI was 2.5 nM as determined by fluorescence resonance energy transfer binding assays. Notably, FABP1 enhanced CPTI activity to metabolize LCFA-CoA to LCFA-carnitine demonstrating facilitation of the rate-limiting step in fatty acid β-oxidation. Given the broad binding specificity of FABP1 and FABP2 for various xenobiotics and their high abundance in the liver and intestine, it is likely that FABPs also impact drug metabolism via similar mechanisms in vivo. This hypothesis is supported by the finding that FABP1 binds Δ9-tetrahydrocannabinol and the rate of Δ9-tetrahydrocannabinol metabolism is altered in FABP1-knockout mice (Elmes et al., 2015).

While FABP interactions with transporters have not been extensively studied, several groups have reported that FABP4 directly interacts with the fatty acid uptake transporter CD36 to mediate fatty acid metabolism (Spitsberg et al., 1995; Glatz and Luiken, 2018; Gyamfi et al., 2021). CD36 appears to act as an intracellular docking site for FABP4 to facilitate fatty acid transfer to the cytoplasm where FABP4 may then shuttle fatty acids to the peroxisomes or mitochondria for fatty acid metabolism.

1.7 CONCLUSIONS AND KNOWLEDGE GAPS

iLBPs are small binding proteins ubiquitously expressed in tissues, which bind a variety of lipophilic compounds and facilitate the cellular uptake, diffusion, and subsequent metabolism of their endogenous ligands. Yet despite the plethora of work that exists to define biochemical functions of iLBPs, their impact on xenobiotic disposition is poorly defined, and very few studies have explored the binding characteristics of various drugs with FABPs. Many xenobiotics also bind to FABPs that are highly expressed in major organs that govern drug absorption and clearance with micromolar to submicromolar affinity in vitro. Based on the high expression of FABPs (up to 11% of all cytosolic protein), it is likely that FABPs also bind xenobiotics in vivo.

The importance of FABP binding in drug disposition is not understood; however, limited studies have shown that absorption and clearance of drugs that bind to FABPs is linked to FABP expression in animal models. These findings suggest that FABPs have the potential to be determinants of xenobiotic disposition. Variability in FABP binding/expression may explain some intra- and interindividual variability in drug disposition as FABP expression changes with diet, disease states, and administration of other therapeutics. Whether FABPs directly affect xenobiotic access to drug-metabolizing enzymes remains a knowledge gap. It is unclear if FABPs may simply provide an intracellular "sink" to increase the partitioning and availability of free drug accessible for metabolism within cells or if FABPs directly interact with metabolic enzymes to alter rates of drug metabolism. Further studies are needed to elucidate these mechanisms, which would provide insight into how FABPs may regulate xenobiotic disposition.

1.8 HYPOTHESIS AND AIMS

The overarching hypothesis for this thesis was that intracellular lipid binding proteins (iLBPs) bind xenobiotics and facilitate the metabolism of xenobiotics by cytochrome P450 (CYP) enzymes in an enzyme specific manner. CRABPs and their impact on *at*RA metabolism via interactions with CYP26 enzymes, and liver FABP1 and its impact on metabolism of CYP2C9 substrates diclofenac and THC were used as models for testing iLBP-CYP interactions. The aims for each chapter of this thesis are described below.

Chapter 2: I hypothesized that CRABP1 and CRABP2 directly interact with CYP26A1 to regulate the metabolism of *all-trans*-retinoic acid (*at*RA), an endogenous ligand of CRABPs. The aim of this chapter was to establish that CRABP1 and 2 interact with CYP26A1. This aim was accomplished by defining the kinetics of 4-hydroxy-*at*RA (4-OH-*at*RA) formation by CYP26A1 in the presence and absence of CRABP1 and 2. Binding of *at*RA to CRABP1 and 2 was characterized by stopped-flow and the unbound formation kinetics of 4-OH-*at*RA was determined in incubations with recombinant CYP26A1 in the presence and absence of CRABPs. Kinetic analysis of 4-OH-*at*RA formation was performed using a protein-protein interaction model.

Chapter 3: I hypothesized that xenobiotics bind to liver fatty acid binding protein (FABP1) *in vivo* and FABP1 alters the disposition of xenobiotics via direct interactions with CYP enzymes. The aim for this chapter was to determine the binding affinities of xenobiotics with liver FABP (FABP1) and to characterize the effect of FABP1 on xenobiotic metabolism by CYP2C9. The binding affinities of a panel of drugs with FABP1 were determined using fluorescence displacement assay with DAUDA. In addition, the formation of ternary drug-DAUDA-FABP1 complexes was determined using native protein mass spectrometry and the effect of FABP1 binding on diclofenac metabolism by recombinant CYP2C9 was tested.

Chapter 4: I hypothesized that FABP1 alters the relative contribution of CYPs to THC metabolism in the liver. The aim of this chapter was to determine the specific CYPs that contribute to the formation of the primary THC metabolites formed in the human liver and the effect of FABP1 on the formation of THC metabolites by specific CYP enzymes. The binding affinity of THC and other cannabinoids with FABP1 were determined using fluorescence displacement assay with DAUDA and the formation kinetics of 11-hydroxy-THC and THC metabolites M2-M4 by recombinant CYPs were defined in the presence and absence of FABP1. The impact of FABP1 on the relative contribution of CYPs toward THC metabolism was also determined in human liver microsomes.

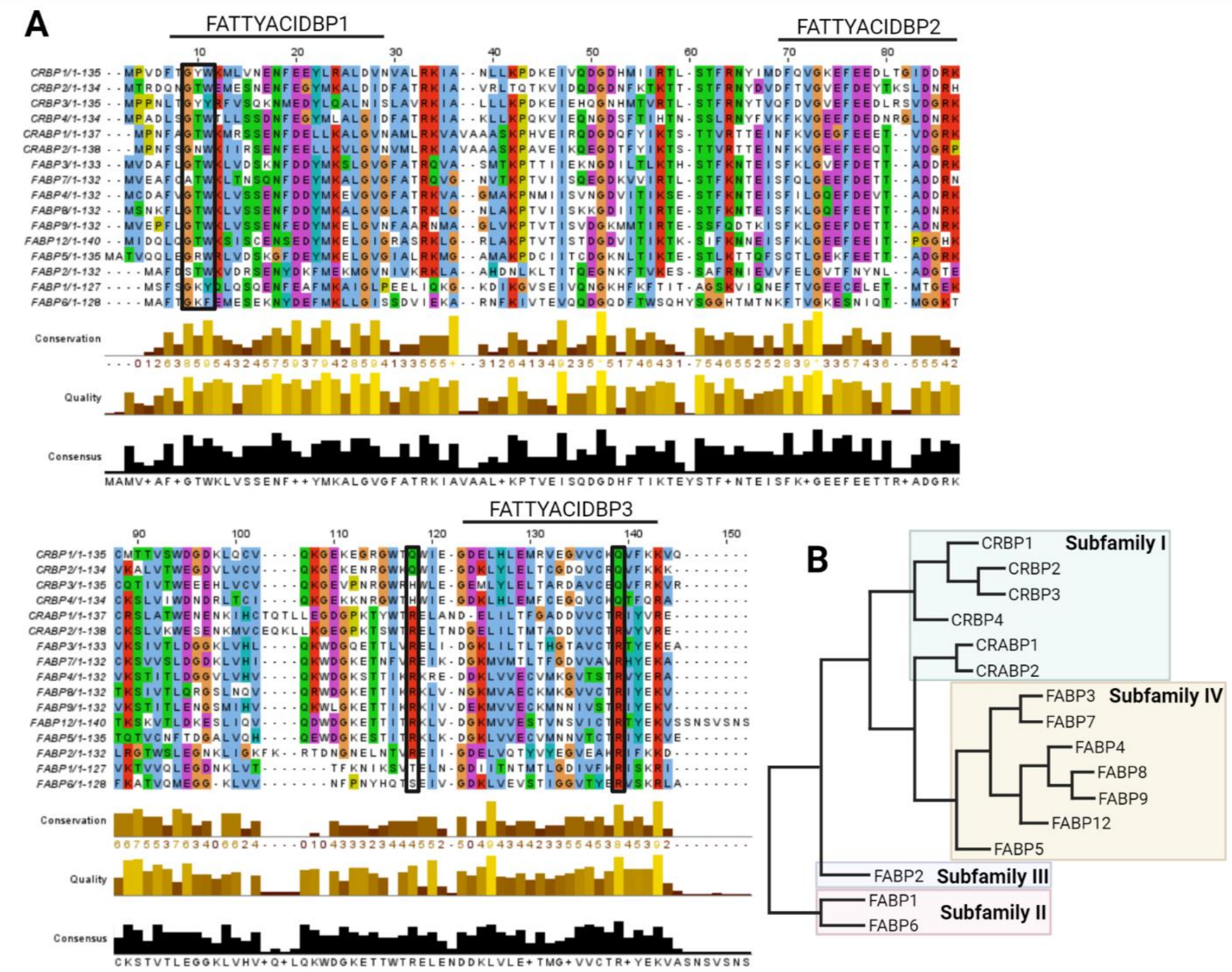A
FATTYACIDBP1
FATTYACIDBP2
FATTYACIDBP3
CRBP1/1-135
CRBP2/1-134
CRBP3/1-135
CRBP4/1-134
CRABP1/1-137
CRABP2/1-138
FABP3/1-133
FABP7/1-132
FABP4/1-132
FABP8/1-132
FABP9/1-132
FABP12/1-140
FABP5/1-135
FABP2/1-132
FABP1/1-127
FABP6/1-128
Conservation
Quality
Consensus
B
CRBP1
CRBP2
CRBP3
CRBP4
CRABP1
CRABP2
Subfamily I
FABP3
FABP7
FABP4
FABP8
FABP9
FABP12
FABP5
Subfamily IV
FABP2
Subfamily III
FABP1
FABP6
Subfamily II

Figure 1.1. Sequence alignment (A) and phylogenetic tree (B) of human iLBPs.
The primary amino acid sequences for all human iLBP family members were collected from the National Center for Biotechnology Information protein database (https://www.ncbi.nlm.nih.gov/protein/). The accession numbers for the amino acid sequences used were P09455.2 (CRBP1), P50120.3 (CRBP2), NP_113679.1 (CRBP3), Q96R05.1 (CRBP4), P29762.2 (CRABP1), P29373.2 (CRABP2), P07148.1 9 (FABP1), P12104.2 (FABP2), P05413.4 (FABP3), P15090.3 (FABP4), Q01469.3 (FABP5), P51161.2 (FABP6), O15540.3 (FABP7), P02689.3 (FABP8), Q0Z7S8.1 (FABP9), A6NFH5.2 (FAPB12). The sequences were aligned using Clustal Omega Multiple Sequence Alignment (https://www.ebi.ac.uk/Tools/msa/clustalo/) (Sievers et al., 2011) and visualized using JalView (Waterhouse et al., 2009). The black bars above the sequence alignment show the three motifs (FATTYACIDBP1-3) that make up the highly conserved fingerprint common to all iLBPs. The colored residues indicate conserved residues based on thresholds set by the Clustal X Color Scheme (https://www.jalview.org/help/html/colourSchemes/clustal.html). Red indicates positively charged residues, blue residues are hydrophobic, magenta are negatively charged, green are polar, orange are glycines, yellow are prolines, and cyan are aromatic. Boxed residues indicate locations of a highly conserved G-x-W triplet common to iLBPs and lipocalins and highly conserved residues involved in ionic interactions with hydroxy and carbonyl groups of ligands. The phylogenetic tree shown in (B) was calculated using the UPGMA clustering method in Simple Phylogeny (https://www.ebi.ac.uk/Tools/phylogeny/simple_phylogeny/) using the multiple sequence alignment data for human iLBPs. Evolutionary distances and phylogenetic relationships should not be inferred from this tree. (Figure created with BioRender.com.)

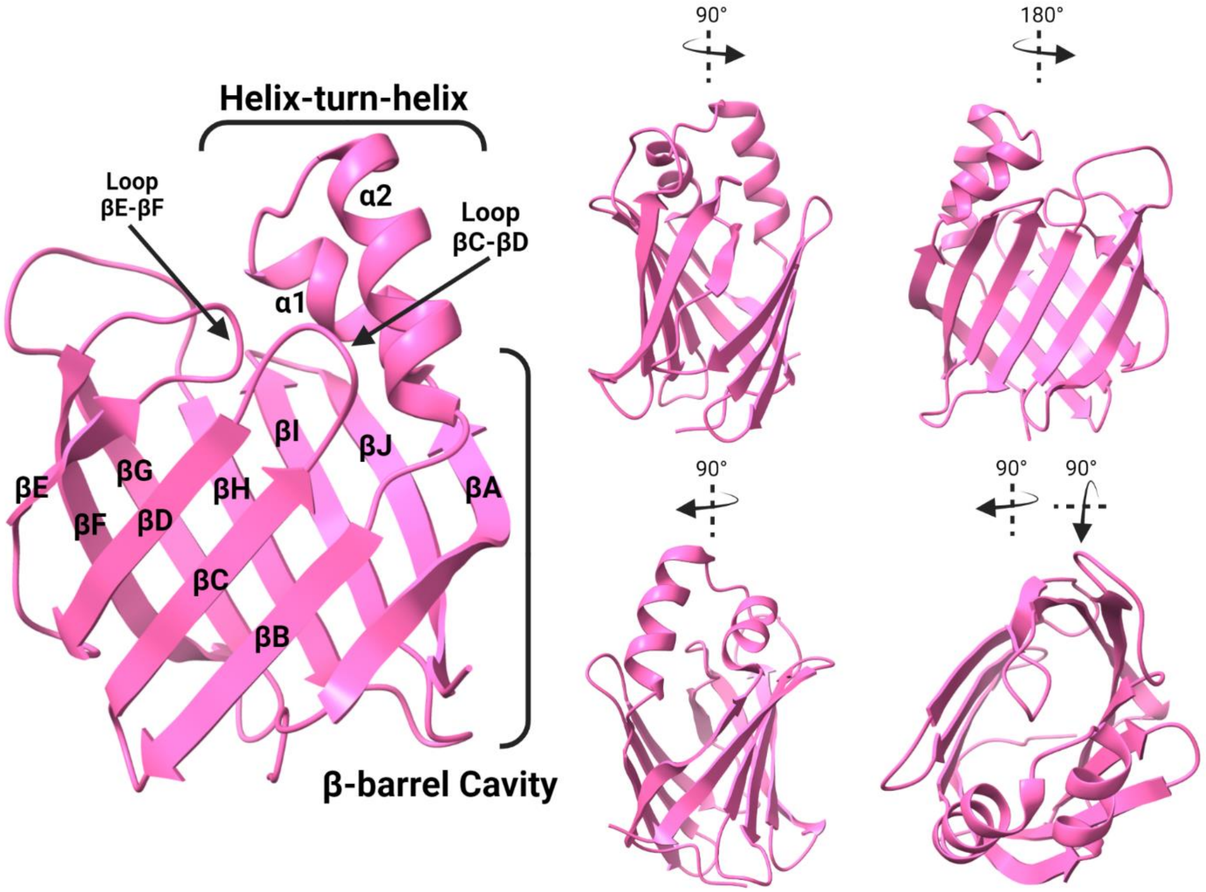

Figure 1.2. The crystal structure of human holo-CRABP2 (PDB 1CBS) showing the overall structural features of iLBPs.

The figure shows the β-barrel cavity composed of 10 β-strands (βA-βJ), the helix-turn-helix cap consisting of the alpha helices (α1 and α2) and the portal to the ligand binding domain with the neighboring loops (loop βC-βD and βE-βF). Two β-sheets, each made up of five β-strands, fold to form the β-clam of the iLBP structure. (Structures generated from PDB using ChimeraX; figure created with BioRender.com.)

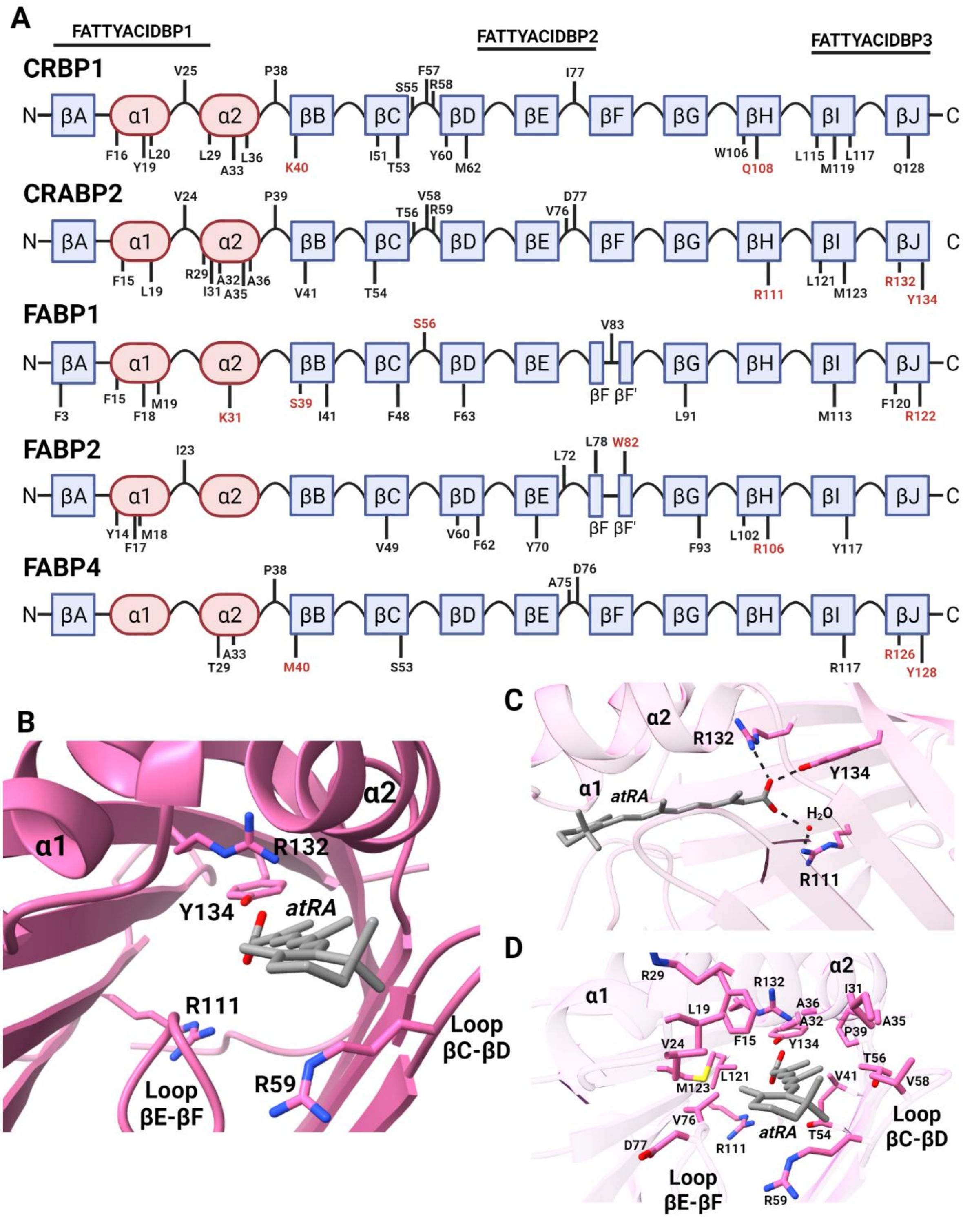
A
FATTYACIDBP1
FATTYACIDBP2
FATTYACIDBP3
CRBP1
N βA α1 α2 βB βC βD βE βF βG βH βI βJ C
V25 P38 S55 F57 R58 I77
F16 Y19 L20 L29 A33 L36 K40 I51 T53 Y60 M62 W106 Q108 L115 M119 L117 Q128
CRABP2
V24 P39 T56 V58 R59 V76 D77
F15 L19 R29 I31 A32 A35 A36 V41 T54 R111 L121 M123 R132 Y134
FABP1
S56 V83
F3 F15 F18 M19 K31 S39 I41 F48 F63 βF βF' L91 M113 F120 R122
FABP2
I23 L72 L78 W82
Y14 F17 M18 V49 V60 F62 Y70 βF βF' F93 L102 R106 Y117
FABP4
P38 A75 D76
T29 A33 M40 S53 R117 R126 Y128
B
α1
α2
R132
Y134
atRA
R111
Loop βC-βD
R59
Loop βE-βF
C
α2
R132
Y134
α1
atRA
H₂O
R111
D
R29
α1
R132
α2
I31
A36
A35
L19
A32
P39
F15
Y134
V24
T56
V58
L121
V41
M123
Loop βC-βD
V76
atRA
T54
D77
R111
Loop βE-βF
R59

Figure 1.3. Binding characteristics of endogenous ligands with iLBPs.
(A) The distribution of residues shown to interact with endogenous ligands for iLBPs are depicted along their structural features. Residues labeled in red font are involved in coordinating with the hydroxy or carbonyl groups of endogenous ligands via ionic interactions. (B) A top-down perspective into the *at*RA binding site of hCRABP2 (PDB 1CBS) with side chains that interact with *at*RA labeled. The position of R111, R132, and Y134 residues that coordinate with the carboxyl group of *at*RA are shown along with the position of R59 which interacts with the β-ionone ring. (C) Side view and positions of residues R111, R132, and Y134 are shown relative to the carboxylate of *at*RA along with hydrogen bonding interactions. (D) The amino acid sidechains that interact with *at*RA and form the *at*RA binding pocket in CRABP2 are shown. (Structures generated from PDB using ChimeraX; figure created with BioRender.com.)

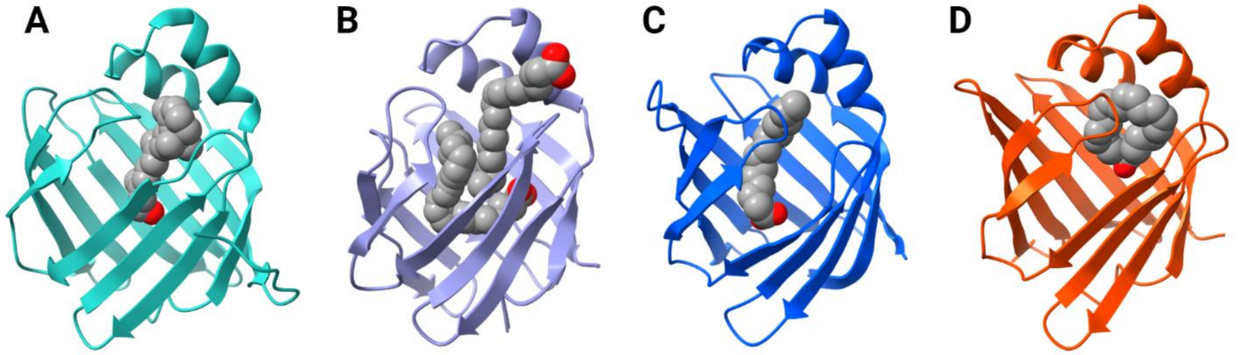

Figure 1.4. Binding orientations of endogenous ligands in the binding cavity of intracellular lipid binding proteins.
Binding orientations is shown for (A) hCRBP1 with all-trans-retinol (PDB 5H8T), (B) hFABP1 with two oleate molecules (PDB 2LKK), (C) rFABP2 with myristate (PDB 1ICM), and (D) mFABP4 with arachidonic acid (PDB 1ADL). (Structures generated from PDB using ChimeraX; figure created with BioRender.com.)

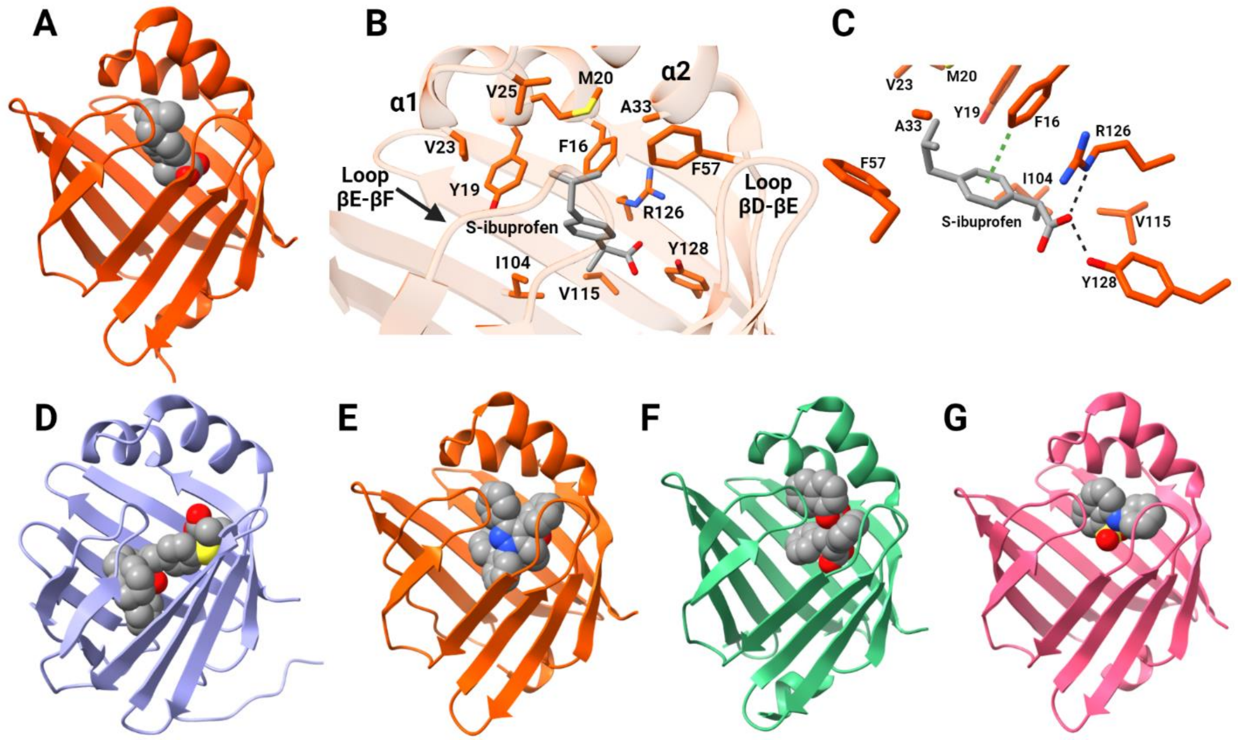

Figure 1.5. Binding characteristics of xenobiotic ligands of FABPs.
(A) Crystal structure of hFABP4 complexed with (S)-ibuprofen (PDB 3P6H). (B) Amino acid side chains that line the binding pocket of (S)-ibuprofen in FABP4. (C) (S)-ibuprofen is stabilized in the binding pocket via ionic interactions between its carboxylate group and R126 and Y128 and edge-to-face aromatic interactions with residue F16 in FABP4. Structures for (D) hFABP1 in complex with PPARα agonist GW7647 (PDB 6DRG), (E) hFABP4 complexed with the inhibitor BMS309403 (PDB 2NNQ), (F) hFABP5 complexed with the antinociceptive SBFI-26 (PDB 5URA), and (G) hFABP3 complexed with ANS (PDB 3WBG). (Structures generated from PDB using ChimeraX; figure created with BioRender.com.)

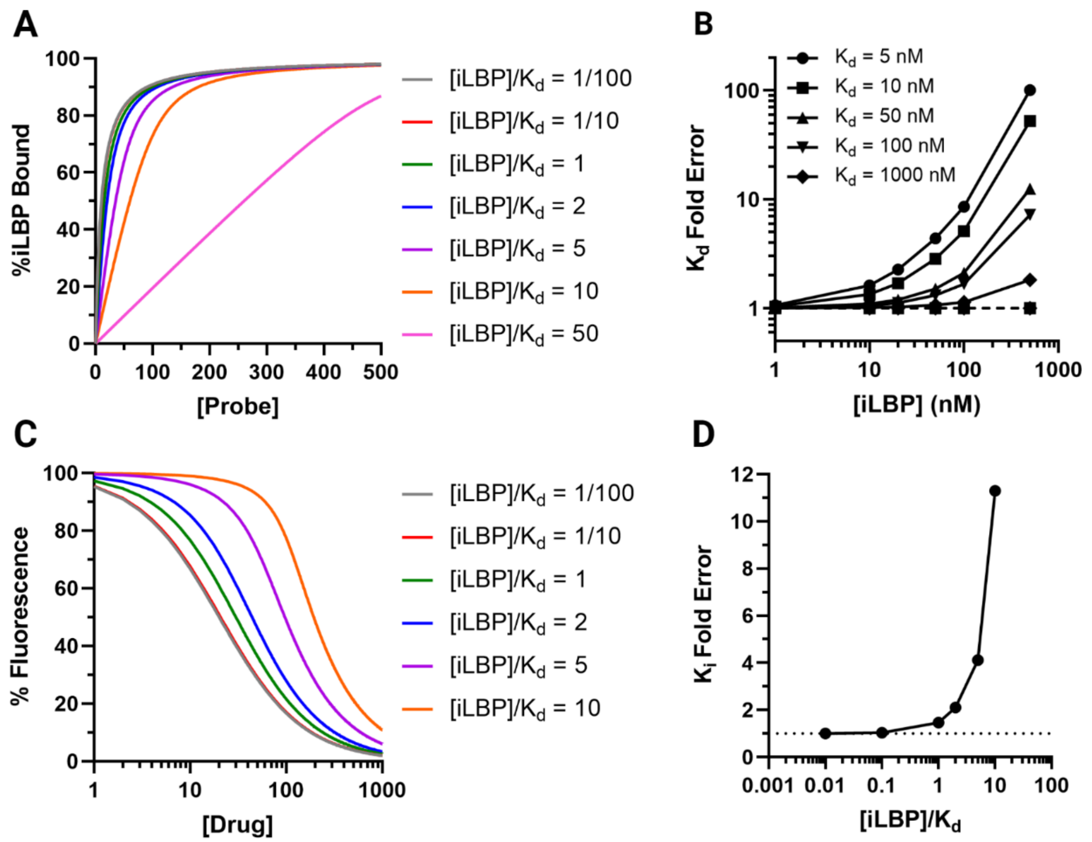

Figure 1.6. Impact of experimental conditions and model fitting on determination of ligand binding affinities.

(A) Simulated binding curves for a hypothetical probe with varying iLBP concentrations for direct titrations. (B) Simulation of the fold error in K$_d$ determination for a hypothetical ligand-iLBP interaction with increasing [iLBP] concentrations used in the binding experiments in relation to different K$_d$ values (symbols) for the ligand. The solid lines show simulated K$_d$ values obtained using a one-site simplified hyperbolic binding equation ($\%\ iLBP\ bound = \frac{\%\ iLBP\ Bound_{max} \times [L]}{K_d + [L]}$) while the dotted line shows the K$_d$ values obtained with a one-site ligand depletion quadratic binding equation ($\%\ iLBP\ bound = \%\ iLBP\ bound_{max}\, \frac{[P] + [L] + K_d - \sqrt{([P] + [L] + K_d)^2 - 4 \times [P] \times [L]}}{2 \times [P]}$) fit to the simulated data. (C) Simulated fluorescence displacement data shown with varying [iLBP] concentrations in relation to the K$_d$ of the fluorescent probe. (D) Simulations of the fold error in K$_i$ determination with varying [iLBP] concentrations relative to the K$_d$ of the fluorescent probe. The K$_d$ used in the simulations for direct binding titrations in (A) was 10 nM. The K$_d$ of the probe and K$_i$ of the drug used in simulations for (C) were 10 and 10 nM, respectively. (Figure created with BioRender.com.) MATLAB code used for simulations is provided in Yabut and Isoherranen, 2023 Supplementary Materials.

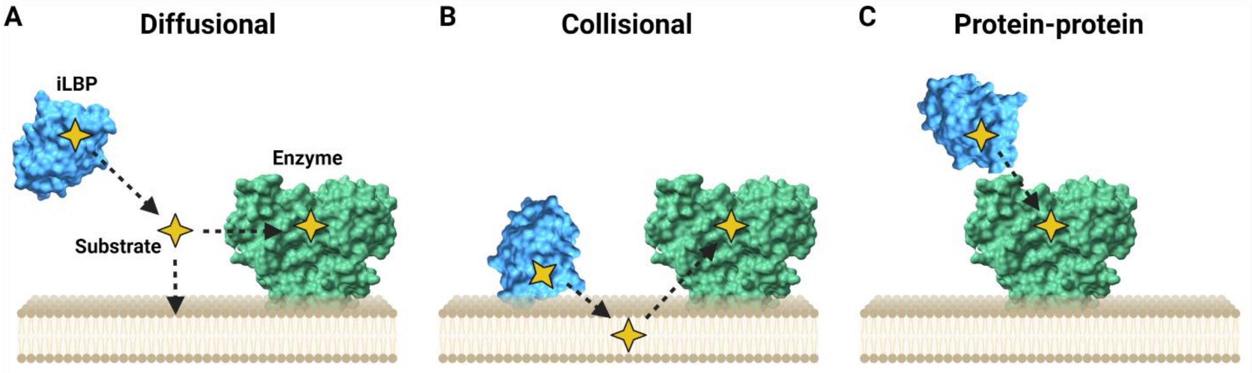

Figure 1.7. Three proposed models of ligand delivery by iLBPs.
(A) The diffusional model requiring ligand release into solution, (B) the collisional model where iLBPs directly interact with phospholipids to transfer substrates to organelle membranes, and (C) direct transfer of substrates to metabolic enzyme via direct protein-protein interactions. (Figure created with BioRender.com.)

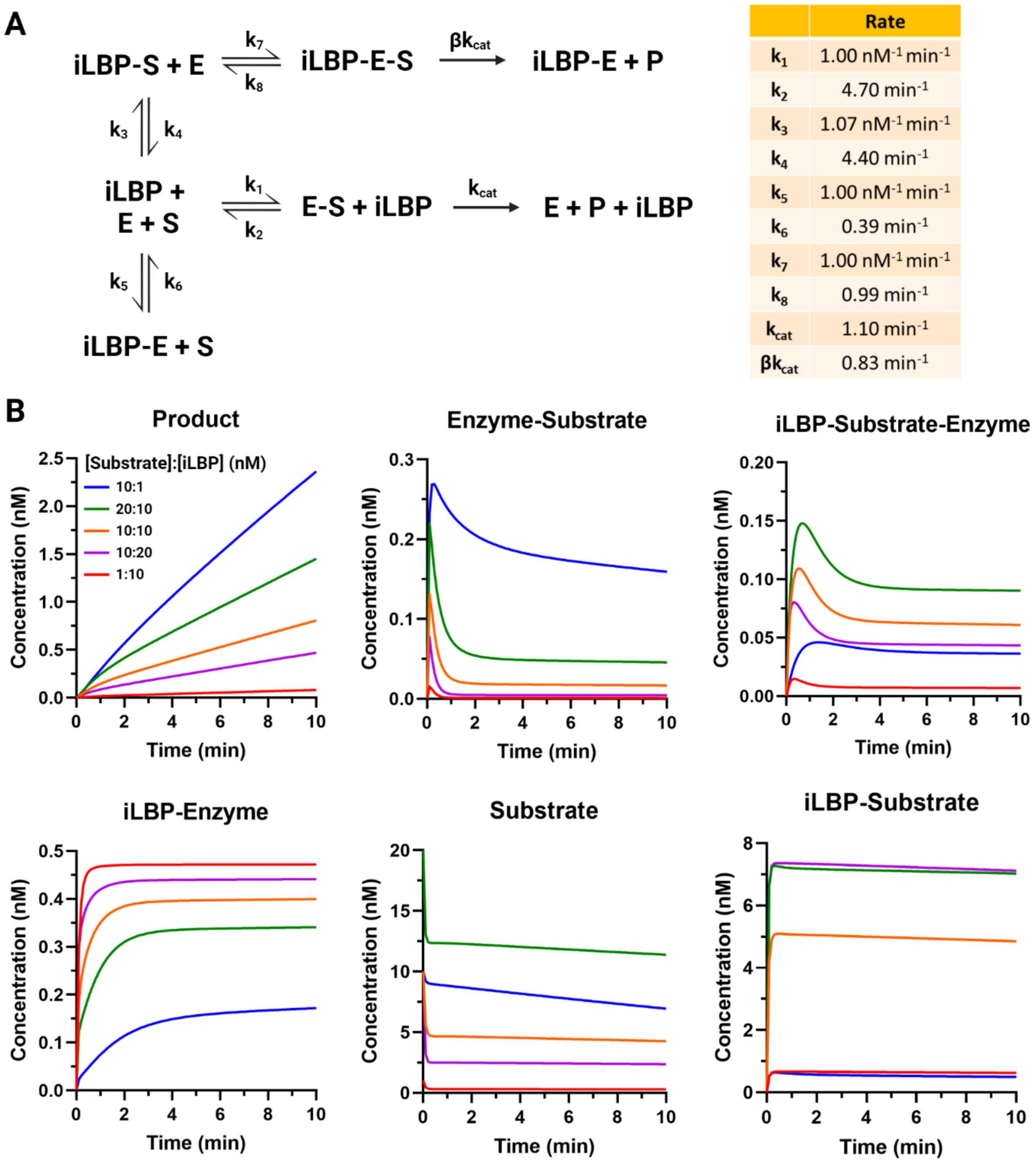

	Rate
k_1	1.00 nM^{-1} min^{-1}
k_2	4.70 min^{-1}
k_3	1.07 nM^{-1} min^{-1}
k_4	4.40 min^{-1}
k_5	1.00 nM^{-1} min^{-1}
k_6	0.39 min^{-1}
k_7	1.00 nM^{-1} min^{-1}
k_8	0.99 min^{-1}
k_{cat}	1.10 min^{-1}
βk_{cat}	0.83 min^{-1}

Figure 1.8. Simulation of the impact of varying ligand to iLBP ratios on metabolic enzyme activity under the circumstances that the iLBP interacts directly with the metabolic enzyme.

(A) An enzyme kinetic scheme showing the overall model used for the simulations where apo-iLBP directly inhibits the enzyme and holo-iLBP can deliver substrate to the enzyme via protein-protein interactions. (B) Simulated concentrations of the metabolite (product) formation, enzyme-substrate complex concentrations, concentrations of the ternary iLBP-substrate-enzyme complex, iLBP-enzyme complex, free substrate in solution, and iLBP-substrate complex as a function of time when the ratio of the substrate concentration to binding protein concentration is varied, and all the processes are simulated according to the scheme in A. The substrate concentrations were 1 nM (red line), 10 nM, (blue, orange, and purple lines) and 20 nM (green line). The iLBP concentration was either 1 nM (blue), 10 nM (green, orange, and red lines), or 20 nM (purple line). The kinetic and catalytic rate constants used in the simulations are listed in a table in (A). The enzyme concentration in all simulations was 0.5 nM. (Figure created with BioRender.com.) MATLAB code used for simulations is provided in Yabut and Isoherranen, 2023 Supplementary Material.

Table 1.1. Tissue expression patterns, genomic localization and endogenous ligands of iLBPs.

Gene	*Protein Name*	*Molecular Weight (kDa)*[b]	*Human Gene Locus*[a]	*Tissue Expression*	*Known Endogenous Ligands*
Subfamily I					
RBP1	CRBP1	15.9	3q23	Adipose, brain, heart, kidney, liver, lung, mammary gland, muscle, ovary, pituitary, spinal cord, skin, spleen, stomach, testis	retinol, retinaldehyde
RBP2	CRBP2	15.7	3q23	Heart, muscle, small intestine, placenta	retinol, retinaldehyde, monoacylglycerols
RBP5	CRBP3	15.9	12p13.31	Adipose, heart, muscle	retinol, retinaldehyde
RBP7	CRBP4	15.5	1p36.22	Large intestine, heart, kidney	retinol, retinaldehyde
CRABP1	CRABP1	15.6	15q25.1	Adipose, adrenal, brain, eye, kidney, liver, lung, lymph nodes, muscle, pancreas, skin, small intestine, spleen, stomach, testis, thymus	retinoic acid, retinoic acid metabolites
CRABP2	CRABP2	15.7	1q23.1	Skin, testis	retinoic acid, retinoic acid metabolites
Subfamily II					
FABP1	Liver FABP	14.2	2p11.2	Kidney, liver, lung, pancreas, small intestine, stomach	LCFAs, fatty acyl CoA, fatty acyl-carnitines, monoacylglycerols, lysophospholipids, bile acids, cholesterol, heme, bilirubin, retinoic acid, endocannabinoids, prostaglandins, vitamin K
FABP6	Ileal FABP	14.4	5q33.3	Adrenal, ovary, small intestine, stomach	Bile acids, LCFAs
Subfamily III					
FABP2	Intestinal FABP	15.2	4q26	Small intestine, liver	LCFAs
Subfamily IV					
FABP3	Heart FABP	14.9	1p35.2	Adipose, adrenal, brain, heart, kidney, liver, lung, mammary gland, muscle, ovary, placenta, spleen, stomach, testis	LCFAs, EETs HETEs, DHETs
FABP4	Adipose FABP	14.7	8q21.13	Adipose, dendritic cells, macrophages, muscle	LCFAs, retinoic acid
FABP5	Epidermal FABP	15.2	8q21.13	Adipose, brain, dendritic cells, eye, heart, kidney, liver, lung, macrophages, mammary gland, muscle, placenta, skin, small intestine, spleen, stomach, testis, tongue	LCFAs, endocannabinoids, retinoic acid
FABP7	Brain FABP	14.9	6q22.31	Brain, central nervous, mammary gland, muscle, system glial cells, eye	LCFAs
FABP8	Myelin FABP	14.9	8q21.13	Peripheral nervous system myelin	Cholesterol, LCFAs
FABP9	Testis FABP	15.1	8q21.13	Mammary gland, salivary gland, testis	LCFAs
FABP12	FABP12	15.6	8q21.13	Retina, testis	LCFAs

[a] *Gene location obtained from the National Center of Biotechnology and Information (NCBI) gene database*

[b] *Molecular weight determined by Expasy ProtParam* (Gasteiger *et al.*, 2005) *based on reference amino acid sequence*

**LCFAs – long chain fatty acids; EETs - epoxyeicosatrienoic acids; HETEs - hydroxyeicosatetraenoic acid; DHETs - dihydroxyeicosatrienoic acids; NSAIDs – nonsteroidal anti-inflammatory drugs*

References (Veerkamp and Zimmerman, 2001; E *et al.*, 2002; Pelsers *et al.*, 2005; Schug *et al.*, 2007; Liu *et al.*, 2008; Storch and Corsico, 2008; Noiri *et al.*, 2009; Rowland *et al.*, 2009; Smathers and Petersen, 2011; Wang *et al.*, 2014; Lee *et al.*, 2015; Rezar *et al.*, 2020)

Table 1.2. Binding affinities of xenobiotic ligands with different FABPs.

	Range of Reported K_i and K_d Values (μM)						
Ligand	**FABP1**		**FABP2**	**FABP3**	**FABP4**	**FABP5**	**FABP7**
Acifluorfen			4.2-8.9				
ANS	1.1-6.0 1.1[a]	12[b]	3.0-31[c]	0.6	0.03-32	0.07-1.3	
Aspirin	348[a]	3780[b]	300-460 NB[c]				
Atenolol	717						
Benzafibrate	NB[a]	44.4[b]	26-100[c]	NB	12	NB	
Benzilic acid			110.8-200[c]				
Benzyl salicylate			NB				
Bifenox			NB				
BMS309403						0.9	
CBD	4.0			1.7		1.9	1.5
Ciprofibrate			24-72[c]				
Clofibrate	6.9						
Clofibric acid			17.7-110[c]	NB	17	NB	
Cortexolone			1600-1900				
DAUDA	0.4-1.4		0.3-0.7[c]				
Dexamethasone	22.1[a]	41.3[b]	1100-1200				
Diazepam	0.5[a]	115[b]	1980-2200 NB[c]	NB	NB	325	
Diclofenac	3.2[a]	35[b]	86.3-520[c]				
Dilitiazem			NB[c]				
Fenbofibric acid	1-1.6, 0.3[a]	27.5[b]	1-6.1[c]	33	24	3.3	
Fenofibrate	2.9 0.02[a]	0.4[b]	0.8 NB[c]				
Fenoprofen			14-64[c]				
Flufenamic acid			3.7-15.5				
(R/S) Flurbiprofen	1.2[a]	222[b]	20-70				
Gemfibrozil	1.9[a]	179[b]	110.5-121.3[c]	NB	3.8	6.1	
GW7647	0.3-0.6		1.3[c]	25	7.6	0.7-8.9	
(R/S) Ibuprofen	47.6[a]	448[b]	32.2-263[c]	325	2.6	138	
3-indolacetic acid			93-200				
Indole-3-butyric acid			72-170				
Indoprofen	1.27[a]	161[b]	129-520.1				
Jasmonic acid			140-350				
Ketoprofen			24-82.4[c]				
Ketorolac	11.6[a]	119[b]	9.4-2300[c]				
Lorazepam	12.9[a]	140[b]	2100-2500				
Meclofenamic acid	0.4[a]	0.3[b]	8.9-21[c]				
Mefenamic acid			63-110	5.8	1.1	4.3	
Mepronil			NB				
Midazolam	7.9		12				
Nabumetone			NB[c]				
Nadolol	2310						
Nalidixic acid			NB				
2-naphthoxyacetic acid			7.2-14				
(S)-(-)-Naproxen	0.06[a,c]	2.8[b,c]	56-180				
Nitrazepam			1200-2300[c]	28	36	20	
Perfluorononanoic acid	1.3-3.1[c]						

Perfluorooctanoic acid	2.4-6.5[c]						
Phenytoin			0.2[a] 4.7[b] NB				
Pioglitazone				33	NB	11	
Prednisolone	2.7[a]	101[b]	95-113				
Progesterone	0.03		20-32				
Propanolol	NB		NB				
Pyrilamine			NB				
Rosiglitazone	2.8			NB	NB	28.8	
Sulfinpyrazone	0.1[c]	8.2[c]					
THC	0.1-2.9			2.0		3.1	1
11-COOH-THC	11.2 NB						
11-COOH-THC-gluc	NB						
11-OH-THC	5-7.2 NB						
Tolfenamic acid			2.8-8.2[c]	1.9	0.1	2.9	
Tolmetin			1300-2200				
Torsemide	0.2[c]	12.3[c]	0.8				
Troglitazone	1.7			11	0.02-16	1	
Valproate			240-470				
Verapamil			NB				

[a] Affinity for first, high affinity binding site [b] affinity for second, low affinity binding site respectively, determined in the same study

[c] Includes studies where binding affinities were determined by SPR, ITC, or thermal shift with SYPRO Orange

NB indicates that binding was tested but no binding was observed in at least one study

References: (Thumser *et al.*, 1996; Veerkamp *et al.*, 1999; Velkov *et al.*, 2005, 2007, 2009; Gillilan *et al.*, 2007; Chuang *et al.*, 2008; Rowland *et al.*, 2009, 2015; Trevaskis *et al.*, 2011; Kaczocha *et al.*, 2012; Velkov, 2013; Patil *et al.*, 2014; Yu *et al.*, 2014; Elmes *et al.*, 2015, 2019; Lee *et al.*, 2015; Sheng *et al.*, 2016; Huang *et al.*, 2018)

Chapter 2. CRABPS ALTER *ALL-TRANS*-RETINOIC ACID METABOLISM BY CYP26A1 VIA PROTEIN-PROTEIN INTERACTIONS

The work presented in this chapter was published in:

Nutrients 14(9): 1784, 2022

Co-author: Nina Isoherranen[a]

[a]*Department of Pharmaceutics, School of Pharmacy, University of Washington, Seattle, WA, United States*

2.1 ABSTRACT

Cellular retinoic acid binding proteins (CRABP1 and CRABP2) bind all-trans-retinoic acid (*at*RA), the active metabolite of vitamin A, with high affinity. CRABP1 and CRABP2 have been shown to interact with the *at*RA-clearing cytochrome P450 enzymes CYP26B1 and CYP26C1 and with nuclear retinoic acid receptors (RARs). We hypothesized that CRABP1 and CRABP2 also alter *at*RA metabolism and clearance by CYP26A1, the third key *at*RA-metabolizing enzyme in the CYP26 family. Based on stopped-flow experiments, *at*RA bound CRABP1 and CRABP2 with K_d values of 4.7 nM and 7.6 nM, respectively. The unbound *at*RA K_m values for 4-OH-*at*RA formation by CYP26A1 were 4.7 ± 0.8 nM with *at*RA, 6.8 ± 1.7 nM with holo-CRABP1 and 6.1 ± 2.7 nM with holo-CRABP2 as a substrate. In comparison, the apparent k_{cat} value was about 30% lower (0.71 ± 0.07 min^{-1} for holo-CRABP1 and 0.75 ± 0.09 min^{-1} for holo-CRABP2) in the presence of CRABPs than with free *at*RA (1.07 ± 0.08 min^{-1}). In addition, increasing concentrations in apo-CRABPs decreased the 4-OH-*at*RA formation rates by CYP26A1. Kinetic analyses suggest that apo-CRABP1 and apo-CRABP2 inhibit CYP26A1 (K_i = 0.39 nM and 0.53 nM, respectively) and holo-CRABPs channel *at*RA for metabolism by CYP26A1. These data suggest that CRABPs play a critical role in modulating *at*RA metabolism and cellular *at*RA concentrations.

2.2 INTRODUCTION

all-trans-retinoic acid (*at*RA) is the active metabolite of vitamin A (retinol) and is essential for a variety of physiological processes critical for life. The biological activity of *at*RA is mediated through *at*RA binding to its canonical nuclear receptors, retinoic acid receptors (RARs). RAR signaling regulates cell growth and differentiation and cell cycle progression during embryonic development and adult life (Chen and Ross, 2004; Tang and Gudas, 2011; Rhinn and Dollé, 2012; Ghiaur *et al.*, 2013). As RARs are ligand activated nuclear receptors, RAR activation and signaling are regulated by changing the cellular concentrations of *at*RA (Amory *et al.*, 2011; Gudas and Wagner, 2011; Raverdeau and Mills, 2014; Nilsson *et al.*, 2016; Karkeni *et al.*, 2017; Stevison *et al.*, 2017; Blaner, 2019; Snyder *et al.*, 2020). For example, postnatal, conditional knock out of the major *at*RA-clearing cytochrome P450s (CYPs) Cyp26a1 and Cyp26b1 in mice results in increased *at*RA concentrations and aberrant physiology in the spleen and skin (Snyder *et al.*, 2020). Similarly, hematopoietic stem cell (HSC) differentiation and renewal is controlled by changes in *at*RA signaling and metabolism. Inhibition of *at*RA synthesizing enzymes promotes HSC self-renewal, while treatment with *at*RA reverses these effects, driving HSCs toward differentiation (Chute *et al.*, 2006). HSC differentiation was also increased with the inhibition of *at*RA-metabolizing enzymes in the bone marrow stroma (Ghiaur *et al.*, 2013), demonstrating that synthesis and metabolism of *at*RA, likely via altering local *at*RA concentrations, control retinoid signaling.

The cellular concentrations of *at*RA are regulated by a network of metabolic enzymes including the CYP26 family of enzymes that oxidize *at*RA to 4-OH-*at*RA and are the main enzymes clearing *at*RA in all chordates (Napoli *et al.*, 1991; Fiorella and Napoli, 1994; Isoherranen and Zhong, 2019). In addition to the CYP26 enzymes (CYP26A1, CYP26B1 and CYP26C1 (Lutz *et al.*, 2009; Topletz *et al.*, 2012; Zhong *et al.*, 2018), other adult and fetal liver CYP enzymes such as CYP3A4, CYP3A7 and CYP2C8 also form 4-OH-*at*RA and may have a role in *at*RA clearance. Yet, their quantitative role in modulating *at*RA concentrations is not well defined (Thatcher *et al.*, 2010). The two major CYP26 enzymes CYP26A1 and CYP26B1 both metabolize *at*RA to 4-OH-*at*RA with high efficiency and the biochemical function of the two enzymes is similar (Topletz *et al.*, 2012). However, both CYP26A1 and CYP26B1 are essential for embryonic development and the two enzymes cannot compensate for each other in vivo (Rhinn and Dollé, 2012; Isoherranen and Zhong, 2019). The expression patterns of CYP26A1 and CYP26B1 are distinct both during embryonic development and in adult animals (Isoherranen and Zhong, 2019). CYP26B1 appears to be the high-affinity, low-capacity CYP26 enzyme while CYP26A1 has a higher capacity and is a lower-affinity enzyme for *at*RA clearance (Topletz *et al.*, 2012; Zhong *et al.*, 2019). CYP26A1 is also the predominant CYP26 in the adult liver and likely the main enzyme clearing exogenous *at*RA (Zhong *et al.*, 2019). In contrast, CYP26B1 is primarily found in extra-hepatic tissues (Isoherranen and Zhong, 2019; Snyder *et al.*, 2020). Overall, both CYP26A1 and CYP26B1 are needed for *at*RA metabolism and regulate tissue *at*RA concentrations, but their tissue-specific functions remain to be fully elucidated.

Vitamin A homeostasis is affected by a number of cellular binding proteins that impact retinol esterification, retinyl ester hydrolysis, retinol, retinaldehyde and *at*RA oxidation, and trafficking of retinoids to different cellular compartments and tissues (Napoli, 2017). Activation of nuclear receptors by *at*RA also appears affected by specific interactions with cellular retinoic acid binding proteins (CRABP1 and CRABP2). CRABPs are intracellular retinoid binding proteins that bind *at*RA with high affinity (Fiorella and Napoli, 1991; Fogh *et al.*, 1993; Norris *et al.*, 1994; Sanquer and Gilchrest, 1994; Wang *et al.*, 1997; Dong *et al.*, 1999) and *at*RA is likely sequestered by CRABPs in cells in which CRABPs are expressed. To coordinate *at*RA signaling, CRABPs have been proposed to have distinct roles in delivering *at*RA to nuclear receptors, with CRABP2 directly channeling *at*RA to RARα (Dong *et al.*, 1999; Schug *et al.*, 2007; Majumdar *et al.*, 2011). Studies in COS-7 cells showed that apo-CRABP2, anchored to the endoplasmic reticulum (ER), dissociates from the ER upon binding to *at*RA and translocates into the nucleus to activate RAR signaling via a SUMOylation dependent mechanism (Majumdar *et al.*, 2011) prior to returning to the ER. On the other hand, holo-CRABP1 did not translocate to the nucleus to activate RARs (Dong *et al.*, 1999). These data suggest that CRABPs play an important role in modulating *at*RA signaling and delivery to target proteins and enzymes. In addition to CRABPs, epidermal fatty acid-binding protein (FABP5) also appears to bind *at*RA and subsequently translocate to the nucleus to drive *at*RA signaling towards cell proliferation genes through PPARβ/δ activation (Schug *et al.*, 2007), but the broader role of FABP5 in retinoid signaling has not been defined.

In addition to channeling *at*RA to nuclear receptors and regulating RAR activation, CRABPs may also channel *at*RA to metabolic enzymes or alter *at*RA clearance (Napoli *et al.*, 1991; Fiorella *et al.*, 1993; Fiorella and Napoli, 1994; Nelson *et al.*, 2016; Napoli, 2017; Zhong *et al.*, 2018). Early studies in rat testis microsomes found that *at*RA was metabolized at similar rates in the presence and absence of CRABP1, while increasing CRABP1:*at*RA ratio to 3:1 resulted in decreased k_{cat} for *at*RA oxidation. These data could not be explained by the free drug hypothesis and suggest that holo-CRABP may channel *at*RA for metabolism (Fiorella and Napoli, 1991, 1994; Napoli *et al.*, 1991; Fiorella *et al.*, 1993). Indeed, subsequent metabolic studies of *at*RA with CYP26B1 and CYP26C1 in the presence of CRABPs showed that the 4-OH-*at*RA formation kinetics in the presence of CRABPs can only be explained by direct protein–protein interactions between CYP26B1/C1 and CRABPs, and likely substrate channeling from holo-CRABPs to CYP26s. The apparent K_m values of *at*RA bound to CRABPs with CYP26B1 and CYP26C1 were lower or similar to the K_m values observed in incubations with *at*RA alone, and the k_{cat} values were decreased in the presence of CRABPs (Nelson *et al.*, 2016; Zhong *et al.*, 2018). This is contrary to expectations based on the free drug hypothesis, where apparent K_m values should increase when *at*RA is bound to CRABPs with no effect on the k_{cat} (Nelson *et al.*, 2016; Zhong *et al.*, 2018). Kinetic modeling of the metabolism of *at*RA by CYP26B1 in the presence of CRABPs suggested a direct protein–protein interaction between CYP26B1 and CRABPs. Similar observations suggesting that holo-CRABP2 is also accepted as a substrate for CYP27C1, a retinoid desaturase in the skin, were recently reported (Glass and Guengerich, 2021a). Whether similar protein–protein interactions occur between CYP26A1 and CRABPs has not been established.

We hypothesized that CRABP1, CRAPB2, and FABP5 bind *at*RA with high affinity and alter the metabolism of *at*RA by CYP26A1 via direct protein–protein interactions. The goal of this study was to determine if CRABP1, CRABP2 or FABP5 have an impact on *at*RA metabolism by CYP26A1 and to elucidate the role that intracellular lipid binding proteins have in regulating *at*RA metabolism through CYP26 enzymes. Our data show that CRABP1 and CRABP2 play a role in modulating cellular *at*RA homeostasis and that the apo- to holo-CRABP ratio has a unique potential role in regulating retinoid concentrations, metabolism and signaling.

2.3 MATERIALS AND METHODS

2.3.1 *Chemicals and Reagents*

Kanamycin, sodium chloride, potassium chloride, Tris, Hepes, potassium phosphate, glycerol, benzonase, lysozyme, thrombin, protease inhibitor tablets, Coomasssie Brilliant Blue and *at*RA were purchased from Millipore-Sigma (St. Louis, MO, USA). The 4-oxo-*at*RA-d_3 was purchased from Santa Cruz Biotechnology (Dallas, TX, USA) and 4-OH-*at*RA was purchased from Toronto Research Chemicals (North York, ON, Canada). Sodium hydroxide, PMSF, imidazole, Pierce BCA protein assay, DTT, EDTA, IPTG, tryptone, yeast extract, high-performance liquid chromatography (HPLC) and mass spectrometry grade acetonitrile, water, and ethyl acetate were purchased from Thermo Fisher Scientific (Waltham, MA, USA). Lipidex-5000 was purchased from Perkin Elmer Inc (Waltham, MA, USA). Mini-PROTEAN TGX protein gels were purchased from Bio-Rad (Hercules, CA, USA). NBD-stearate was purchased from Avanti Polar Lipids (Birmingham, AL, USA). Pooled human liver microsomes were purchased from Gibco (Thermo Fisher Scientific, Waltham, MA, USA). Recombinant CYP3A4 and CYP2C8 Supersomes co-expressed with cytochrome P450 reductase and cytochrome b5 were purchased from Corning (Glendale, AZ, USA). Recombinant CYP26A1 was expressed in Sf9 insect cells, as previously described (Lutz *et al.*, 2009; Thatcher *et al.*, 2010). Rat P450 reductase was expressed in E. coli and purified, as previously described (Shen *et al.*, 1989).

2.3.2 *Expression and Purification of CRABP1 and CRABP2*

CRABP1 and CRABP2 expression constructs were a gift from Noa Noy (Case Western Reserve University). These CRABP1 and CRABP2 clones, in a pET28a vector, contained a thrombin cleavage site and an N-terminal hexa-histidine (6×his) tag. CRABP1 contained an additional N-terminal T7 tag. Both proteins were expressed in Rosetta 2 E. coli (Novagen, Madison, WI). A 25 mL starter culture with a freshly transformed colony in LB-kanamycin (50 μg/mL) was grown for 6 h at 37 °C in a shaking incubator at 250 RPM. A total of 15 mL of the starter culture was used to inoculate 1 L of LB-kanamycin which was grown to an OD600 ≈ 0.6. The culture was cooled to room temperature over 20 min prior to adding 0.1 mM IPTG to induce CRABP1 and CRABP2 expression. The proteins were expressed at 18 °C for 18 h in a shaking incubator at 220 RPM. Cells were harvested by centrifugation at 5000 g for 20 min, washed with PBS containing 1 mM PMSF, pelleted, decanted and stored at −80 °C.

Frozen pellets were thawed on ice in 25 mL of lysis buffer per one L of culture (20 mM Tris pH 7.4, 500 mM NaCl and 30 mM imidazole) with protease inhibitor cocktail (Roche, cOmplete Mini EDTA-free), 1 mM PMSF and 25 U of benzonase. A total of 1 mg/mL lysozyme was added to the resuspended cells and the suspension was rocked on ice for 20 min. To ensure complete lysis, cells were sonicated at 75% power for 30 s with a 1 min rest on ice (5 rounds). The lysate was cleared via centrifugation at 20,000 g for 30 min and supernatant filtered through a 0.45 µm Amicon syringe filter (Milipore-Sigma, St. Louis, MO, USA). The filtered lysate was loaded onto a 90 mL Dynaloop (Biorad, Hercules, CA, USA) coupled to a DuoFlow fast protein liquid chromatography (FPLC) (Bio-Rad, Hercules, CA, USA) and a 1 mL HisTrap affinity column (GE Healthcare, Chicago, IL, USA), equilibrated in lysis buffer at flow rate of 15 mL/min. For protein purification, the column was washed with 10 column volumes of wash buffer (20 mM Tris pH 7.4, 500 mM NaCl, 30 mM imidazole) and CRABPs were eluted with 300 mM imidazole in elution buffer (20 mM Tris pH 7.4, 500 mM NaCl) in 1 mL fractions over 10 column volumes. Protein elution was detected at 280 nm absorbance and the CRABP-containing fractions combined. The eluted protein was concentrated, and buffer exchanged into thrombin cleavage buffer (20 mM Tris, pH 7.4, 500 mM NaCl) using a 10 kDa molecular weight cutoff (MWCO) Amicon concentrator (Milipore-Sigma, St. Louis, MO, USA). After buffer exchange, the protein concentration was measured by Nanodrop (Thermo Fisher, Waltham, MA, USA) by absorbance at 280 nm. The N-terminal 6×his tag was cleaved by adding 0.03 U of thrombin protease per 10 µg of CRABP into the solution and incubating overnight (>12 h) at 4 °C. Cleavage of the N-terminal tag was confirmed via SDS-PAGE with Coomassie staining and an anti-his (mouse anti-His antibody from Qiagen, Valencia, CA, USA) Western blot. The cleaved protein was then injected into a Superdex 75 size exclusion column (GE Healthcare, Chicago, IL, USA) equilibrated with HEK buffer (10 mM Hepes, pH 8, 100 mM KCl, 0.1 mM EDTA) using DuoFlow FPLC at a flow rate of 0.5 mL/min. After injection, the flow rate of the HEK buffer was increased to 1 mL/min and the CRABP-containing fractions, as detected at 280 nm, were collected, pooled and concentrated using a 10 kDa MWCO Amicon concentrator. The final concentration of CRABPs was quantified by a BCA protein assay. DTT (0.5 mM final concentration) and glycerol (50% final concentration) were added to the protein solution in HEK buffer and the CRABPs were stored at −20 °C. The binding of *at*RA to the CRABPs was verified via fluorescence titrations, as previously described (Fiorella and Napoli, 1991). Briefly, titrations were prepared in a 96-well black-walled plate with 2 µM CRABP and 0–2.8 µM *at*RA in 100 mM potassium phosphate, pH 7 under protection from light. The quenching of CRABP tryptophan fluorescence (excitation at 290 nm and emission at 340 nm) by *at*RA binding was measured at 37 °C with a Gemini Em fluorescence plate reader (Molecular Devices, San Jose, CA, USA) with the emission auto-cutoff set to on. Endpoint fluorescence scans were carried out with the photomultiplier tube (PMT) sensitivity set to auto with 6 reads and auto-calibration and auto-mixing for 2 s.

2.3.3 *Expression and Purification of FABP5*

Human FABP5 from OriGene (Rockville, MD, Cat. No. SC119223) was amplified with an N-terminal NdeI restriction site and a C-terminal HindIII restriction site and subcloned into pET28a with a 6×his tag and thrombin cleavage site. Constructs were restriction-digested and sequence-verified and FABP5 was expressed in Rosetta 2 cells under the same conditions as described above for CRABPs.

FABP5 was purified using the method described above for CRABPs with the following changes: 50 mM Hepes pH 7.2, 250 mM NaCl, 30 mM imidazole was used as lysis and wash buffers, and FABP5 was eluted with a stepwise imidazole gradient (30–500 mM) over 10 column volumes. The eluted FABP5-containing fractions were pooled, concentrated using an Amicon concentrator with a 10 kDa MWCO and injected into a Superdex 75 column equilibrated with gel filtration buffer (30 mM Tris, pH 7.6, 100 mM NaCl), coupled to a DuoFlow FPLC at a flow rate of 0.5 mL/min. Fractions containing FABP5 were collected, pooled and passed five times through a 5 mL Lipidex-5000 gravity flow column equilibrated with gel filtration buffer to remove any contaminating E. coli lipids from the FABP5. Delipidated FABP5 was concentrated using an Amicon concentrator (10 kDa MWCO), flash frozen and stored in −80 °C in 30 mM Tris, pH 7.6, 100 mM NaCl. FABP5 protein concentration was quantified via a BCA protein assay and NBD-stearate binding to FABP5 was confirmed via fluorescence, as described previously (Berger *et al.*, 2012).

2.3.4 *Preparation of CYP26A1 Microsomes from Sf9 Insect Cells*

To prepare CYP26A1 microsomes, insect cell pellets containing expressed recombinant CYP26A1 (Lutz *et al.*, 2009) were resuspended in homogenization buffer (10 mM potassium phosphate, 0.25 M sucrose, 0.2 mM PMSF, pH 7.4) and sonicated for 10 s with a 30 min rest on ice for 3 rounds. The cells were further lysed with one pass through a Thomas tube and a Teflon pestle attached to a hand power drill. The homogenized cells were centrifuged at 20,000 g for 20 min to remove cellular debris, nuclei and other large organelles. The supernatant was collected and centrifuged at 100,000 g for 60 min to pellet the microsomal fraction (ER membrane fragments). After decanting, the pellet was rinsed with storage buffer (50 mM potassium phosphate, 0.1 mM EDTA, 20% glycerol, pH 7.4) and resuspended in 2 mL of storage buffer, flash frozen in liquid nitrogen and stored at −80 °C. The concentration of CYP26A1 was determined via a CO-difference spectrum (Omura and Sato, 1964).

2.3.5 *Determination of atRA-Binding Kinetics with CRABP1 and CRABP2 by Stopped-Flow*

Binding kinetics of *at*RA with CRABP1 and CRABP2 were measured using an SX20 stopped-flow instrument (Applied Photophysics, Leatherhead, Surrey, UK) with a 1 ms dead time. A 2 mm optical pathlength was used and the detector voltage was set to 300 V. The excitation wavelength was set to 350 nm and the increase in *at*RA fluorescence due to binding to CRABPs was monitored with a 455 nm emission cut-off filter. All binding experiments were carried out at room temperature and protected from light. To measure *at*RA-binding kinetics with CRABP1 and CRABP2, separate solutions of 1 μM CRABP1 or CRABP2 and 4 μM *at*RA were prepared in an assay buffer in amber glass vials, and CRABP and *at*RA solutions were loaded into separate stopped-flow drive syringes. After injection, the final mixed concentrations were 0.5 μM CRABP and 2 μM *at*RA. Data were acquired for 2 sec with 1000 measurements per injection. Replicate experiments were conducted on three different days and each replicate experiment consisted of 5 subsequent injections.

To determine the concentrations of observed holo-CRABP in stopped-flow experiments, the fluorescence per mol of holo-CRABP was measured. The steady state fluorescence of holo-CRABP1 and holo-CRABP2 was measured at a final mixed concentration of 0.5 μM of CRABP and 2 and 5 μM of *at*RA. Two different concentrations of *at*RA in excess were used to ensure saturation of CRABP binding. The fluorescence yield of holo-CRABP was calculated from the average fluorescence between 0.4 and 0.8 s, and 0.6 and 1.0 s for holo-CRABP1 and holo-CRABP2, respectively. This average fluorescence from all experiments was divided by the total concentration of CRABP (0.5 μM) to obtain the value of CRABP fluorescence per mol of CRABP. The fluorescence per mol of holo-CRABP determined above was used to calculate the concentrations of observed holo-CRABP1 or holo-CRABP2 in kinetic stopped-flow experiments and a 2-state kinetic binding model was fitted to the observed holo-CRABP concentration versus time data using MATLAB (R2021b, MathWorks, Natick, MA, USA).

$$\text{CRABP} + at\text{RA} \rightleftharpoons \text{CRABP}{-}at\text{RA}$$

The differential equations for the model were solved by numerical methods with ode15s. Initial concentrations for CRABPs, *at*RA and holo-CRABPs were set according to experimental conditions. The association (k_{on}) and dissociation (k_{off}) rate constants were fitted by minimizing the sum of the difference of squares between the numerical solution of the model and the observed data with lsqcurvefit.

2.3.6 *Effect of Binding Proteins on the 4-OH-atRA Formation by CYP3A4, CYP2C8, CYP26A1 and Human Liver Microsomes (HLMs)*

To determine whether FABP5, CRABP1 and CRABP2 alter the metabolism of *at*RA by CYP3A4, CYP2C8 and CYP26A1, *at*RA was incubated with CYP3A4 and CYP2C8 Supersomes and with recombinant CYP26A1 insect cell microsomes reconstituted with rat P450 reductase, as previously described (Lutz *et al.*, 2009). The formation of 4-OH-*at*RA as the metabolite of *at*RA was monitored following liquid–liquid extraction and LC-MS/MS analysis, as described previously (Nelson *et al.*, 2016; Zhong *et al.*, 2018). In brief, at the end of the incubations, reactions were quenched with 1 mL ice-cold acetonitrile containing 10 nM of 4-oxo-*at*RA-d_3 as an internal standard, 4 mL of ethyl acetate was added, the mixture vortexed to extract metabolites and centrifuged to separate organic and aqueous phases. The upper organic layer was transferred to a borosilicate glass tube and dried in a 25 °C water bath under gentle nitrogen flow. Samples were reconstituted in 100 µL of methanol, transferred to MS vials and analyzed by liquid chromatography-tandem mass spectrometry (LC-MS/MS) using a Sciex API5500 Q/LIT mass spectrometer (Sciex, Concord, ON, Canada) coupled to an Agilent 1290 Infinity

UHPLC (Agilent Technologies, Santa Clara, CA, USA) with methods previously described (Zhong *et al.*, 2018). Briefly, 4-OH-*at*RA was separated with a Zorbax Extend-C18 column (3.5 µm, 2.1 × 100 mm) and a mobile phase flow rate of 0.35 mL/min. Mobile phase A was water with 0.1% formic acid and mobile phase B was acetonitrile. The mobile phase gradient was as follows: 0–3 min 90% A, 10% B; then, increasing B to 50% by 3.5 min and to 85% by 7.5 min and then washing at 95% B from 7.5 to 10 min before returning to 90% A, 10% B and keeping at initial conditions until 11.5 min. The metabolites were monitored in negative ion electrospray mode and the MRM transitions used were 315 > 253 m/z for 4-OH-*at*RA and 316 > 272 m/z for 4-oxo-*at*RA-d_3.

In initial experiments, reactions containing either 5 nM CYP3A4, 5 nM CYP2C8, 5 nM CYP26A1 reconstituted with 10 nM P450 reductase or pooled HLMs (0.2 mg/mL) were pre-incubated with 1 mM NADPH for 5 min at 37 °C in 1 mL incubation buffer (100 mM potassium phosphate, pH 7.4). The reactions were initiated by an addition of substrate, *at*RA, 1:10 *at*RA:FABP5 (CYP2C8, CYP3A4 and HLM incubations), 1:250 *at*RA:FABP5 (CYP26A1 incubations only), or 1:1 *at*RA:CRABP1, as previously described (Nelson *et al.*, 2016). For all incubations, *at*RA was prebound with the binding proteins in the above ratios prior to the experiments. In the incubations with CYP3A4 and CYP2C8, 1 µM *at*RA was used, 20 nM *at*RA was used in experiments with CYP26A1 and 500 nM *at*RA-d_6 was used in experiments with HLMs. CYP3A4 and CYP2C8 reactions were allowed to proceed for 10 min, HLM experiments for 30 min and CYP26A1 incubations for 2 min (to stay within linear range of product formation) before quenching the reactions with acetonitrile and extracting the metabolites for analysis, as described above.

In a separate set of experiments, CYP3A4, CYP2C8 and CYP26A1 (reconstituted with P450 reductase) were preincubated with substrate (*at*RA only, 1:1 *at*RA:CRABP1 or *at*RA:CRABP2, or 1:2 *at*RA:CRABP1 or *at*RA:CRABP2) for 5 min at 37 °C to achieve binding equilibrium prior to initiation of catalytic reactions with NADPH. In experiments with CYP3A4 and CYP2C8, 1 µM of *at*RA was used in incubations with 1:1 *at*RA:CRABP and 500 nM *at*RA was used in incubations with 1:2 *at*RA:CRABP. A total of 50 nM of *at*RA was used in incubations with CYP26A1 with 1:1 and 1:2 *at*RA:CRABP ratios. After incubation at 37 °C for 10 min for CYP3A4 and CYP2C8 and 2 min for CYP26A1, reactions were quenched with 1 mL ice-cold acetonitrile containing 10 nM 4-oxo-*at*RA-d_3 as an internal standard and the samples were extracted and analyzed by LC-MS/MS, as described above. All incubations with CRABP1, CRABP2 and FABP5 were carried out with uncleaved, his-tagged proteins for the experiments described above.

One-way ANOVA with Dunnett's post hoc test was used to test for differences in the 4-OH-*at*RA formation between incubations in the presence and absence of the binding proteins. A p-value < 0.01 was considered significant.

2.3.7 *Simulations of the Impact of CRABPs on the 4-OH-atRA Formation Assuming the Free Drug Hypothesis*

To test whether CRABPs function as a binding sink in the incubations, and the free drug hypothesis can explain the observed impact of CRABPs on the 4-OH-*at*RA formation by CYPs, the 4-OH-*at*RA formation as a function of free *at*RA in solution in the incubations containing CRABPs was simulated according to Equation (2.1):

$$v = \frac{k_{cat} \times [atRA]_u}{K_m + [atRA]_u} \tag{2.1}$$

In Equation (2.1), v is the velocity of the 4-OH-*at*RA formation expressed in units of pmol/min/pmol CYP, k_{cat} is the catalytic rate constant for a given CYP of interest as measured previously and K_m is the affinity of *at*RA to the CYP of interest. K_m and k_{cat} values used for CYP3A4 were 19 µM and 4 min^{-1}, respectively, and the values used for CYP2C8 were 13.4 µM and 4.8 min^{-1} (Zhong *et. al.*, 2018). K_m and k_{cat} values used for CYP26A1 were determined in this study. $[atRA]_u$ is the unbound concentration of *at*RA in the incubations calculated from Equation (2.2), as previously described (Nelson *et al.*, 2016):

$$[atRA]_u = \frac{\sqrt{([CRABP]_t - [atRA] + K_d)^2 + 4K_d[atRA]_t} - [CRABP]_t - [atRA]_t + K_d}{2} \qquad (2.2)$$

In Equation (2.2), $[CRABP]_t$ and $[atRA]_t$ are the total concentrations of CRABP and *at*RA used in the incubations, and K_d is the equilibrium dissociation constant for *at*RA with CRABP1 or CRABP2, as determined from stopped-flow experiments.

2.3.8 *4-OH-atRA Formation Kinetics with CYP26A1 in the Presence and Absence of CRABPs*

To determine the effects of CRABPs on the kinetics of the 4-OH-*at*RA formation by CYP26A1, a solution of holo-CRABP1 or holo-CRABP2 was first prepared by mixing *at*RA and CRABP1 or CRABP2 in a 2:1 ratio in incubation buffer. Excess *at*RA was removed by running the solution through a spin desalting column with a 7 kDa molecular weight cutoff (Zeba, Thermo Scientific, Waltham, MA, USA). Holo-CRABP concentrations were verified with a BCA protein assay and with a fluorescence measurement against a standard curve prepared by mixing known concentrations of CRABP with 2-fold excess *at*RA. The intrinsic CRABP fluorescence for the desalted holo-CRABP and standard curve were measured as described above. In catalytic assays, 0.5 nM CYP26A1 reconstituted with 1 nM P450 reductase was preincubated with varying concentrations of *at*RA only (5–320 nM) or holo-CRABPs (5–320 nM) in 1 mL incubation buffer at 37 °C. After a 5 min preincubation, reactions were initiated with 1 mM NADPH and allowed to proceed for 2 min at 37 °C before quenching with 1 mL ice-cold acetonitrile. A total of 4 mL of ethyl acetate and 100 pmol of 4-oxo-*at*RA-d_3 internal standard were added and the samples were extracted with ethyl acetate and 4-OH-*at*RA concentrations were analyzed by LC-MS/MS, as described above. All incubations were carried out as technical duplicates. The tight binding (Morrison) equation was fitted to the 4-OH-*at*RA formation data in Graphpad Prism 9 and the apparent unbound K_m ($K_{m,u}$) and k_{cat} values were reported as the means (± S.D.) of replicate experiments conducted on three separate days.

2.3.9 *Impact of Increasing CRABP to atRA Ratio on the 4-OH-atRA Formation*

To determine the effect of excess apo-CRABP1 and apo-CRABP2 on the 4-OH-*at*RA formation by CYP26A1, inhibition experiments were carried out with increasing CRABP to *at*RA ratios. A total of 0.5 nM CYP26A1 reconstituted with 1 nM P450 reductase, 50 nM of *at*RA and 0–400 nM CRABP1 or CRABP2 were preincubated for 5 min in 1 mL incubation buffer at 37 °C before initiation of catalysis with 1 mM NADPH (final concentration). Reactions were quenched with 1 mL ice-cold acetonitrile after 2 min. A total of 4 mL of ethyl acetate and 100 pmol of 4oxo-*at*RA-d_3 were added and 4-OH-*at*RA was extracted and analyzed via LC-MS/MS, as described in Section 2.6. To ensure the correct ratios of *at*RA:CRABP were used, holo-CRABPs were prepared with spin desalting columns, as described in Section 2.3.8. For incubations with excess *at*RA, holo-CRABPs were diluted to 0–40 nM and *at*RA was added to 50 nM total *at*RA. For incubations with excess CRABP, holo-CRABPs were diluted to 50 nM and apo-CRABP was added for final concentrations of 50–400 nM total CRABP. Experiments were carried out in technical duplicates on three separate days for CRABP1 and two separate days for CRABP2.

2.3.10 *Analysis of the Kinetics of Protein–Protein Interactions between CYP26A1, CYP26B1 and CRABPs*

It has been previously suggested that CRABP1 and CRABP2 interact directly with CYP26B1 both via apo-CRABPs inhibiting CYP26B1 activity and via holo-CRABPs directly channeling *at*RA for metabolism with CYP26B1 (Nelson *et al.*, 2016). To test whether similar protein–protein interactions can explain the kinetics of the 4-OH-*at*RA formation by CYP26A1 in the presence of CRABP1 and CRABP2, the previously described Equation (2.3) was fitted to the combined 4-OH-*at*RA formation data from the experiments described in Section 2.8:

$$v = \frac{k_{cat}[atRA]_u(1+\frac{\beta[CRABP]_u}{\alpha K_d})}{K_m\left(1+\frac{[CRABP]_u}{K_i}\right)+[atRA]_u(1+\frac{[CRABP]_u}{\alpha K_d})} \qquad (2.3)$$

In Equation (2.3), v is the velocity of the 4-OH-*at*RA formation in the presence of CRABP expressed in units of pmol/min/pmol CYP; k_{cat} is the rate of catalysis for the 4-OH-*at*RA formation by the CYP26 in the absence of CRABP; [*at*RA]u and [CRABP]u are the concentrations for unbound *at*RA and unbound CRABP, respectively; K_m is the Michaelis–Menten constant for the 4-OH-*at*RA formation in the absence of CRABP; α and β are model parameters to describe the effect of CRABP on K_m and k_{cat}, respectively; K_i is the affinity of apo-CRABP to CYP; and K_d is the binding affinity of *at*RA to the specific CRABP. The unbound *at*RA and CRABP concentrations were calculated according to Equation (2.2) under the assumption that concentrations of the CYP-RA, CRABP-CYP and CRABP-CYP-RA complexes were negligible in comparison to *at*RA and CRABP concentrations in the experiments. Observed 4-OH-*at*RA formation velocities were fit globally with the fixed K_m and k_{cat} values determined in this study in incubations without CRABPs, and K_d values were fixed to values determined from stopped-flow experiments confirmed with fluorescence titrations.

2.4 RESULTS

2.4.1 *FABP5 Does Not Affect atRA Hydroxylation by CYPs*

FABP5 has been previously shown to facilitate *at*RA-induced PPARβ/δ signaling (Schug *et al.*, 2007). However, it is not known whether FABP5 affects *at*RA metabolism by CYPs. The impact of FABP5 on the 4-OH-*at*RA formation by CYPs previously shown to metabolize *at*RA (Thatcher *et al.*, 2010) was evaluated in comparison to the effect by CRABP1. FABP5 in 10-fold excess to *at*RA had no effect on the 4-OH-*at*RA formation by CYP3A4 (97 ± 0.5% activity remaining) or CYP2C8 (94 ± 6% activity remaining) (Figure 2.1A, B). In contrast, CRABP1 (in 1:1 ratio to *at*RA) decreased 4-OH-*at*RA formation by CYP3A4 and CYP2C8 by 88 ± 3% and 87± 5% (p-value < 0.01), respectively, in comparison to free *at*RA (in the absence of CRABP as a substrate) (Figure 2.1). FABP5 did not alter the 4-OH-*at*RA formation by CYP26A1 either when *at*RA was incubated in the presence of 250-fold excess of FABP5. The 4-OH-*at*RA formation by CYP26A1 was 90 ± 10% of control in the presence of FABP5 and not significantly (p-value > 0.01) different from the 4-OH-*at*RA formation from free *at*RA. In comparison, the 4-OH-*at*RA formation was significantly (p-value < 0.001) reduced to 16 ± 1% of the free *at*RA control in the presence of CRABP1 (Figure 2.1C). Furthermore, a 10-fold excess of FABP5 had little effect on the 4-OH-*at*RA formation in pooled HLMs compared to CRABP1 (1:1) (88 ± 6% vs. 48 ± 2% activity remaining) (Figure 2.1D). Taken together, these results suggest that FABP5 does not sequester *at*RA to prevent metabolism by CYPs while CRABP1 has a significant effect on *at*RA metabolism by CYPs including CYP26A1.

2.4.2 *atRA Binds CRABPs with Nanomolar Affinity*

The binding kinetics for *at*RA with CRABP1 and CRABP2 were determined with stopped-flow (Figure 2.2) and the k_{on} and k_{off} were estimated from a 2-state binding model (Materials and Methods). The k_{on} and k_{off} values and the calculated equilibrium dissociation constants (K_d, 4.7 ± 3.8 nM and 7.6 ± 4.0 nM for CRABP1 and CRABP2, respectively) from three replicate experiments were averaged and the mean values are shown in Table 2.1.

2.4.3 *CRABPs Sequester atRA from CYP3A4 and CYP2C8 as Predicted by the Free Drug Hypothesis*

The binding of *at*RA with CRABP1 or CRABP2 has been shown to decrease the 4-OH-*at*RA formation by CYP3A4 and CYP2C8 (Nelson *et al.*, 2016), likely due to sequestration of *at*RA from metabolic enzymes according to the free drug hypothesis. To test this hypothesis, *at*RA was incubated with CYP3A4, CYP2C8 and CYP26A1 in the presence and absence of equimolar concentrations of CRABP1 and CRABP2 or a 2-fold excess of CRABPs, and the 4-OH-*at*RA formation velocities were measured following the initiation of the catalytic reactions with the addition of NADPH. In the presence of equimolar concentrations of CRABP1 or CRABP2 with *at*RA, CRABP1 decreased the 4-OH-*at*RA formation by CYP3A4 and CYP2C8 by about 85% and CRABP2 decreased the 4-OH-*at*RA formation by about 95% when compared to no CRABP present (Figure 2.3A, B, p-value < 0.01). The 4-OH-*at*RA formation by CYP3A4 was completely abolished in the presence of 2-fold excess CRABP (>99%, p-value < 0.001, Figure 2.3A). CRABP1 and CRABP2 decreased the 4-OH-*at*RA formation in incubations with CYP26A1 by about 50% with equimolar concentrations of CRABP and *at*RA compared to incubations with no CRABP (p-value < 0.05, Figure 2.3C). The 4-OH-*at*RA formation was further decreased to about 20% and 30% of no CRABP controls with 2-fold excess CRABP1 and CRABP2, respectively (p-value < 0.01, Figure 2.3C).

To test whether these effects could be explained by the free drug hypothesis (i.e., *at*RA being sequestered to CRABPs and only free *at*RA being available for metabolism by CYPs), the 4-OH-*at*RA formation by the CYPs in the presence of CRABPs was simulated with unbound concentrations of *at*RA calculated with the binding kinetics of *at*RA to CRABPs determined using stopped-flow, and assuming that CRABPs would not interact with the CYPs. The free drug hypothesis predicted a 93% and 91% decrease in the 4-OH-*at*RA formation by both CYP3A4 and CYP2C8 in the presence of equimolar concentrations of CRABP1 and CRABP2, respectively, when compared to free *at*RA, while a 2-fold excess of CRABPs was predicted to eliminate nearly all 4-OH-*at*RA formation by CYP3A4 and CYP2C8 (>99%, Figure 2.3D) due to binding of free *at*RA to CRABPs. These predictions were in good agreement with observed values and are consistent with the notion that CRABPs bind *at*RA tightly to sequester *at*RA from metabolism. In contrast, the free drug hypothesis over-predicted the 4-OH-*at*RA formation by CYP26A1 compared to the observed values. The 4-OH-*at*RA formation was predicted to decrease by about 20% in the presence of equimolar concentrations of CRABP1 and CRABP2, and by 50% and 40% with 2-fold excess CRABP1 and CRABP2, respectively. These predictions suggest that, unlike CYP3A4 and CYP2C8 activity, the binding proteins have an additional inhibitory effect on CYP26A1 activity in addition to binding *at*RA.

2.4.4 *Determination of the Kinetics of the 4-OH-atRA Formation by CYP26A1 in the Presence of CRABPs*

To define the kinetics of the 4-OH-*at*RA formation by CYP26A1 in the presence of CRABP1 and CRABP2, varying concentrations of holo-CRABPs or free *at*RA were incubated with recombinant CYP26A1 and the 4-OH-*at*RA formation measured (Figure 2.4A–C). The apparent K_m values of the 4-OH-*at*RA formation increased in the presence of CRABP1 (11.7 ± 3.44 nM) and CRABP2 (9.7 ± 3.2 nM) when compared to *at*RA alone (4.7 ± 0.81 nM) but the unbound K_m values were unchanged in the presence of CRABPs (Figure 2.4). The apparent k_{cat} values decreased in the presence of CRABP1 (0.71 ± 0.07 min^{-1}) and CRABP2 (0.75 ± 0.09 min^{-1}) when compared to the k_{cat} with *at*RA alone (1.07 ± 0.08 min^{-1}). While the finding of the unchanged unbound K_m is consistent with the free drug hypothesis, the decrease in k_{cat} cannot be explained via simple Michaelis–Menten kinetics.

Previous studies with CYP26B1 have suggested that CRABP1 and CRABP2 interact directly with CYP26B1, and apo-CRABPs were shown to inhibit the 4-OH-*at*RA formation by CYP26B1. To test whether apo-CRABPs inhibit *at*RA metabolism by CYP26A1 as well, CYP26A1 was incubated with *at*RA in the presence of increasing concentrations of CRABP. Increasing concentrations of apo-CRABPs decreased the 4-OH-atRA formation by CYP26A1 (Figure 2.4D), suggesting that CRABPs may directly interact with CYP26A1.

Increasing concentrations of CRABPs beyond *at*RA concentrations result in a decrease in free concentration of *at*RA in the incubations in addition to potentially inhibiting the activity of CYP26A1 via direct protein–protein interactions. To define the kinetic constants of CRABP–CYP26A1 interactions, a previously described model incorporating protein–protein interactions between CRABPs and CYP26A1 (Figure 2.5A) was fitted to the data of the 4-OH-*at*RA formation by CYP26A1 in the presence of increasing concentrations of CRABPs. Based on model parameter fits (Figure 2.5B, C), apo-CRABP1 and apo-CRABP2 inhibit CYP26A1 (K_i = 0.39 nM and 0.53 nM, for CRABP1 and CRABP2, respectively). In addition, holo-CRABP1 and holo-CRABP2 had higher affinities to CYP26A1 than free *at*RA (αK_m = 0.99 nM and 0.75 nM for CRABP1 and CRABP2, respectively), while the catalytic rate was lower from the ternary complex than from the *at*RA–CYP26A1 complex (βk_{cat} = 0.80 min⁻1 and 0.77 min⁻1, respectively).

2.5 DISCUSSION

Cellular *at*RA concentrations are regulated by a network of enzymes that catalyze the oxidation of retinol to *at*RA and the clearance of *at*RA. Tight regulation of *at*RA concentrations is necessary for cellular health and for biological processes, as even small, 2- to 5-fold changes in retinoid concentrations alter *at*RA signaling (Hogarth *et al.*, 2015; Stevison *et al.*, 2017; Snyder *et al.*, 2020). Notably, it has been shown that short duration pulses of altered *at*RA concentrations likely trigger cyclic spermatogenesis, and gradients of *at*RA concentrations are established across the seminiferous epithelium to control cell differentiation (Hogarth *et al.*, 2015). Despite the critical function of such *at*RA gradients in regulating cellular processes, the mechanisms that regulate the establishment of these critical gradients and pulses of increased *at*RA concentrations have not been established. Although the CYP26 enzymes CYP26A1 and CYP26B1 and the ALDH1A enzymes are the main enzymes responsible for *at*RA clearance and synthesis during embryonic development and adult life (Napoli, 2012; Isoherranen and Zhong, 2019), neither CYP26 nor ALDH1A enzyme expression changed across the spermatogenic cycle in the mouse testis (Hogarth *et al.*, 2015). This suggests that other mechanisms are present to regulate rapid changes and pulses of *at*RA concentrations, essential for retinoid signaling. One such potential signal is the change in CRABP1 expression across the spermatogenic cycle (Hogarth *et al.*, 2015) that may regulate *at*RA clearance in a stage-specific manner via functioning as a regulator of *at*RA clearance through protein–protein interactions with the CYP26 enzymes. The data shown here are consistent with a mechanism in which the changes in

CRABP1 and CRABP2 expression regulate *at*RA clearance and 4-OH-*at*RA formation via direct interactions with CYP26 enzymes to allow rapid changes in cellular *at*RA concentrations without altering CYP26 and ALDH1A expressions.

The CRABPs have been previously shown to have distinct effects on *at*RA 4-hydroxylation by CYP26B1 and CYP26C1 (Nelson *et al.*, 2016; Zhong *et al.*, 2018) and *at*RA desaturation by CYP27C1 (Glass and Guengerich, 2021a). In addition, *at*RA oxidation by CYP3A4 and CYP2C8 is completely abolished in the presence of CRABPs, a finding consistent with the free drug hypothesis and tight binding of *at*RA with CRABPs. CRABP1 and CRABP2 binding decreased the apparent K_m values (determined from fitting the Michaelis–Menten model to total *at*RA concentration versus product formation) of *at*RA with CYP26B1 (Nelson *et al.*, 2016), while the apparent K_m values of *at*RA hydroxylation were similar for CYP26C1 in the presence and absence of CRABP1 and CRABP2 (Zhong *et al.*, 2018). For *at*RA desaturation by CYP27C1, both CRABP1 and CRABP2 increased the apparent K_m values (Glass and Guengerich, 2021a). In this study, the apparent K_m value of *at*RA with CYP26A1 increased in the presence of CRABPs in contrast to previous observations with CYP26B1 where the apparent K_m was decreased in the presence of CRABPs. However, the unbound K_m values for *at*RA with CYP26A1 were not different in the presence of CRABPs, a finding supporting an interpretation that only free *at*RA interacts with CYP26A1 to undergo oxidation. Yet, CRABP1 and CRABP2 decreased the apparent k_{cat} value of *at*RA hydroxylation by CYP26A1, similar to prior findings with CYP26B1, CYP26C1 and rat testis microsomes (Napoli *et al.*, 1991; Fiorella and Napoli, 1994; Nelson *et al.*, 2016; Zhong *et al.*, 2018) and of *at*RA desaturation by CYP27C1 (Glass and Guengerich, 2021b). With CYP26B1 and CYP27C1, CRABP1 had a greater effect on k_{cat} values than CRABP2 while, with CYP26C1 and CYP26A1, the decrease in k_{cat} values for *at*RA 4-

hydroxylation were similar with both CRABPs. The decrease in the apparent k_{cat} value has previously been explained via a protein–protein interaction between CRABPs and CYP26 enzymes, with apo-CRABPs inhibiting the CYP26B1 mediated hydroxylation of *at*RA. Similarly, apo-CRABPs were found to inhibit the desaturation of *at*RA by CYP27C1 (Glass and Guengerich, 2021a). The differences in the effects on apparent k_{cat} values with the different CYP enzymes are likely due to specific and unique allosteric interactions between the CRABP1 and CRABP2 and the specific CYP enzymes. Further studies to identify the interacting residues between CRABPs and CYPs are needed to define the mechanisms of the protein–protein interactions.

Analyses of the kinetics of the protein–protein interactions between CRABPs and CYPs hinge on the knowledge of the binding kinetics of *at*RA with CRABP1 and CRABP2. The K_d values of *at*RA with CRABPs are typically measured with fluorescence titrations under equilibrium assumptions yielding K_d values ranging from 0.4–16 nM for CRABP1 and 2–39 nM for CRABP2 (Fiorella and Napoli, 1991; Fogh *et al.*, 1993; Norris *et al.*, 1994; Wang *et al.*, 1997). Stopped-flow was previously used to measure the k_{on} and k_{off} for *at*RA binding with CRABPs (Dong *et al.*, 1999). These studies used a large lipid sink to trap dissociated *at*RA and a simple monoexponential was fit to the dissociation data to estimate k_{off}. The resulting K_d estimates (0.06 nM and 0.13 nM for CRABP1 and CRABP2, respectively) were considerably lower than those measured by fluorescence titrations or by stopped-flow here, likely due to the differences in the model fit to the data. When the previously published data was analyzed fitting the same model to the data as shown here, the K_d value for CRABP1 was 2.2–5.5 nM and for CRABP2 2.6–15 nM. The k_{on} ranged from 2.7 × 106 (dissociation experiment) to 1.9 × 109 (association experiment) M^{-1} min^{-1} for CRABP1 and from 9.4 × 106 (dissociation experiment) to 1.8 × 109 (association experiment) M^{-1} min^{-1} for CRABP2. For k_{off} the values ranged from 0.015 (dissociation experiment) to 4.7 (association experiment) min^{-1} for CRABP1 and from 0.025 (dissociation experiment) to 28 (association experiment) min^{-1} for CRABP2, demonstrating the low confidence in the individual kinetic constants. A simple monoexponential fit as used previously fails to account for the simultaneous binding and dissociation processes that occur during the stopped-flow experiments resulting in inaccurate estimates for the kinetic parameters. In addition, the lipid sink likely affects some of the fluorescence data and kinetics of binding in the dissociation experiment. To explore whether the kinetics of *at*RA binding with CRABPs reported previously could be replicated, single concentration stopped-flow experiments were undertaken in this study. The k_{on} values for CRABP1 and CRABP2 were found to be similar to what was previously reported, but the k_{off} was found to be substantially faster (4.4 min^{-1} and 7.9 min^{-1} for CRABP1 and CRABP2, respectively) than previously reported but consistent with the previous data when the same model was used to analyze both datasets. The resulting K_d values (4.7 nM and 7.60 nM for CRABP1 and CRABP2, respectively) are similar to those measured via fluorescence titrations (0.4–16 nM and 2–39 nM for CRABP1 and CRABP2, respectively) (Fiorella and Napoli, 1991; Fogh *et al.*, 1993; Norris *et al.*, 1994; Wang *et al.*, 1997) and those calculated here from the previously published stopped-flow data (Dong *et al.*, 1999). A limitation of these experiments is that we and the previous publication only tested the binding kinetics at a single concentration of *at*RA and CRABP and further experiments are needed to fully characterize the binding kinetics (individual k_{on} and k_{off} values) and the impact of conformational changes on the binding kinetics including the most appropriate kinetic model to fit to the data.

Determination of the K_d for *at*RA with CRABPs allowed fitting of the complete model of CRABP–CYP26A1 protein–protein interactions and the 4-OH-*at*RA formation by CYP26A1 (Figure 2.5A) (Nelson *et al.*, 2016) globally to the 4-OH-*at*RA formation data in the presence of different concentrations of CRABP1 and CRABP2. Fitting the model to the data established that apo-CRABP1 and apo-CRABP2 bind to CYP26A1 with high affinity. As suggested previously for both CYP26B1 and CYP27C1, CRABP1 and CRABP2 appear to also channel *at*RA for metabolism by CYP26A1 with the observed catalytic rate (βk_{cat}) somewhat slower (0.8 min^{-1}) in the presence of CRABPs than in their absence (1.1 min^{-1}) either due to slow off-rate of *at*RA from CRABP to CYP26A1 via the ternary CRABP–*at*RA–CYP26A1 complex or due to a lower catalytic rate of the 4-OH-*at*RA formation by the ternary complex. The current kinetic analyses do not allow the differentiation of these mechanistic possibilities. The parameter estimates suggest that apo-CRABPs have a slightly higher affinity to CYP26A1 than holo-CRABPs. The αK_m of holo-CRABP1 was 0.99 nM in comparison to the K_i of apo-CRABP1 of 0.39 nM with CYP26A1. Similarly, the αK_m of holo-CRABP2 with CYP26A1 was 0.75 nM while the K_i of apo-CRABP2 was 0.53 nM with CYP26A1. Taken together, this suggests that CRABP-CYP interactions alter the rate of *at*RA metabolism via a network of protein–protein interactions that involve both the inhibition of metabolism by apo-CRABP and channeling of *at*RA for metabolism via protein–protein interactions of holo-CRABP (Figure 2.6).

The high affinity of CRABPs with CYP26s is consistent with the observations by fluorescence microscopy, showing that CRABPs localize to the ER membrane (Majumdar *et al.*, 2011). The data shown here suggest that this localization is driven by the affinity of apo-CRABPs to the CYP26 enzymes expressed in the ER and allow the development of a model (Figure 2.6) of the overall regulation of *at*RA metabolism and CYP26A1 activity by CRABPs.

This is consistent with a previous suggestion that CRABPs may play a role in modulating *at*RA concentrations in the cells by fine-tuning *at*RA clearance at different *at*RA concentrations via interactions with CYP enzymes in the ER (Fiorella and Napoli, 1994; Noy, 2000; Nelson *et al.*, 2016; Napoli, 2017; Isoherranen and Zhong, 2019). It is notable that the affinity of *at*RA (K_d) to CRABPs is similar to the cellular concentration of *at*RA (5–10 nM) in mammals (Zhong *et al.*, 2019). For example, if CRABP concentrations in the cells are around 5 nM, at low *at*RA concentrations (1–5 nM), the majority of CRABP would be in the apo-CRABP form and inhibit CYP26A1 activity to preserve free *at*RA, while at high *at*RA concentrations (10–20 nM), nearly all CRABP would be bound with *at*RA and the holo-CRABP would act predominantly via channeling *atRA* for metabolism, bringing *at*RA concentrations back to the desired concentrations rapidly. Similarly, under the circumstances that CRABP expression levels change, a lower CRABP expression would ensure higher free *at*RA concentrations in the cell, potentially allowing for pulses of *at*RA concentrations to be established prior to *at*RA getting cleared effectively by CYP26s. Similarly, high CRABP expression levels would sequester free *at*RA and inhibit *at*RA clearance by CYP26s, preventing further metabolism of *at*RA when *at*RA is scarce. It is noteworthy that the interactions of CRABP1 and CRABP2 with CYP26A1 appear kinetically very similar. However, only CRABP2 translocates to the nucleus upon *at*RA-binding and channels *at*RA to RAR while CRABP1 is restricted to cytosolic and ER localization. As such, in the context of CRABP1, low CRABP1 expression would liberate free *at*RA for signaling while low CRABP2 may facilitate *at*RA metabolism. Further studies of the cellular network of CRABP interactions and localization are needed to fully elucidate the mechanisms on how the CRABP expression affects retinoid signaling.

In addition to CRABPs, FABP5 has been shown to bind *at*RA with a K_d of 57 nM (Schug *et al.*, 2007) and FABP5 has been suggested to modulate *at*RA signaling in cells. Hence, we also assessed whether FABP5 binding would impact *at*RA metabolism similar to CRABPs. No effect of FABP5 on *at*RA metabolism was observed in incubations with CYP3A4, CYP2C8, CYP26A1 or HLMs, suggesting that the impact of FABP5 on *at*RA homeostasis is limited to effects on nuclear receptor signaling in select cell types. It is also possible that the binding affinity of *at*RA to human FABP5 is lower than that measured previously (Schug *et al.*, 2007) resulting in insignificant binding of *at*RA to FABP5 in the incubations.

In conclusion, apo- and holo-CRABP1 and CRABP2 interact with CYP26A1 with high affinity and alter the metabolism of *at*RA by CYP26A1. The data collected support a model where CRABPs serve as a switch to regulate *at*RA concentrations and signaling in cells dictated by the ratio of apo- to holo-CRABP. The apo-CRABPs appear to inhibit the clearance of *at*RA, while holo-CRABPs likely play a dual role of channeling *at*RA to nuclear receptors and to CYP26 enzymes. Taken together, these results suggest that cellular *at*RA signaling and *at*RA gradients and pulses may be modulated by temporary changes in the CRABP expression.

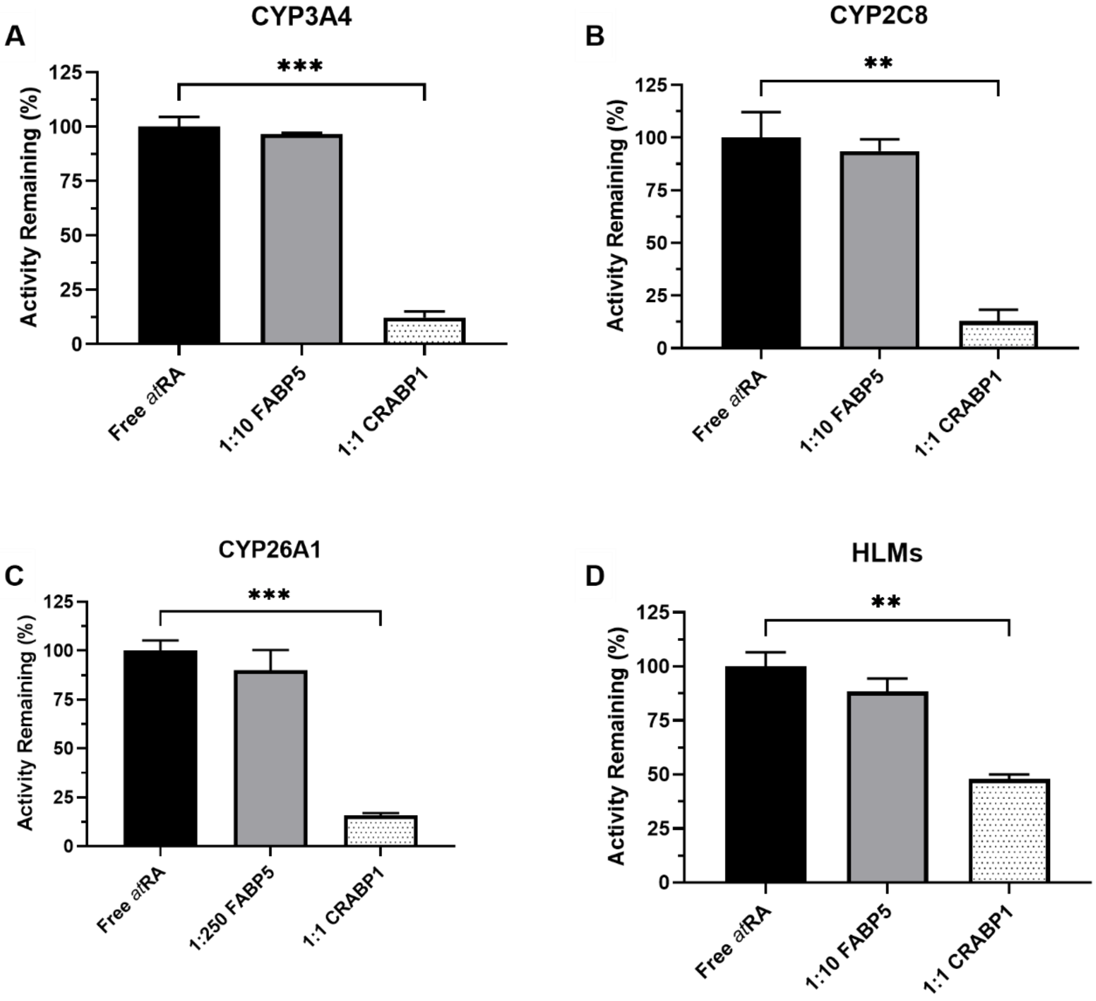

Figure 2.1. Effect of FABP5 and CRABP1 on the metabolism of *at*RA.

The 4-OH-*at*RA formation was measured in incubations with recombinant CYPs and HLMs in the presence and absence of binding proteins. The incubations were conducted, as described in Materials and Methods, with all reactions initiated by adding the substrate pre-complexed with the binding protein. The impact of FABP5 (10 or 250-fold excess to *at*RA) and CRABP1 (equal concentrations as *at*RA) on 4-OH-*at*RA formation by (A) CYP3A4, (B) CYP2C8, (C) CYP26A1 and (D) human liver microsomes (HLMs) is shown. *at*RA concentration was 1 µM in (A,B), 20 nM in (C) and 500 nM in (D). ** p-value < 0.01, *** p-value < 0.001, one-way ANOVA with Dunnett's post hoc test.

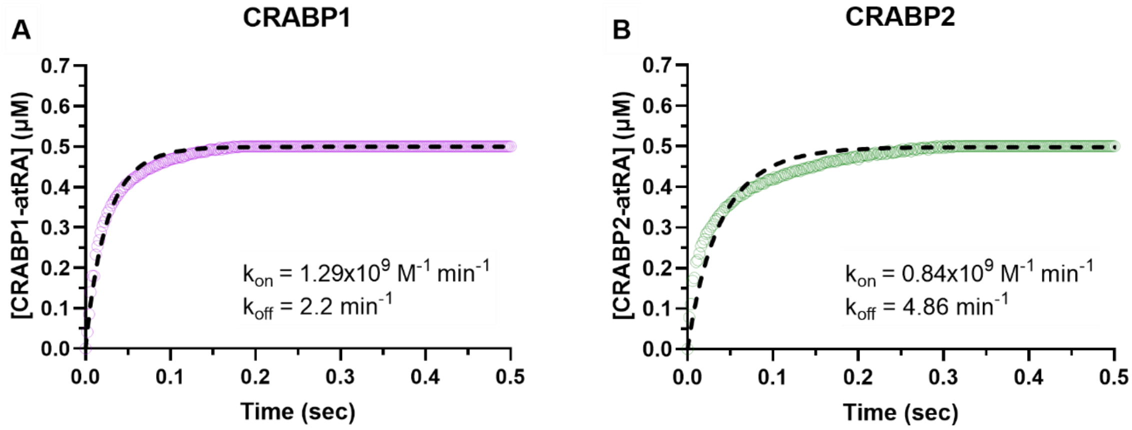

Figure 2.2. CRABP–*at*RA-binding kinetics determined with stopped-flow.
Association of *at*RA (2 µM) with CRABP1 (A) and CRABP2 (B) (0.5 µM) was monitored from the increase in *at*RA fluorescence due to CRABP binding, as described in Materials and Methods. The concentration of holo-CRABP was calculated based on the fluorescence yield of holo-CRABP. The shaded line in panels (A,B) show the observed time course of change in holo-CRABP1 (A) and holo-CRABP2 (B) concentrations following mixing of CRABPs with *at*RA. The dashed line shows the model fits to the data. The fitted association (k_{on}) and dissociation (k_{off}) constants for the specific experiment are shown in insets.

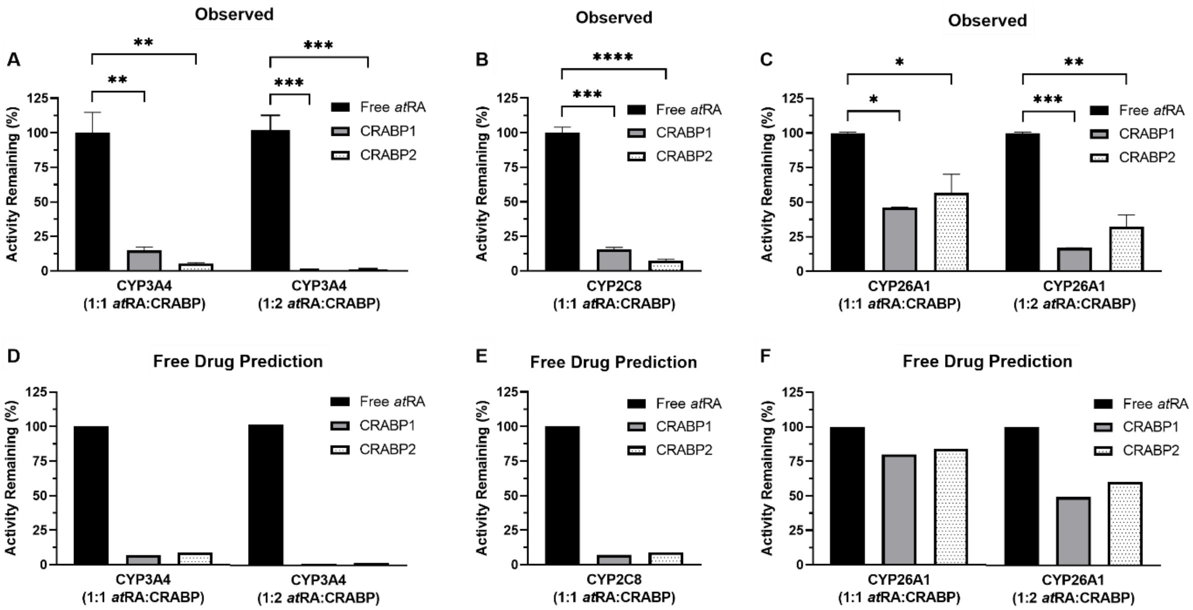

Figure 2.3. The 4-OH-*at*RA formation by CYP3A4, CYP2C8 and CYP26A1 in the presence of CRABPs.

The impact of CRABPs on the 4-OH-*at*RA formation by CYP3A4, CYP2C8 and CYP26A1 was assessed in incubations with recombinant enzymes. At a 1:1 ratio of CRABP to *at*RA, both CRABP1 and CRABP2 decreased the 4-OH-*at*RA formation by CYP3A4 (A) (to 15 ± 2% and 5 ± 0.7% of control, respectively) and CYP2C8 (B) (to 16 ± 2% and 7 ± 1% of control, respectively), and completely abolished CYP3A4 activity at a 1:2 *at*RA to CRABP ratio (A) (>99% decrease). The observed activity of CYP3A4 and CYP2C8 in the presence of CRABPs is consistent with predictions made via calculating the unbound concentrations of *at*RA (D,E) present in the incubations based on the experimental K_d values from stopped-flow experiments. (C) The 4-OH-*at*RA formation by CYP26A1 was decreased by about 50% at a 1:1 ratio of CRABP to *at*RA and > 70% in the presence of 2-fold excess CRABPs. Calculated unbound concentrations of *at*RA predicted higher 4-OH-*at*RA formation by CYP26A1 (F) than observed, suggesting that the free drug hypothesis cannot explain CYP26A1 activity in the presence of CRABPs. (* p-value < 0.05, ** p-value < 0.01, *** p-value < 0.001, **** p-value < 0.0001, one-way ANOVA with Dunnett’s post hoc test).

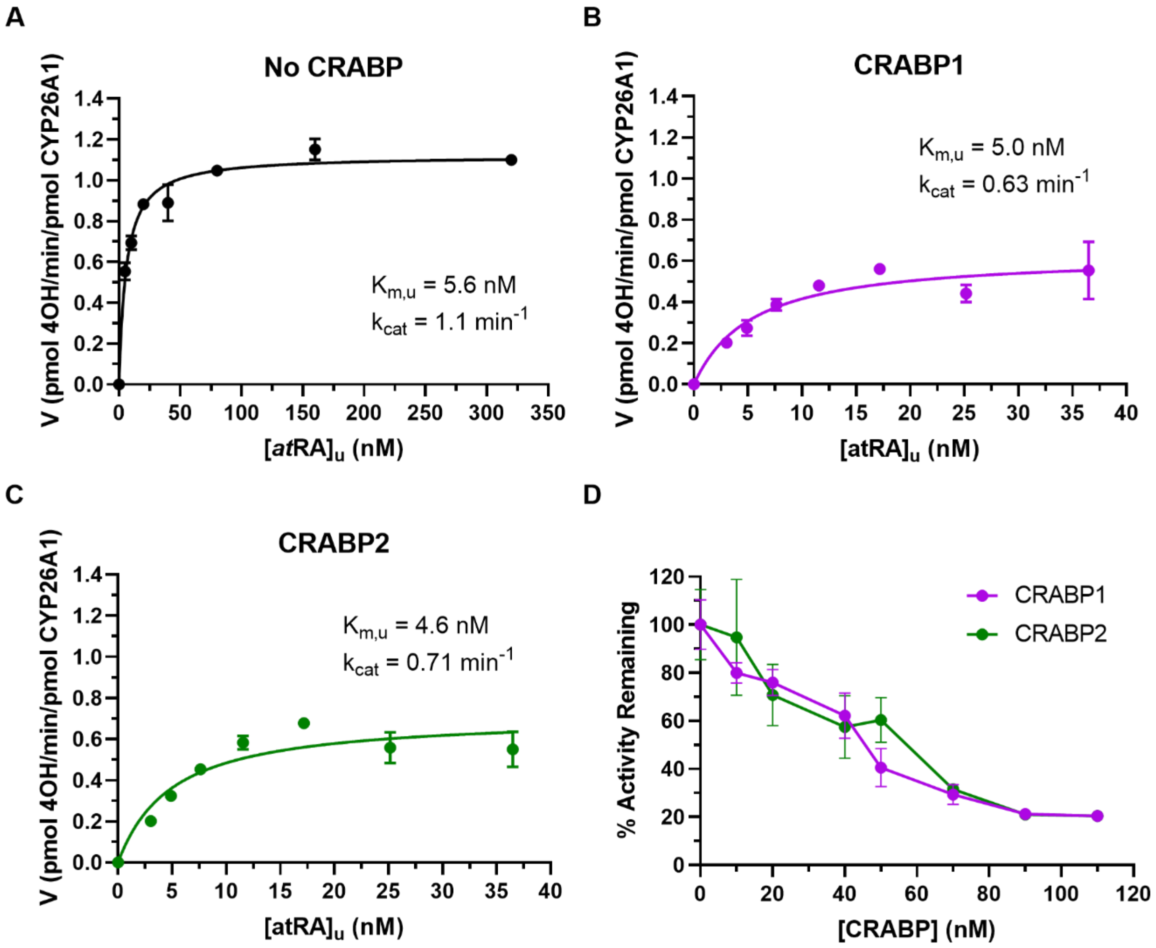

Figure 2.4. The 4-OH-*at*RA formation kinetics by CYP26A1 in the presence of CRABPs. Varying concentrations of holo-CRABP1 and holo-CRABP2 (5–320 nM) were incubated with recombinant CYP26A1, as described in Material and Methods. (A–C) Representative experiments of the 4-OH-*at*RA formation by CYP26A1 in the presence and absence of CRABPs. The Morrison tight binding equation was fitted to the data and the unbound K_m and k_{cat} values are shown in the inset for the representative experiment shown. (D) Inhibition of theCYP26A1 mediated 4-OH-*at*RA formation by CRABPs is shown with increasing CRABP1 and CRABP2 concentrations relative to *at*RA (50 nM).

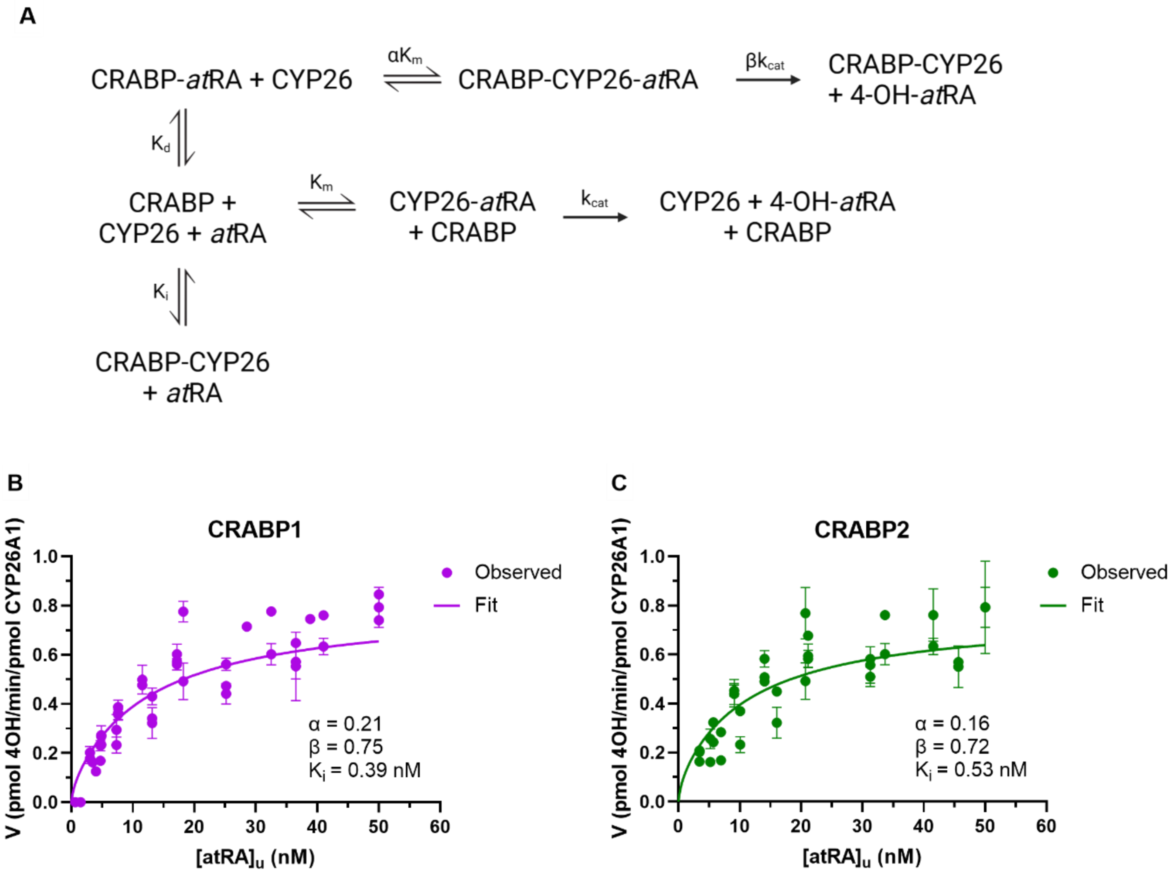

Figure 2.5. The CRABP-CYP26 interaction model and fit of the interaction model to the 4-OH-*at*RA formation data.

The kinetic scheme for the model of the 4-OH-*at*RA formation by CYP26s in the presence of CRABPs that incorporates holo-CRABP and apo-CRABP-CYP26 interactions is shown in (A) (created with BioRender.com accessed on 8 April 2022). αK_m is the affinity of holo-CRABP for CYP26, Ki is the affinity of apo-CRABP for CYP26 and βkcat is the rate of catalysis for an *at*RA-CRABP-CYP26 ternary complex. The model was globally fit to the data with CYP26A1 as described in Materials and Methods, and plots with observed 4-OH-*at*RA formation data (circles) and model fits (solid lines) for CYP26A1 in the presence of CRABP1 (A) and CRABP2 (B) are shown.

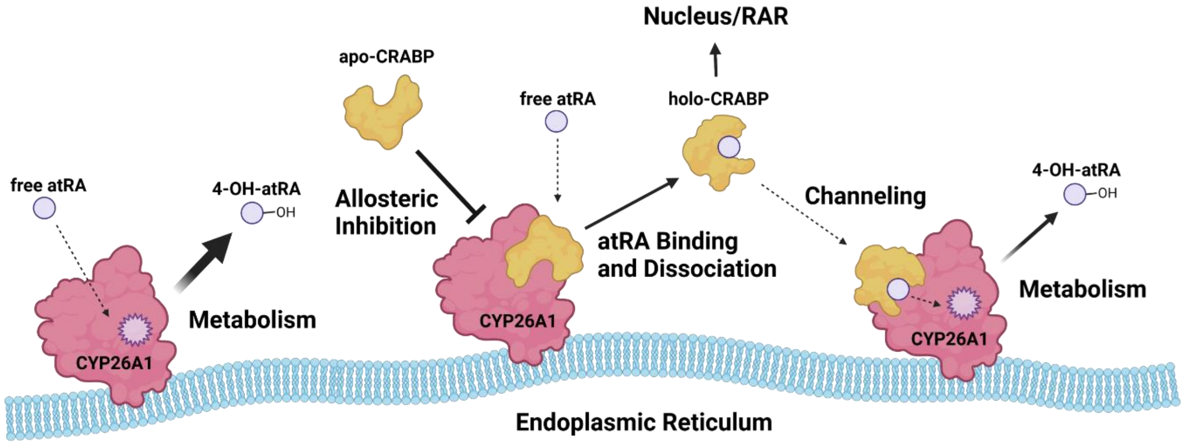

Figure 2.6. Kinetics informed model of CRABP cellular functions in regulating *at*RA metabolism and homeostasis.

CYP26A1 metabolizes *at*RA to 4-OH-*at*RA to facilitate *at*RA clearance from the cell. Apo-CRABP is bound to CYP26A1 in the ER to prevent *at*RA metabolism when *at*RA levels are scarce and an excess of apo-CRABP is present. When *at*RA is abundant, more CRABP is bound to *at*RA, releasing holo-CRABP from CYP26A1 and increasing holo-CRABP levels in the cell. Holo-CRABP may facilitate the delivery of *at*RA to nuclear receptors or directly channel *at*RA to CYP26A1 for metabolism (figure created with BioRender.com accessed on 8 April 2022).

Table 2.1. CRABP–*at*RA binding kinetics as measured by stopped-flow.

	k_{on} (M^{-1} min^{-1})	k_{off} (min^{-1})	K_d (nM)
CRABP1	$1.07 \times 10^9 \pm 2.7 \times 10^8$	4.40 ± 2.4	4.7 ± 3.8
CRABP2	$0.96 \times 10^9 \pm 2.2 \times 10^8$	7.89 ± 6.0	7.6 ± 4.0

Data reported as means ± S.D. from three separate experiments. Due to limited stopped-flow data the K_d value cannot be solely determined from these experiments with confidence and should be considered together with published (Napoli, 2017) K_d values.

Chapter 3. DRUGS FORM TERNARY COMPLEXES WITH HUMAN LIVER FATTY ACID BINDING PROTEIN (FABP1) AND FABP1 BINDING ALTERS DRUG METABOLISM

This chapter was adapted from work published in *bioRxiv* and submitted to *Molecular Pharmacology* on January 17, 2024

Co-authors: Alice Martynova[b], Abhinav Nath[c], Benjamin P. Zercher[b], Matthew F. Bush[b], Nina Isoherranen[a]

[a]*Department of Pharmaceutics, School of Pharmacy, University of Washington, Seattle, WA, United States*

[b]*Department of Chemistry, University of Washington, Seattle, WA, United States*

[c]*Department of Medicinal Chemistry, University of Washington, Seattle, WA*

3.1 ABSTRACT

Liver fatty acid binding protein (FABP1) binds diverse endogenous lipids and is highly expressed in the human liver. Binding to FABP1 alters the metabolism and homeostasis of endogenous lipids in the liver. Drugs have also been shown to bind to rat FABP1, but limited data is available for human FABP1 (hFABP1). FABP1 has a large binding pocket and up to two fatty acids can bind to FABP1 simultaneously. We hypothesized that drug binding to hFABP1 results in formation of ternary complexes and that FABP1 binding alters drug metabolism. To test these hypotheses, native protein mass spectrometry (MS) and fluorescent 11-(dansylamino)undecanoic acid (DAUDA) displacement assays were used to characterize drug binding to hFABP1 and diclofenac oxidation by cytochrome P450 2C9 (CYP2C9) was studied in the presence and absence of hFABP1. DAUDA binding to hFABP1 involved high ($K_{d,1}$=0.2 µM) and low affinity ($K_{d,2}$ >10 µM) binding sites. Nine drugs bound to hFABP1 with K_d values ranging from 1 to 20 µM. None of the tested drugs completely displaced DAUDA from hFABP1 and fluorescence spectra showed evidence of ternary complex formation. Formation of DAUDA-hFABP1-diclofenac ternary complex was verified with native MS. Docking placed diclofenac in the portal region of FABP1 with DAUDA in the binding cavity. The k_{cat} of diclofenac hydroxylation by CYP2C9 was decreased by ~50% ($p<0.01$) in the presence of FABP1. Together, these results suggest that drugs form ternary complexes with hFABP1 and that hFABP1 binding in the liver will alter drug metabolism and clearance.

3.2 INTRODUCTION

Fatty acid binding proteins (FABPs) are intracellular lipid binding proteins broadly expressed in tissues (Smathers and Petersen, 2011; Yabut and Isoherranen, 2023). They bind essential endogenous lipids such as fatty acids, bile acids, cholesterol and eicosanoids (Smathers and Petersen, 2011; Yabut and Isoherranen, 2023). FABPs are critical for lipid homeostasis and signaling in variety of tissues through regulation of the uptake, metabolism and cellular trafficking of their ligands (Smathers and Petersen, 2011; Yabut and Isoherranen, 2023). FABPs influence the pharmacological effects of drugs that bind FABPs. For example, FABPs impact nuclear receptor activation by hypolipidemic drugs (Hughes *et al.*, 2015) and alter behavior and cognition associated with cannabinoid signaling (Elmes *et al.*, 2019; Penman *et al.*, 2023). With regard to drug pharmacokinetics, changes in FABP expression in the intestines and brain result in altered tissue uptake and disposition of drugs (Trevaskis *et al.*, 2011; Penman *et al.*, 2023). Surprisingly, little is known about how drug binding to FABPs in the liver alters drug metabolism and liver uptake.

FABP1 is the predominant FABP in the liver. It constitutes 7-10% of all cytosolic protein in the human liver (0.7-1 mM) (Wang *et al.*, 2015) and accounts for ~80% of long chain fatty acid (LCFA) binding in the liver cytosol (Schroeder *et al.*, 2016). Despite the extensive characterization of binding of endogenous ligands to FABP1, a comprehensive understanding of drug binding to human FABP1 (hFABP1) remains elusuive. Nonsteroidal anti-inflammatory drugs (NSAIDs), fibrates, benzodiazepines, glitazones, β-blockers, steroids and psychoactive cannabinoids bind to rat FABP1 (rFABP1) (Chuang *et al.*, 2008; Huang *et al.*, 2018). However, rFABP1 and hFABP1 have distinct structural and biochemical differences that likely result in different ligand binding specificities and affinities. rFABP1 and hFABP1 share only 83% amino acid identity with 10% of the sequence being nonconservative amino acid replacements (Schroeder *et al.*, 2016). hFABP1 is less alpha helical, has a larger binding cavity, higher thermal stability, and different binding affinities with long chain fatty acid (LCFA) than rFABP1. For drugs, fenofibrate and fenofibric acid bound to hFABP1 with 7 to 23-fold greater binding affinity when compared to rFABP1 (Martin *et al.*, 2013). Similarly, some cannabinoids bound to hFABP1 (Elmes *et al.*, 2019) but no binding was detected to rFABP1 (Huang *et al.*, 2018). Hence, data for drug binding to rFABP1 may not translate to hFABP1 and a more thorough understanding of general drug binding kinetics with hFABP1 is needed.

Fluorescence displacement assays are widely used to identify FABP ligands and characterize ligand binding to FABPs (Thumser and Wilton, 1994; Velkov *et al.*, 2007; Chuang *et al.*, 2008; Zhou *et al.*, 2019; Yabut and Isoherranen, 2023). However, FABP1 has a large binding cavity and multiple endogenous ligands have been shown to bind FABP1 simultaneously (Santambrogio *et al.*, 2013; Favretto *et al.*, 2015). This suggests that in fluorescence displacement assays drug ligands may only partially displace the fluorescent ligand which may lead to a loss of assay sensitivity and confound assessment of ligand binding affinity. With FABP2 such effects were shown with ketorolac (Patil *et al.*, 2014). Ketorolac did not displace the fluorescent probe 8-anilino-1-naphthalenesulfonic acid (ANS) from FABP2 and NMR analysis suggested that ketorolac and ANS bind simultaneously to FABP2 (Patil *et al.*, 2014). NMR studies have also suggested that drugs form ternary complexes with rFABP1 (Chuang *et al.*, 2008). Based on these findings we hypothesized that drug ligands form ternary complexes with hFABP1 either with a fluorescent probe, or with two drug molecules binding simultaneously. To test this hypothesis, we developed a DAUDA displacement assay with singular value decomposition (SVD) analysis in conjunction with native mass spectrometry to characterize ligand binding to hFABP1.

FABP1 has profound effects on the metabolism of endogenous ligands in the liver. FABP1 knockout mice have decreased hepatic fatty acid β-oxidation, decreased triglyceride formation, decreased [^{3}H]oleate incorporation into cellular triglycerides and diacylglycerol, and altered hepatic lipid profiles (Martin *et al.*, 2003, 2005; Newberry *et al.*, 2003; Storch and Corsico, 2008). In perfused rat livers, higher FABP1 expression resulted in higher clearance of palmitate (Hung *et al.*, 2003). Notably, FABP1 also interacts directly with carnitine palmitoyl transferase I (CPTI) facilitating LCFA-CoA metabolism (Hostetler *et al.*, 2011). Consistent with a role of FABP1 facilitating metabolism, FABP1-knockout mice had decreased rates of Δ9-tetrahydrocannabinol (THC) metabolism (Elmes *et al.*, 2019). Based on these data we hypothesized that the metabolism of drugs that bind to hFABP1 is altered in the presence of FABP1 binding. This hypothesis was tested using diclofenac metabolism by recombinant CYP2C9 as a model reaction.

3.3 MATERIALS AND METHODS

3.3.1 *Chemicals and Reagents*

Kanamycin, Trizma base (Tris), sodium chloride, sodium phosphate, potassium phosphate, protease inhibitor tablets, benzonase, thrombin, Coomassie Brilliant Blue R, 11-(Dansylamino)undecanoic acid (DAUDA), arachidonic acid, diazepam, diclofenac, fluoxetine, racemic flurbiprofen, gemfibrozil, ibuprofen, sulfaphenazole and tolbutamide were purchased from Millipore-Sigma (St. Louis, MO). (R)- and (S)- flurbiprofen were purchased from Cayman Chemical (Ann Arbor, MI). Pioglitazone was purchased from Altan Biochemicals. Tryptone, yeast extract, IPTG, PMSF, imidazole, BCA protein assay and low melt agarose were from Thermo Fisher Scientific (Waltham, MA). SeaKem agarose was purchased from Lonza (Basel, Switzerland). Lipidex-5000 slurry in methanol was purchased from Perkin Elmer Inc (Waltham, MA, USA). Mini-PROTEAN TGX protein gels were purchased from Bio-Rad (Hercules, CA). HindIII and NdeI restriction enzymes were purchased from New England BioLabs (Ipswich, MA). Lyophilized ribonuclease A was purchased from Sigma Aldrich (St. Louis, MO). Ultrapure ammonium acetate salt was purchased from VWR Scientific (San Francisco, CA) and tuning mix for ESI-time-of-flight mass spectrometry was purchased from Agilent (Santa Clara, CA). 4’OH-diclofenac and 4’OH-5-Cl-diclofenac were a gift from Dr. Allan Rettie (Department of Medicinal Chemistry, University of Washington).

3.3.2 *Cloning, Expression and Purification of Human FABP1*

The human FABP1 open reading frame was purchased from Origene (Rockville, MD, Cat. No. SC119222) and cloned into pET28a+ with an N-terminal hexa-histidine (6xHis) tag and a thrombin cleavage site using N-terminal NdeI and C-terminal HindIII restriction sites. The expression construct was transformed into Rosetta 2 E. coli (Novagen, Madison, WI) and a freshly transformed colony was inoculated into a 25 mL starter culture of Luria Broth (LB) with kanamycin (50 μg/mL) and grown for 6 hours at 37°C in a shaking incubator at 250 rpm. 15 mL of starter culture was used to inoculate 1 L of LB-kanamycin which was then grown to an OD600 ≈ 0.6. The culture was cooled at room temperature for 20 minutes prior to adding 0.1 mM IPTG to induce FABP1 expression. The protein was expressed at 18°C for 18 hours in a shaking incubator at 250 rpm. Cells were harvested by centrifugation at 4,000 g for 20 minutes then washed with phosphate buffered saline (PBS) containing 1 mM PMSF, pelleted, decanted and stored at -80°C until purification.

Frozen pellets were thawed on ice in lysis buffer (20 mM Tris pH 7.4 at 4°C, 500 mM NaCl, 30 mM imidazole) with protease inhibitor cocktail (Roche, cOmplete Mini EDTA-free), 1 mM PMSF and 25 U of benzonase. 1 mg/mL lysozyme was added and the cells were rocked on ice for 30 minutes. Cells were sonicated at 75% power for 30 seconds with a 1-minute rest on ice for 5 rounds. The lysate was cleared at 20,000 g for 30 minutes and the supernatant filtered through a 0.22 μm syringe filter (Minisart, Sartorius, Göttingen, Germany). The filtered lysate was loaded onto a 90 mL Dynaloop (Bio-Rad, Hercules, CA) coupled to a DuoFlow fast protein liquid chromatograph (FPLC) (Bio-Rad, Hercules, CA) and run over a 1 mL HisTrap HP affinity column (GE Healthcare, Chicago, IL) equilibrated in lysis buffer at a flow rate of 0.75 mL/min. The column was washed with 10 column volumes of wash buffer (20 mM Tris pH 7.4 at 4°C, 500 mM NaCl, 30 mM imidazole) and FABP1 eluted using elution buffer (20 mM Tris pH 7.4 at 4°C, 500 mM NaCl) with a step gradient of increasing concentrations of imidazole (0-500 mM) in 1 mL fractions over 10 column volumes. The eluted protein was detected at 280 nm absorbance and the peak FABP1 containing fractions were pooled for subsequent steps of purification.

The peak fractions from the HisTrap purification were combined and diluted with an equivalent volume of 20 mM Tris pH 7.4 at 4°C, 100 mM NaCl. The concentration of FABP1 was measured using a Nanodrop A280. The N-terminal his-tag was then cleaved by adding 0.03 U of thrombin protease per 1 µg of FABP1 and incubating the mixture in a water bath for 1 hour at 37°C. Complete cleavage of the N-terminal tag was confirmed via SDS-PAGE and Coomassie staining and with an anti-His (mouse anti-His antibody from Qiagen, Valencia, CA) western blot. The cleaved protein (2 mL) was then injected into a Superdex 75 size exclusion column (GE Healthcare, Chicago, IL) equilibrated with gel filtration buffer (10 mM potassium phosphate pH 7.4, 150 mM KCl) using a DuoFlow FPLC at a flow rate of 0.5 mL/min. After injection, the flow rate was increased to 1 mL/min and FABP1 elution monitored by UV absorbance at 280 nm. 1 mL fractions were collected and the FABP1 containing fractions corresponding to the UV peak were verified by SDS-PAGE and Coomassie staining. Monomeric FABP1 was verified using gel filtration and by comparison of the molecular weight to standards from a calibration kit (Cytiva, Marlbough, MA). FABP1 containing fractions (up to 4 mL) were pooled for removal of copurifying lipids using the final delipidation protocol.

For delipidation an equivalent volume of butanol was added to the FABP1 containing fractions. The butanol and FABP1 mixture was rocked at room temperature in a glass tube for 10 minutes. The mixture was then centrifuged at low speed for 30 seconds to separate butanol and aqueous phases and the butanol phase was removed with a Pasteur pipette. Butanol extraction was repeated for a total of 3 rounds. The aqueous phase containing FABP1 was then transferred to a 10 mL Poly-Prep chromatography column (Bio-Rad, Hercules, CA) containing Lipidex-5000 (0.1 g of Lipidex-5000 per 1 mg of FABP1) pre-conditioned overnight after sonication in gel filtration buffer. FABP1 was incubated with Lipdex-5000 with rocking at 21°C for 30 minutes. After incubation with Lipidex-5000, traces of butanol were removed by gel filtration chromatography. The Superdex 75 size exclusion column was equilibrated with 10 mM potassium phosphate pH 7.4 with 150 mM KCl. FABP1 containing gel filtration fractions were pooled, stored on ice and the concentration of delipidated FABP1 was quantified via bicinchoninic acid (BCA) (Pierce, Waltham, MA) assay prior to adding 0.5 mM DTT. Optimization details of the purification and delipidation of human FABP1 can be found in (Yabut *et al.*, 2024).

3.3.3 *Fluorescence Assay for DAUDA Binding to FABP1*

All fluorescence spectra were collected using a Cary Eclipse fluorescence spectrophotometer (Agilent, Santa Clara, CA). The scan rate was set to medium (600 nm/min) and the photomultiplier tube voltage was set to high (800V). Stock solutions of DAUDA were prepared in methanol and DAUDA concentrations confirmed using a Cary 60 UV-Vis spectrophotometer (Agilent, Santa Clara, CA) assuming a DAUDA molar absorption coefficient of 4400 M^{-1} cm^{-1} at 335 nm in methanol (Thumser *et al.*, 1996). The fluorescence spectrum of DAUDA was initially verified in the presence and absence of FABP1. Briefly, solutions of DAUDA (0.08, 0.28, 0.68 µM) in the absence or presence of FABP1 (5 µM) were made in 50 mM potassium phosphate buffer, pH 7.4 with 100 mM KCl. DAUDA binding to FABP1 was monitored via the enhancement of fluorescence in the presence of FABP1 using an excitation wavelength of 335 nm and emission was monitored from 400-700 nm. Spectra were collected in 2 mL of assay buffer (100 mM potassium phosphate, pH 7.4) in a 4 mL clear quartz cuvette at 21°C. The final concentration of organic solvent was kept <1.6%. All titration experiments were repeated on at least three separate days and with at least two independent batches of purified protein.

The equilibrium dissociation constant (K_d) for DAUDA with FABP1 was determined using reverse and forward fluorescence titrations. A range of concentrations of FABP1 and DAUDA were initially tested to optimize experimental conditions based on detector sensitivity and ligand binding/depletion. Reverse titrations were then performed with a constant concentration of DAUDA (0.05 µM) and increasing concentrations of FABP1. Forward titrations were performed with a constant concentration of FABP1 (0.3 µM) and increasing DAUDA concentrations. The emission spectrum of DAUDA in solution overlaps with that of DAUDA-FABP1 preventing direct measurement of DAUDA-FABP1 fluorescence in titration experiments. Singular value decomposition (SVD) was therefore used to deconvolute fluorescence titration spectra. SVD can be used to analyze spectral data and quantify contributions from spectrally distinct species measured over the course of a titration (Hendler and Shrager, 1994; Nath *et al.*, 2008). SVD yields a set of singular values that reveal how many spectrally distinct species contribute to a titration: if there are *n* species that make independent contributions, there will be *n* singular values that are greater than 0 (all subsequent singular values will be close to 0, and simply reflect noise in the data). Singular values in titration experiments were determined to be above noise if they were identified as outliers in Iglewicz and Hoaglin’s robust test for multiple outliers using a Z score of 3.5 (Iglewicz and Hoaglin, 1993).

Spectral deconvolution requires selection of basis spectra corresponding to the individual species that contribute to the observed fluorescence signal. Basis spectra of DAUDA in solution and DAUDA-FABP1 complex were used for deconvolution of titration spectra and determination of the specific fluorescence of DAUDA-FABP1 complex. The details of the SVD analysis including construction of basis spectra are provided in Materials and Methods Section 3.3.4.

The high affinity equilibrium dissociation constant ($K_{d,1}$) for DAUDA binding to FABP1 was determined by fitting a tight-binding quadratic equation (Jarmoskaite *et al.*, 2020) to ‘reverse’ titration data, wherein DAUDA concentrations were held constant and FABP1 concentrations were varied.

$$F = F_{max} \times \frac{([FABP1]+[DAUDA]+K_{d,1}) - \sqrt{([FABP1]+[DAUDA]+K_{d,1})^2 - 4[FABP1][DAUDA]}}{2[DAUDA]} \tag{3.1}$$

In Equation 3.1, the dependent variable F is the fluorescence arising from the DAUDA-FABP1 complex upon addition of FABP1, F_{max} is the fluorescence of DAUDA in the presence of saturating concentrations of FABP1, [DAUDA] is the constant concentration of DAUDA added, and the independent variable [FABP1] is the concentration of FABP1 used in reverse titration experiments. The best-fit values of F_{max} and $K_{d,1}$ were determined by non-linear least squares optimization in Prism 10 (GraphPad Software, Boston, MA).

Results from the quadratic equation fit were verified by numerical simulations implemented in COPASI (Hoops *et al.*, 2006). Fitting to numerical simulations can be used to estimate thermodynamic and kinetic parameters, and often requires fewer assumptions than traditional analytical equations such as Equation 3.1. Reaction 1 describes the bimolecular association of DAUDA and FABP1:

Reaction 1: $$DAUDA + FABP1 \underset{k_2}{\overset{k_1}{\rightleftharpoons}} DAUDA\text{-}FABP1$$

Here, k_1 and k_2 are the association and dissociation rate constants for DAUDA binding with FABP1, and the $K_{d,1}$ of DAUDA with FABP1 is equal to the ratio k_2/k_1. It is then possible to solve the system of differential equations that describe the rates of change of DAUDA, FABP1, and DAUDA-FABP1 concentrations to determine the equilibrium concentrations of all three species from any given starting conditions. The Parameter Estimation task in COPASI can use this approach to optimize the values of specified model parameters by minimizing the sum of the squares of the residuals between the simulated concentrations and experimental observations (Hoops *et al.*, 2006). To fit reverse titration data, the starting concentrations of DAUDA (0.05 µM) and FABP1 (varied) were set to match experimental values. A scaling factor (*Scale*) was defined as a Global Quantity in COPASI to relate the observed fluorescence (*F*) to the concentration of the DAUDA-FABP1:

$$F = Scale \cdot [DAUDA\text{-}FABP1] \tag{3.2}$$

The association rate constant (k_1) was set to 1 $\mu M^{-1}\,s^{-1}$ based on observed association rate constant of retinoic acid with cellular retinoic acid binding proteins 1 and 2, two other members of the intracellular lipid binding protein family (Yabut and Isoherranen, 2022). Note that the simulations used here deal with equilibrium rather than kinetic behavior, and so the value of k_1 itself is not relevant; the relevant parameter is the ratio $K_{d,1} = k_2/k_1$. This was confirmed by sensitivity analysis using k_1 values ranging from 0.01 to 100 $\mu M^{-1}\,s^{-1}$. The results for $K_{d,1}$ was unaffected by the value of k_1 as expected. The values of the dissociation rate constant (k_2) and *Scale* were optimized using the Levenberg-Marquardt method in the Parameter Estimation task in COPASI to maximize agreement with experimentally observed binding curves. The lower and upper bound values for k_2 were 0.1 and 10, respectively, and the lower and upper bound values for *Scale* were 1,000-1,000,000, respectively. The results were insensitive to the start values for k_2 and *Scale* within this range. Values of $K_{d,1}$ for the reverse titration determined from Equation 3.1 and from numerical simulations were in excellent agreement.

The binding constant for the low affinity site ($K_{d,2}$) was estimated by extending the numerical simulations to account for a second binding site, and fitting to 'forward' titration data with a fixed concentration of FABP1 and a range of DAUDA concentrations. In addition to Reaction 1 described above, another reaction describing sequential binding of a second DAUDA molecule binding to FABP1 was added to the model:

Reaction 2: $$DAUDA + DAUDA\text{-}FABP1 \underset{k_4}{\overset{k_3}{\rightleftharpoons}} DAUDA\text{-}FABP1\text{-}DAUDA$$

Here, k_3 and k_4 are the association and dissociation rate constants for the second DAUDA binding site on FABP1, such that the equilibrium binding constant for the second DAUDA molecule ($K_{d,2}$) is equal to k_4/k_3. For COPASI simulations, the total fluorescence (F_{tot}) observed from singly (DAUDA-FABP1) and doubly (DAUDA-FABP1-DAUDA) bound complexes was defined by the following equation:

$$F_{tot} = Scale \cdot ([DAUDA\text{-}FABP1] + 2 \cdot [DAUDA\text{-}FABP1\text{-}DAUDA]) \tag{3.3}$$

Here, [DAUDA-FABP1] and [DAUDA-FABP1-DAUDA] are the simulated equilibrium concentrations of singly and doubly bound DAUDA-FABP1 complexes, respectively. *Scale* is, as described above, a factor that relates the observed fluorescence to the simulated concentrations of [DAUDA-FABP1] and [DAUDA-FABP1-DAUDA]. Equation 3.3 makes the assumption that the doubly-bound complex fluorescence is twice as intense as the singly-bound. While this assumption could not be verified because it was not possible to saturate the second binding site at experimentally tractable DAUDA concentrations, without this constraint the parameter optimization is overparameterized and fails to produce robust results. Starting concentrations of

FABP1 (0.3 µM) and DAUDA were set to match experimental values. k_1 and k_2 for Reaction 1 were fixed to 1 μM^{-1} s^{-1} and 0.2 s^{-1}, respectively, matching the optimal single site binding affinity ($K_{d,1}$) determined from reverse titrations. k_3 was also fixed to 1 μM^{-1} s^{-1}, and as expected sensitivity analysis showed that the values of $K_{d,2}$ obtained by parameter estimation were not affected by k_3 values ranging from 0.01 to 100 μM^{-1} s^{-1}. The values of k_4 and *Scale* were optimized using the Levenberg-Marquardt method in the Parameter Estimation task in COPASI. The lower and upper bounds for k_4 were 0.1 and 10, and the lower and upper bound values for *Scale* were 1,000 and 1,000,000. Results were insensitive to the starting values of k_4 and *Scale*. DAUDA binding affinities are reported from a single optimization using data combined from replicate experiments performed on separate days and with FABP1 from different purifications.

3.3.4 *Analysis of Titration Spectra by Singular Value Decomposition*

Experimental fluorescence spectra in titration experiments with DAUDA and FABP1 are composed of a mixture of spectrally distinct bound and unbound DAUDA species (i.e spectral components). The observed fluorescence spectrum at a given concentration of DAUDA and FABP1 is the sum of the individual contributions of these spectral components. Hence, deconvolution of titration spectra with DAUDA is necessary to avoid confounding the fluorescence of DAUDA bound with FABP1 with DAUDA free in solution. Singular value decomposition (SVD) is an analytical technique based on linear algebra that can be used to deconvolute observed fluorescence spectra into individual spectral components. A general approachable review of the linear algebra, theory and application of SVD can be found in (Hendler and Shrager, 1994). In brief, observed fluorescence spectra from a titration experiment was constructed into a matrix, *A*, where each column of *A* represents a separate observed fluorescence spectrum for a given concentration of the binding partner that is titrated (i.e. DAUDA, FABP1 or ligand), and the rows of *A* correspond to the observed fluorescence at a specific wavelength in the spectrum. SVD results in a factorization of matrix *A* into three different matrices *U*, *S* and *V*:

$$A = USV^T \qquad (3.4)$$

U is the basis vector which contains unique spectral components ranked by their relative contributions to the observed data, *S* is the singular value matrix that quantifies the relative contributions of each of the components in *U*, and *V* is a matrix that contains the titration profile of the spectral components in *U*. (A superscript *T* indicates that the relevant matrix is transposed.) The fluorescence titration spectra can be reconstructed to filter out the noise in the data by including only the most relevant unique spectral components in *U* (i.e., those components with the highest singular values in *S*). Iglewicz and Hoaglin's robust test for multiple outliers, using a Z score of 3.5 (Iglewicz and Hoaglin, 1993), was used to identify singular values that were significantly above baseline (i.e., noise). For each of the titrations presented here, this meant that the filtered data included only the top 3 or 4 spectral components.

Furthermore, *basis spectra* (i.e., spectra of each of the molecular species that contribute to the observed data) can be derived from suitable combinations of spectral components in *U* or through separate experiments. If A_r is the reconstructed (i.e., SVD-filtered) fluorescence data and *D* is the matrix of basis spectra, it is then possible to calculate how the concentrations of each molecular species vary over the course of the titration:

$$F = (D^+ A_r)^T \qquad (3.5)$$

Here, the matrix *F* contains the calculated concentrations of each of the pure components in *D* at each point in the titration. (A superscript + denotes the pseudoinverse of the indicated matrix.)

Spectral filtering and deconvolution of fluorescence spectra from titration experiments with DAUDA was done with a previously described in house SVD program (Nath *et al.*, 2008).

The program and source code are available at the following web address: http://marvin.mchem.washington.edu/pca/. Titration emission spectra from a single experiment were formatted to tab-delimited text files (.txt) where the first column indicated the wavelength and each subsequent column were the observed fluorescence values corresponding to a single concentration of the ligand being titrated. An example of properly formatted data can be found at the web address above. Explicit basis spectra of DAUDA alone in solution and DAUDA-FABP1, constructed as described below (Figure 3.6C), were uploaded for use in deconvolution of titration spectra. A flat line was included in the basis spectra file to account for any residual fluorescence that was not described by the basis spectra of DAUDA or DAUDA-FABP1. Binding isotherms were constructed using the specific fluorescence for DAUDA alone and DAUDA-FABP1 obtained from the matrix F^T (i.e., the concentration vectors of the corresponding basis spectra). These values were plotted against the concentrations of titrated ligand to generate binding curves for reverse and forward titrations and DAUDA displacement titration experiments.

The basis spectra for DAUDA alone in solution and DAUDA-FABP1 were obtained from experimental spectra of titrations with DAUDA alone or DAUDA in the presence of excess FABP1. The experimental titration spectra were first SVD-filtered as described above. The basis spectrum of DAUDA alone corresponded to the emission spectrum of 1.03 µM DAUDA in assay buffer (Figure 3.6B). The basis spectrum of DAUDA bound to FABP1 (DAUDA-FABP1) was similarly constructed from measurements of DAUDA in the presence of an excess of FABP1 (0.05 µM DAUDA with 1.5 µM FABP1, and 0.02 µM DAUDA with 0.3 µM FABP1) (Figure 3.7). The basis spectra of the unique components of (R)- and (S)-flurbiprofen (Figure 3.14) could not be isolated experimentally and were estimated based on visual inspection of the filtered spectral components. Basis spectra were normalized based on the peak area (Figure 3.6C) before use in spectral deconvolution.

3.3.5 *DAUDA displacement assay for hFABP1 binding*

Arachidonic acid (AA) was first used as a model ligand to develop a method to measure ligand binding to FABP1 via DAUDA displacement. AA in methanol was titrated into a solution of FABP1 (0.3 µM) prebound with DAUDA (0.5 µM). AA was confirmed to have no background fluorescence in buffer or in the presence of 0.3 µM FABP1. The concentrations of DAUDA-FABP1 complex in AA titration experiments were determined by SVD analysis using basis spectrum for DAUDA in buffer and DAUDA-FABP1 as described in Materials and Methods Section 3.3.4. For analysis of the fluorescence displacement data, the total fluorescence of DAUDA-FABP1 observed at a given AA concentration ($F_{tot,[Ligand]}$) was normalized to the maximum observed fluorescence in the absence of AA ($F_{tot,0}$) using Equation 3.6, so that the normalized fluorescence value ($F_{tot,normalized}$) with 0.5 µM DAUDA and 0.3 µM FABP1 in the absence of AA is 100:

$$F_{tot,normalized} = \frac{F_{tot,[Ligand]}}{F_{tot,0}} \times 100 \qquad (3.6)$$

To determine the apparent binding affinity of AA with hFABP1, a competitive displacement model (Figure 3.13A) was constructed that added a third reaction to the two-site sequential binding model described above for DAUDA:

Reaction 3: $$AA + FABP1 \underset{k_6}{\overset{k_5}{\rightleftharpoons}} AA\text{-}FABP1$$

Here, k_5 and k_6 are the association and dissociation rate constants of AA with FABP1. The equilibrium dissociation constant (K_d) of AA with FABP1 is equal to the ratio k_6/k_5.

Because of the normalization described by Equation 3.6, the scaling of DAUDA-FABP1 concentrations to observed fluorescence had to be adjusted slightly. *Scale2* was defined as a Global Quantity in COPASI to relate the total normalized fluorescence ($F_{tot,normalized}$) to the simulated concentrations of DAUDA bound with FABP1 in the AA titration according to Equation 3.7:

$$F_{tot,normalized} = Scale2 \cdot ([DAUDA\text{-}FABP1] + 2 \cdot [DAUDA\text{-}FABP1\text{-}DAUDA]) \qquad (3.7)$$

In Equation 3.7, the maximum value for $F_{tot,normalized}$ is 100 which is achieved in the absence of AA. Hence, *Scale2* was fixed so that the maximum value of $F_{tot,normalized}$ was 100 in the absence of AA. The fixed value of *Scale2* was calculated using Equation 3.7 when $F_{tot,normalized} = 100$. The equilibrium concentrations of [DAUDA-FABP1] and [DAUDA-FABP1-DAUDA] in the displacement assay before addition of AA were 0.179 and 0.005 µM, respectively, based on the optimized values of $K_{d,1}$ and $K_{d,2}$, and initial concentrations of 0.3 µM FABP1 and 0.5 µM DAUDA. Substituting these values into Equation 3.7 yields a value of 529 for *Scale2*.

To estimate the K_d for AA binding, k_5 was set to 1 μM^{-1} s^{-1} as above and k_6 was optimized using the Levenberg-Marquardt method in the Parameter Estimation task in COPASI. The lower and upper bounds for k_6 were 0.001 and 1000, and results were insensitive to the fixed value of k_5 ranging from 0.01 to 100 μM^{-1} s^{-1}. The value for k_6 was independent of the initial value used. The K_d from the ratio of k_6/k_5 is reported as the mean ± standard deviation from three replicate experiments performed on separate days with at least two different purifications from a single expression of hFABP1.

Drug binding to hFABP1 was screened using simple DAUDA displacement. Diazepam, diclofenac, fluoxetine, racemic flurbiprofen, gemfibrozil, racemic ibuprofen, pioglitazone, sulfaphenazole and tolbutamide solutions were prepared in methanol and added at 30 µM to FABP1 (0.3 µM) prebound with DAUDA (0.5 µM). All drugs were confirmed to have no appreciable background fluorescence at 30 µM in buffer or in the presence of 0.3 µM FABP1. For ligands that reduced the DAUDA-FABP1 fluorescence >15% in initial screening, titrations were performed with a range of ligand concentrations added to FABP1 (0.3 µM) prebound with DAUDA (0.5 µM). Fluorescence measurements and SVD analysis were performed as described for AA above. (R)- and (S)-flurbiprofen were used in titrations instead of racemic flurbiprofen.

Because residual DAUDA-FABP1 fluorescence was observed even at saturating concentrations of many ligands, and the SVD analysis indicated a presence of a ternary complex of DAUDA-FABP1-Drug, a ternary complex binding model (Figure 3.13B) was used to determine the binding affinity of drugs (K_d) with hFABP1. The ternary binding model was based on the two-site sequential binding model described above for DAUDA (Reactions 1 and 2) with the addition of a third reaction:

Reaction 4: $$Drug + DAUDA\text{-}FABP1 \underset{k_8}{\overset{k_7}{\rightleftharpoons}} DAUDA\text{-FABP1-}Drug$$

Here, k_7 and k_8 are the association and dissociation rate constants for drug binding with FABP1, respectively, with the equilibrium binding constant (K_d) of drug ligands with FABP1 equal to k_8/k_7. This is the simplest model that adequately fits the data, but it does rely on the assumption that drug binding does not alter the affinity of DAUDA for either its high- or low-affinity binding sites. The SVD data from drug titrations was normalized to the fluorescence of DAUDA bound with FABP1 in the absence of drug as described above for AA (Equation 3.6) so that $F_{tot,normalized}$ = 100 (arbitrary fluorescence units). The normalized total fluorescence $F_{tot,normalized}$ observed from singly and doubly bound DAUDA-FABP1 complexes and DAUDA-FABP1-drug ternary complexes was defined by the following equation:

$$F_{tot,normalized} = Scale2 \cdot ([DAUDA\text{-}FABP1] + \; 2 \cdot [DAUDA\text{-}FABP1\text{-}DAUDA]) + Scale3 * [DAUDA\text{-}FABP1\text{-}Drug] \quad (3.8)$$

Here, *Scale2* was defined as described above for AA and fixed to 529, while *Scale3* is a scaling factor defined as a Global Quantity in COPASI that relates the normalized fluorescence ($F_{tot,normalized}$) to the concentration of the DAUDA-FABP1-drug ternary complex yielded by the numerical simulations. k_7 was set to 1 μM^{-1} s^{-1}, and k_8 and *Scale3* were optimized using the Levenberg-Marquardt method in the Parameter Estimation task in COPASI. Results were insensitive to fixed values of k_7 ranging from 0.01 to 100 μM^{-1} s^{-1}. The lower and upper bounds for k_8 were set to 0.001 and 1000, and the initial value was fixed to the EC_{50} determined as described below. The lower and upper bounds for *Scale3* were set to 0 and 1000, respectively, and an initial value of 500 was used. The K_d values for drug ligands were calculated from the ratio of k_8/k_7 and are reported as means ± standard deviation from three replicate experiments done on separate days with at least two different purifications of FABP1.

EC_{50} values were also determined as an alternative measurement of drug binding affinity. To determine the concentration of ligand at half maximal displacement of DAUDA (EC_{50} value), the % fluorescence remaining for DAUDA-FABP1 as determined by SVD analysis was plotted as a function of ligand concentration. Equation 3.9 was fit to the data in GraphPad Prism 10.

$$\%\ Fluorescence\ Remaining = Min + \frac{Max - Min}{1 + \frac{[Ligand]}{EC_{50}}} \qquad (3.9)$$

Here, [Ligand] is the concentration of AA or the test drug and *Min* and *Max* are the minimum and maximum values for % fluorescence remaining, respectively. *Min* values were constrained to be > 0 and *Max* values were fixed to 100. The EC_{50} values are reported as a mean ± standard deviation from replicate experiments done on three separate days with FABP1 from different purifications. The residual fluorescence remaining (F_{res}) at saturating drug concentrations was taken as *Min* from Equation 3.9.

3.3.6 *Native mass spectrometry (MS) methods for characterization of DAUDA and diclofenac binding to FABP1*

Non-delipidated and delipidated FABP1 samples were prepared for native MS using Micro Bio-Spin Size-Exclusion Spin Columns (Bio-Rad, Hercules, CA) that had been equilibrated with four washes of 1M ammonium acetate adjusted to pH 7. FABP1 aliquots were diluted in 1M ammonium acetate to 50 µL prior to loading onto the equilibrated column. FABP1 was eluted from the column by centrifugation at 1,000 g for four and a half minutes. Assuming 100% recovery from the column and negligible protein loss due to adsorption, the volume of recovered FABP1 solution was then measured and diluted with additional 1 M ammonium acetate and DTT to reach a final concentration of 10 µM FABP1 and 10 mM DTT. FABP1 and FABP1-ligand complex ions were generated using nano-electrospray ionization (Davidson *et al.*, 2017). MS analysis was performed on a Q-Tof Premier Mass Spectrometer (Waters Corp., Wilmslow, UK). Ion source and transfer conditions were optimized to minimize ion activation.

To characterize ligand binding, DAUDA and diclofenac dissolved in methanol were pipetted directly into 1 M ammonium acetate solution of FABP1 (10 µM) to achieve the desired stoichiometric molar ratios of ligand and protein while keeping the final concentration of methanol below 5% by volume. After addition of ligands, samples were allowed to equilibrate at 4 °C overnight. Approximately 1-3 µL of protein solution was loaded into glass emitters that were made in-house using borosilicate capillaries and a micropipette puller (Sutter Instruments Model P-97, Novato, CA). A platinum wire was inserted into the solution and approximately 0.5-1 kV was applied to the wire to generate ions. Native mass spectra were acquired with a 35 V bias between the sampling and extraction cones in the ion source, which was operated at room temperature. A 3-5 V bias was applied between the quadrupole mass filter and the entrance to the collision cell, which were the least activating setting that allowed for sufficient ion transmission. External calibration of the mass spectra was performed using nano-electrospray generated ions from a commercially available calibration standard (Agilent, Santa Clara, CA). Native mass spectra were manually processed using MassLynx (Waters Corp., Wilmslow, UK) and software written for this project.

In native MS analyses, nonspecific ligand binding can occur during the electrospray process due to concentration effects (Kitova *et al.*, 2012). One well documented method to verify the specificity of an interaction between a protein (P) and ligand (L) is the reference protein experiment (Sun *et al.*, 2006). In this experiment, an additional protein (P_{ref}) is added to the sample solution that is not expected to interact with L. Any observed peaks corresponding to P_{ref}+L are attributed to nonspecific interactions that are an artifact of the electrospray process and can be subtracted from P+L peaks (Kitova *et al.*, 2012). Any nonspecific interactions should be independent of the identify of P_{ref}. Using this strategy, the native mass spectrum of FABP1 with DAUDA was generated with the addition of ribonuclease A (data not shown) as a reference protein. These experiments were performed by adding 10 µL of 20 µM ribonuclease A in 1 M ammonium acetate during the final dilution of FABP1 to 10 µM. The total volumes of the FABP1 solutions with and without ribonuclease A were the same, ensuring consistent relative concentrations of FABP1 and ligands. DAUDA and diclofenac were added to FABP1/ribonuclease A solutions and allowed to equilibrate at 4 °C overnight prior to native mass spectrometry analysis. There was no evidence for DAUDA association with ribonuclease A, while both singly and doubly bound DAUDA with FABP1 peaks were present. These results corroborate that DAUDA-associated peaks in the native mass spectra result from specific condensed-phase interactions.

3.3.7 *Molecular Docking of DAUDA and Drugs to FABP1*

DAUDA, diclofenac, (R)-flurbiprofen and (S)-flurbiprofen were docked to a holo-FABP1 solution structure determined by NMR and in complex with two oleic acid molecules (PDB 2LKK, chain A.1) (Cai *et al.*, 2012). Docking was performed with AutoDock4 using AutoDock Tools (1.5.7) (Rizvi *et al.*, 2013). Protonated 3D structures of the drugs and endogenous ligands were downloaded from PubChem. Polar hydrogens and Kollman charges were added to FABP1 using AutoDock Tools (1.5.7). Ligand torsions were automatically selected with AutoDock Tools and verified according to the 3D ligand structure, and the ligand aromaticity criterion was set to 7.5. Grid parameter files were prepared using a grid box size of 80x100x90 (X, Y, Z) centered on FABP1 to encompass the entire β-barrel binding domain of FABP1. Docking parameter files were prepared using a rigid structure of FABP1. The Genetic Algorithm (GA) was used with default settings with the number of GA runs set to 50. The docking parameters were set as the default and the docking parameter file was output as LamarkianGA (4.2). For docking studies with two ligands, a single ligand was first docked to the holo-FABP1 structure, and the top scoring pose (lowest $\Delta G_{binding}$) was used as the holo-FABP1 structure for additional docking studies with a second ligand. Docking poses were visualized using ChimeraX 1.1 (University of California, San Francisco) (Pettersen *et al.*, 2004).

3.3.8 *Kinetics of 4'OH-diclofenac Formation by CYP2C9 in the Presence and Absence of FABP1*

The kinetics of 4'OH-diclofenac formation by CYP2C9 in the presence and absence of hFABP1 were determined in CYP2C9 Supersomes co-expresed with P450 reductase and cytochrome b5 (BD Gentest, Franklin Lakes, NJ) under conditions of protein and time linearity. CYP2C9 Supersomes (1 nM CYP2C9, 0.0015 mg total microsomal protein/mL, cytochrome P450 reductase activity 290 nmol min^{-1} mg^{-1} for total microsomal protein) were preincubated with 8 different concentrations of diclofenac ranging from 0.4 to 20 µM for 5 min at 37°C in 180 µL incubation buffer (100 mM potassium phosphate, pH 7.4) in a 96-well plate. Reactions were initiated with 1 mM NADPH (final concentration) to a final volume of 200 µL and quenched after 10 min by transferring 100 µL of the incubation to 0.6 mL Eppendorf tubes containing three incubation volumes of acetonitrile with 1% formic acid and 17 nM of 4'OH-5-Cl-diclofenac as an internal standard. The incubations in the presence of hFABP1 were conducted in a similar manner as those without hFABP1. For incubations with diclofenac and hFABP1, CYP2C9 was preincubated with diclofenac and 20 µM hFABP1 for all concentrations of diclofenac tested prior to initiation of the catalytic reactions with NADPH.

For incubations in the presence and absence of FABP1, quenched reactions were centrifuged at 18,000 g for 20 minutes at 4°C and 200 µL of supernatant was collected and transferred to glass MS vials for LC-MS/MS analysis. Diclofenac samples were analyzed using an AB Sciex API6500 qTrap mass spectrometer (Concord, ON, Canada) coupled to an Agilent 1290 Infinity II Ultra-High-Performance Liquid Chromatography (UHPLC, Santa Clara, CA). For 4'OH-diclofenac separation, a Synergi Max-RP column (150 x 4.6 mm, 4 µM, Phenomenex, Torrance, CA) was used. A gradient elution at a flow rate of 1 mL/min was used as follows: mobile phase A (water with 0.1% formic acid) was kept at 65% and B (acetonitrile with 0.1% formic acid) at 35% for the first 18 minutes, then B was increased to 80% by 25 minutes, returned to initial conditions by 30 minutes and held at initial conditions for an additional 5 minutes. 4'OH-diclofenac and 4'OH-5-Cl-diclofenac were monitored in positive ion mode with electrospray ionization and the MS parameters used were as follows: IS 4500 V, TEM 400 °C, CUR 35 p.s.i., GS1 62, GS2 62, CAD-low, EP 10 V, DP 60 V, CXP 14 V, and the CE were 22 and 19 V for

4’OH-diclofenac and 4’OH-5-Cl-diclofenac, respectively. The MRM transitions used were 312>266 *m/z* for 4’OH-diclofenac and 346>300 *m/z* for 4’OH-5-Cl-diclofenac.

3.3.9 *Determination of Diclofenac Unbound Fraction in CYP2C9 Incubations*

To determine the unbound concentrations of diclofenac in incubations with recombinant CYP2C9, magnetic silica beads (MGSBs, G-Biosciences, St. Louis, MO) were used to separate microsomal protein (Horspool *et al.*, 2020) from free diclofenac in solution. Prior to experiments the beads were conditioned and washed with 3 mL (1 mL x 3) of assay buffer (100 mM potassium phosphate, pH 7.4). Initial experiments without microsomal protein present were done to verify that diclofenac and FABP1 did not bind non-specifically to MGSBs. To measure non-specific binding of diclofenac and FABP1 to MGSBs, 1.9 µM diclofenac or 10 µM FABP1 were incubated separately with 100 µL of MGSB in 0.5 mL assay buffer in 1.7 mL Eppendorf tubes for 30 minutes at 37°C. After 30 minutes, 100 µL of the mixture containing MGSBs with diclofenac or FABP1 were collected as the total sample, then the MGSBs were separated from solution using a DynaMag-2 Magnet (Thermo Fisher Scientific, Waltham, MA) and the supernatant was collected. For supernatant containing FABP1, FABP1 was quantified using BCA protein assay. For diclofenac samples, 300 µL of acetonitrile containing 1% formic acid and 1 µM 4’OH-5-Cl-diclofenac internal standard were added to 100 µL of the total and supernatant samples containing diclofenac. The samples were centrifuged at 18,000 g for 20 minutes and the supernatant was transferred to MS vials for analysis. Diclofenac concentrations in the samples were measured using a Synergi Max-RP column (150 x 4.6 mm, 4 µM, Phenomenex, Torrance, CA) coupled to an Agilent 1200 Series High-Performance Liquid Chromatography (HPLC)-UV system (Santa Clara, CA). A flow rate and elution gradient for diclofenac were used as described above. Diclofenac and

4’OH-5-Cl-diclofenac UV absorbances were monitored at 280 nm and integration of the peaks was done in ChemStation B.04.02 (Agilent, Santa Clara, CA).

To determine the free concentrations of diclofenac in incubations with CYP2C9, 100 μL of MGSBs (10.5 x 10^9 beads) (Horspool *et al.*, 2020) were washed 3 times with 1 mL of assay buffer and pre-equilibrated with CYP2C9 Supersomes (1 nM CYP2C9, 0.0015 mg total microsomal protein/mL) on ice for 30 minutes in 0.5 mL of assay buffer in 1.7 mL Eppendorf tubes. Diclofenac was then added to the mixture of MGSBs and CYP2C9 at concentrations corresponding to each of the nominal concentrations used in kinetic experiments. Samples were then incubated for an additional 30 minutes in a shaking water bath at 37°C, then removed from the water bath and cooled at room temperature for 5 minutes. For experiments with FABP1, FABP1 (20 µM) was pre-equilibrated together with CYP2C9 and MGSBs prior to the addition diclofenac. After cooling, 100 μL of the mixture containing the MGSBs, Supersomes, and diclofenac with and without FABP1 were collected as the total drug sample. The MGSBs were then separated from solution using a DynaMag-2 Magnet and 100 μL of supernatant were collected as the free diclofenac or free diclofenac together with FABP1-bound diclofenac sample. 300 μL of acetonitrile containing 1% formic acid and internal standard were added and samples analyzed as described above. Diclofenac concentrations were determined via HPLC-UV as described above. The binding experiments were done as technical duplicates and the data are reported as means ± S.D. from experiments done on three separate days.

Unbound diclofenac concentrations in the absence of FABP1 were determined from supernatant samples and were measured for every diclofenac concentration used in kinetic experiments. The unbound fraction (fu) was calculated as the ratio of the concentration of drug measured in supernatant (C_{free}) to the concentration of total drug measured prior to magnetic separation (C_{total}).

The unbound fraction of diclofenac in the presence of FABP1 was directly measured using Pierce Nickel-nitrilotriacetic acid (Ni-NTA) Magnetic Agarose Beads (Thermo Fisher Scientific, Waltham, MA) for all diclofenac concentrations used in kinetic experiments. A solution of 0.5 mL of 6xHis tagged FABP1 (20 μM) in assay buffer was prebound to diclofenac at room temperature for 10 minutes in 1.7 mL Eppendorf tubes. After 10 minutes, the FABP1 and diclofenac solution was added to magnetic Ni-NTA agarose beads (MNABs) that were prewashed 3 times with 1 mL assay buffer. The mixture of FABP1, diclofenac and MNABs were incubated in a shaking incubator at 25 °C for an additional 30 minutes to bind FABP1 to the MNABs. After 30 minutes, 100 μL of the mixture were taken to measure total diclofenac, then the MNABs were separated from solution using a DynaMag-2 Magnet and 100 μL of supernatant was taken to measure free diclofenac concentration in solution. Diclofenac concentrations were determined via HPLC-UV as described above and the unbound (f_u) was calculated. BCA protein assay was used to measure FABP1 in supernatant samples after magnetic separation to verify that FABP1 bound to MNABs. The binding affinity of diclofenac to 6xhis tagged FABP1 were similar to FABP1 purified with removal of the 6xhis tag (data not shown).

3.3.10 *Kinetic Analysis of 4’OH-diclofenac Formation by CYP2C9 in the Presence and Absence of FABP1*

The Michaelis-Menten equation was fit to the 4’OH-diclofenac formation data in GraphPad Prism 10 using nominal and free concentrations of diclofenac to determine the apparent and unbound 4’OH-diclofenac formation kinetics with CYP2C9, respectively. Experiments in the presence and absence of FABP1 were done as matched pairs on the same day with technical duplicates. K_m and k_{cat} values are reported as means ± S.D. from experiments done on three separate days. For every replicate experiment, a one-tailed Z-test was used to evaluate differences between K_m values for 4'OH-diclofenac formation in the presence and absence of FABP1 and the results were interpreted collectively from the replicate experiments. One-tailed Z-test was used to compare the K_m values as previously described (Isoherranen *et al.*, 2003). In brief, standard errors for the K_m values in a paired experiment (with and without FABP1) were calculated using the upper and lower limit of the 95% confidence interval of the K_ms according to Equations 3.10 and 3.11:

$$\sigma_{low} = \frac{X - K_{m,low}}{1.96} \qquad (3.10)$$

$$\sigma_{high} = \frac{K_{m,high} - Y}{1.96} \qquad (3.11)$$

In Equation 3.10, *X* is the upper limit of the 95% confidence interval for the K_m value that is numerically lower in the paired experiment ($K_{m,low}$). In Equation 3.11, *Y* is the lower limit of the 95% confidence interval for the K_m value that is numerically greater in the paired experiment ($K_{m,high}$). In both Equations 1.96 is the critical value for $\alpha = 0.05$ and σ is the standard error. The resulting standard errors were then used to calculate Z to test for differences between K_m values in the presence and absence of FABP1 using Equation 3.12:

$$Z = \frac{K_{m,high} - K_{m,low}}{\sqrt{\sigma_{high}^2 + \sigma_{low}^2}} \qquad (3.12)$$

In Equation 3.12, $K_{m,high}$ and $K_{m,low}$ are apparent or unbound K_m values in the presence and absence of FABP1, respectively, and σ_{high} and σ_{low} are the standard errors for the K_m values (calculated from Equation 3.10 or 3.11). The p-value corresponding to the Z-score was then used to compare K_ms. The K_m values were considered different if all three experiments collectively yielded the same conclusion ($p < 0.05$). For k_{cat} values a simple paired t-test was used to evaluate differences in the presence and absence of FABP1 and $p < 0.05$ was considered statistically significant.

3.4 RESULTS

3.4.1 *Expression, Purification, Delipidation and Characterization of Recombinant hFABP1*

FABPs are promiscuous proteins that bind diverse ligands including native *E. coli* lipids and molecules present in expression and purification media (Velkov *et al.*, 2008; Wang *et al.*, 2017). Such ligands may be bound to recombinant purified FABPs as contaminating copurifying molecules (CPMs). These CPMs may alter the binding characteristics of other ligands (Velkov *et al.*, 2008) via competition for FABP binding or via allosteric mechanisms. Hence, a method is needed to monitor the presence of CPMs in purified hFABP1. A native mass spectrometry (MS) method was developed to assess the extent of CPMs bound to hFABP1 at different stages of the purification (Figure 3.1-3.4) and to confirm efficient delipidation of the final purified protein (Figure 3.5). Native MS is well suited to monitor the presence of CPMs and is more suitable for routine monitoring of delipidation than previously described methods such as protein NMR which requires isotope labeled protein. It is important to note that due to the limitations of the method, the CPM region likely includes also peaks from modifications to the protein that are unrelated to the purification method, peaks related to presence of sodium and potassium adducts, and peak tailing. Due to these factors, the efficiency of delipidation could not be quantitatively assessed using peak integration.

In the preliminary experiments, majority of the hFABP1 was observed bound with CPMs after nickel purification and before gel filtration and delipidation treatments (Figure 3.2A). Lipidex-5000 and butanol extraction have been reported to efficiently delipidate FABP1 (Velkov *et al.*, 2008; Wang *et al.*, 2017; Lai *et al.*, 2020). Various levels of CPMs were removed with individual treatments with Lipidex-5000, 1:1 (v/v) butanol and 1:3 (v/v) butanol based on the native MS analysis (Figure 3.2). Surprisingly, none of the individual treatments achieved complete delipidation of hFABP1. To accomplish complete removal of the CPMs, a combination of treatments with butanol and Lipidex-5000 were optimized (Figure 3.4). The best efficiency of delipidation was achieved when hFABP1 was treated 3 times with 1:1 butanol followed by a 30-minute incubation with Lipidex-5000 (Figure 3.4D). The final purification protocol is outlined in Figure 3.5 and the efficiency of the delipidation is shown for the final purified hFABP1.

3.4.2 *Characterization of DAUDA Binding to FABP1*

The fluorescence emission spectrum of free DAUDA in solution overlapped with the spectrum of DAUDA bound to hFABP1 (Figure 3.6A). The emission peak of DAUDA-FABP1 was observed at 509 nm. Free DAUDA in solution contributes to the total fluorescence signal observed at this wavelength. This fluorescence overlap can confound titration experiments in which the fraction of total DAUDA that is free in solution changes with DAUDA concentration. Hence, singular value decomposition (SVD) analysis was used to distinguish the fluorescence of DAUDA-FABP1 from free DAUDA in solution in titration experiments (Figure 3.7).

The binding affinity of DAUDA to hFABP1 was first determined by 'reverse' titrations with a constant concentration (0.05 μM) of DAUDA and hFABP1 concentrations ranging from 0 to 1.7 μM (Figure 3.7A). Under these conditions, it is expected that the presence of doubly occupied hFABP1 is negligible. This is borne out by SVD analysis (Figure 3.7C), which shows primarily the monotonic increase of a species with emission maximum at 509 nm (corresponding to DAUDA bound to hFABP1) with only a small contribution from free DAUDA (λ_{max} = 559 nm). For this and subsequent spectral deconvolution, the basis spectrum for the DAUDA-FABP1 complex was determined from a sample of DAUDA with hFABP1 in excess (Materials and

Methods, Section 3.3.4, Figure 3.6C). The basis spectrum for free DAUDA in solution was also determined experimentally (Figure 3.6C). Following spectral deconvolution, the quadratic binding equation was fit to the data of specific fluorescence of the DAUDA-FABP1 complex as a function of hFABP1 concentration yielding a DAUDA K_d of 0.20 µM (95% CI [0.15, 0.25]). These results were verified by fitting a numerical simulation of bimolecular association to the data which also yielded a K_d value of 0.2 µM. This K_d value corresponds to a single high affinity binding site of DAUDA with hFABP1.

The potential of multiple DAUDA molecules binding hFABP1 was then explored using 'forward' titrations with a constant concentration of hFABP1 (0.3 µM) and DAUDA concentrations ranging from 0 to 12.7 µM. Saturation was not achieved despite the highest DAUDA concentrations exceeding the K_d determined via the reverse titrations by over 50-fold (Figure 3.7B). This suggests that multiple DAUDA molecules bind to hFABP1 simultaneously. However, only two spectral components were observed that made significant contributions to the observed signal in the SVD analysis (Figure 3.7D), suggesting that the fluorescence spectrum of the doubly bound DAUDA-FABP1 complex is indistinguishable from a singly bound complex. The specific fluorescence of DAUDA-FABP1 was fit to numerical simulations of a sequential two-site binding numerical model with $K_{d,1}$ fixed to the value obtained from reverse titrations in order to determine $K_{d,2}$. While the best fit value for $K_{d,2}$ was 10.7 µM, the specific fluorescence of DAUDA-FABP1 had not saturated even at 12.7 µM DAUDA, and so only the lower bound of $K_{d,2}$ (3.3 µM based on the 95% confidence interval) can be estimated with confidence.

To directly confirm the multiple DAUDA binding inferred from fluorescence titrations and determine the stoichiometry of DAUDA and hFABP1 complexes, native MS was used. Upon addition of one and two equivalents of DAUDA to hFABP1 (10:10 and 20:10 µM), an *m/z* peak corresponding to apo-FABP1 was observed, as were additional higher-intensity peaks shifted to larger *m/z* values (Figure 3.8). Upon charge-state deconvolution, mass shifts of +434 and +868 Da corresponding to singly and doubly bound DAUDA-FABP1 complexes, respectively, were observed supporting the findings from the fluorescence titrations. A considerable portion of apo-FABP1 was also observed which may be due to dissociation of the non-covalent DAUDA-FABP1 complexes in the electrospray process and in the gas phase. Alternatively, DAUDA binding to FABP1 may be weaker in the 1 M ammonium acetate solution used in native MS binding experiments than in the phosphate buffer used in fluorescence binding assays.

To explore the binding modes of the two DAUDA within the binding cavity of hFABP1, two DAUDA were docked sequentially to hFABP1 (Figure 3.8C-E). The first DAUDA was predicted to bind to the center-bottom of the hFABP1 binding cavity in a bent, U-shaped conformation with the DAUDA carboxyl group oriented toward R122 and S39 to form hydrogen bonds ($\Delta G_{binding}$ = -8.05 kcal/mol) (Figure 3.8C and 3.8E). This binding orientation is likely to correspond to the high-affinity DAUDA binding site determined via fluorescence titrations and is consistent with the orientation of oleic acid (OA) (Cai *et al.*, 2012) and palmitic acid (PA) (Sharma and Sharma, 2011) within hFABP1 determined by NMR and crystallography. The second DAUDA was then docked sequentially and predicted to bind to a site near the portal region of hFABP1 (Figure 3.8D). Binding of the second DAUDA was also predicted to have a U-shaped conformation where both the carboxyl and dansyl groups of the molecule are oriented away from the hFABP1 binding cavity ($\Delta G_{binding}$ = -5.97 kcal/mol) (Figure 3.8D and 3.8E). This binding site was predicted to correspond to the low affinity binding site of DAUDA detected in the fluorescence titrations.

3.4.3 *Arachidonic Acid as a Model Ligand for DAUDA Displacement Assays with hFABP1*

AA is an endogenous fatty acid ligand for multiple FABPs including FABP1 (Veerkamp *et al.*, 1999). AA was used as a model ligand to assess DAUDA displacement by ligands of hFABP1. The concentrations of DAUDA (0.5 µM) and hFABP1 (0.3 µM) used in these studies were chosen to keep DAUDA concentration low enough to ensure negligible formation of the doubly bound DAUDA-FABP1 complex. hFABP1 concentration was chosen to be as low as possible based on fluorescence assay sensitivity. Under these conditions, AA appeared to completely displace DAUDA fluorescence (Figure 3.9A). When hFABP1 binding was saturated with AA, the fluorescence spectrum resembled the spectrum of DAUDA free in solution. As with SVD analysis of reverse and forward titrations, only two spectral components were identified corresponding to DAUDA-FABP1 and DAUDA in solution (Figure 3.9B). The specific fluorescence of DAUDA in solution increased with the addition of AA (Figure 3.9C) consistent with DAUDA displacement from hFABP1 by AA. These results suggest a lack of a ternary DAUDA-FABP1-AA complex formation, and that AA completely displaces DAUDA from hFABP1, with an apparent K_d of 0.08 ± 0.01 µM (Figure 3.9D, Table 3.1). These results are consistent with the $K_{i,app}$ reported previously (0.11 µM) for AA in displacement assays using ANS (Huang *et al.*, 2014).

3.4.4 *A Variety of Drug Ligands Bind to FABP1 and Form Ternary DAUDA-FABP1-drug Complexes*

The DAUDA displacement assay developed with AA was used to test the binding of diazepam, diclofenac, fluoxetine, flurbiprofen, gemfibrozil, ibuprofen, pioglitazone, sulfaphenazole and tolbutamide to hFABP1. These drugs were selected based on previous data on binding to rFABP1 and feasibility for future study of CYP mediated metabolism. All of the drugs tested except fluoxetine decreased DAUDA fluorescence, indicating these drugs bound to hFABP1 (Figure 3.10). Binding was confirmed via titrations using DAUDA displacement (Figure 3.11 and 3.12). Numerical simulations yielded robust apparent K_d values for all drugs except (R)-flurbiprofen and diazepam. Therefore, the EC_{50} values are reported instead for these two ligands, with the caveat that this empirical parameter may conceal some more complex binding behavior. Diazepam, sulfaphenazole and tolbutamide in particular did not achieve saturation in the tested concentration range, and so the uncertainty in EC_{50} is high. The apparent affinity values for most of the drugs characterized were within the low micromolar range (Table 3.1). This is consistent with hFABP1 having promiscuous binding and suggests that various drug classes may bind hFABP1.

None of the drugs completely eliminated the fluorescence of DAUDA to the levels observed for free DAUDA in solution (gray shaded spectrum in Figure 3.11). Diclofenac, gemfibrozil and pioglitazone decreased the fluorescence of DAUDA-FABP1 by >82 % at saturation (i.e., F_{res} <18%), while the maximal decrease for (R)- and (S)-flurbiprofen and ibuprofen ranged between 52-72% (Table 3.1). The F_{res} values for diazepam, sulfaphenazole and tolbutamide could not be determined with confidence. Inspection of the fluorescence spectra with drug ligands showed that for all tested drugs the spectra at saturation were blue shifted relative to the spectrum of free DAUDA in solution (Figure 3.11). Moreover, unlike titrations with AA, the specific fluorescence of DAUDA in solution did not increase with increasing concentrations of drug (Figure 3.12). Taken together these findings suggest that, unlike AA which appeared to completely displace DAUDA from hFABP1, drug ligands bound to hFABP1 simultaneously with DAUDA as a ternary complex altering the fluorescence characteristics of DAUDA-FABP1. In support of the presence of such ternary complexes, SVD analysis identified unique spectral components that were different than DAUDA alone in solution or DAUDA-FABP1 in (R)- and (S)-flurbiprofen titrations (Figure 3.14). The SVD analysis could not, however, consistently identify the presence of such species that were spectrally distinct in other drug titrations.

Native MS was used to directly detect ternary DAUDA-FABP1-diclofenac complexes (Figure 3.15). The native mass spectra showed *m/z* shifts corresponding to DAUDA-FABP1, diclofenac-FABP1, ternary DAUDA-FABP1-diclofenac and ternary DAUDA-FABP1-DAUDA complexes. High intensity peaks were also observed for apo-FABP1. No peaks were observed corresponding to hFABP1 bound with 2 diclofenac molecules under these experimental conditions. Consistent with the higher binding affinity of DAUDA in comparison to diclofenac with hFABP1, the majority of hFABP1 was in complex with DAUDA with a small fraction of hFABP1 found complexed with diclofenac.

The potential binding orientation of diclofenac when in complex with DAUDA and hFABP1 were assessed via molecular docking (Figure 3.15C-E). Similar to DAUDA, the carboxyl head group of singly bound diclofenac was predicted to orient toward S39 and R122 centered within the hFABP1 binding cavity and interacted via hydrogen bonding ($\Delta G_{binding}$ = -7.2 kcal/mol) (Figure 3.15C). Since diclofenac decreased DAUDA fluorescence by ~85%, but the free DAUDA signal did not increase proportionately and the resulting blue shifted spectrum indicated a ternary DAUDA-FABP1-diclofenac complex, we explored the possibility of sequential binding modes of DAUDA and diclofenac. Sequential docking studies were performed where either DAUDA or diclofenac were first docked to hFABP1 before subsequent docking of the other ligand (Figure 3.15D and 3.15E). With DAUDA in the hFABP1 binding cavity, diclofenac was predicted to bind to a site near the portal region where the carboxyl group was predicted to oriented away from the binding cavity interacting with residues K31 and S56 ($\Delta G_{binding}$ = -6.5 kcal/mol). When DAUDA was docked with diclofenac in the binding cavity, DAUDA was predicted to adopt an elongated "head out" conformation (Figure 3.15E). The simulated orientation of DAUDA showed the carboxyl head group of DAUDA was oriented near the portal domain facing away from the binding cavity while the dansyl group was buried within the hFABP1 binding cavity ($\Delta G_{binding}$ = -7.2 kcal/mol). This was in contrast to the simulated U-shape confirmation of the second DAUDA resulting from sequential docking of two DAUDA (Figure 3.8D).

Distinct spectral components in (R)- and (S)-flurbiprofen titration spectra identified by SVD analysis indicated the formation of ternary DAUDA-FABP1-flurbiprofen complexes. Hence, docking studies were also performed with (R)- and (S)-flurbiprofen to explore the potential binding orientations of flurbiprofen in complex with DAUDA and FABP1. Both singly docked (R)- and (S)-flurbiprofen (Figure 3.16A and 3.16B, respectively) were predicted to have similar orientations within the FABP1 binding cavity ($\Delta G_{binding}$ = -7.6 and -7.5 kcal/mol, respectively). The carboxyl groups for both (R)- and (S)-flurbiprofen were predicted to interact with residues S39, S134 and R122 via hydrogen bonding. When (R)- and (S)-flurbiprofen were independently docked to hFABP1 with DAUDA present (Figure 3.16C and 3.16D), both flurbiprofen molecules were predicted to be positioned near the portal region and the α-helical domain of hFABP1. However, (R)-flurbiprofen binding was predicted further in the hFABP1 binding cavity than (S)-flurbiprofen and was closer in proximity to DAUDA ($\Delta G_{binding}$ = -6.9 kcal/mol) (Figure 3.16E). In contrast, (S)-flurbiprofen was simulated to be bound within the opening of the portal region where the carboxyl group interacted with residues K31 and S56 ($\Delta G_{binding}$ = -6.8 kcal/mol).

3.4.5 *hFABP1 Binding Alters 4'-OH-diclofenac Formation Kinetics by CYP2C9*

To determine the effect of hFABP1 on diclofenac metabolism by CYP2C9, the formation kinetics of 4'-OH-diclofenac by recombinant CYP2C9 was characterized in the presence and absence of 20 µM hFABP1 (Figure 3.17). At this hFABP1 concentration, more than half of diclofenac is expected to be bound to hFABP1 based on the K_d value determined for diclofenac using DAUDA displacement assay. The apparent nominal K_m for 4'-OH-diclofenac formation by CYP2C9 was significantly higher (p = 0.003, 0.009, 0.03 for paired replicate experiments) in the presence of hFABP1 (5.8 ± 1.5 µM) compared to in the absence of hFABP1 (1.4 ± 0.2 µM) (Table 3.2, Figure 3.17). This suggests that hFABP1 sequesters diclofenac from CYP2C9 mediated metabolism. Surprisingly, the apparent k_{cat} was decreased in the presence of hFABP1 when compared to the incubations done in the absence of hFABP1 (Figure 3.17).

To test whether the effect of hFABP1 on diclofenac K_m could be explained by the free drug hypothesis, unbound concentrations of diclofenac were determined in the incubations with and without hFABP1. The mean unbound fraction (f_u) of diclofenac in the absence of FABP1 was 1.0 ± 0.04 while the f_u in the presence of 20 µM FABP1 ranged from 0.1-0.5 and was diclofenac concentration dependent (Figure 3.18). Based on the free concentrations of diclofenac determined in these experiments, the $K_{m,u}$ and the k_{cat} in the presence of hFABP1 for 4'-OH-diclofenac formation were 0.4 ± 0.1 µM and 7.3 ± 0.7 min^{-1}, respectively (Figure 3.18, Table 3.2). The k_{cat} value was significantly lower (*p* = 0.007) in the presence of hFABP1 (7.3 ± 0.7 min^{-1}) than in the absence of hFABP1 (14.5 ± 0.8 min^{-1}). A trend towards a decrease in $K_{m,u}$ was observed (Table 3.2) but based on the confidence intervals from paired replicate experiments the $K_{m,u}$ values were collectively not significantly different (*p* = 0.03, 0.05, 0.11 for the paired replicate experiments). These data suggest that in addition to sequestering and binding diclofenac, hFABP1 may directly interact with CYP2C9 or P450 reductase to noncompetitively inhibit diclofenac metabolism and CYP2C9 catalytic activity. Such protein-protein interaction could result in a change in regioselectivity of diclofenac hydroxylation but no alternative sites of oxidation were detected in incubations with diclofenac (Figure 3.19).

3.5 DISCUSSION

hFABP1 is highly abundant in the liver and intestines and serves as a major binding protein for lipophilic compounds. Yet, drug binding to hFABP1 and the role of hFABP1 in drug distribution and metabolism have been poorly defined. *In vivo*, hFABP1 is likely present as a mixture of apo-FABP1 and endogenous lipid bound holo-FABP1 (Schroeder *et al.*, 1998). The binding capacity of FABP1 *in vivo* is increased by the possibility of two ligands binding simultaneously to FABP1 as shown for oleate and palmitate using native MS (Santambrogio *et al.*, 2013), NMR (Cai *et al.*, 2012) and crystallography (Sharma and Sharma, 2011). Drug binding to FABP1 can be complicated as drugs may bind to apo-FABP1 or as a second ligand to FABP1 already bound with fatty acids. To probe these drug binding modalities, DAUDA was chosen as the fluorescent ligand in this study. DAUDA is a well characterized fatty acid derivative that is a larger ligand than the commonly used ANS and binds FABP1 with higher affinity (Thumser and Wilton, 1994; Davies *et al.*, 2002; Luebker *et al.*, 2002a; Norris and Spector, 2002). Hence, DAUDA binding likely mimics native lipid binding to FABP1.

Fluorescence titrations and native MS studies, together with the docking studies, support the conclusion that DAUDA binding captures the two binding sites of endogenous ligands with hFABP1. Based on fluorescence titrations, DAUDA has a high (K_{d1} = 0.2μM) and a low (K_{d2} > 3.3 μM) affinity binding site on hFABP1 that likely correspond to the binding sites of endogenous fatty acids. Indeed, the K_d values for DAUDA are comparable to the high (0.009-0.2 μM) and low (0.06-7.6 μM) affinity binding sites determined for OA with bovine and rFABP1 and PA for rFABP1 (Richieri *et al.*, 1994, 1996; Rolf *et al.*, 1995; Santambrogio *et al.*, 2013). In docking studies, DAUDA bound within the bottom-center of the hFABP1 binding cavity in a U-shape orientation consistent with the orientation of OA and PA in the high affinity binding site (Sharma and Sharma, 2011; Cai *et al.*, 2012). Docking of a second DAUDA resulted in DAUDA binding near the portal region where a second putative low affinity binding was also reported.

The use of DAUDA in fluorescence displacement assays can be challenging due to the background fluorescence of DAUDA which interferes with direct measurements of DAUDA-FABP1 fluorescence. Background correction methods subtracting free DAUDA fluorescence have been reported (Thumser *et al.*, 1996; Davies *et al.*, 2002; Luebker *et al.*, 2002b; Elmes *et al.*, 2019). These methods do not account for the different free DAUDA concentrations in the presence and absence of FABP1 or for the fact that multiple DAUDA may bind to FABP1 simultaneously (Norris and Spector, 2002). To address these concerns, SVD analysis was introduced here to determine the specific contribution of DAUDA-FABP1 to observed fluorescence spectra. The SVD-based spectral deconvolution allowed separation of the DAUDA-FABP1 signal from fluorescence due to free DAUDA, enabling rigorous ligand binding analysis using the DAUDA displacement assay.

Of the drugs studied here and found to bind to hFABP1, diazepam, diclofenac, flurbiprofen, gemfibrozil and ibuprofen have been previously shown to bind to rFABP1 (Chuang *et al.*, 2008). Their binding to rFABP1 was measured based on ANS fluorescence displacement, and a two-site competition model was fit to the data. For all five drugs, two binding sites in rFABP1 were detected with high affinity binding K_is ranging from 1 to 47 µM and low affinity binding K_is being 10-200-fold higher, 35-448 µM (Chuang *et al.*, 2008). The K_d values determined here for diclofenac, flurbiprofen, gemfibrozil and ibuprofen with hFABP1 using DAUDA displacement and SVD analysis ranged from 2 to 10 µM. The apparent EC_{50} for diazepam with hFABP1 was > 50 µM.

K_d values for diclofenac, (S)-flurbiprofen and gemfibrozil for hFABP1 in this study were within 2-fold of the high affinity K_i values reported for rFABP1. However, the affinity of ibuprofen was ~5 times greater for hFABP1 than rFABP1, and the affinity of diazepam was at least 2 orders of magnitude lower for hFABP1 than rFABP1. Although the potential for multiple binding sites and formation of ternary complexes complicates the comparison and interpretation of these affinity values, these data suggest that while drug binding characteristics for rFABP1 and hFABP1 are qualitatively similar, drug binding data with rFABP1 does not translate quantitatively to hFABP1.

Previous NMR studies identified two different binding sites in rFABP1 for ANS, ketorolac and ibuprofen (Chuang *et al.*, 2008). Residues located in the bottom of the FABP1 β-barrel were perturbed by ligand binding. In the presence of ligand concentrations in 2-fold excess of the protein concentration, additional residues were perturbed in the portal region. These findings are consistent with the high affinity binding site for drugs in the bottom of the β-barrel and the low affinity binding site in the portal region. The data collected in this study with fluorescence displacement of DAUDA, native MS and docking studies with hFABP1 support similar binding characteristics with hFABP1 with drug molecules occupying one of the two binding sites with DAUDA occupying the other simultaneously.

Fluorescence data suggest that all drugs tested here form ternary complexes with DAUDA and hFABP1. F_{res} values at saturation ranged from 5 to 48% between drugs suggesting that in contrast to AA, drug ligands do not completely displace DAUDA from hFABP1 but rather bind to hFABP1 simultaneously with DAUDA. The formation of ternary complexes was supported by the observation of a clear blue shift in the fluorescence spectrum of DAUDA in the presence of drug ligands (Figure 3.11) and by the lack of increase in the fluorescence signal of DAUDA free in solution in the titrations (Figure 3.12). Ternary complex formation was confirmed with diclofenac by native MS where both diclofenac and DAUDA bound to hFABP1 simultaneously.

One may speculate that drugs (diclofenac, pioglitazone, gemfibrozil) that decrease DAUDA fluorescence almost completely bind in the high affinity site in hFABP1 while the drugs ((R)- and (S)-flurbiprofen and ibuprofen) that decrease DAUDA fluorescence by only 52-72% bind in the α-helical lid region resulting in different fluorescence spectra at saturation due to the different orientation of DAUDA within hFABP1. Indeed, SVD analysis did not identify unique spectral components with diclofenac but did so with (R)- and (S)-flurbiprofen. Docking studies where DAUDA was sequentially docked to hFABP1, with diclofenac in the binding cavity predicted DAUDA binding in a head out position near the portal region of hFABP1, supporting the hypothesis that DAUDA binds to the low affinity site in the presence of diclofenac. Sequential docking studies with DAUDA bound to hFABP1 predicted (R)- and (S)-flurbiprofen binding at the portal region with distinct binding orientations possibly explaining differences in the fluorescence spectra for the enantiomers. Notably, (R)- and (S)-flurbiprofen do not have regiospecific oxidation by CYP2C9 (Tracy *et. al.*, 1996), however, the results here indicate that flurbiprofen binding to FABP1 is stereospecific. A limitation of the analysis presented here is that it does not account for potential changes in DAUDA binding affinity due to the presence of other hFABP ligands. Further studies are needed to explore the drug binding with hFABP1 and how different binding orientations and conformations alter drug metabolism and disposition as well as lipid metabolism and signaling.

The impact of drug binding to apo-hFABP1 on drug metabolism by CYPs was evaluated using diclofenac metabolism by CYP2C9 as a model reaction. The k_{cat} of 4’OH-diclofenac formation was decreased in the presence of hFABP1 by ≥ 50%. One possible explanation for this decrease is a protein-protein interaction between hFABP1 and CYP2C9 that results in decreased CYP2C9 activity. Similar effects of binding proteins on CYP activity have been observed with cellular retinoic acid binding proteins and CYP26 enzymes with retinoic acid hydroxylation (Nelson *et al.*, 2016; Zhong *et al.*, 2018; Yabut and Isoherranen, 2022). As shown previously (Nelson *et al.*, 2016), the impact of the binding proteins on k_{cat} cannot be explained by simple competition for the ligand when free substrate concentrations are considered. Yet, other protein-protein or protein-lipid interactions cannot be overruled as potential explanations of the observed kinetics. FABP1 has been proposed to deliver ligands directly to lipid membranes (Davies *et al.*, 2002), but another report suggests FABP1 releases its ligands into solution rather than interacting with lipid membranes (Hsu and Storch, 1996). FABP1 has also been found to enhance the activity of CPTI toward LCFA-CoA (Hostetler *et al.*, 2011), and PPARα towards gene transcription via protein-protein interactions (Hostetler *et al.*, 2009). Further research is needed to define the mechanism by which FABP1 decreases CYP2C9 mediated diclofenac oxidation and to explore whether such effects occur with other CYPs and other drugs that bind FABPs.

The results shown here unequivocally establish that many chemically diverse CYP substrate drugs bind to hFABP1 and strongly suggest that hFABP1 binding may alter drug metabolism in the human liver. These findings have important implications for modeling drug disposition in the liver and for predicting drug clearance for drugs that bind to hFABP1. The formation of drug-DAUDA-FABP1 complexes suggests that drug ligands may not have to compete with endogenous ligands for hFABP1 binding but rather that in the human liver drugs may bind to hFABP1 as a ternary complex with an endogenous lipid. However, this is likely drug dependent as the binding modes of different drugs to hFABP1 bound with DAUDA likely vary as suggested by fluorescence and docking results for diclofenac and flurbiprofen. Future studies are needed with mixed lipid-FABP1-drug complexes to fully unravel the role of hFABP1 in modulating drug metabolism.

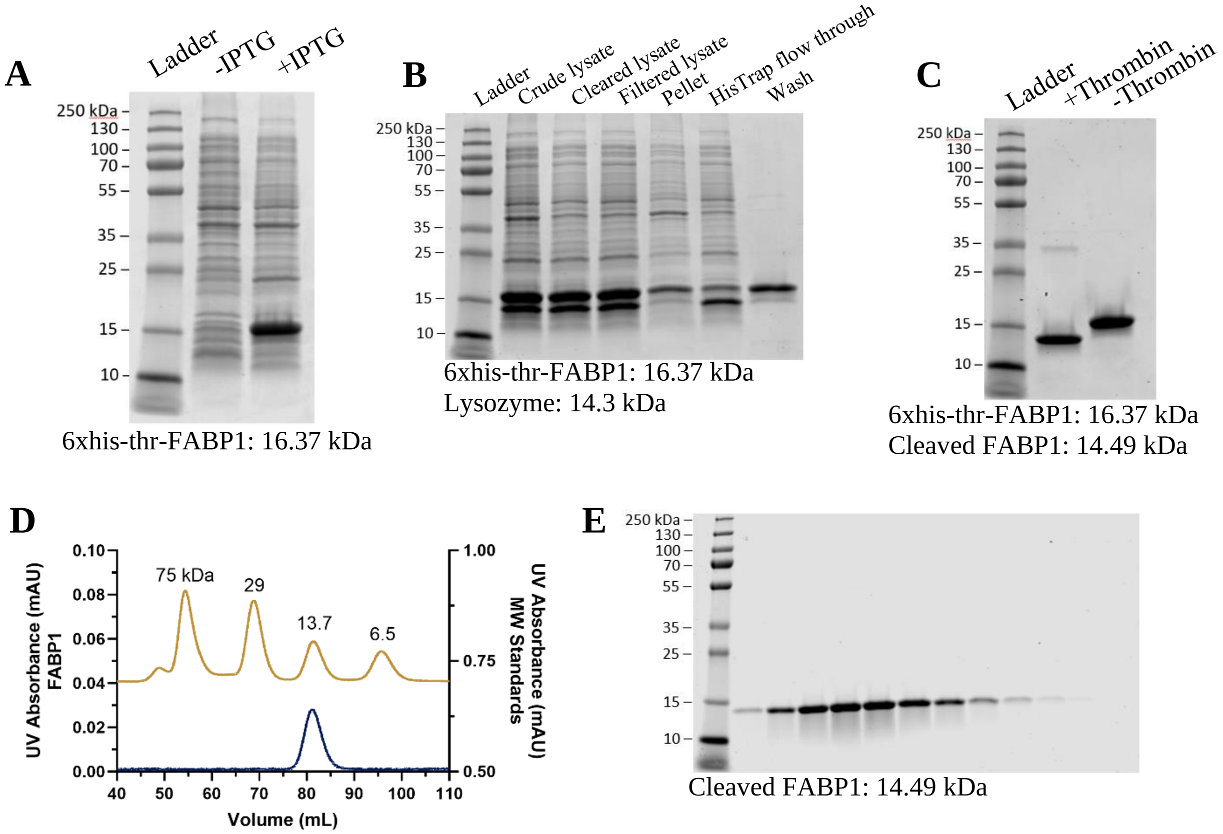

6xhis-thr-FABP1: 16.37 kDa

6xhis-thr-FABP1: 16.37 kDa
Lysozyme: 14.3 kDa

6xhis-thr-FABP1: 16.37 kDa
Cleaved FABP1: 14.49 kDa

Cleaved FABP1: 14.49 kDa

Figure 3.1. Expression and purification of FABP1.
SDS-PAGE Coomassie stained gels of (**A**) whole cell *E. coli* lysate of his-tagged FABP1 induced with isopropyl β-D-1-thiogalactopyranoside (IPTG), (**B**) HisTrap purification steps and (**C**) thrombin cleavage of FABP1. Predicted molecular weights based on amino acid sequences are listed below the gel images. Panel (**D**) shows a gel filtration (Superdex 75) A280 chromatogram of monomeric thrombin-cleaved FABP1 post delipidation (dark blue trace) along with molecular weight standards (gold trace). The elution fractions (1 mL each) from the final gel filtration step are shown in the Coomassie stained gel in **E**.

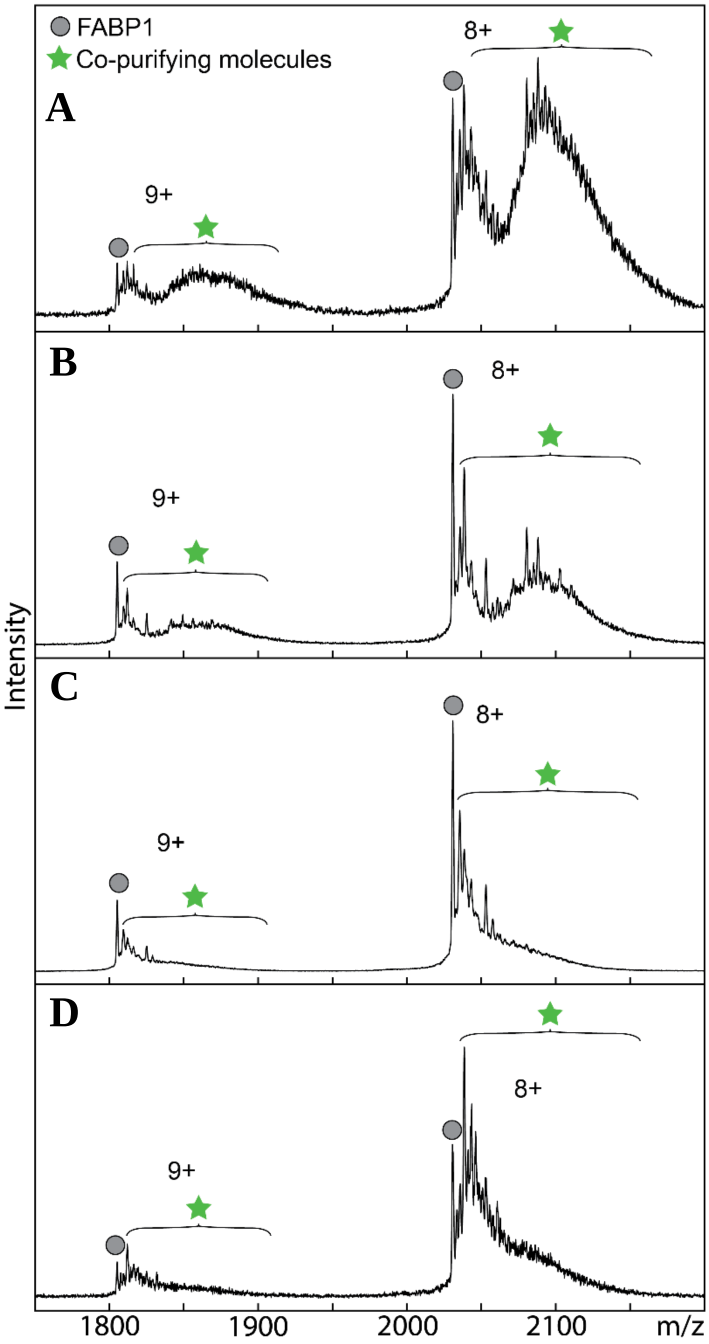

Figure 3.2. Comparison of FABP1 delipidation methods by native mass spectrometry.

Native mass spectra of purified his-tagged FABP1 with no delipidation treatment (**A**) and following individual delipidation treatments of Lipidex-5000 (**B**), 1:1 (v/v) butanol (**C**) and 1:3 (v/v) butanol (**D**). Purification and delipidation protocols are described in detail in Supplemental Materials Section S.2. Mass spectra for 10 µM FABP1 are shown for the two most abundant charge states (n+). Circle markers denote apo-his-tagged FABP1 and star markers designate the *m/z* region where co-purifying molecules are observed. The calculated intact mass of his-tagged apo-FABP1 (16,372 Da) aligns with the predicted mass from the amino acid sequences. Figure courtesy of Alice Martynova.

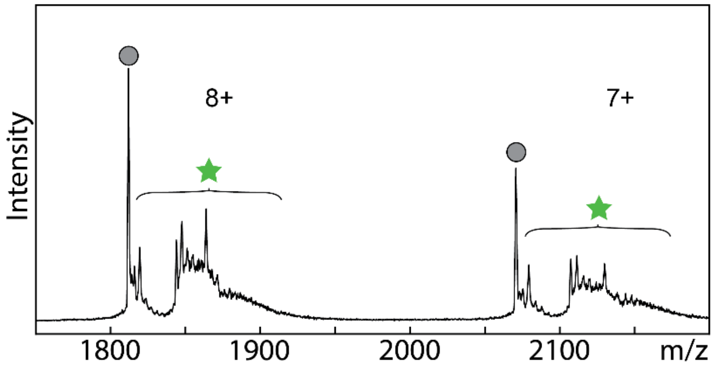

Figure 3.3. Native mass spectrum of FABP1 delipidated with 5 passes through a Lipidex-5000 gravity flow column.

The 7+ and 8+ charge states for apo-FABP1 are denoted with circle markers. Star markers denote the region of the spectrum where *m/z*-shifted peaks are observed corresponding to co-purifying molecules. Figure courtesy of Alice Martynova.

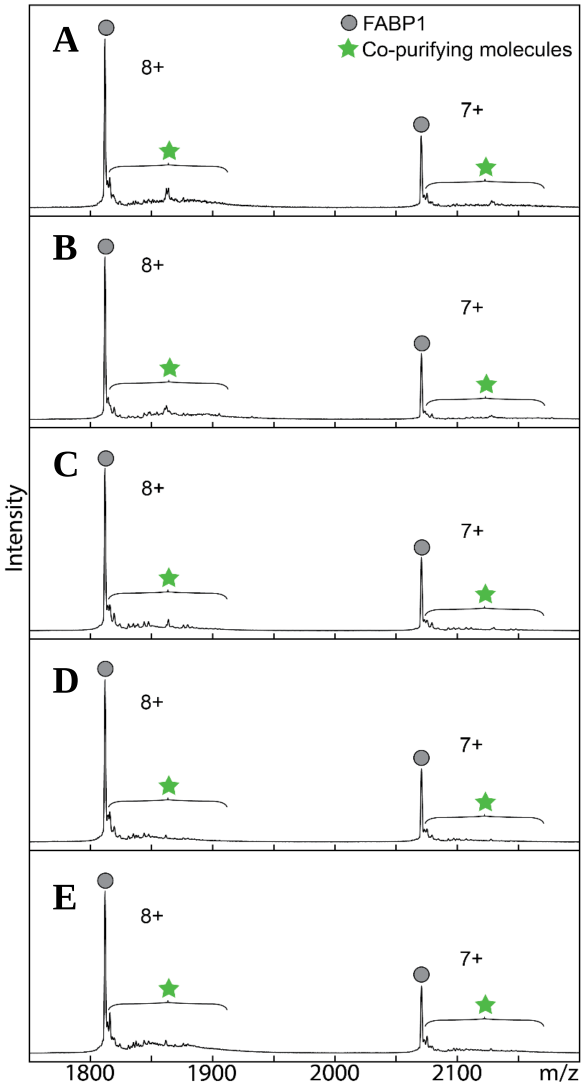

Figure 3.4. Comparison of FABP1 delipidation with sequential treatments of Lipidex-5000 and butanol.
Native mass spectra are shown for FABP1 post thrombin cleavage and gel filtration (**A**), then subsequent treatment with 3 rounds of 1:1 (v/v butanol to FABP1 solution) butanol (**B**), 30 minute incubation with Lipidex-5000 (**C**), a combination of 3 rounds 1:1 butanol then 30 minute incubation with Lipidex-5000 (**D**), or a combination of 3 rounds of 30 minute incubation with Lipidex-5000 then 3 rounds of 1:1 butanol (**E**). Figure courtesy of Alice Martynova.

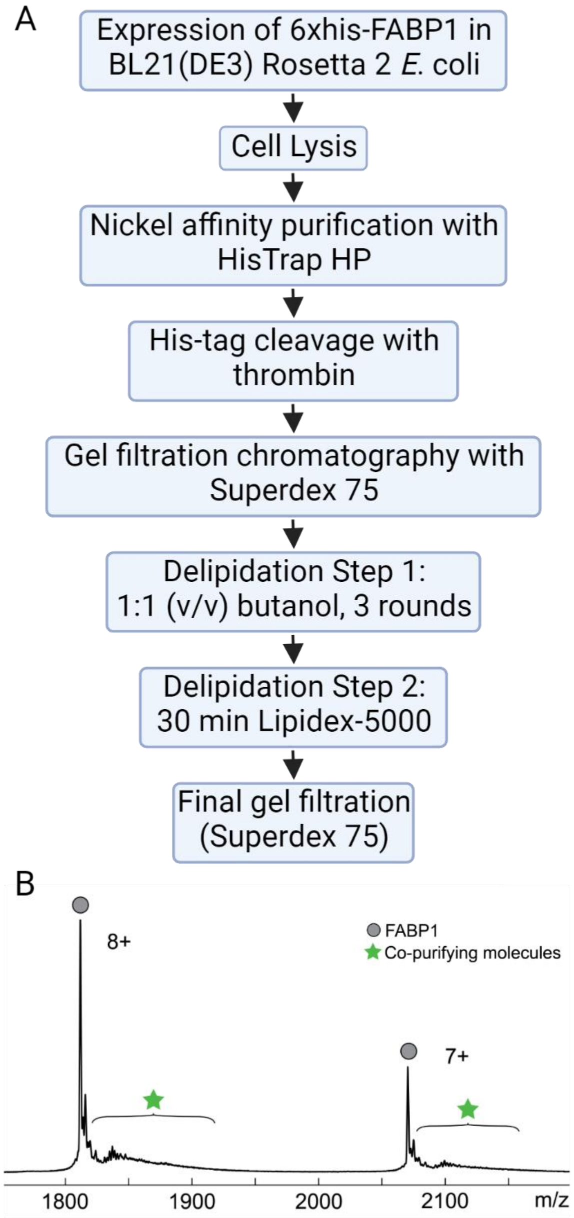

Figure 3.5. Purification protocol and mass spectrum for recombinant human FABP1. (**A**) Flow chart of final purification protocol for hFABP1 including an optimized delipidation method. (**B**) Mass spectrum of 10 µM cleaved hFABP1 after final gel filtration step is shown for the two most abundant charge states (n+). Circle markers represent *m/z* spectral peaks for apo-hFABP1 and the star markers indicate the region in the spectra where copurifying molecules are observed or expected to be observed. The calculated intact mass of cleaved apo-hFABP1 (14,489 Da) aligns with the predicted mass from the amino acid sequence. Flow chart in panel A created with BioRender.com. Figure panel B courtesy of Alice Martynova.

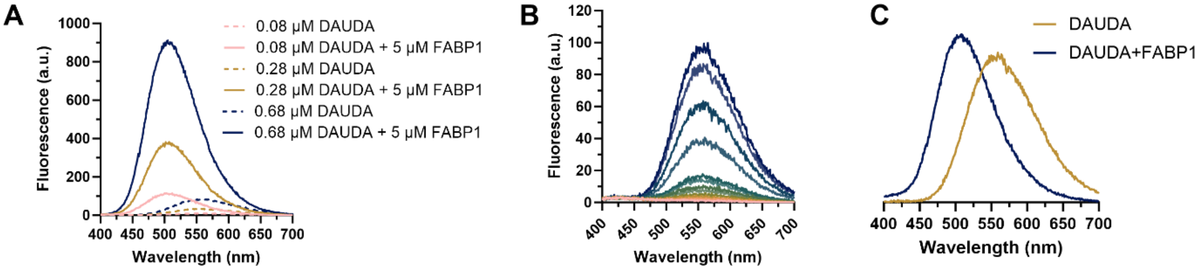

Figure 3.6. Fluorescence emission spectra and basis spectra of DAUDA in the presence and absence of FABP1.

(**A**) Raw fluorescence spectra for different concentrations of DAUDA alone (0.08, 0.28, 0.68 µM) in buffer (dotted lines) and in the presence of 5 µM FABP1 (solid lines). (**B**) Raw fluorescence spectra of free DAUDA in buffer. Each colored line represents a different concentration of DAUDA (0.02-1.03 µM). (**C**) Normalized basis spectra used for spectral deconvolution of fluorescence spectra. Gold spectrum is the basis spectrum for DAUDA in solution and dark blue spectrum is the basis spectrum of DAUDA-FABP1. Both spectra have been normalized to have equal areas.

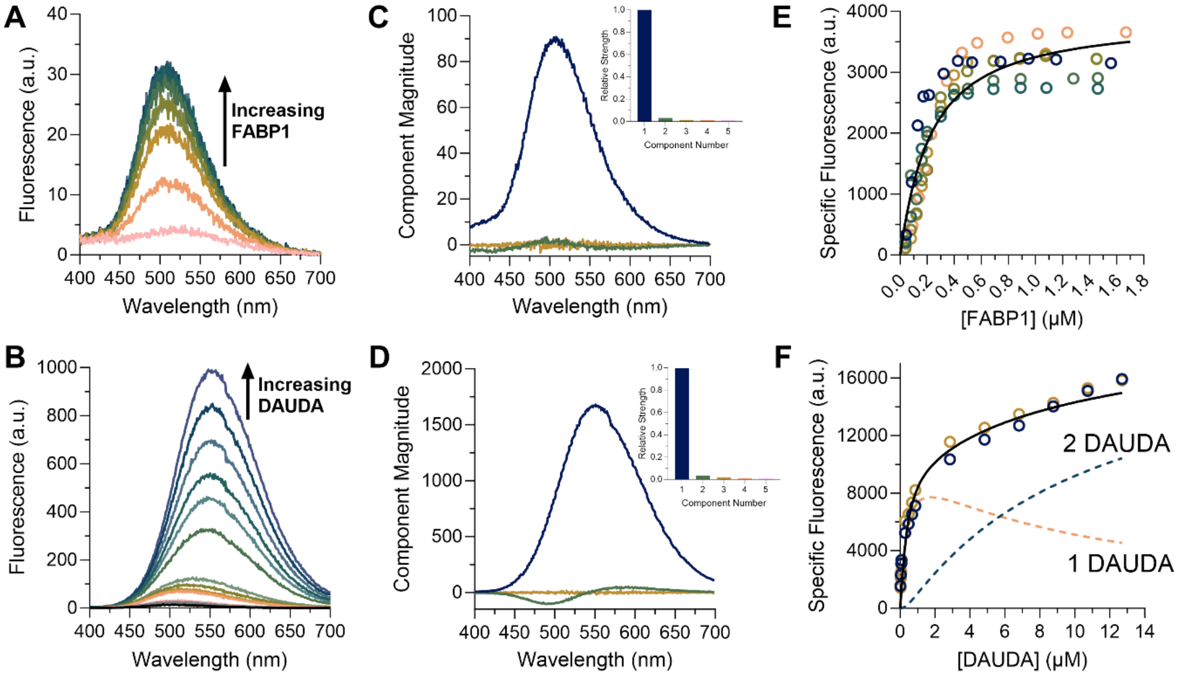

Figure 3.7. Characterization of DAUDA binding to FABP1 by fluorescence spectroscopy. Raw fluorescence emission spectra of (**A**) reverse and (**B**) forward titrations. Reverse titrations were done with constant DAUDA (0.05 μM) and increasing FABP1 (0.04-1.7 μM). Forward titrations were done with constant FABP1 (0.3 μM) and increasing DAUDA (0.02-12.7 μM). (**C and D**) Spectral components identified from SVD analysis for the reverse titration (C) and forward titration (D) are shown. The spectral components from SVD are distinct fluorescence species which change in intensity through the course of the titration and are shown scaled by their relative strength (singular value) in C and D. Scree plots showing the relative strength (singular value) of the first 5 spectral components from SVD analysis of the reverse and forward titration spectra are shown in the insets. (**E and F**) Binding isotherms for the reverse (E) and forward (F) titrations. Replicate titrations done on separate days are represented as different colored open circles. Solid lines show fits to a single site binding model (E) and two-site sequential model (F) used to estimate $K_{d,1}$ and $K_{d,1}$, respectively. The dashed lines in F show the formation of singly and doubly bound DAUDA-FABP1 in the forward titration.

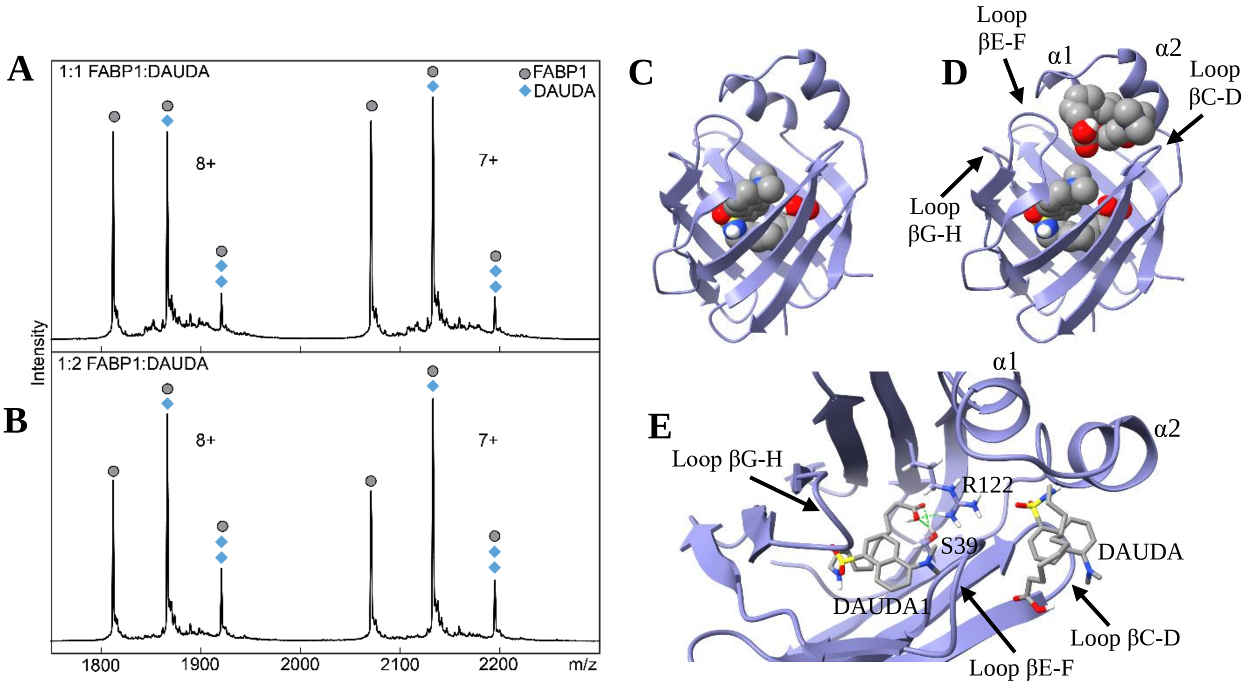

Figure 3.8. Native mass spectra and docking of DAUDA with hFABP1.
Native mass spectra of a mixture of hFABP1 and DAUDA at (**A**) 1:1 (10:10 µM) and (**B**) 1:2 (10:20 µM) FABP1:DAUDA ratios. The mass of apo-FABP1 for each charge state (*n*+) is observed with additional *m*/*z*-shifted peaks corresponding to the molecular mass of 1 and 2 DAUDA (+434 and +868, respectively). Circle markers denote the apo form of the protein, while diamond markers denote peaks that correspond to DAUDA-FABP1 and DAUDA-FABP1-DAUDA complexes at the given charge state. (**C** and **D**) Structure of hFABP1 (PDB: 2LKK) docked with 1 (C) and 2 (D) molecules of DAUDA. (**E**) Top-down view of the docked structure in D. DAUDA1 corresponds to the DAUDA in center-bottom of the binding cavity. DAUDA1 interacts with sidechains from residues S39 and R122. DAUDA2 is located in the portal region in close proximity to the alpha helical domains. Figure panel A and B courtesy of Alice Martynova.

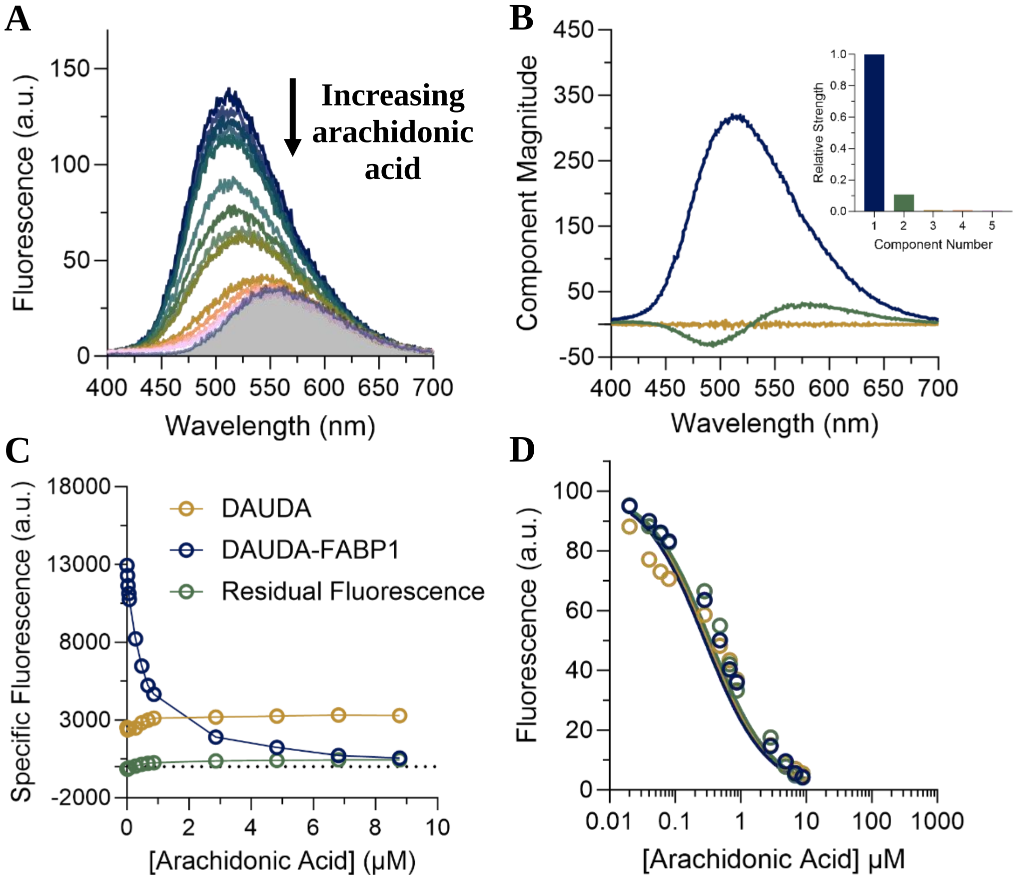

Figure 3.9. Displacement of DAUDA (0.5 μM) from FABP1 (0.3 μM) by increasing concentrations of arachidonic acid (0.02-8.8 μM).
(**A**) The raw fluorescence spectra of the arachidonic acid titration are shown. Different colored spectra represent varying concentrations of arachidonic acid, increasing from top (dark blue, 0 μM) to bottom (pink, 8.8 μM). The shaded area is the spectrum of 0.5 μM unbound DAUDA in buffer. (**B**) Spectral components identified by singular value decomposition (SVD) in the arachidonic acid titration in A are shown, scaled by their relative strength (singular values). Each spectral component reflects correlated changes in the data: the primary component (dark blue) reflects overall quenching of DAUDA fluorescence as AA is added, while the second component (green) reflects a red-shift of fluorescence as DAUDA is displaced from FABP1 into solution. The inset is a scree plot showing the strength (singular value) of the first 5 spectral components from SVD analysis of the spectra in A. (**C**) Relative change in the specific fluorescence of DAUDA in solution (gold) and DAUDA bound to hFABP1 (dark blue) with increasing arachidonic acid concentrations. (**D**) Decrease in DAUDA-FABP1 fluorescence with increasing arachidonic acid concentration with fluorescence at a given arachidonic acid concentration calculated from Equation 4. Solid lines indicate fits to a competitive binding model comprised of Reactions 1-3 implemented in COPASI, which yielded a best-fit K_d value for arachidonic acid as described in Materials and Methods. Fits to 3 replicate experiments done on separate days (dark blue, green and gold) are shown. The resulting K_d parameter estimates are summarized in Table 3.1.

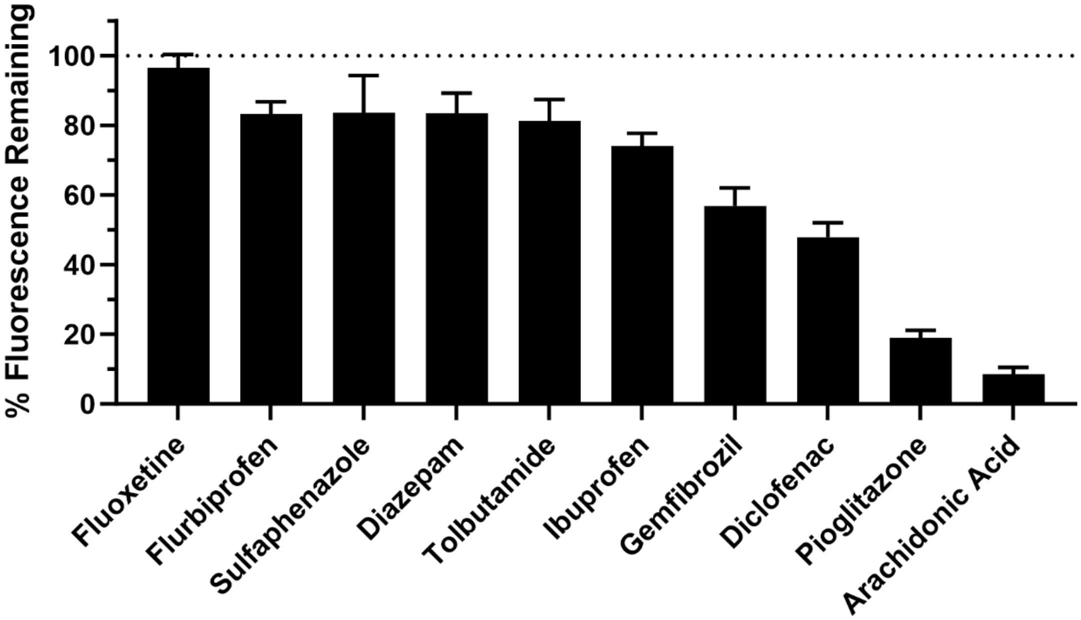

Figure 3.10. Screening of DAUDA displacement by potential drug ligands.
Each drug was screened at 30 µM concentration added to FABP1 (0.3 µM) prebound with DAUDA (0.5 µM). The % fluorescence remaining based on the decrease in fluorescence intensity at 500 nm relative to a no ligand control is shown (mean ± standard deviation) from replicate experiments performed on 3 separate days.

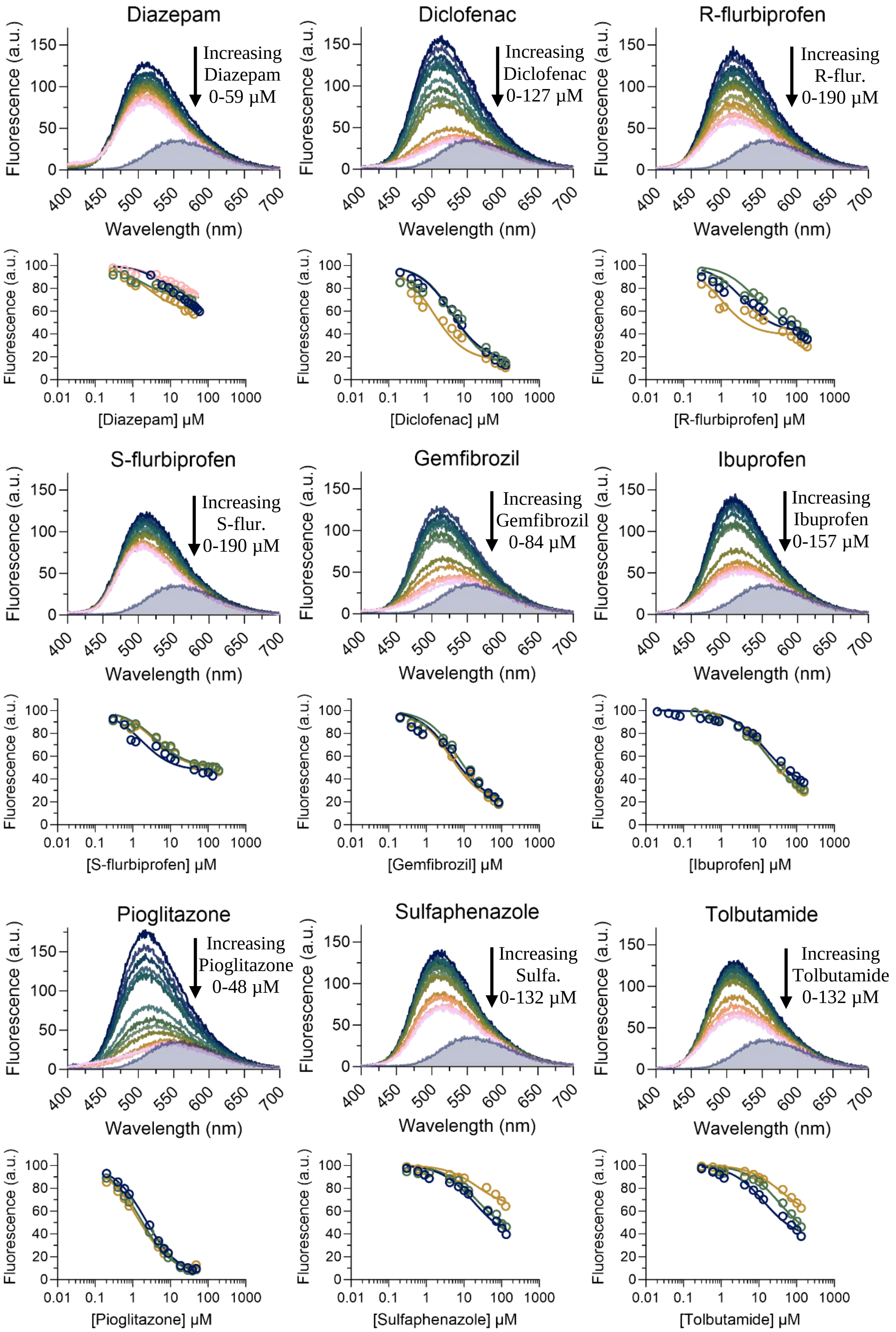
Diazepam
Increasing Diazepam 0-59 µM
Diclofenac
Increasing Diclofenac 0-127 µM
R-flurbiprofen
Increasing R-flur. 0-190 µM
S-flurbiprofen
Increasing S-flur. 0-190 µM
Gemfibrozil
Increasing Gemfibrozil 0-84 µM
Ibuprofen
Increasing Ibuprofen 0-157 µM
Pioglitazone
Increasing Pioglitazone 0-48 µM
Sulfaphenazole
Increasing Sulfa. 0-132 µM
Tolbutamide
Increasing Tolbutamide 0-132 µM
Fluorescence (a.u.)
Wavelength (nm)
400
450
500
550
600
650
700
0
50
100
150
0
20
40
60
80
100
0.01
0.1
1
10
100
1000
[Diazepam] µM
[Diclofenac] µM
[R-flurbiprofen] µM
[S-flurbiprofen] µM
[Gemfibrozil] µM
[Ibuprofen] µM
[Pioglitazone] µM
[Sulfaphenazole] µM
[Tolbutamide] µM

Figure 3.11. DAUDA displacement from FABP1 by drug ligands.

The raw fluorescence spectra for DAUDA displacement titrations with diazepam, diclofenac, (R)- and (S)-flurbiprofen, gemfibrozil, ibuprofen, pioglitazone, sulfaphenazole and tolbutamide as ligands are shown across the rows. In each titration, the top dark blue spectrum represents DAUDA (0.5 µM) prebound with FABP1 (0.3 µM) in the absence of ligand and each subsequent colored spectrum represents increasing concentrations of ligand. The shaded areas show the spectrum of 0.5 µM unbound DAUDA in the absence of hFABP1 and drug ligand. Corresponding DAUDA displacement curves are shown below each spectra. Solid lines indicate fits to a ternary complex binding model comprised of Reactions 1, 2 and 4 which yielded best-fit K_d values for the test drugs as described in Materials and Methods. Data and fits are shown for replicate experiments done on separate days (dark blue, green, gold and pink circles). The resulting K_d values are summarized in Table 3.1.

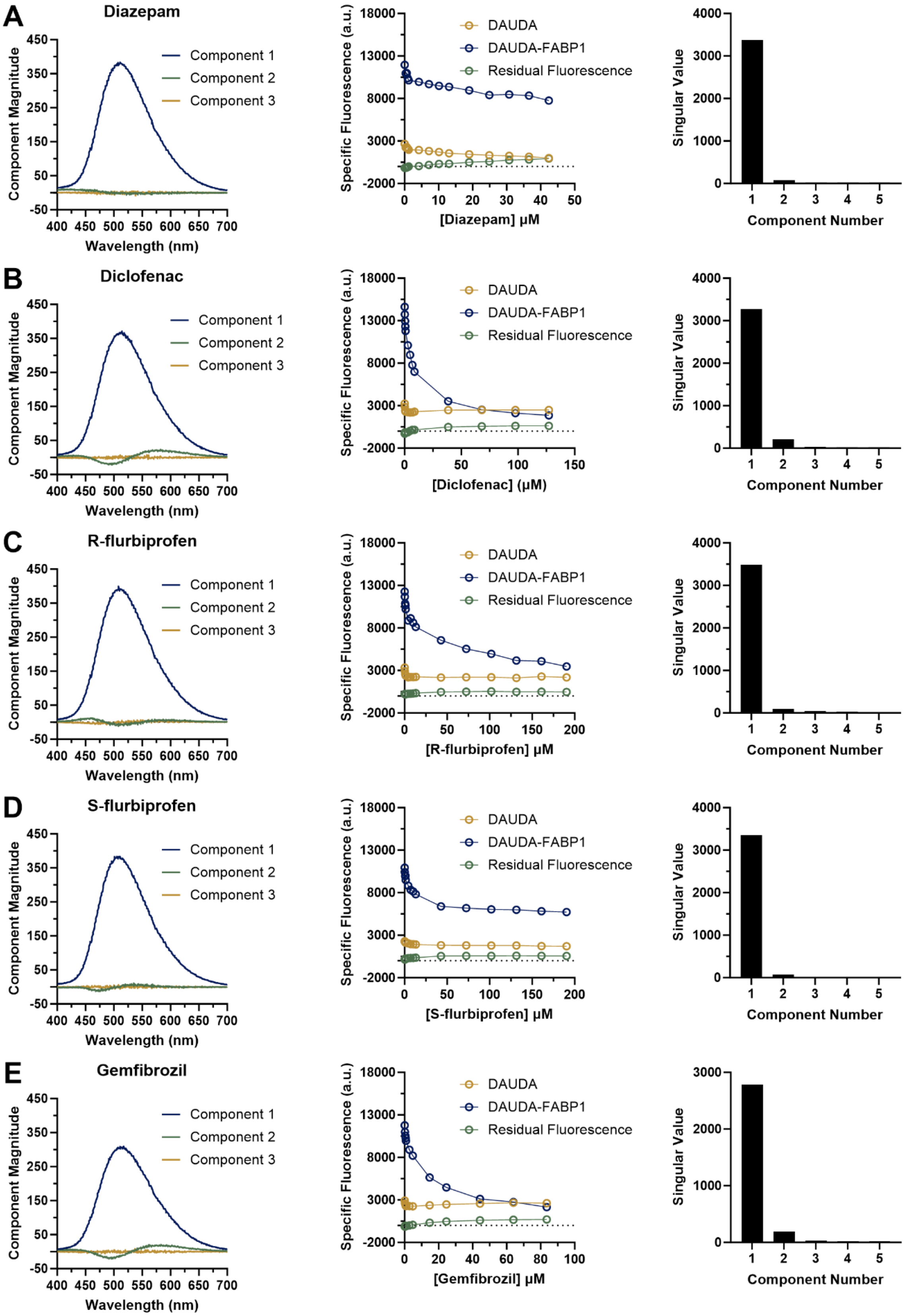
A
Diazepam
Component Magnitude
Component 1
Component 2
Component 3
Wavelength (nm)
Specific Fluorescence (a.u.)
DAUDA
DAUDA-FABP1
Residual Fluorescence
[Diazepam] μM
Singular Value
Component Number
B
Diclofenac
Component Magnitude
Component 1
Component 2
Component 3
Wavelength (nm)
Specific Fluorescence (a.u.)
DAUDA
DAUDA-FABP1
Residual Fluorescence
[Diclofenac] (μM)
Singular Value
Component Number
C
R-flurbiprofen
Component Magnitude
Component 1
Component 2
Component 3
Wavelength (nm)
Specific Fluorescence (a.u.)
DAUDA
DAUDA-FABP1
Residual Fluorescence
[R-flurbiprofen] μM
Singular Value
Component Number
D
S-flurbiprofen
Component Magnitude
Component 1
Component 2
Component 3
Wavelength (nm)
Specific Fluorescence (a.u.)
DAUDA
DAUDA-FABP1
Residual Fluorescence
[S-flurbiprofen] μM
Singular Value
Component Number
E
Gemfibrozil
Component Magnitude
Component 1
Component 2
Component 3
Wavelength (nm)
Specific Fluorescence (a.u.)
DAUDA
DAUDA-FABP1
Residual Fluorescence
[Gemfibrozil] μM
Singular Value
Component Number

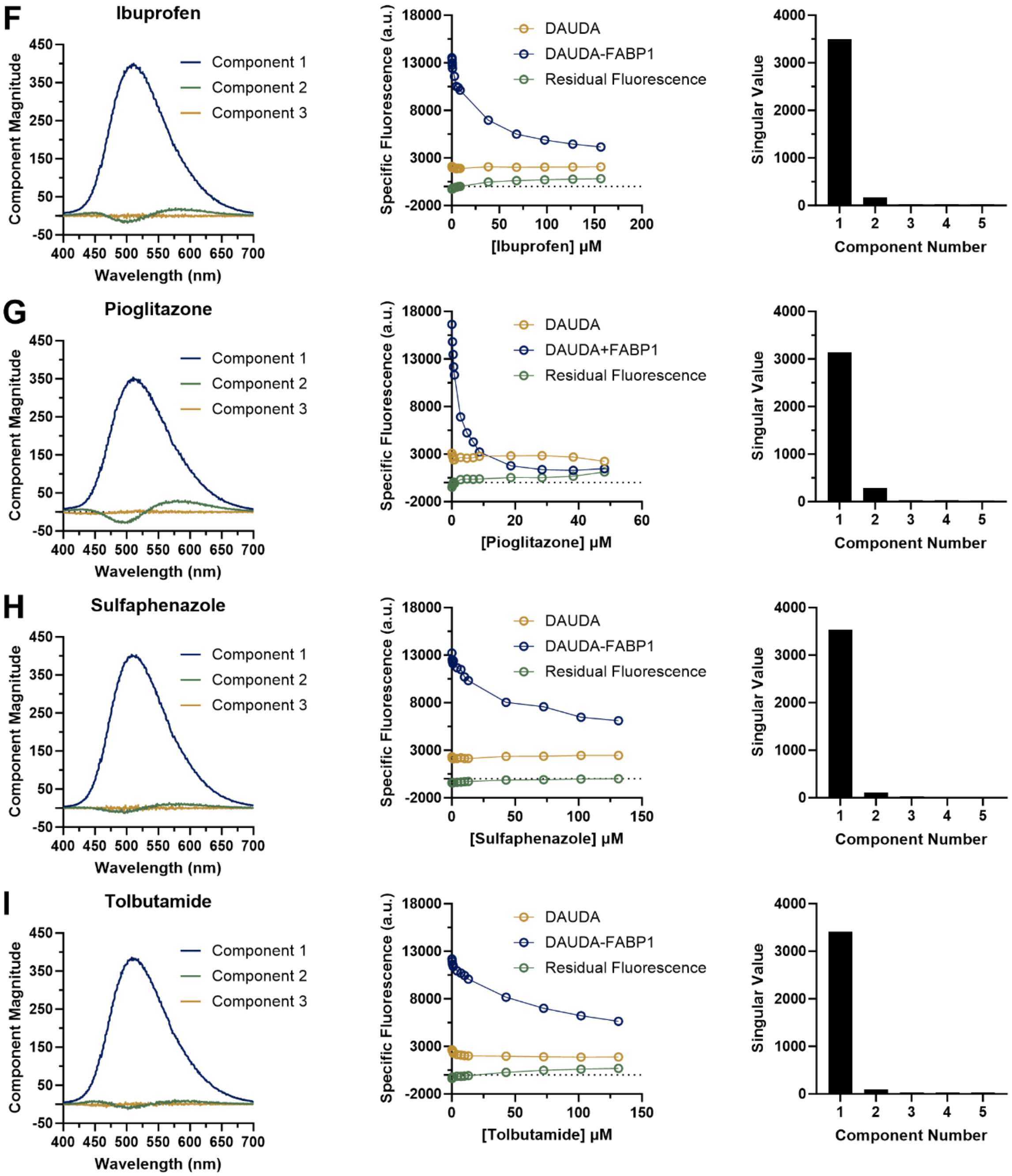

Figure 3.12. Singular value decomposition (SVD) analysis of DAUDA displacement titration for all drug ligands tested.

Each lettered panel (A-I) shows the SVD analysis for a representative replicate titration for each drug ligand tested in DAUDA displacement assays. For each drug titration, plots on the left are the spectral components identified from SVD analysis, scaled by the corresponding singular values (i.e., relative contributions to the signal). The middle panels show the change in specific fluorescence of DAUDA and DAUDA-FABP1 with increasing ligand concentration. The 'scree' plots on the right show the singular values of the first 5 spectral components identified by SVD.

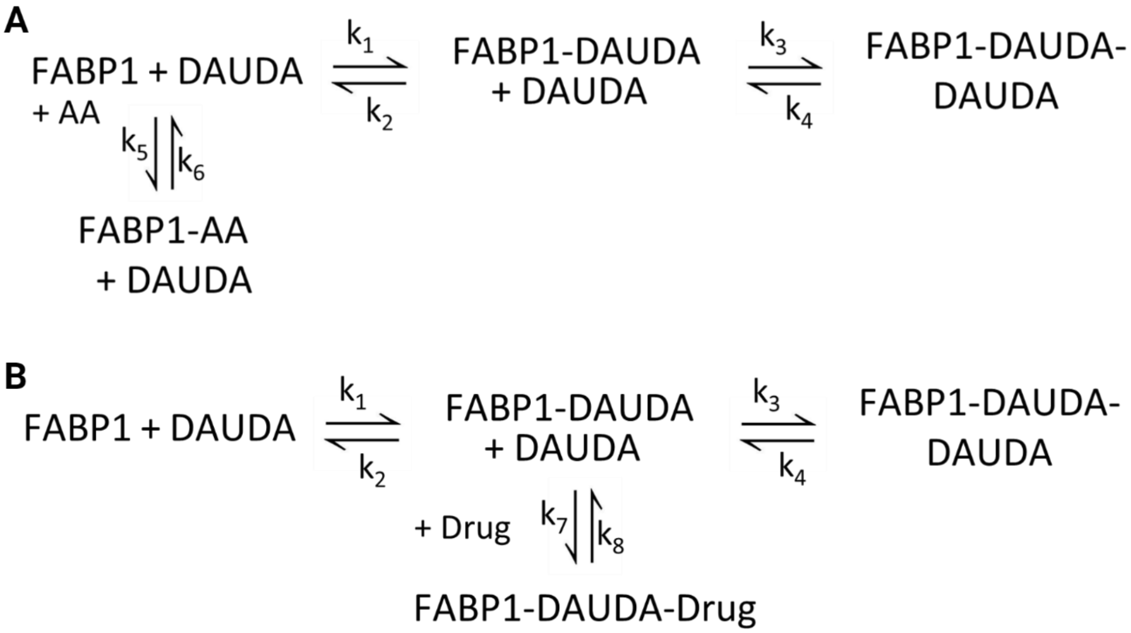

Figure 3.13. Kinetic schemes for arachidonic acid (AA) and drugs interacting with the DAUDA-FABP1 system.

(**A**) Competitive binding model for AA. AA competes with DAUDA for binding to FABP1 occupying both DAUDA binding sites. (**B**) Ternary binding model for drugs. Drugs bind at a second binding site in FABP1 without displacing DAUDA to form a ternary complex. Schemes created by BioRender.com.

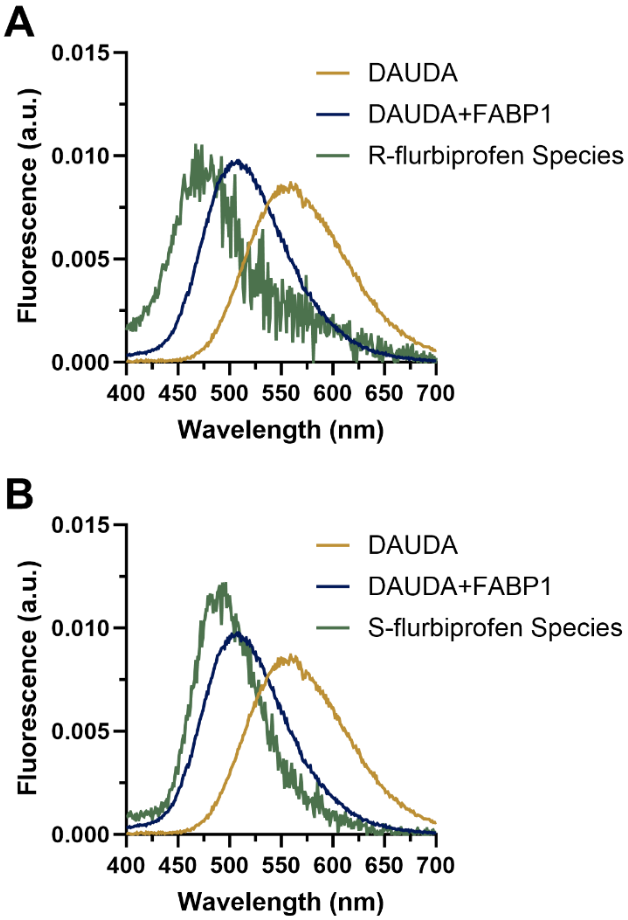

Figure 3.14. (R)- and (S)-flurbiprofen basis spectra.
The basis spectra for (**A**) (R)- and (**B**) (S)-flurbiprofen used for spectral deconvolution of titration data. DAUDA (gold) and DAUDA-FABP1 (blue) basis spectra were experimentally determined as described above. The basis spectra for bound (R)- and (S)-flurbiprofen (green) were generated based on unique spectral components identified from SVD analysis of titration spectra with (R)- and (S)-flurbiprofen. All basis spectra were normalized to have equal areas.

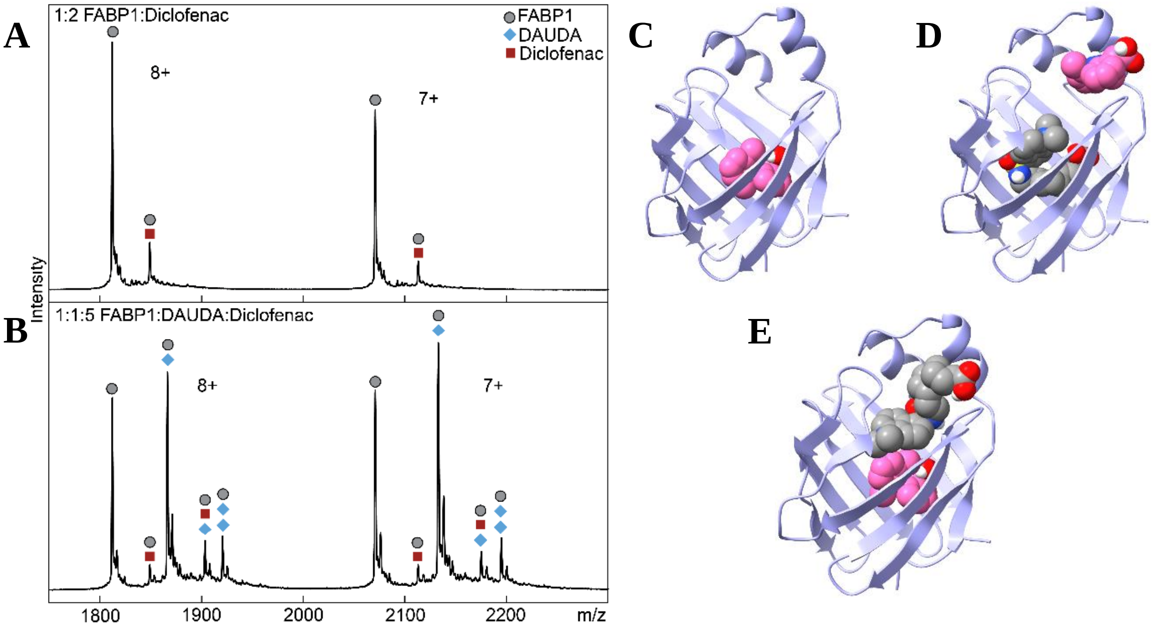

Figure 3.15. Characterization of diclofenac binding to hFABP1 via native mass spectrometry and molecular docking.
(**A**) Native mass spectrum of hFABP1 and diclofenac at a 1:2 (10:20 µM) hFABP1:diclofenac ratio. Circle markers represent the apo form of the protein, while square markers denote *m/z*-shifted peaks that correspond to diclofenac. (**B**) Native mass spectrum of hFABP1, DAUDA, and diclofenac at 1:1:5 (10:10:50 µM) ratios, which uses the same marker labels as A, with the addition of diamond markers that denote *m/z*-shifted peaks corresponding to the association of DAUDA. (**C-E**) Predicted structures of hFABP1 complexes showing potential binding orientations of singly bound diclofenac (C, pink) and diclofenac in complex with DAUDA (D and E, gray). Docking studies were carried out using an NMR solution structure of holo-hFABP1 (PDB ID: 2LKK) in AutoDock4. Ligands in D and E were docked sequentially with DAUDA docked first in D and diclofenac docked first in E. The binding orientations shown were the top scoring (lowest $\Delta G_{\text{binding}}$) poses from 50 docking runs. Figure panel A and B courtesy of Alice Martynova.

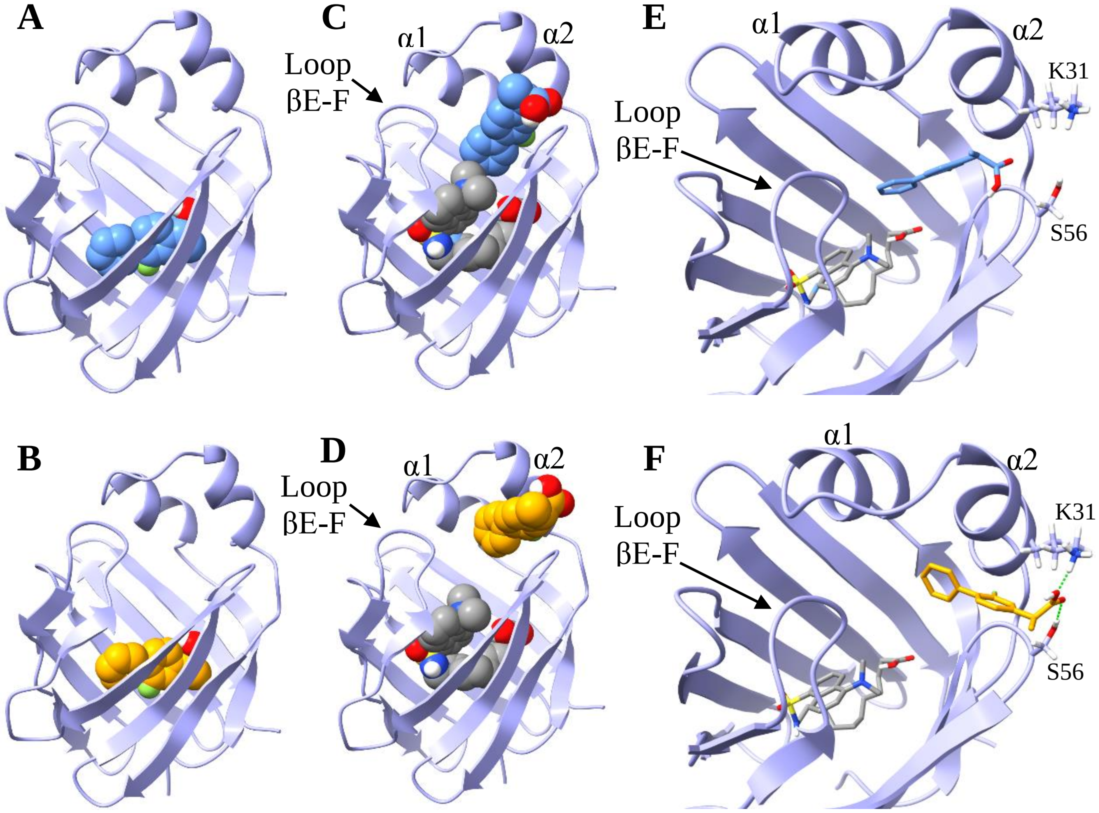

Figure 3.16. Docking of (R)- and (S)-flurbiprofen to hFABP1 with DAUDA.
(**A** and **B**) Predicted binding orientations of singly bound (R)-flurbiprofen (A, blue) and (S)-flurbiprofen (B, orange) in the absence of DAUDA. (**C** and **D**) Predicted binding orientations of (R)- and (S)-flurbiprofen are shown in the presence of DAUDA (gray) in the hFABP1 binding cavity. DAUDA was first docked to hFABP1 prior to docking of flurbiprofen molecules. (**E** and **F**) Molecular stick models showing the simulated distinct positions of (R)- (E) and (S)-flurbiprofen (F) at the portal domain of hFABP1 in the presence of DAUDA in the binding cavity. Predicted hydrogen bonding for the carboxyl group of (S)-flurbiprofen is shown in green. Docking studies were carried out using an NMR solution structure of holo-hFABP1 (PDB ID: 2LKK) in AutoDock4. The binding orientations shown were the top scoring (lowest $\Delta G_{binding}$) poses from 50 docking runs.

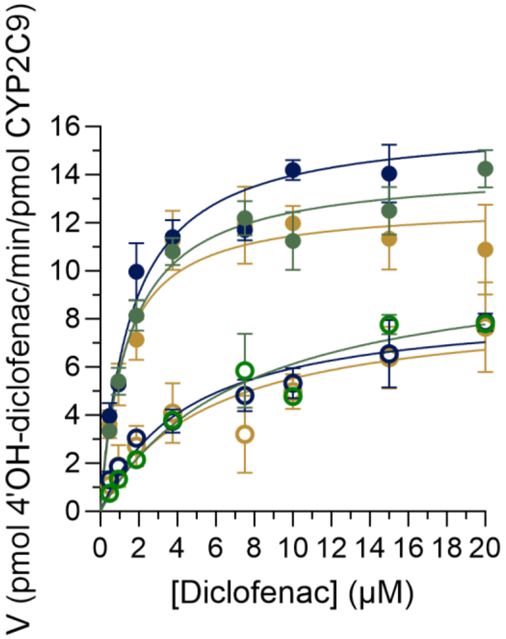

Figure 3.17. 4’OH-diclofenac apparent formation kinetics by CYP2C9 in the presence and absence of FABP1. 4’OH-diclofenac formation velocity is shown as a function of total diclofenac concentration in CYP2C9 Supersomes as measured in the presence (open circles) and absence (solid circles) of 20 µM FABP1. Paired replicate experiments performed on three separate days are shown in dark blue, green and gold. The error bars show the standard deviation of the technical replicates within an experiment. The x-axis shows the nominal concentration of diclofenac added to the incubations. The corresponding free concentrations of diclofenac and free fractions are shown in Figure 9.

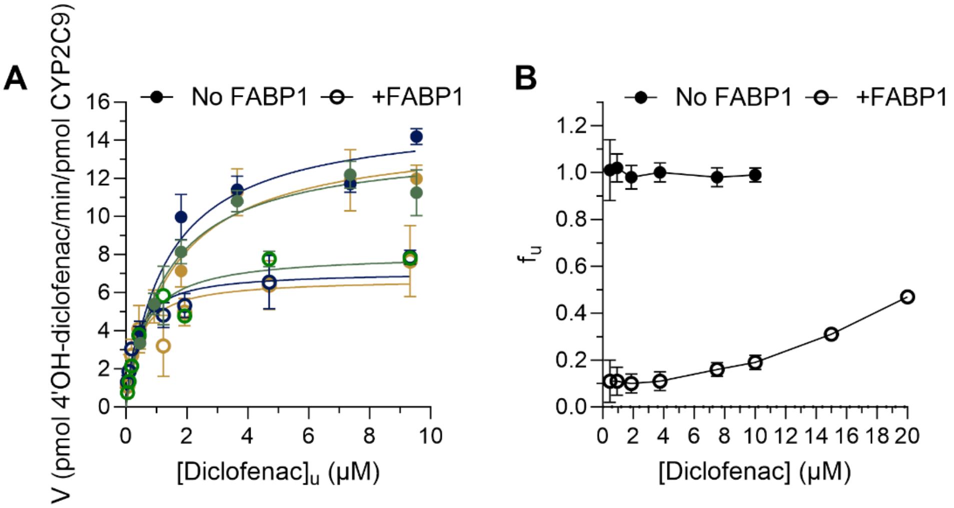

Figure 3.18. Impact of FABP1 on 4’-OH-diclofenac formation kinetics by CYP2C9.
(**A**) 4’-OH-diclofenac formation velocity as a function of free diclofenac concentration by recombinant CYP2C9 Supersomes (2nM) in the presence (open circles) and absence (solid circles) of 20 µM FABP1 is shown. The nominal diclofenac concentrations ranged from 0.4-20 µM and the free concentrations were calculated as the product of the measured unbound fraction (B) and the nominal concentration. Paired replicate experiments from three separate days are shown in dark blue, green and gold. (**B**) The unbound fraction (f_u) of diclofenac measured for all nominal diclofenac concentrations used in the kinetic experiments in the absence (solid symbols) and presence (open symbols) of FABP1 (20 µM). The unbound fraction was determined using magnetic silica beads and magnetic Ni-NTA agarose beads as described in Materials and Methods. The unbound K_m and k_{cat} values for diclofenac are summarized in Table 3.2.

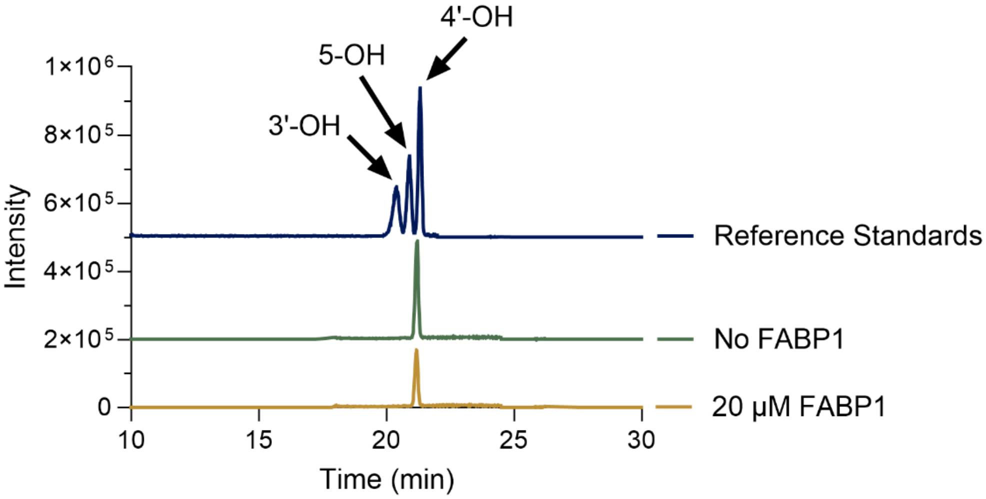

Figure 3.19. LC-MS/MS chromatograms of reference standards of diclofenac hydroxylation products and of incubations of diclofenac with CYP2C9 Supersomes in the presence and absence of FABP1.

The top dark blue trace shows the baseline resolved peaks of 3’OH-, 5-OH- and 4’OH-diclofenac metabolite reference standards. The green middle trace depicts the formation of diclofenac hydroxylation products when diclofenac (20µM) was incubated with CYP2C9 (0.2 pmol) Supersomes in the absence of FABP1. The trace shows the lack of formation of 3’OH-diclofenac and 5-OH-diclofenac. The bottom gold trace depicts the formation of diclofenac hydroxylation products when diclofenac (20 µM) was incubated with CYP2C9 (0.2 pmol) Supersomes in the presence of 20 µM FABP1. No formation of 3’OH-diclofenac and 5-OH-diclofenac was observed.

Table 3.1. Summary of binding affinities for FABP1 ligands from DAUDA fluorescence displacement experiments.

K_d is the equilibrium binding affinity for the ternary complex formation based on reaction 4 and estimated using numerical simulations conducted in COPASI. EC_{50} is the concentration of ligand that results in a decrease in fluorescence by 50 % of the residual fluorescence (F_{res}) value determined from a three-parameter dose response curve fit (Equation 3.9) to the data obtained from the SVD analysis of the fluorescence titrations. All values are reported as means ± S.D. from 3 replicate experiments conducted on separate days. N.D. indicates parameters that could not be determined with confidence.

	K_d (μM)	**EC_{50} (μM)**	**F_{res} (% fluorescence remaining)**
Arachidonic acid	0.08 ± 0.010	0.42 ± 0.11	2.2 ± 3.6
Diazepam	N.D.	>50	N.D.
Diclofenac	2.5 ± 1.3	3.9 ± 2.1	15 ± 3.0
R-flurbiprofen	N.D.	4.4 ± 3.8	40 ± 1.6
S-flurbiprofen	2.2 ± 0.93	3.3 ± 1.4	48 ± 1.1
Gemfibrozil	3.6 ± 1.1	5.6 ± 1.7	18 ± 2.8
Ibuprofen	9.9 ± 0.60	15 ± 0.85	28 ± 4.9
Pioglitazone	1.0 ± 0.30	1.8 ± 0.47	5.2 ± 2.4
Sulfaphenazole	15 ± 1.7	> 40	N.D.
Tolbutamide	20 ± 9.6	> 40	N.D.

Table 3.2. Michaelis Menten kinetic parameters for 4'-OH-diclofenac formation from diclofenac by recombinant CYP2C9.

The apparent K_m values ($K_{m,apparent}$) for diclofenac were determined from fitting the Michaelis-Menten equation to the data of 4'-OH-diclofenac formation velocity as a function of nominal diclofenac concentrations in the absence (-FABP) and presence (+FABP) of 20 µM FABP1. The $K_{m,u}$ and k_{cat} values for diclofenac were determined from fitting the Michaelis-Menten equation to 4'-OH-diclofenac formation velocity data as a function of free diclofenac concentration in the absence (-FABP) and presence (+FABP) of 20 µM FABP1. Unbound diclofenac concentrations were directly measured for all nominal concentrations used in incubation experiments. The data are reported as means ± S.D. from experiments done on 3 separate days. The p-value refers to whether the parameter estimate is different in the presence and absence of FABP1.

	-FABP1	***+FABP1***	***p-value***
$K_{m,apparent}$ **(µM)**	1.4 ± 0.2	5.8 ± 1.5	0.003, 0.009, 0.03
$K_{m,unbound}$ **(µM)**	1.4 ± 0.1	0.4 ± 0.1	0.03, 0.05, 0.11
k_{cat} **(min^{-1})**	14.5 ± 0.8	7.3 ± 0.7	0.007

Chapter 4. CYP2C9, CYP3A AND CYP2C19 METABOLIZE Δ9-TETRAHYDROCANNABINOL TO MULTIPLE METABOLITES BUT METABOLISM IS AFFECTED BY HUMAN LIVER FATTY ACID BINDING PROTEIN

This chapter is adapted from work submitted to *Biochemical Pharmacology* on January 22, 2024

Co-authors: Yue Wen, Keiann T. Simon and Nina Isoherranen

Department of Pharmaceutics, School of Pharmacy, University of Washington, Seattle, WA United States

4.1 ABSTRACT

Δ9-tetrahydrocannabinol (THC) is the psychoactive constituent of cannabis. It is predominantly cleared in humans via metabolism. The main clearance pathway of THC involves metabolism to 11-OH-THC by cytochrome P450 (CYP) 2C9. The estimated THC fraction metabolized (f_m) by CYP2C9 is ~70%. The remaining clearance pathways are not well established, and it is unknown how THC is eliminated in individuals with reduced CYP2C9 activity. The goal of this study was to systematically identify the CYP enzymes contributing to THC clearance and characterize the metabolites formed. Further, this study aimed to characterize the impact of liver fatty acid binding protein (FABP1) on THC metabolism by human CYPs. In human liver microsomes (HLMs) and with recombinant CYPs, THC was metabolized to at least four different metabolites, including 11-OH-THC. With recombinant CYPs 11-OH-THC formation was mainly by CYP2C9 ($K_{m,u} = 0.77$ nM, $k_{cat} = 12$ min^{-1}) with a minor contribution from CYP2C19 ($K_{m,u} = 2.2$ nM, $k_{cat} = 14$ min^{-1}). The other three major metabolites were formed mainly by CY3A4/5 ($K_{m,u} > 10$ nM). HLM experiments confirmed the contributions of CYP2C9, CYP2C19 and CYP3A to THC metabolism. FABP1 binding significantly decreased the k_{cat} of THC metabolite formation by recombinant CYPs. This suggests that FABP1 interacts with the CYP enzymes and FABP1 may alter the f_m by CYPs towards THC metabolism. FABP1 also altered THC metabolism in HLMs in an enzyme and metabolite specific manner. In conclusion, this study is the first to systematically establish the complete metabolic profile of THC by CYPs and characterize how FABP1 binding alters THC metabolism by CYPs.

4.2 INTRODUCTION

Cannabis use in the U.S. is at an all-time high, with more than 48 million people reportedly having consumed cannabis at least once in 2019 (Centers for Disease Control and Prevention, 2022). In 2021, 43% of young adults (19-30 years) reported using cannabis and 11% reported daily use (National Institute on Drug Abuse (NIDA), 2022). Δ-9-tetrahydrocannabinol (THC) is the major psychoactive component found in cannabis. It is also the main circulating bioactive cannabinoid found in humans after smoking cannabis. Its primary circulating metabolite in humans is 11-hydroxy-THC (11-OH-THC), but several dozen different metabolites of THC have been identified (Agurell *et al.*, 1986; Watanabe *et al.*, 2007; Dinis-Oliveira, 2016). Following cannabis consumption via edibles the relative exposure to 11-OH-THC is greater than that observed after smoking, largely due to the high hepatic clearance of THC and first pass formation of 11-OH-THC (Naef *et al.*, 2004; Lunn *et al.*, 2019). 11-OH-THC is also pharmacologically active (Lemberger *et al.*, 1970, 1973) and has been shown to be formed by cytochrome P450 2C9 (CYP2C9) *in vitro* (Watanabe *et al.*, 1995, 2007; Bland *et al.*, 2005; Patilea-Vrana *et al.*, 2019). Other CYP enzymes do, however, also produce 11-OH-THC (Watanabe *et al.*, 2007; Patilea-Vrana *et al.*, 2019). 11-OH-THC is further eliminated by CYP mediated oxidation and by alcohol and aldehyde dehydrogenase enzymes to form 11-COOH-THC (Patilea-Vrana and Unadkat, 2019; Patilea-Vrana *et al.*, 2019; Beers *et al.*, 2023), the main circulating metabolite of THC.

THC pharmacokinetics in humans is altered in individuals with CYP2C9 polymorphisms (Sachse-Seeboth *et al.*, 2009). Individuals with a CYP2C9*3/*3 genotype retain about 7% of the CYP2C9 activity when compared to CYP2C9*1/*1 homozygotes (Kumar *et al.*, 2008). The exposure (AUC) of THC is 3-fold greater in CYP2C9*3/*3 homozygotes compared to

CYP2C9*1/*1 homozygotes after oral dosing (Sachse-Seeboth *et al.*, 2009). Based on these data, CYP2C9 controls ~70% of THC clearance ($f_m = 0.7$), on average, in the reference population. At present, it is unclear what other enzymes are responsible for the remaining ~30% of THC clearance in CYP2C9*1/*1 individuals. The main elimination pathways of THC in individuals who are CYP2C9 poor metabolizers or in individuals who are taking CYP2C9 inhibitors are also unknown. Interestingly, the AUC of THC was increased by ~80% when co-administered with ketoconazole (Stott *et al.*, 2013), a strong inhibitor of CYP3A4 (inhibits other CYP enzymes too), suggesting that CYP3A4 may contribute to THC clearance. *In vitro*, 8β-OH-THC and 9α, 10α-THC-epoxide were identified as THC metabolites formed by human liver microsomes (HLMs) when very high concentrations of THC were used (Yamamoto *et al.*, 1984; Bornheim *et al.*, 1992; Watanabe *et al.*, 2007) and formation of these products was attributed to CYP3A4 (Watanabe *et al.*, 2007). 8β-OH-THC and the di-hydroxylated metabolite 8β,11-diOH-THC were also detected in plasma from cannabis users (Gasse *et al.*, 2018), supporting a role of CYP3A4 in THC metabolism *in vivo*.

The relative importance of the enzymes and metabolites identified in the previous studies may be confounded by the concentrations of THC used. For example, CYP3A4 contribution was detected at 64 and 130 μM THC (Bornheim *et al.*, 1992; Watanabe *et al.*, 2007), concentrations that greatly exceed plasma THC maximum concentration (C_{max}) even in heavy cannabis users (Huang *et al.*, 2022). For 11-OH-THC formation the apparent K_ms in HLMs and with recombinant CYP2C9 were measured as 0.8-5.2 μM (Bland *et al.*, 2005). The unbound K_m ($K_{m,u}$) for 11-OH-formation in HLM was estimated as 8 nM and for THC depletion as 7 nM (Patilea-Vrana and Unadkat, 2019). The observed circulating concentrations of THC in plasma vary widely depending on route of administration (Hunault *et al.*, 2008; Sachse-Seeboth *et al.*,

2009) and cannabis usage patterns (Huang *et al.*, 2022). If several enzymes with different K_m values contribute to THC clearance, the relative contributions of these enzymes to THC clearance and metabolite formation in cannabis users may vary depending on THC concentrations and usage (e.g., dose route). Quantitative determination of the kinetics (K_m) of THC metabolism by individual CYPs is needed to accurately assess the contribution of CYPs in the context of the wide range of THC C_{max} values observed *in vivo*.

A challenge in studying THC metabolism *in vitro* is the high lipophilicity of THC (logP = 6.97) (Thomas *et al.*, 1990) and the "stickiness" of THC that results in extensive nonspecific binding to plastics and other labware. To address these issues, bovine serum albumin (BSA) was previously added to *in vitro* incubations to prevent nonspecific binding to plastics (Patilea-Vrana *et al.*, 2019). Using this approach and via measurement of THC depletion at 500 nM nominal concentration, the majority (91%) of THC metabolic clearance in pooled HLMs was assigned to CYP2C9 with the remaining 9% assigned to CYP2D6 ($f_m = 0.09$) (Patilea-Vrana and Unadkat, 2019; Patilea-Vrana *et al.*, 2019). At 500 nM THC, recombinant CYP1A1, CYP1A2, CYP2C19 and CYP3A4 were also found to efficiently deplete THC, but based on inhibition studies these enzymes were not considered to be important for THC clearance in human liver (Patilea-Vrana *et al.*, 2019). At present, it is unclear how the incorporation of 0.2% BSA (which is not present in humans) into incubations altered the relative contribution of specific CYPs to THC clearance. Albumin has been previously shown to have enzyme specific effects on CYP mediated metabolism (Kandel and Lampe, 2014), and has been shown to increase the activity of CYP2C9 in HLMs (Zhou *et al.*, 2004; Rowland *et al.*, 2008). Whether albumin has a similar effect on CYP3A4, CYP2C19, CYP2D6 or CYP1A is unclear. In addition, albumin effects are unlikely to be present in human hepatocytes *in vivo*, and hence, effects of BSA may skew the relative contribution assessment of individual CYPs to THC clearance.

Liver fatty acid binding protein (FABP1) is an intracellular binding protein that binds and solubilizes endogenous lipids, including fatty acids (Storch and Corsico, 2008; Yabut and Isoherranen, 2023). FABP1 is highly expressed in the liver cytosol with concentrations ranging from 0.7 mM to 1 mM (Schroeder *et al.*, 2016; Yabut and Isoherranen, 2023). FABP1 modulates the liver distribution and metabolism of fatty acids (Storch and Corsico, 2008; Yabut and Isoherranen, 2023). Binding to FABP1 was recently shown to also alter the metabolism of diclofenac by CYP2C9 (Yabut *et al.*, 2024). THC binds to FABP1 (Huang *et al.*, 2018; Elmes *et al.*, 2019), and FABP1 also appears to alter THC disposition *in vivo* in mice (Elmes *et al.*, 2019). FABP1 knockout mice had decreased rates of THC metabolism, suggesting that FABP1 may be facilitating THC clearance (Elmes *et al.*, 2019). We hypothesized that in the human liver FABP1 may affect the efficiency of THC metabolism and alter the relative importance of individual CYP enzymes to THC clearance. To test this hypothesis we first identified the major THC metabolites formed in human liver microsomes and determined the specific contribution of CYP enzymes to the formation of THC metabolites. We then characterized the binding of major cannabinoids to human FABP1 and established the effect of FABP1 on THC metabolism by human liver CYPs.

4.3 MATERIALS AND METHODS

4.3.1 *Chemicals and Reagents*

Kanamycin, Trizma base (Tris), sodium chloride, sodium phosphate, potassium phosphate, protease inhibitor tablets, benzonase, butanol, thrombin, Rosetta 2 *E. coli*, Coomassie Brilliant Blue R, 11-(Dansylamino)undecanoic acid (DAUDA), β-Nicotinamide-adenine dinucleotide phosphate (NADPH) tetrasodium salt, tienilic acid, (+)-N-3-benzylnirvanol, CYP3cide, tolbutamide, 4-hydroxytolbutamide, midazolam, 1-hydroxymidazolam, and 1-hydroxymidazolam-d_4 were purchased from Millipore-Sigma (St. Louis, MO). (S)-mephenytoin, (±)4-hydroxymephenytoin, and (±)4-hydroxymephenytoin-d_3 and ethanol solutions (1 mg/mL) of anandamide (AEA) and 2-arachidonyl glycerol (2AG) were purchased from Cayman Chemical Company (Ann Arbor, MI). (-)-Δ^9-THC (1 mg/ml), (-)-Δ^9-THC-d_3 (0.1 mg/ml), (±)-11-OH-THC (1 mg/mL), (±)-11-OH-THC-d_3 (0.1 mg/mL), and cannabidiol (CBD, 1 mg/mL) were purchased as methanol solutions from Millipore-Sigma (St. Louis, MO). Tryptone, yeast extract, isopropyl β- d-1-thiogalactopyranoside (IPTG), phenylmethylsulfonyl fluoride (PMSF), dithiothreitol (DTT), imidazole, sodium dodecyl sulfate (SDS), Pierce bicinchoninic acid (BCA) protein assay, low melt agarose, magnetic silica beads, high-performance liquid chromatography (HPLC) and mass spectrometry (Optima) grade acetonitrile, methanol, water and formic acid were purchased from Thermo Fisher Scientific (Waltham, MA). Lipidex-5000 suspension was purchased from Perkin Elmer Inc (Waltham, MA, USA). Glycine and Mini-PROTEAN TGX protein gels were purchased from Bio-Rad (Hercules, CA).

4.3.2 *Recombinant Enzymes and Human Liver Tissue*

Recombinant CYP1A2, CYP2A6, CYP2B6, CYP2C8, CYP2C9, CYP2C19, CYP2J2, CYP3A4, CYP3A5, CYP3A7 and CYP4F3A Supersomes co-expressed with cytochrome P450 reductase and cytochrome b5 and CYP2D6 co-expressed with cytochrome P450 reductase were purchased from BD Gentest (Franklin Lakes, NJ). Human liver microsomes (HLMs) pooled from 50 different donors were purchased from Gibco (Cat. HMMCPL, Thermo Fisher Scientific, Waltham, MA). Human liver microsomes from individual donors were obtained from the University of Washington (UW) and St. Jude (SJ) human liver banks. A total of 22 human livers from the University of Washington human liver bank were included and one from SJ human liver bank. For the HLMs from the UW liver bank, donors' ages ranged from 7 to 64 years. The demographics of these donors comprised 7 females and 15 males, with 20 being white (non-Hispanic), 1 Asian, and 1 Black or African American. The demographic information for the HLM from the SJ liver bank was not available. Of all donors, the genotype of fourteen were CYP2C9 *1/*1, three were CYP2C9 *1/*2, and six were CYP2C9 *1/*3. Seven donors were CYP3A5 expressors (*1/*3 genotype) and sixteen non expressors (*3/*3 genotype). For CYP2C19, five donors were *1/*1, six *1/*17, seven *1/*2, two *17/*17, and three *1/*17 genotype.

4.3.3 *Incubation Conditions to Identify THC Metabolites Formed in HLMs and Identification of the Recombinant Cytochrome P450 Enzymes that Metabolize THC*

To determine the metabolite profile of THC in human liver and to systematically characterize the CYP enzymes that metabolize THC, THC was incubated with pooled HLMs and a panel of individual recombinant CYPs (CYP1A2, CYP2A6, CYP2B6, CYP2C8, CYP2C9, CYP2C19, CYP2D6, CYP2J2, CYP3A4, CYP3A5, CYP3A7 and CYP4F3A). For metabolite identification, THC-d_3 was also incubated with HLMs and each of the recombinant CYPs using identical methods as THC. Pooled HLMs (0.1 mg/mL) or recombinant CYP enzymes (10 pmol/mL) were preincubated with 10 µM THC for 5 minutes at 37°C in 180 µL incubation buffer (100 mM potassium phosphate, pH 7.4) placed in 1.7 mL Eppendorf tubes. Reactions were initiated with addition of 20 µL NADPH (1 mM final concentration) and incubated at 37°C for 15 min. The reactions were quenched with the addition of 600 µL of acetonitrile with 1% formic acid and 10 nM of 11-OH-THC-d_3 as an internal standard. The samples were then centrifuged at 18,000 g for 20 minutes at 4°C and 200 µL of the supernatant was transferred to a mass spectrometry vial with glass inserts. Samples were analyzed by LC-MS/MS as described in

Section 2.4. The relative formation of metabolites was determined as the ratio of the metabolite peak area to the peak area of the 11-OH-THC-d_3 internal standard. Metabolite peaks below a signal to noise (S/N) of 5 were not quantified. An M4 background peak (S/N ~ 10) was observed in no NADPH and substrate only controls in incubations with HLMs and recombinant CYPs. Therefore, only NADPH dependently formed peaks with S/N > 50 were considered quantifiable for M4 analysis. Metabolite identification incubations were repeated by K.C.B.Y. and K.T.S on separate days, using the same conditions.

4.3.4 *Quantification of THC metabolites by UHPLC-MS/MS*

The concentrations of THC and THC metabolites were analyzed using an AB Sciex API6500 QTRAP mass spectrometer (Framingham, MA) coupled to an Agilent 1290 Infinity II Ultra-High-Performance Liquid Chromatography system (UHPLC, Santa Clara, CA). THC and its metabolites were separated using a Kinetex Evo C18 column (2.1 x 100 mm, 2.6 µM, Phenomenex, Torrance, CA) with the column oven set to 50°C. Mobile phases A and B were composed of water and acetonitrile, respectively, both containing 0.1% formic acid. A gradient elution at a flow rate of 0.25 mL/min was used as follows: mobile phase A was kept at 60% and B at 40% for the first 5 minutes, then B was increased to 100% by 7 minutes, returned to initial conditions by 8 minutes, and the column was re-equilibrated to initial conditions for an additional 4 minutes. THC, THC-d_3, THC metabolites and 11-OH-THC-d_3 were monitored in positive ion mode with electrospray ionization and the MS parameters set as follows: IS 5500 V, TEM 550 °C, CUR 35 p.s.i., GS1 70, GS2 70, CAD medium, DP 35 and 60 (THC metabolites and THC, respectively), EP 4 and 8 (THC metabolites and THC, respectively), CE33 and 29 (THC metabolites and THC, respectively), CXP 10 V. Two multiple reaction monitoring (MRM) transitions (331>193 *m/z* and 331>201 *m/z*) were used to monitor THC metabolites, as previously described for 11-OH-THC (Manuzak *et al.*, 2018). Each metabolite was quantified using the more sensitive transition of the two for the given metabolite. For 11-OH-THC and for M4 metabolites 331>193 *m/z* was used for quantification. The 331>201 *m/z* transition was used to quantify the M1, M2, M2a and M3 metabolites. The MRM transitions used for 11-OH-THC-d_3, THC and THC-d_3 were 334>196 *m/z*, 315>193 *m/z* and 318>196 *m/z*, respectively (Manuzak *et al.*, 2018). A signal to noise cutoff of 5 was used as the lower limit of quantification and the linearity of detector response for M2, M3 and M4 metabolites was verified via analysis of a dilution series of an incubation sample containing high concentrations of the three metabolites.

To identify the oxidation products of THC formed in HLMs and CYP incubations and to gain structural information about the formed metabolites, enhanced product ion (EPI) scans in positive ion mode were performed. The MS/MS spectra of the $[M+H]^+$ ions of the oxidation products, 331 *m/z* for THC incubations and 334 *m/z* for THC-d_3 incubations, were collected within the mass range of 50–340 *m/z*. EPI scan rate was set at 10,000 Da/s, dynamic fill time was used for the linear ion trap, Q1 was set at unit resolution, and Q3 entry barrier was set at 8 V. LC-MS/MS settings and parameters were identical as described above except for the collision energy (CE), which was varied stepwise between 10 and 50 V in increments of 10 V to explore fragmentation patterns. The CE of 40 V was chosen for detailed spectral interpretation due to the fragmentation efficiency of the parent ions 331 *m/z* and 334 *m/z* observed, while still maintaining some detection of the parent ion in the MS/MS spectrum.

4.3.5 *Characterization of CYP2C9, CYP3A and CYP2C19 Activity in the Human Liver Microsome Panel*

The activities of CYP2C9, CYP3A4/5 and CYP2C19 were characterized in the panel of 23 HLMs from individual donors. Tolbutamide (TBU), midazolam (MDZ) and (S)-mephenytoin

(MPH) were chosen as probe substrates for CYP2C9, CYP3A4/5 and CYP2C19 activity, respectively. All HLM experiments were performed in duplicate at 0.1 mg/mL microsomal protein concentration in incubation buffer in 96-well plates and repeated on two separate days by Y.W. After a 5-minute preincubation at 37°C in the presence of substrate, reactions were initiated with NADPH (1 mM final concentration) and allowed to proceed at 37°C in a water bath with a total reaction volume of 100 µL. The substrate concentrations used (10 µM for TBU, 1 µM for MDZ, and 6 µM for MPH) were > 80% lower than the K_ms towards the target CYP (Schmider *et al.*, 1997; Lutz *et al.*, 2013). The incubations were allowed to proceed for 30 minutes [TBU], 4 minutes [MDZ], and 30 minutes [MPH] at 37°C before quenching with an equal volume of acetonitrile containing 1% formic acid and 10 nM internal standard as listed below. The samples were then centrifuged at 3,600 g for 40 minutes at 4°C and 100 µL of the supernatant was transferred to a 96 well MS plate. Samples were analyzed via LC-MS/MS as described below to quantify the formation of 4-OH-TBU from TBU, 1-OH-MDZ from MDZ, and 4-OH-MPH from MPH for CYP2C9, CYP3A and CYP2C19 specific activity, respectively.

The concentrations of 4-OH-TBU and 1-OH-MDZ were analyzed using AB Sciex API5500 and the concentrations of 4-OH-MPH were analyzed using AB Sciex API6500 QTRAP mass spectrometer (Framingham, MA) both coupled to an Agilent 1290 Infinity II Ultra-High-Performance Liquid Chromatography system (UHPLC, Santa Clara, CA). 4-OH-MPH-d_3 was used as the internal standard for 4-OH-TBU and 4-OH-MPH quantification, whereas 1-OH-MDZ-d_4 was used as the internal standard for 1-OH-MDZ quantification. 4-OH-TBU, 1-OH-MDZ and 4-OH-MPH were separated using a Zorbax Eclipse Plus C18 column (2.1 x 50 mm , 5 µM, Agilent Technologies, Santa Clara, CA) with the column oven set to 35°C. Mobile phases A and B consisted of water and acetonitrile, respectively, both containing 0.1% formic acid. A gradient elution at a flow rate of 0.4 mL/min was used as follows: mobile phase A was kept at 95% and B at 5% for the first 0.1 minutes, then B was increased to 70% and 95% by 3.5 and 4.0 minutes respectively, returned to initial conditions by 5 minutes, and the column was re-equilibrated in initial conditions for an additional 1.5 minutes. 4-OH-TBU, 1-OH-MDZ, 1-OH-MDZ-d_4, 4-OH-MPH, and 4-OH-MPH-d_3 were monitored in positive ion mode with electrospray ionization and the MS parameters were set as follows: IS 5000 V, TEM 600 °C, CUR 35 p.s.i., GS1 50, GS2 50, CAD medium, DP 21, 90, 80, 80, and 90 (4-OH-TBU, 4-OH-MPH-d_3, 1-OH-MDZ, 1-OH-MDZ-d_4, and 4-OH-MPH, respectively), EP 14, 5, 10, 10, and 5 (4-OH-TBU, 4-OH-MPH-d_3, 1-OH-MDZ, 1-OH-MDZ-d_4, and 4-OH-MPH, respectively), CE 24, 27, 37, 35, and 27 (4-OH-TBU, 4-OH-MPH-d_3, 1-OH-MDZ, 1-OH-MDZ-d_4, and 4-OH-MPH, respectively), CXP 15, 4, 14, 14, and 4 V (4-OH-TBU, 4-OH-MPH-d_3, 1-OH-MDZ, 1-OH-MDZ-d_4, and 4-OH-MPH, respectively). Five different MRM transitions (287>171 *m/z*, 238>150 *m/z*, 342>203 *m/z*, 346>203 *m/z*, and 235>150 *m/z*) were used to monitor 4-OH-TBU, 4-OH-MPH-d_3, 1-OH-MDZ, 1-OH-MDZ-d_4, and 4-OH-MPH, respectively. A signal-to-noise (S/N) cutoffs of 3 and 5 were used as the lower limit of detection (LLOD) and lower limit of quantification (LLOQ). For signals that were below LLOQ but above LLOD, LLOQ/2 was used as the quantification value for data presentation and statistical analyses. The linearity of detector response for all the metabolites was verified. All analytes were quantified based on a standard curve ranging from 1.56 nM to 200 nM for 4-OH-TBU and 4-OH-MPH quantification, and from 1.56 to 400 nM for 1-OH-MDZ quantification.

4.3.6 *Characterization of THC Metabolism in the Panel of Human Liver Microsomes*

Formation of THC metabolites was characterized in the panel of HLMs from 23 individual liver donors described above. THC (2 µM) was pre-incubated with 0.1 mg/mL HLM for 5 minutes at 37°C in incubation buffer prior to initiating the reactions with 1 mM NADPH (200 µL total reaction volume). Reactions were incubated for 2 minutes at 37°C and quenched with 600 µL of acetonitrile containing 1% formic acid and 10 nM 11-OH-THC-d_3. Quenched reactions were centrifuged and analyzed by LC-MS/MS as described in *Section 2.4*. A small (S/N~5) peak was observed at M4 retention time in no NADPH and no enzyme incubation controls. The area of this peak was integrated and subtracted from the enzymatic formation of M4 in THC incubation samples. All incubations with HLMs were performed under conditions within time linearity for the formation of all THC metabolites. Incubations were repeated by K.C.B.Y and Y.W. on two separate days and done in technical duplicate on each day.

4.3.7 *Correlation of THC Metabolism with Probe Substrates*

To evaluate the relative importance of CYP2C9, CYP3A4 and CYP2C19 in the formation of the individual THC metabolites the correlation between individual metabolite formation and the formation of the probe metabolite was determined. Linear regression and statistical analyses were performed using R statistical computing software (version 4.3.1; R Core Team 2023). Package *tidyverse* was used for data processing*, ggplot2, ggeasy, ggpubr, scatterplot3d, and car* for preparing figures, and Rmarkdown for text. Correlations with *p-values* < 0.01 were considered statistically significant.

Correlations between the specific activity of each CYP (formation of probe metabolite) and 11-OH-THC formation velocity or M2, M3, or M4 relative formation were initially tested using simple linear regression. By both data visualization and based on spearman correlation, CYP2C9 and CYP3A specific activities correlated with each other (rho = 0.8053 and *p-value* = 0.000005). This co-linearity confounds interpretation of individual correlations between CYP specific activity and the metabolite formation using simple linear regression. Thus, multiple regressions were performed using the F-test to detect which CYP isoform activity can best explain the variability seen in the THC metabolite formation across all HLM donors. Variation inflation factors (VIF) for CYP2C9, CYP3A, and CYP2C19 were 4.1, 4.1, and 1.2, signifying moderate correlations (VIF < 5) between CYP2C9 and CYP3A and reasonable inclusions of CYP2C9, CYP3A, and CYP2C19 activities in the multiple regression model (Kim, 2019). Subsequently, CYP2C9, CYP3A, and CYP2C19 activities were adjusted as covariates to determine if any of them were significantly correlated (*p-value* < 0.01) with 11-OH-THC, M2, M3, or M4 formation. To further establish the importance of CYP enzymes that may play a role in THC metabolism and drive inter-individual variability in THC clearance, stepwise linear regressions were performed. One CYP activity was incorporated as a predictor at a time into the linear regression and analysis of variance (ANOVA) was used to compare the calculated F-statistic to the critical value. A *p-value* < 0.01 was used to determine whether inclusion of different CYP predictors improved model fit significantly.

4.3.8 *Impact of Selective CYP Inhibitors on THC Metabolism in Human Liver Microsomes from Individual Donors*

Selective inhibitors were used to determine the contribution of CYP2C9, CYP2C19 and CYP3A4 to the formation of the main THC metabolites detected in HLMs. Individual HLMs from donors with known CYP3A5 genotype were included with n=2 livers with CYP3A5 expression and n=4 that had no CYP3A5. The time dependent (irreversible) inhibitors used were tienilic acid for CYP2C9 and CYP3cide for CYP3A4 (Hutzler *et al.*, 2009; Walsky *et al.*, 2012). (+)-N-3-benzyl-nirvanol (benzylnirvanol) was used as a selective reversible inhibitor for CYP2C19 (Suzuki *et al.*, 2002). CYP inactivation by irreversible inhibitors was achieved by pre-incubating 1 mg/mL total HLM protein with tienilic acid (50 µM) for 30 minutes or CYP3cide

(0.5 µM) for 10 minutes in the presence of 1 mM NADPH in incubation buffer. Ethanol for tienilic acid or methanol for CYP3cide were added instead of inhibitors in pre-incubations for no inhibitor (vehicle) controls. After preincubation, the HLM solution was diluted 40-fold (0.025 mg/mL final HLM protein) in incubation buffer containing 1 mM NADPH in a 1.7 mL Eppendorf tube. THC (2 µM) was then added immediately to initiate reactions (final volume of 200 µL). Reactions were allowed to proceed for 2 minutes prior to quenching with 600 µL of acetonitrile containing 1 % formic acid and 10 nM 11-OH-THC-d_3. Inhibition experiments with benzylnirvanol were performed by co-incubating benzylnirvanol (5 µM) with THC (2 µM) and 0.025 mg/mL total HLM protein in 180 µL incubation buffer in 1.7 mL Eppendorf tubes. Methanol was added instead of benzylnirvanol for no inhibitor (vehicle) controls. Reactions were initiated with 1 mM NADPH (200 µL final volume), were allowed to proceed for 2 minutes and quenched with 600 µL of acetonitrile containing 1 % formic acid and 10 nM 11-OH-THC-d_3. Quenched samples were centrifuged and prepared for LC-MS/MS analysis as described in *Section 2.4*. The % activity remaining was determined by normalizing the relative formation of THC metabolites in the presence of inhibitors to the formation in the absence of inhibitors. Incubations for the six HLMs from different donors were done in duplicate.

4.3.9 *Kinetics of THC Metabolite Formation in Human Liver Microsomes*

The kinetics of 11-OH-THC, M2, M3, and M4 metabolite formation was determined in pooled HLMs with 0.1 mg/mL total microsomal protein using nominal THC concentrations ranging from 0.05-5 µM. The M1 metabolite was detected but below the limit of quantification (signal to noise < 5) in these kinetic experiments. Incubations were done under conditions of time linearity in 200 µL volumes of incubation buffer in 1.7 mL Eppendorf tubes. Reactions were preincubated in a 37°C shaking water bath for 5 minutes before reactions were initiated with 1 mM NADPH. The reactions were incubated for 2 minutes at 37°C before quenching with 600 µL of acetonitrile containing 1% formic acid and 10 nM 11-OH-THC-d_3. Quenched reactions were centrifuged at 18,000 g for 20 minutes and the resulting supernatant was transferred to MS vials for LC-MS/MS analysis as described in *Section 2.4*. The incubations were repeated on three separate days by K.C.B.Y and Y.W. and conducted as technical duplicates on each day. Free concentrations of THC were determined for all nominal THC concentrations used as described in *Section 2.13*. Metabolite formation velocities (absolute velocity for 11-OH-THC formation and relative product formation based on peak area ratio for M2, M3, and M4) were plotted against free THC concentrations to determine the unbound K_m ($K_{m,u}$) and k_{cat}. The Michaelis-Menten equation was fit to the 11-OH-THC, M2 and M3 formation data in HLMs using GraphPad Prism 10. No saturation was observed for M4 formation and hence only the linear portion of metabolite formation data was analyzed. A linear regression model was fit to M4 formation data in GraphPad Prism 10. $K_{m,u}$ and k_{cat} values for 11-OH-THC, M2 and M3 are reported as means ± S.D. from experiments done on three separate days.

4.3.10 *Expression and Purification of Human Recombinant FABP1*

Hexa-histidine-tagged (his-tag) human FABP1 was expressed in Rosetta 2 *E. coli* (Novagen, Madison, WI) and was purified according to a previously published protocol (Yabut *et al.*, 2024). Briefly, his-tagged FABP1 was purified using a HisTrap HP affinity column (GE Healthcare, Chicago, IL). The his-tag was cleaved by thrombin followed by gel filtration with a Superdex 75 (Marlborough, MA) equilibrated with gel filtration buffer (10 mM potassium phosphate pH 7.4, 150 mM KCl). Delipidation was performed on the cleaved FABP1 using multiple rounds of butanol treatment and Lipidex-5000 (Perkin Elmer Inc., Waltham, MA, USA) as previously described (Yabut *et al.*, 2024). The concentration of purified FABP1 was quantified via bicinchoninic acid (BCA) assay (Pierce, Waltham, MA). The final purified FABP1 was stored on ice in gel filtration buffer containing 0.5 mM DTT and used in downstream assays within 4 weeks after purification.

4.3.11 *Characterization of Cannabinoid Binding to Human FABP1 via DAUDA Displacement Assay*

Binding of cannabinoids to FABP1 was determined using fluorescence displacement assay with 11-(dansylamino)undecanoic acid (DAUDA) according to previously published protocols (Yabut *et al.*, 2024). In brief, a solution of 0.5 µM DAUDA pre-bound with 0.3 µM FABP1 was prepared in 2 mL of incubation buffer in a 4 mL quartz cuvette. THC, 11-OH-THC, cannabidiol (CBD), 2-archidonyl glycerol (2-AG) or anandamide (AEA) were titrated into the solution of prebound FABP1 and DAUDA and the fluorescence emission throughout the course of the titration was monitored from 400-700 nm with an excitation wavelength of 335 nm. Fluorescence spectra were collected on a Cary Eclipse fluorescence spectrophotometer (Agilent, Santa Clara, CA) with the scan rate set to medium (600 nm/min) and the photomultiplier tube voltage set to high (800 V). The specific fluorescence of DAUDA bound with FABP1 from titration spectra was determined using singular value decomposition (SVD) as previously described (Yabut *et al.*, 2024). EC_{50} values and binding affinities (K_d) of cannabinoids with FABP1 were determined from the SVD data as previously described using COPASI (Yabut *et al.*, 2024). EC_{50} and K_d values are reported as means (± standard deviation) from replicate experiments done on three separate days and with at least two different batches of purified FABP1 protein.

4.3.12 *THC Incubations with Recombinant CYP2C9, CYP3A4 and CYP2C19 in the Presence and Absence of FABP1*

The kinetics of 11-OH-THC formation by CYP2C9, M2, M3 and M4 metabolite formation by CYP3A4, and 11-OH-THC and M3 formation by CYP2C19 were determined in the presence and absence of FABP1. All incubations were done under conditions of time linearity. The total protein concentrations in the individual Supersomes were quantified via BCA assay as the expression level of each CYP is different when normalized to the total amount of microsomal protein. For experiments with CYP2C9 in the absence of FABP1, 1 nM CYP2C9 (0.0016 mg total microsomal protein/mL) was preincubated with seven different nominal concentrations of THC ranging from 10 to 640 nM for 5 minutes at 37°C in 180 µL incubation buffer in 1.7 mL Eppendorf tubes. Methanol solutions of THC were added to the incubation mixtures and the total solvent volume did not exceed 1% in any of the incubations. Reactions were then initiated with 1 mM NADPH (final concentration) in a final volume of 200 µL. A control reaction with no NADPH was included in all experiments. Reactions were quenched after 1 minute incubation at 37°C with the addition of three incubation volumes (3:1 ratio of organic to aqueous) of acetonitrile containing 1% formic acid and 10 nM 11-OH-THC-d_3. The samples were centrifuged at 18,000 g for 20 minutes and the resulting supernatant was transferred to MS vials for analysis as described in *Section 2.3*. CYP2C19 incubations were performed similarly using 1 nM of CYP2C19 (0.013 mg total microsomal protein/mL) with an incubation time of 2 minutes and nominal THC concentrations ranging from 0.02-1.0 µM. CYP3A4 incubations were also performed as described for CYP2C9 with 0.625 nM CYP3A4 (0.004 mg total microsomal protein/mL) and with seven THC concentrations ranging from 0.156-3.75 µM. Incubations with FABP1 were performed similarly as described above except that 20 µM FABP1 was added to the solutions containing CYP and THC before pre-incubation to achieve binding equilibrium.

Reactions were then initiated with NADPH. Kinetic experiments with and without FABP1 were performed as matched pairs. All incubations were conducted as duplicates per experiment and all experiments repeated on three separate days.

Eadie-Hofstee plots were constructed for all kinetic experiments and based on the Eadie-Hofstee plots the Michaelis-Menten model was fit to the 11-OH-THC formation data by CYP2C9 and CYP2C19, M3 formation data by CYP2C19, and the M2 and M3 formation data by CYP3A4 using GraphPad Prism 10. Based on the concave Eadie-Hofstee plot of M4 formation by CYP3A4, the allosteric sigmoidal model (Equation 4.1) was fit to the data of M4 formation by CYP3A4 in GraphPad Prism 10:

$$relative\ M4\ formation = \frac{Max_{M4} \times [S]^h}{{K_{0.5}}^h + [S]^h} \qquad (4.1)$$

In Equation 4.1, Max_{M4} is the maximum value for the relative formation of M4 in kinetic experiments, [S] is the nominal THC concentration, $\text{K}_{0.5}$ is the concentration of THC as half of Max_{M4}, and h is the hill slope. The unbound K_{m} ($\text{K}_{\text{m,u}}$) and k_{cat} values were determined by fitting the Michaelis-Menten model to the metabolite formation data plotted with free concentrations of THC and determined as described in *Section 2.13*. $\text{K}_{\text{m,u}}$ and k_{cat} values are reported as means ± S.D. from replicate experiments done on separate days. Differences in the $\text{K}_{\text{m,u}}$ for 11-OH-THC and M3 formation by CYP2C19 in the presence and absence of FABP1 were evaluated using a one-tailed Z-test as previously described (Yabut *et. al.*, 2024; Isoherranen *et. al.*, 2003). A simple paired t-test was used to evaluate differences in k_{cat} for 11-OH-THC formation by CYP2C19 the presence and absence of FABP1 and $p < 0.05$ was considered statistically significant.

4.3.13 *Determination of THC Unbound Fraction in Incubations with Recombinant CYPs and in Human Liver Microsomes*

To determine the unbound concentrations of THC in incubations with recombinant CYPs and with HLMs, magnetic silica beads (MGSBs, G-Biosciences, St. Louis, MO) were used to separate microsomal protein (Horspool *et al.*, 2020) from free THC in solution. Initial experiments without microsomal protein present were done to verify that THC did not bind in a non-specific manner to MGSBs. To measure non-specific binding of THC, 500 nM THC was incubated separately with 100 µL of MGSB in 0.5 mL incubation buffer in 1.7 mL Eppendorf tubes for 30 minutes at 37°C. After 30 minutes, 100 µL of the mixture containing MGSBs with THC was collected as the total THC present sample (this was necessary as THC binds extensively to plastic surfaces), then the MGSBs were separated from solution using a DynaMag-2 Magnet (Thermo Fisher Scientific, Waltham, MA) and the supernatant was collected for measurement of free THC in solution. Acetonitrile (300 µL) containing 1% formic acid and 30 nM of THC-d_3 internal standard were added to 100 µL of the total and supernatant samples containing THC. The samples were centrifuged at 18,000 g for 20 minutes and the supernatant was transferred to MS vials for analysis. THC concentrations in the samples were measured via LC-MS/MS using the same method as described in *Section 2.4*.

To determine the free concentrations of THC in incubations with recombinant CYPs and HLMs, 50 µL of MGSBs (5.25×10^9 beads) (Horspool *et al.*, 2020) were used with recombinant CYPs and 200 µL of MGSBs (21×10^9 beads) were used for HLMs. All of these experiments were conducted using identical Eppendorf tubes, protein concentrations and buffers as described for incubations to maintain constant partitioning of THC to nonspecific plastic surfaces. Before the experiment, the beads were washed 3 times with 1 mL of assay buffer and pre-equilibrated with either recombinant CYP or HLM at the above described protein concentrations on ice for 30 minutes in 0.2 mL of incubation buffer for recombinant CYPs and 0.5 mL of incubation buffer for HLMs in 1.7 mL Eppendorf tubes. THC was then added to the mixture of MGSBs containing CYP or HLM protein at THC concentrations corresponding to each of the nominal concentrations used for kinetic experiments. Samples were then incubated for an additional 30 minutes in a shaking water bath at 37°C, then removed from the water bath and cooled at room temperature for 5 minutes. After cooling, 75 µL of the mixture containing the MGSBs, and recombinant CYPs with THC was collected as the total THC sample. The mixture containing the MGSBs and HLMs with THC was collected (100 µL) as the total THC sample for HLMs. The MGSBs were then separated from solution using a DynaMag-2 Magnet and 75 µL of supernatant was collected as the free THC sample for CYP samples and 100 µL was collected for HLM samples. Three sample volumes of acetonitrile containing 1% formic acid and internal standard were added to the total and supernatant samples. The samples were centrifuged as described above and prepared for analysis by LC-MS/MS as described above. THC concentrations were determined via LC-MS/MS as described in *Section 2.4*.

The unbound fraction (f_u) in microsomes was calculated as the ratio of the concentration of drug measured in supernatant (C_{free}) to the concentration of total drug measured prior to magnetic separation (C_{total}):

$$f_u = \frac{C_{free}}{C_{total}} \qquad (4.2)$$

The amount of THC bound to microsomes ($A_{microsome}$) was calculated as the difference between the total amount of drug measured in solution in the presence of MGSBs and the amount of drug measured in the supernatant (amount of drug in the supernatant = concentration in supernatant measured*volume of supernatant):

$$A_{microsome} = A_{total} - A_{supernatant} \quad (4.3)$$

For the experiments containing FABP1, the free and FABP1 bound THC could not be feasibly separated and nonspecific binding of THC to nickel beads prevented use of alternative methods to determine free concentrations of THC in the presence of FABP1. Hence, the concentrations of unbound THC in the presence of 20 µM FABP1 were calculated from Equation 4.4 assuming that the thermodynamic equilibrium between unbound THC in solution and THC bound to microsomes is unaffected by the presence of FABP1:

$$\frac{A_{free}}{A_{microsome}} = \frac{A_{free,FABP1}}{A_{microsome,FABP1}} \qquad (4.4)$$

In Equation 4.4, A_{free} is the amount of unbound THC measured in the absence of FABP1, $A_{microsome}$ is the amount of THC bound to microsomes in the absence of FABP1, $A_{free,FABP1}$ is the amount of unbound THC in the presence of FABP1 and $A_{microsome,FABP1}$ is the amount of THC bound to microsomes as measured in the presence of FABP1. This equation is based on the fact that due to the excessive nonspecific binding of THC to plastics the FABP1 effectively diminishes the amount of THC nonspecifically bound to plastics without affecting the ratio between THC bound to microsomes and free THC in solution at equilibrium. The volumes of microsomes and supernatant solution were assumed to be constant between the experiments. $A_{free,FABP1}$ was calculated based on experimentally determined values of A_{free}, $A_{microsome}$ and $A_{microsome,FABP1}$. The unbound concentration of THC in the presence of FABP1 was then calculated as the $A_{free,FABP1}/V_{incubation.}$ The f_u of THC in the presence of FABP1 was calculated as the ratio of unbound THC to total THC measured prior to magnetic separation. $K_{m,u}$ and k_{cat} values were determined by fitting appropriate kinetic models (Michaelis-Menten or sigmoidal) to metabolite formation data plotted as a function of free concentrations of THC. Similarly, unbound CL_{int} ($CL_{int,u}$) values were determined by fitting a linear regression to metabolite formation data plotted with free concentrations of THC for metabolites for which $K_{m,u}$ and k_{cat} (or maximum relative formation) could not be determined.

4.3.14 *Impact of FABP1 on THC Metabolism in Human Liver Microsomes from Individual Donors*

The impact of FABP1 on THC metabolism was further studied in HLMs from individual donors. THC (2 µM) was preincubated with 0.025 mg/mL HLM protein from 3 individual liver donors in the presence or absence of 20 µM FABP1 in 180 µL of incubation buffer. Reactions were initiated with 1 mM NADPH (200 µL final volume), allowed to proceed for 2 minutes, quenched, centrifuged, and prepared for LC-MS/MS analysis as described in *Section 2.3*. Incubations for all donors were done in technical duplicate on two separate days. Free concentrations of THC in incubations with and without FABP1 were determined as described in *Section 2.13*.

4.4 RESULTS

4.4.1 *11-OH-THC, M2, M3 and M4 are the Major Metabolites of THC Formed in HLMs and by Recombinant CYPs*

Multiple metabolites of THC were identified in HLM incubations and their formation by individual CYP enzymes was defined using recombinant CYPs (Figure 4.1). 11-OH-THC along with three mono-oxidation products (+16 Da) labeled as M2, M3 and M4 were the 4 major metabolites detected in THC incubations in HLMs. Another oxidation product (M1) eluting before M2 was also observed in HLMs but this metabolite was minor compared to the other four metabolites. The M2 and M4 metabolites appeared more abundant in the incubations with pooled HLMs than was 11-OH-THC. This is likely due to the high THC concentration used in these experiments (10 µM), as these metabolites became relatively less abundant than 11-OH-THC when THC concentration was decreased (data not shown). The change in metabolite ratios with substrate concentration suggested that M2 and M4 are formed by a different enzyme in HLMs than 11-OH-THC and that the K_m towards the enzyme forming M2 and M4 is much higher than that towards the predominant CYP forming 11-OH-THC.

The identity of the CYPs forming the individual metabolites detected in pooled HLMs was evaluated using recombinant CYPs. With the exception of CYP2A6 and CYP4F3A, all other CYPs tested metabolized THC, forming several different THC metabolites (Figure 4.1C). Based on incubations with recombinant CYPs, 11-OH-THC was formed by CYP2C9, CYP2C19, CYP2C8, CYP2B6, CYP1A2, CYP2J2 and CYP2D6 (Figure 4.1C). However, the velocity of 11-OH-THC formation (10-12 pmol min^{-1}pmol CYP^{-1}) by CYP2C9 and CYP2C19 was ~3-fold higher than that observed with CYP2D6 and >10-fold higher than that by other CYPs (0.06-0.9 pmol min^{-1}pmol CYP^{-1}) suggesting these other enzymes do not significantly contribute to 11-OH-THC formation. The M2 metabolite was observed in incubations with CYP3A4, CYP3A5, and the fetal liver CYP3A isoform, CYP3A7. M3 was formed by CYP1A2, CYP2C8, CYP2C19, CYP2D6, CYP2J2, CYP3A4, CYP3A5, and CYP3A7. However, based on the absolute peak area ratios per pmol CYP, CYP2C19 and CYP3A5 formed M3 with the greatest velocity followed by CYP3A4 (35% of CYP3A5 velocity). The other enzymes that formed M3 had > 70% lower velocity than CYP3A4 at this substrate concentration. M4 was solely formed by CYP3A4, CYP3A5 and CYP3A7 (Figure 4.1C).

M1 formation was observed in incubations with CYP1A2, CYP2D6, CYP2C8, CYP2J2 and CYP3A5, with M1 appearing as the most abundant metabolite in CYP2D6 and CYP2J2 incubations based on peak areas. However, in comparison to the abundance of the metabolites observed by recombinant CYPs overall, the peak areas for M1 with these enzymes were only ~5% of those observed for 11-OH-THC or M2 and M4 with CYP2C9, CYP2C19 and CYP3A. An oxidation product coeluting with M2 was detected in CYP1A2, CYP2D6, CYP2C8 and CYP2J2 incubations, but this metabolite was subsequently found to have a different fragmentation pattern than M2 (Figure 4.2) and was considered a different metabolite (M2a).

To elucidate the identity of M1-M4 metabolites of THC, MS/MS spectra were collected for each metabolite formed in incubations of THC and THC-d_3 by HLMs and by recombinant CYPs (Figure 4.2). The deuterium labels in THC-d_3 are in the terminal methyl group in the aliphatic side chain and hence provide information for assessment of hydroxylation sites and fragmentation patterns. Several fragments were used to define the oxidation sites in THC. The presence of the 191 *m/z* fragment observed in a metabolite formed from THC corresponding to the 194 *m/z* fragment in a metabolite formed from THC-d_3, is characteristic for a hydroxylation in the aliphatic side chain of THC (Figure 4.2B). Hence M1 and M2a were considered oxidations in the aliphatic side chain. In contrast the 193 *m/z* fragment in the metabolites formed in THC incubations corresponding to the 196 *m/z* fragment in the metabolites formed in THC-d_3 incubations, is indicative of an intact aliphatic side chain and lack of oxidation in the aromatic A-ring (Figure 4.2C). The presence of fragment 257 *m/z* in the metabolites formed in THC incubations, corresponding to 260 *m/z* in the metabolites formed in THC-d_3 incubations, corroborates lack of hydroxylation in the side chain or in the aromatic A-ring (Figure 4.2C). Metabolites containing these fragments were considered hydroxylation products in the cyclohexenyl C- ring. The proposed structures of the major fragments observed in the MS/MS spectra are shown in Figure 4.2B and 4.2C.

Previously, the hydroxylation product formed by CYP2J2 was proposed to be 1’OH-THC (Arnold *et al.*, 2018). The main metabolite formed by CYP2J2 in this investigation was M1, which may be 1’OH-THC. However, the fragmentation observed for M1 was inconclusive for determining the hydroxylation site in the aliphatic side chain. Previous studies have also proposed 3’OH-THC formation in human liver (Yamamoto *et al.*, 1984). The fragmentation observed here for M2a is consistent with 3’OH-THC but similar to M1. The 191 *m/z,* 257 *m/z* and 242 m/z fragments in the MS/MS spectrum of M1 and M2a formed from THC and the 194 *m/z*, 257 *m/z* and 242 m/z fragments in the MS/MS spectrum of M1 and M2a formed from THC-d_3 (Figure 4.2) can all be products of hydroxylation in any of the carbons in the aliphatic side chain (Figure 4.3). Further studies are needed to fully elucidate the exact positions of THC hydroxylation on the aliphatic side chain. Metabolomic studies have in fact proposed hydroxylation on all the carbons in the side chain (Dinis-Oliveira, 2016).

M2, M3 and M4 were tentatively identified as hydroxylations in the C-ring based on the 271 *m/z* fragment and corresponding 274 *m/z* with THC-d_3. These metabolites may be 8-OH-THC or 7-OH-THC (Figure 4.3). In previous studies, two 8-OH-THC metabolites, 8α- and 8β-OH-THC were identified (Bornheim and Correia, 1991) and have been previously shown to be formed by CYP3A4 (Watanabe *et al.*, 2007). If present, the fragmentation pattern of 8α- and 8β-OH-THC would be expected to be close to identical. Indeed, M2 and M3 mass spectra have the same characteristic fragmentation pattern (Figure 4.2) and are formed by CYP3A4. These data suggest that M2 and M3 are likely 8α- and 8β-OH-THC. M4 may represent 7-OH-THC (Figure 4.3). The 7-OH-metabolite has been previously reported for Δ-8-THC (Gurny *et. al.*, 1972). The current data does not exclude the formation of additional hydroxylation products that have not been previously identified. Notably, M3 was also formed by other CYPs not just CYP3A4, showing that more CYPs metabolize THC than previously assumed (Yamamoto *et al.*, 1984; Watanabe *et al.*, 2007).

None of the metabolites detected showed spectral evidence of 9α,10α-THC-epoxide formation, although previous reports have suggested 9α,10α-THC-epoxide is formed by CYP3A4 (Yamamoto *et al.*, 1984; Watanabe *et al.*, 2007). This may be due to the much lower substrate concentrations used in this study than in the previous experiments (Yamamoto *et al.*, 1984; Bornheim *et al.*, 1992; Watanabe *et al.*, 2007). An epoxide metabolite would be expected to fragment differently to the hydroxylation products, and the epoxide would be expected to be present in the MS/MS fragments containing the C-ring (271 *m/z* and 274 *m/z*, Figure 4.2). The presence of the 271 *m/z* and 274 *m/z* in M4 suggests this metabolite is a hydroxylation product rather than an epoxide, possibly the 7-OH-THC even though its late retention time would support a less polar epoxide rather than hydroxylation. In addition, the fragmentation pattern to the 271 *m/z* fragment is not consistent with hydroxylations at the gem-dimethyl group on the pyran B-ring. The expected metabolic sites of the major THC metabolites formed by human liver CYPs are illustrated in Figure 4.3. Based on MS/MS spectral analyses of HLM incubations M2a was absent in the HLM incubations even though it was detected in recombinant CYP incubations.

4.4.2 *THC Metabolite Formation Correlates Strongly with CYP2C9, CYP3A4 and CYP2C19 Activity in Human Liver Microsomes from Individual Donors*

The metabolite formation data in incubations of THC with recombinant CYPs showed that specific CYPs form distinct THC metabolites. To explore the formation of these metabolites and the interindividual variability in THC metabolism, THC metabolism was characterized in a panel of HLMs from individual liver donors with varying CYP2C9, CYP2C19 and CYP3A activity (Figure 4.4). The formation of 11-OH-THC varied by 10.5-fold across the 23 individual

HLMs tested. The formation of M2, M3, and M4 was more variable than 11-OH-THC formation between donors and varied 129-fold, 40-fold, and 112-fold, respectively (Figure 4.4). M2, M3 and M4 formation was detected in all 23 HLM donors. The ratio of M2/M3 varied between livers (mean ± S.D.: 3.7 ± 1.8; range: 0.9 – 6.3) suggesting different enzymes contribute to M2 and M3 formation. In contrast M2/M4 ratio was relatively constant between donors (mean ± S.D.: 3.0 ± 0.6; range: 2.1 – 4.6) suggesting that M2 and M4 are formed by the same enzyme(s).

Based on the data of metabolite formation in individual HLMs together with the information of recombinant CYPs that form the specific metabolites, we hypothesized that 11-OH-THC is formed in HLMs by CYP2C9 and CYP2C19, M2 and M4 are formed by CYP3A4 and CYP3A5, and M3 is formed by CYP2C19 and CYP3A enzymes. This hypothesis was first tested via correlation analysis between the THC metabolite formation and the formation of specific CYP probe metabolites 4-OH-tolbutamide (4-OH-TBU; CYP2C9), 1-OH-midazolam (1-OH-MDZ; CYP3A) and 4-OH-mephenytoin (4-OH-MPH; CYP2C19). Correlation between the formation of THC metabolites and the activity of CYP2C9, CYP3A and CYP2C19 for individual HLMs was examined using simple linear regression (Figure 4.5). 11-OH-THC formation correlated significantly with 4-OH-TBU and 1-OH-MDZ but not 4-OH-MPH formation (Table 4.1). This was surprising as 11-OH-THC formation was not observed with recombinant CYP3A4 (Figure 4.1). We hypothesized that this may be due to a correlation between CYP2C9 and CYP3A4 activity. Indeed, co-linearity of CYP2C9 and CYP3A activity was detected with *p-value* < 0.01. This co-linearity also impacted correlation analyses between M2, M3, and M4 formation and 4-OH-TBU and 1-OH-MDZ formation. Formation of all three THC metabolites correlated with CYP2C9 and CYP3A4 activity (Table 4.1) although recombinant CYP2C9 did not form any of these three metabolites. Only M3 formation correlated significantly with 4-OH-

MPH formation (Table 4.1). To address the co-linearity, multiple linear regression was used to assess which CYP isoform(s) likely explain metabolite formation in the dataset (Table 4.1). In the multiple linear regression analysis, the formation of 11-OH-THC strongly correlated with CYP2C9 activity (*p-value* <0.01). CYP3A activity correlated with M2, M3, and M4 formation (*p-value* <0.01) and CYP2C19 activity correlated with M3 formation (*p-value* <0.01) (Table 4.1).

To further confirm the statistical rigor of the correlation analyses in establishing the relevant CYPs forming the THC metabolites, stepwise linear regression for predictor selection in multiple linear regression models was performed (Table 4.2). The model fit for M3 formation improved significantly when CYP2C19 activity was included in addition to CYP3A activity, suggesting contribution of both CYP3A and CYP2C19 towards M3 formation (*p-value* <0.01). No significant improvement with any other combinations of the three CYPs analyzed was detected for other metabolites in the ANOVA test. Therefore, the correlation analysis suggests that 11-OH-THC is predominantly formed by CYP2C9, M2 and M4 formation is by CYP3A, and M3 formation is dependent on CYP3A and CYP2C19 activities.

4.4.3 *Contribution of CYPs to the Formation of 11-OH-THC, M2, M3 and M4 Varies Between Individual Donors*

In vivo data have suggested that the majority of THC metabolism is mediated by CYP2C9 (Sachse-Seeboth *et al.*, 2009). The metabolite formation data from recombinant CYPs and correlation analysis data in HLMs suggest that CYP2C19 and CYP3A may also contribute to THC metabolism. Therefore, the contribution of CYP2C9, CYP3A4 and CYP2C19 to the formation of THC metabolites in HLMs from six different donors was determined using selective inhibitors of CYP2C9 (tienilic acid), CYP3A4 (CYP3cide) and CYP2C19 ((+)-N-3-

benzylnirvanol) (Figure 4.6). To assess the relative role of CYP3A5 in THC metabolites two CYP3A5 expressing donors were included in the inhibition studies. CYP3cide only inhibits CYP3A4 and not CYP3A5 and hence % inhibition by CYP3cide can be interpreted as the fractional formation of the metabolite by CYP3A4 specifically.

Tienilic acid inhibited 65-78% of 11-OH-THC formation in the six donor HLMs (Figure 4.6A), supporting the predominant role of CYP2C9. CYP3cide had little to no impact on 11-OH-THC formation (0-12% inhibition). Benzylnirvanol inhibited 11-OH-THC formation by up to ~17% in donors. The greatest percent inhibition by benzylnirvanol was observed in donors with high CYP2C19 activity. The tienilic acid inhibition was also the weakest in these donors with high CYP2C19 activity (HL-105 and HL-114) supporting a role of CYP2C19 in THC clearance in individuals with either low CYP2C9 activity/expression or high CYP2C19 activity.

Tienilic acid had no effect on M2, M3 and M4 formation (Figure 4.6B-D), a finding consistent with the lack of formation of these metabolites by recombinant CYP2C9. Inactivation of CYP3A4 by CYP3cide inhibited the majority of M2 (57-90%) and M4 formation (63-96%) in all six donors supporting the major role of CYP3A4 in formation of these THC metabolites. The extent of inhibition of M4 formation by CYP3cide was greater in HLMs with no CYP3A5 expression compared to HLMs with CYP3A5 expression (Figure 4.6D) consistent with specific inhibition of CYP3A4 by CYP3cide and contribution of CYP3A5 to M4 formation when expressed.

Benzylnirvanol inhibited M3 formation by up to 67 % but did not inhibit M2 and M4 formation (Figure 4.6C). In one donor who had low CYP2C19 activity, high CYP3A activity and did not express CYP3A5 (HL-109), benzylnirvanol had no impact on M3 formation and CYP3cide inhibited nearly 100% of M3 formation in this donor. In the other three HLMs that had no CYP3A5 expression, benzylnirvanol inhibited 67, 66 and 22% of M3 formation and inhibition by CYP3cide accounted for the remaining M3 formation in the same livers (28, 39, and 81 %). These data suggest that CYP3A4 and CYP2C19 are the only contributors to M3 formation in the absence of CYP3A5 expression. In contrast, total M3 formation in livers expressing CYP3A5 could not be completely accounted for by CYP3cide and benzylnirvanol inhibition suggesting that CYP3A5 also contributes to M3 formation when expressed.

Taken together, the inhibitor studies are consistent with CYP2C9 being responsible for forming 11-OH-THC, CYP3A contributing to the majority of M2 and M4 formation, and CYP3A and CYP2C19 both contributing to M3 formation. These data also show that the contributions by CYP2C9, CYP3A4, CYP3A5 and CYP2C19 toward THC metabolism vary considerably between individuals based on specific CYP activity. The genetic background of individuals relating to these enzymes may have an impact on the metabolism and clearance of THC.

The relative contribution of individual enzymes to substrate metabolism can be dependent on the substrate concentration if multiple enzymes contribute to the formation of the metabolite, and if the K_m values for the enzymes are sufficiently different. The contribution of multiple enzymes can also be apparent in biphasic Eadie-Hofstee plots. To further explore the kinetics of THC metabolism in HLMs and to determine the potential dependence of the relative contribution of individual enzymes on THC concentration, the formation kinetics of 11-OH-THC, M2, M3 and M4 were characterized in pooled HLMs (Figure 4.7, Table 4.3). The unbound fraction (f_u) of THC measured for each nominal concentration of THC used in kinetic experiments was 0.015 ± 0.001 and did not change within the range of THC concentrations used. The $K_{m,u}$ for 11-OH-THC formation was 1.4 ± 0.2 nM and resulted in a linear Eadie-Hofstee plot

(Figure 4.7A). This result is consistent with the inhibition data in HLMs from individual donors showing that CYP2C9 is likely the major contributor to 11-OH-THC formation. The formation kinetics for M2, M3 and M4 formation were different from each other suggesting different CYPs contribute to the formation of these metabolites in the pooled HLMs. The $K_{m,u}$ values for M2, M3 and M4 formation were > 10-fold higher than the $K_{m,u}$ for 11-OH-THC. Based on model fits, the $K_{m,u}$ values for M2 and M3 were > 45 nM. Eadie-Hofstee plots were non-linear for M2 and M3 formation (Figure 4.7B and 4.7C) suggesting that multiple enzymes contribute to M2 and M3 formation in HLMs. This result was consistent with both CYP3A4 and CYP3A5 contributing to M2 formation and CYP3A and CYP2C19 contributing to M3 formation.

M4 formation was linear within the range of THC concentrations tested suggesting that the $K_{m,u}$ for M4 formation is >> 45 nM (Figure 4.7D). As CYP3cide inhibited nearly all of M4 formation in all the individual livers, the $K_{m,u}$ of M4 formation likely reflects the $K_{m,u}$ of THC with CYP3A4. The kinetic data in HLMs suggested the $K_{m,u}$ for CYP3A4 is greater than the $K_{m,u}$ of CYP2C9 and CYP2C19. Therefore, *in vivo* CYP3A4 contribution to THC metabolism will likely be greater with higher circulating concentrations of THC and after oral dosing in the gut where local THC concentrations are expected to be high.

4.4.4 *THC and 11-OH-THC Bind to Human Liver Fatty Acid Binding Protein (FABP1)*

Previous reports have shown that THC binds to the liver fatty acid binding protein (FABP1) (Elmes *et al.*, 2019) and that FABP1 alters substrate metabolism by recombinant CYP2C9 (Yabut *et al.*, 2024). Hence, we hypothesized that FABP1 binding of cannabinoids may alter their metabolism by CYPs. To test this hypothesis recombinant FABP1 was expressed and purified, and binding of the key cannabinoids THC, 11-OH-THC, CBD, 2AG and AEA to FABP1 was characterized prior to testing the impact of FABP1 on THC metabolism by CYPs.

None of the cannabinoids tested fully diminished the specific fluorescence of DAUDA bound to FABP1 when cannabinoid binding was saturated in DAUDA displacement assays (E_{min} = 34-77 %) (Figure 4.8, Table 4.4). In addition, the fluorescence spectra for all cannabinoids tested were blue-shifted relative to the spectrum of DAUDA in solution (Figure 4.8). These results suggest that cannabinoids do not fully displace DAUDA from FABP1 but rather that cannabinoids form ternary complexes with FABP1 and DAUDA. Similar findings were previously reported for other drug ligands of human FABP1 (Yabut *et al.*, 2024). Based on these results, the binding affinities (K_d) of cannabinoids were determined by fitting a ternary complex binding model to fluorescence data from DAUDA displacement assays. All cannabinoids bound to FABP1 with sub-micromolar binding affinities (Table 4.4). Given the high expression of FABP1 in the liver (0.7-1 mM) (Schroeder *et al.*, 2016; Yabut and Isoherranen, 2023), these data suggest that the pharmacologically active cannabinoids THC, 11-OH-THC and CBD are likely bound to FABP1 in the liver *in vivo.* These findings also suggest that THC, 11-OH-THC and CBD may form ternary complexes with endocannabinoids or other fatty acids and FABP1 that may impact endocannabinoid signaling and metabolism.

4.4.5 *FABP1 Alters the Kinetics of THC Metabolite Formation by CYP2C9, CYP3A4 and CYP2C19*

To determine if THC binding to FABP1 would impact metabolism of THC by CYP enzymes, THC metabolite formation kinetics by recombinant CYP2C9, CYP3A4 and CYP2C19 was characterized in the presence and absence of 20 µM FABP1 (Figure 4.9). Free concentrations of THC were determined with and without FABP1 present using magnetic silica beads as described in Materials and Methods Section 4.3.13. $K_{m,u}$ and k_{cat} values determined using free THC concentrations as measured are summarized in Table 4.5. In the absence of

FABP1, the f_u of THC was 0.42 ± 0.04 with CYP2C9, 0.15 ± 0.02 with CYP3A4 and 0.07 ± 0.01 with CYP2C19 and unchanged across THC concentrations used (Figure 4.9G-I). However, f_u decreased with increasing concentrations of total microsomal protein. The microsomal protein content in the incubations was 0.0016 mg/mL for CYP2C9, 0.004 mg/mL for CYP3A4 and 0.013 mg/mL for CYP2C19. As such the highest f_u was observed with the CYP with the highest recombinant expression level per mg microsomal protein and lowest total microsomal protein content in the incubations.

In the absence of FABP1 the $K_{m,u}$ for 11-OH-THC formation by CYP2C9 (0.8 nM) was lower than the $K_{m,u}$ for 11-OH-THC (2.2 nM) and M3 (2.2 nM) formation by CYP2C19. The k_{cat} values for 11-OH-THC formation by CYP2C9 and CYP2C19 were comparable (12 and 14 min^{-1}, respectively) (Table 4.5). Surprisingly, M4 formation by CYP3A4 was allosteric while the formation of M2 and M3 was not (Figure 4.9). The $K_{m,u}$ values for M2 and M3 formation, and the $K_{0.5,u}$ for M4 formation by CYP3A4 (29 ± 19, 18 ± 13 and 43 ± 25 nM, respectively) were over 8-fold greater than $K_{m,u}$ values determined for either CYP2C9 or CYP2C19. The k_{cat} for M2, M3 and M4 formation by any of the CYPs could not be determined due to the lack of available reference standards for these metabolites.

FABP1 had a considerable effect on THC metabolism by all three CYPs although the impact differed between the three CYPs. The f_u values for THC in the presence of FABP1 were 0.08 ± 0.02 with CYP2C9, 0.02 ± 0.01 with CYP3A4 and 0.01 ± 0.01 with CYP2C19 and lower than those measured (0.07-0.42) in the absence of FABP1 (Figure 4.9G-I). This is consistent with THC binding to FABP1. The f_u was not THC concentration dependent across the THC concentrations used. The $K_{m,u}$ and k_{cat} could not be estimated for THC metabolism with CYP2C9 and CYP3A4 in the presence of FABP1 due to the significant decrease in metabolite formation

(Figure 4.9A and 4.9D-F). FABP1 had no significant effect on the $K_{m,u}$ of 11-OH-THC ($p = 0.14$, 0.04, 0.05 for replicate experiments done on separate days) or M3 ($p = 0.32$, 0.07, 0.09 for replicate experiments done on separate days) formation by CYP2C19 (Table 4.5). The k_{cat} for 11-OH-THC formation by CYP2C19 decreased in the presence of FABP1 (8.0 ± 2.0 min^{-1}) compared to the k_{cat} in the absence of FABP1 (14.0 ± 0.7 min^{-1}), however, this decrease was not statistically significant ($p = 0.06$).

4.4.6 *FABP1 Decreases THC Metabolism in Human Liver Microsomes Altering Relative Contributions of CYP Enzymes to THC Metabolism*

Data with recombinant CYPs suggests that FABP1 impacts THC metabolite formation by CYP2C9, CYP3A4 and CYP2C19 and that the effects are enzyme specific. We hypothesized that the effects of FABP1 on THC metabolism in recombinant systems will translate to altered THC metabolite formation in HLMs when FABP1 is present. To determine how FABP1 affects THC metabolism by CYP2C9, CYP3A4 and CYP2C19, incubations were done with HLMs from three donors (non-CYP3A5 expressors) in the presence and absence of 20 µM FABP1 (Figure 4.10). The formation of M2 and M4 metabolites was decreased by 65-75 % and 76-85%, respectively, in the presence of FABP1. This is consistent with the significant decrease in the formation of these metabolites by recombinant CYP3A4 in the presence of FABP1. The decrease in the formation of the M3 metabolite was smaller 49-68%. This was surprising, as with the recombinant CYP3A4, M3 formation was completely abolished in the presence of FABP1. This suggests that in the presence of FABP1 CYP2C19 is the predominant enzyme forming M3, as CYP2C19 still formed this metabolite in the presence of FABP1. Surprisingly, there was little to no effect on the formation of 11-OH-THC in the three donor HLMs (0-9%) in the presence of FABP1. To determine if free drug hypothesis could explain these results, free concentrations of

THC were measured in the incubations in the presence and absence of FABP1. Based on these measurements, FABP1 decreased the free concentrations of THC in incubations with FABP1 by 86 % compared to incubations in the absence of FABP1 (2 vs 14 nM free THC in the presence and absence of FABP1, respectively) confirming THC binding to FABP1 in HLM incubations.

4.5 DISCUSSION

THC is cleared in humans mainly by metabolism with less than 1% of dose recovered unchanged in urine and feces after iv administration of THC (Hunt and Jones, 1980). The metabolic clearance of THC is high, with the hepatic extraction ratio around 0.8 despite the high plasma protein binding (f_u= 0.01) and low blood to plasma ratio (0.67) (Giroud *et al.*, 2001). The high metabolic clearance leads to poor oral bioavailability of THC (<20%) (Huestis, 2005). Yet, the exact contribution of CYPs to THC metabolism in the liver and in the gut mucosa upon first pass remains uncertain. The increase in THC AUC following oral administration of THC to individuals with CYP2C9 poor metabolizer genotype suggested that CYP2C9 contribution to THC oral clearance is ~70%. Similarly, following administration of THC oromucosal spray, inhibition of CYP3A4 by ketoconazole led to nearly two-fold increase in THC AUC (Stott *et al.*, 2013) suggesting that CYP3A4 may contribute to THC metabolism *in vivo*. Surprisingly, no CYP3A4 contribution to THC depletion in *in vitro* metabolic studies was detected (Patilea-Vrana *et al.*, 2019) and instead, in human liver microsomes, CYP2C9 was estimated to contribute to > 90% of THC clearance with a minor contribution from CYP2D6 (Patilea-Vrana and Unadkat, 2019). This is despite previous identification of metabolites of THC formed by CYP3A4 (Yamamoto *et al.*, 1984; Watanabe *et al.*, 2007) and depletion of THC by recombinant CYP3A4, CYP2C19 and CYP1A1 (Patilea-Vrana *et al.*, 2019). Taken together, these discrepancies highlight remaining gaps in the understanding of THC metabolism by specific CYPs and the need for systematic evaluation of the metabolites formed by CYPs in the human liver and intestines.

The primary metabolite of THC detected *in vivo* is 11-OH-THC (Lemberger, Louis *et al.*, 1972; Huestis, 2005). 11-OH-THC has been shown to be formed by CYP2C9, CYP2C19, CYP1A2 and CYP2D6 (Watanabe *et al.*, 2007; Patilea-Vrana *et al.*, 2019). The data shown here agrees with the prior work on 11-OH-THC formation (Figure 4.1). However, our data also show that the intrinsic clearance of 11-OH-THC formation by CYP2C9 (CL_{int} = 13.9 $mL \cdot min^{-1} \cdot pmol\ P450^{-1}$) is ~3-fold higher than that by CYP2C19 (CL_{int} = 4.7 $mL \cdot min^{-1} \cdot pmol\ P450^{-1}$), and that the formation of 11-OH-THC by CYP2D6 and CYP1A2 is minor compared to CYP2C9. Notably, CYP2C9 did not form any other oxidation products from THC except 11-OH-THC while, in pooled HLMs, four other metabolites were formed (Figure 4.1). This clearly indicates that multiple CYPs in the HLMs oxidize THC. Of the four metabolites designated as M1 through M4, M2, M3 and M4 were relatively major products while M1 was minor in comparison in pooled HLMs and not detected in individual HLMs. The metabolite profile and metabolite ratios of THC also showed large variability across the 23 donor HLMs tested. The variation in the ratio of M2-M4 to 11-OH-THC between individuals strongly suggests that multiple enzymes, likely CYP2C9, CYP2C19 and CYP3A are responsible for THC metabolism in human liver.

The detection of the additional oxidation products is consistent with early studies that observed multiple oxidation products of THC using TLC and identified these metabolites as 11-OH-THC, 8α/β-OH-THC, 9α,10α-THC-epoxide and 3’OH-THC in HLMs from a single Japanese male donor (Yamamoto *et al.*, 1984). More recently, 1’OH-THC instead of 3’OH-THC was reported as a THC metabolite formed by CYP2J2 (Arnold *et al.*, 2018). The data shown here supports multiple metabolites (M1 and M2a) resulting from hydroxylation of the aliphatic side chain, but the oxidation site in the side chain is inconclusive. The data here also suggest that M2 and M3 are 8α- and 8β-OH-THC and are not the sole hydroxylation products formed by CYPs, in addition to 11-OH-THC. Instead, the data suggest that M4 is likely 7-OH-THC and is also formed by human liver CYPs. Notably, M3 was also efficiently formed by CYP2C19, a finding that has not been previously reported (Yamamoto *et al.*, 1984; Watanabe *et al.*, 2007). Overall, these data show that THC metabolism in the human liver is more complex than suggested by analysis of 11-OH-THC formation alone and multiple CYPs contribute to THC oxidation in the human liver. Whether these metabolites identified are present *in vivo* in humans is currently unknown.

All the data collected in HLMs support the conclusion that CYP2C9, CYP3A4 and CYP2C19 contribute to THC metabolism in HLMs with enzyme specific contributions to each detected metabolite. The data presented here are consistent with previous *in vitro* work showing that CYP2C9 is the major contributor to 11-OH-THC formation (Watanabe *et al.*, 1995, 2007; Patilea-Vrana *et al.*, 2019). CYP2C9 activity correlated significantly with 11-OH-THC formation although stepwise regression analysis showed a trend towards better correlation when CYP2C19 activity was added. In agreement with these findings, formation of 11-OH-THC was inhibited by > 80% with tienilic acid, a selective irreversible inhibitor of CYP2C9, but was largely unaffected by (+)-N-3-benzylnirvanol, a selective inhibitor of CYP2C19. CYP2C9 has ~3-fold greater CL_{int} than CYP2C19 towards 11-OH-THC formation and the expression level of CYP2C9 is ~15-fold greater in human liver than CYP2C19 (Nakamura *et al.*, 2016). These two findings explain the dominant role of CYP2C9 in 11-OH-THC formation. CYP2C19 may, however, be important in 11-OH-THC formation if CYP2C9 activity is impaired by genetic polymorphisms or if CYP2C19 activity is high as seen in two donors here in whom (+)-N-3-benzylnirvanol inhibited portion of 11-OH-THC formation (Figure 4.6).

These data support a role for CYP3A4 in forming the cyclohexenyl hydroxylated metabolites M2, M3 and M4. This is in agreement with previous findings of the role of CYP3A4 in THC metabolism (Yamamoto *et al.*, 1984; Watanabe *et al.*, 2007). The formation of M2 and M4 in donor HLMs correlated strongly with CYP3A activity suggesting that CYP3A enzymes are the predominant enzymes forming these two metabolites. The inhibition of M2 formation by CYP3cide in HLM donors that did not express CYP3A5 was however less efficient than the inhibition of M4 (Figure 4.6). This indicates possible other enzyme contributions to M2 formation. CYP3cide inhibited nearly 100% of M4 formation in donors without CYP3A5 expression consistent with this metabolite being CYP3A specific. However, CYP3A5, when expressed, likely is important in formation of the M2-M4 metabolites of THC.

The data shown suggests that in addition to CYP3A4, CYP2C19 plays an important role in M3 formation. The correlation of M3 formation was improved when both CYP3A and CYP2C19 activities were included as predictors in multiple linear regression analysis compared to CYP3A activity alone. The CYP2C19 inhibitor (+)-N-3-benzylnirvanol inhibited up to 67 % of M3 formation in high CYP2C19 activity donors. To our knowledge, this is the first evidence reported for the contribution of CYP2C19 to the formation of THC metabolites formed in human liver other than 11-OH-THC.

The relative contribution of CYP3A4 to M3 formation and the overall contribution of individual enzymes to THC clearance are likely concentration dependent. The $K_{m,u}$ for CYP3A4 is > 10-fold higher than the $K_{m,u}$ for CYP2C9 and CYP2C19 suggesting that CYP3A4 will likely have greater contribution to THC metabolism at higher concentrations of THC. Overall, in heavy cannabis users who may have free THC plasma concentrations that saturate CYP2C9 (> 2 nM) the contribution of CYP3A and CYP2C19 to THC clearance is expected to be higher than in individuals with lower THC concentrations. CYP3A enzymes are also expected to be particularly important following oral consumption of cannabis/THC due to the high expression of CYP3A in the gut. Similarly, these data predict that in individuals with CYP2C9 polymorphisms THC will be cleared mainly by CYP3A and CYP2C19. This is important in the context of drug-drug interactions as one may expect that CYP3A and CYP2C19 inhibitors will result in decreased clearance of THC. These data suggest that CYP3A4 contribution may also be a major metabolic pathway for individuals with high CYP3A activity such as following administration of CYP3A inducers. Indeed, this aligns with *in vivo* findings that co-administration of rifampicin, an inducer of CYP3A, decreases THC exposure following oral dosing of THC (Stott *et al.*, 2013). Similarly, co-administration of ketoconazole, an inhibitor or CYP3A, with THC increases the exposure to THC (Stott *et al.*, 2013).

The finding of contributions of CYP3A4 and CYP2C19 to THC clearance is in contrast to previous *in vitro* work (Patilea-Vrana *et al.*, 2019). This discrepancy may be due to the presence of 0.2% BSA in previously reported incubations with HLMs to address non-specific binding of THC. BSA has been shown to increase CYP2C9 activity in HLMs (Zhou *et al.*, 2004; Rowland *et al.*, 2008) and to inhibit CYP2C19 (Kandel and Lampe, 2014). Whether BSA also alters CYP3A4 activity in HLMs is not known. However, BSA may have artificially increased the contribution of CYP2C9 to THC metabolism and 11-hydroxylation in particular. Although human serum albumin may be present in hepatocytes *in vivo* (Kandel and Lampe, 2014), its impact on CYP mediated metabolism is likely minor *in vivo*. In contrast, FABP1 is likely to play an important role in modulating drug metabolism in human liver due to its high expression in the liver. THC and 11-OH-THC as well as the endocannabinoids AEA and 2AG were found to bind to FABP1 using fluorescence DAUDA displacement assay and singular value decomposition (SVD) analysis. The binding affinities (K_d) for THC and 11-OH-THC with human FABP1 (0.3 and 0.9 µM, respectively) determined here are lower than previously reported (2.9 and 7.1 µM, respectively) (Elmes *et al.*, 2019). The differences in the K_d values are likely due to the more rigorous analysis of FABP1-DAUDA fluorescence by SVD and more appropriate model fitting based on ternary FABP1-DAUDA-THC complex formation than what was previously reported. Based on these data and the high abundance of FABP1 in the liver, THC and 11-OH-THC are likely bound to FABP1 in the liver *in vivo*. However, as FABP1 can bind multiple ligands simultaneously, it is possible that THC binds to FABP1 in the liver together with endocannabinoids or other fatty acids. How such ternary binding complexes alter THC and endocannabinoid metabolism requires further study.

FABP1 had a substantial effect on THC metabolism by recombinant CYP2C9, CYP2C19 and CYP3A4. Although $K_{m,u}$ and k_{cat} values for 11-OH-THC, M2, M3 and M4 formation by different CYPs could not be completely characterized due to the substantial impact of FABP1 on the formation of these metabolites, the data here suggests that FABP1 decreased the intrinsic clearance of THC metabolism by recombinant CYPs. This appeared to be largely due to a decrease in the k_{cat} by each CYP although FABP1 binding also decreased free concentrations of THC in incubations with recombinant CYPs and in HLMs consistent with the tight binding of THC to FABP1. The decrease in k_{cat} is likely due to a direct protein-protein interaction between FABP1 and CYPs. FABP1 has been shown to directly interact with other metabolic enzymes to modulate enzyme activity. However, direct protein-protein interactions between FABP1 and carnitine palmitoyl transferase I (CPTI) enhance CPTI activity toward acyl-CoA (Hostetler *et al.*,

2011) rather than decrease the activity. The results here with CYP2C9 align with the finding that FABP1 decreases the k_{cat} of the metabolism of diclofenac by CYP2C9 (Yabut *et al.*, 2024). The mechanisms of FABP1-CYP interactions require further study to fully elucidate enzyme specific interactions and the mechanisms of protein-protein interactions.

The impact of FABP1 on THC metabolism in recombinant CYPs translated to enzyme specific effects of FABP1 on THC metabolism in HLMs (Figure 4.10). However, the impact of FABP1 on THC metabolism in HLMs could partially be explained by FABP1 functioning as a binding sink of THC and altering the free concentrations of THC in the incubations. The decrease in the formation of M2 and M4 metabolites in the presence of FABP corresponded with the decrease in free THC in the incubations. The impact of FABP1 on M3 formation was not as large as the impact on M2 and M4, consistent with the contribution of CYP2C19 toward M3 formation and suggesting that CYP2C19 activity is increased in the presence of FABP1. The lack of decrease in 11-OH-THC formation in the presence of FABP1 was unexpected and suggests that in HLMs FABP1 may in fact activate CYP2C9 rather than decrease the k_{cat}. While the mechanisms of these effects are currently unknown and require further study, collectively, these data suggest that the presence of FABP1 alters CYP activity and modulates the relative contribution of individual CYPs to substrate clearance. FABP1 appeared to have the largest impact on CYP3A4 activity likely leading to an increase in the relative contribution of CYP2C9 and CYP2C19 to THC clearance in vivo.

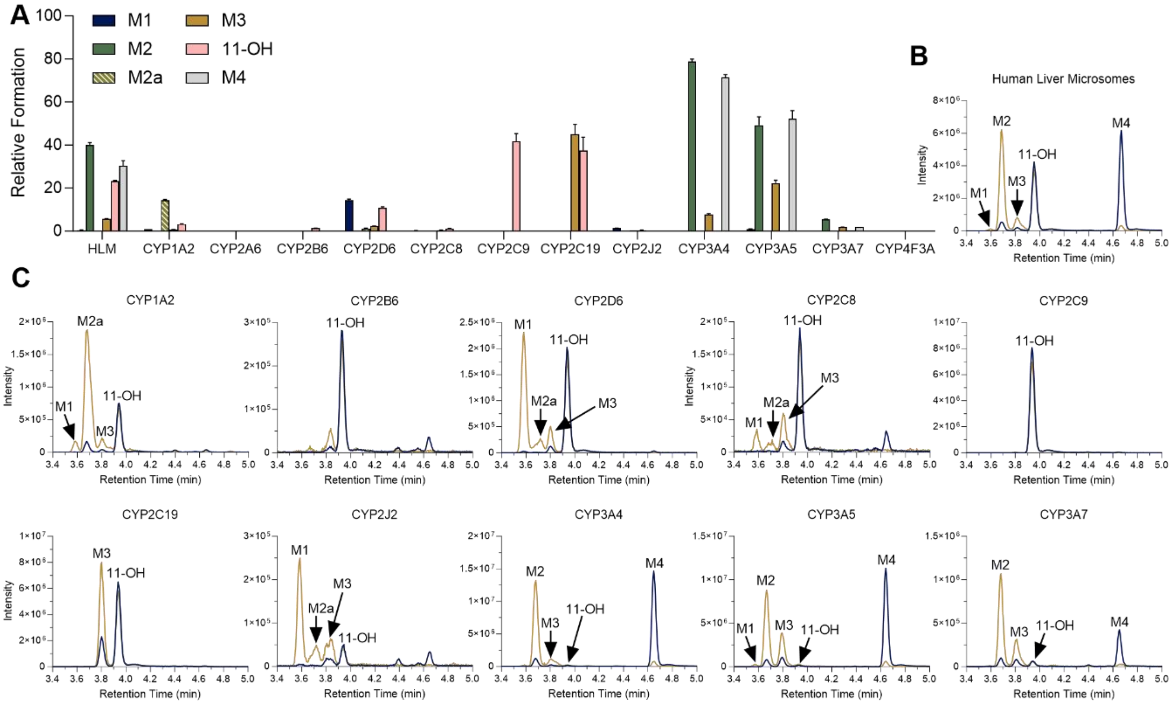

Figure 4.1. Characterization of THC metabolism by human liver microsomes (HLMs) and recombinant cytochrome P450 (CYP) enzymes.

Pooled human HLMs and by recombinant CYPs were incubated with THC (10 µM) and the formation of primary single oxidation products of THC (+16 Da of THC parent mass) was monitored using LC-MS/MS. THC concentration of 10 µM was chosen to ensure that all potential metabolites formed could be detected. (**A**) The formation of THC metabolites in incubations with HLMs and CYPs is shown for a representative experiment. Relative formation is reported as the absolute peak area for each metabolite as normalized to the internal standard 11OH-THC-d_3 (**B**) Selected ion chromatograms (dark blue 331>193 *m/z*, gold 331>201 *m/z*) for detection of THC metabolites M1, M2, M3, 11-OH-THC and M4 identified in HLMs. (**C**) Selected ion chromatograms (dark blue 331>193 *m/z*, gold 331>201 *m/z*) depicting the metabolite formation by recombinant cytochrome P450 enzymes that metabolized THC. For each panel, chromatograms are scaled to the largest peak observed in the sample.

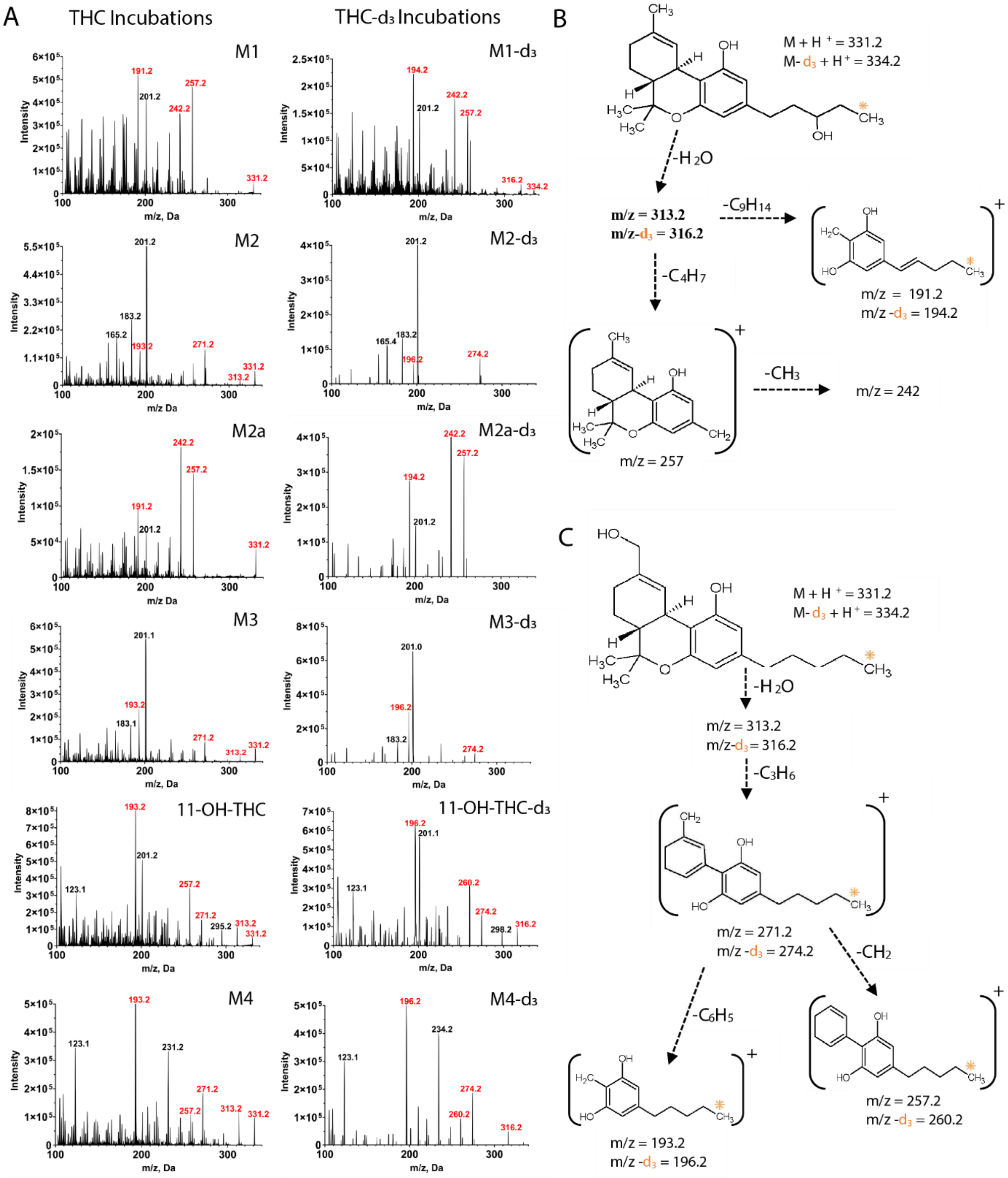

A
THC Incubations
THC-d3 Incubations
M1
M1-d3
M2
M2-d3
M2a
M2a-d3
M3
M3-d3
11-OH-THC
11-OH-THC-d3
M4
M4-d3
Intensity
m/z, Da
191.2
201.2
257.2
242.2
331.2
194.2
316.2
334.2
183.2
165.2
193.2
271.2
313.2
165.4
196.2
274.2
201.1
183.1
201.0
123.1
295.2
260.2
298.2
231.2
234.2
B
M + H + = 331.2
M- d3 + H + = 334.2
-H2O
m/z = 313.2
m/z-d3 = 316.2
-C9H14
m/z = 191.2
m/z -d3 = 194.2
-C4H7
m/z = 257
-CH3
m/z = 242
C
M + H + = 331.2
M- d3 + H + = 334.2
-H2O
m/z = 313.2
m/z-d3 = 316.2
-C3H6
m/z = 271.2
m/z -d3 = 274.2
-CH2
-C6H5
m/z = 193.2
m/z -d3 = 196.2
m/z = 257.2
m/z -d3 = 260.2

Figure 4.2. MS/MS spectra and proposed fragmentation of THC metabolites formed from THC and THC-d_3 in human liver microsome (HLMs) and recombinant cytochrome P450 (CYP) incubations.
(**A**) Enhanced product ion (MS/MS) spectra are shown for the six specific metabolites detected. The representative spectra are from incubations with CYP2D6 (M1), CYP3A4 (M2), CYP1A2 (M2a) CYP2C19 (M3), CYP2C9 (11-OH-THC) and CYP3A4 (M4). (**B**) Proposed fragmentation and fragment structures for THC and THC-d_3 metabolites hydroxylated on the aliphatic side chain using 3'OH-THC as an example. (**C**) Proposed fragmentation and fragment structures for THC and THC-d_3 metabolites hydroxylated on the cyclohexenyl C-ring using 11-OH-THC as an example. Masses in the spectra that correspond to the proposed fragmentation structures are labeled in red. Asterisks indicate the location of deuterium (d_3) labels on the metabolites and MS/MS fragments. Figure courtesy of Keiann Simon.

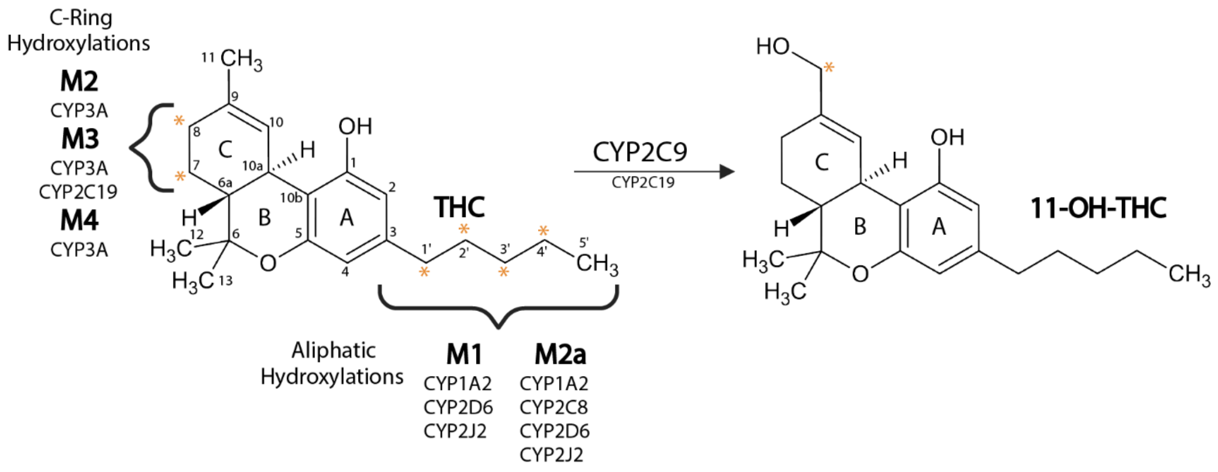

Figure 4.3. Proposed structures and sites of oxidation in THC by human liver cytochrome P450 (CYP) enzymes and main CYPs that form the individual metabolites.
The location of putative hydroxylation sites are indicated by asterisk for the primary THC metabolites formed in HLMs. M2, M3 and M4 metabolites are hydroxylated in the cyclohexenyl C-ring. M1 and M2a metabolites are hydroxylated at the aliphatic side chain. The major CYPs that contribute to the formation of each metabolite are listed. Figure created with Biorender.com.

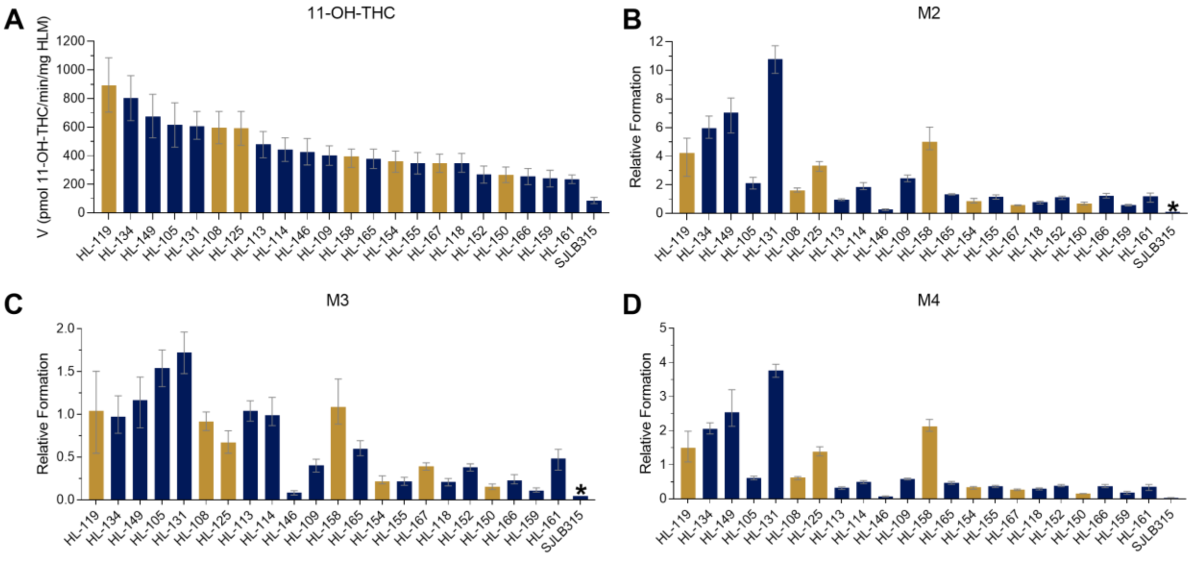

Figure 4.4. Characterization of THC metabolite formation and interindividual variability in THC metabolism in a panel of individual human livers.

The formation of (**A**) 11-OH-THC, (**B**) M2, (**C**) M3 and (**D**) M4 metabolites in HLMs from 23 individual donors is shown in incubations with THC (2 µM). THC concentration of 2 µM was chosen to capture formation of all four metabolites at a THC concentration reflecting C_{max} concentrations in heavy cannabis users. Gold bars indicate livers that express CYP3A5 while blue bars are HLMs without CYP3A5 expression. The mean value of replicate experiments each done in duplicate is shown for each donor. Asterisks indicate metabolite formation below limit of quantification for at least one technical replicate within the data set.

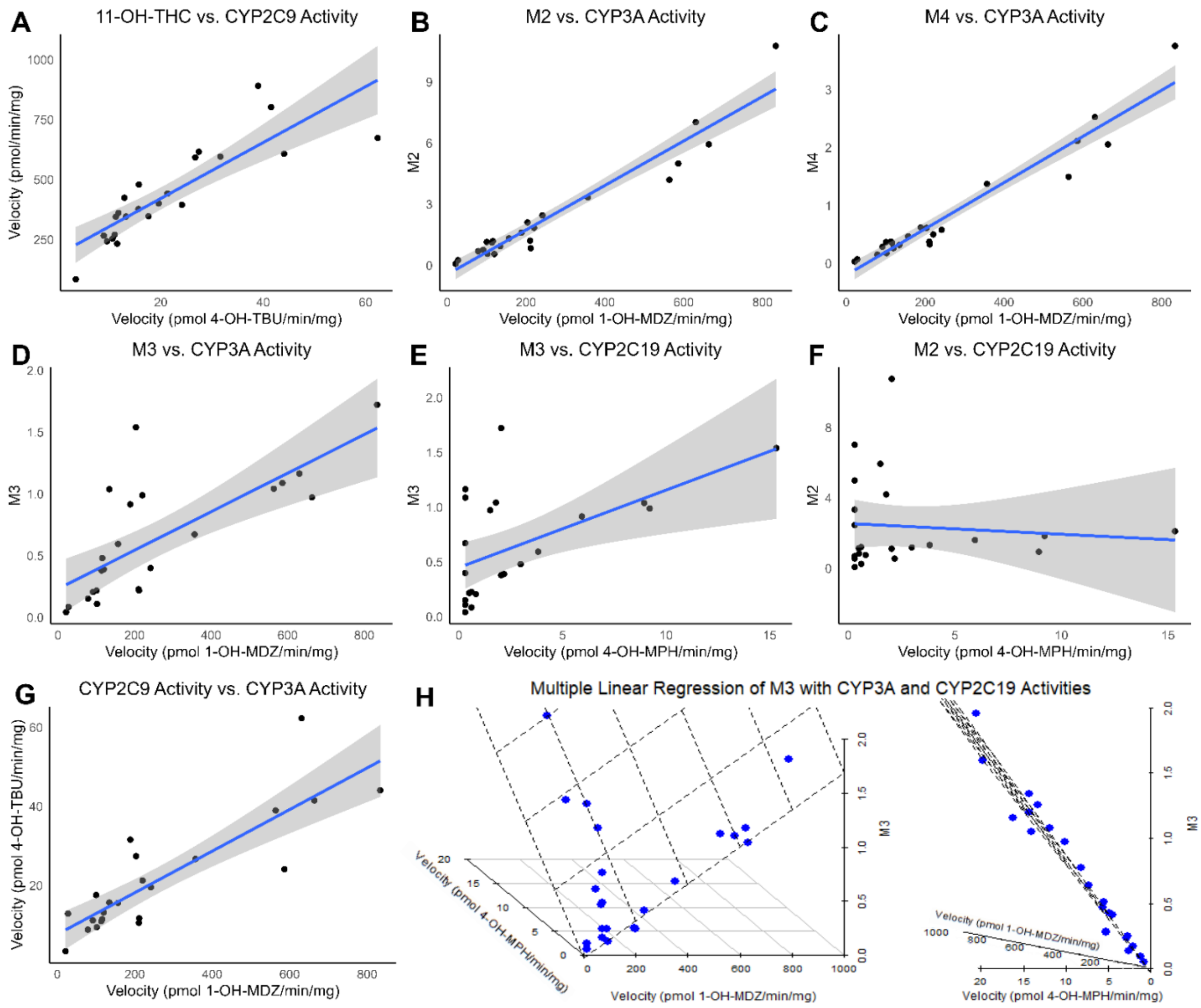

Figure 4.5. Correlation of THC metabolite formation with Cytochrome P450 (CYP) probe metabolism in the human liver microsome (HLM) panel.

Panels A through F show simple linear regression between metabolite formation and CYP specific activity in HLM donors (n = 23). Panel G shows simple linear regression between CYP2C9 and CYP3A specific activities in HLM donors (n = 23). Correlations between (**A**) velocity of 11-OH-THC formation and CYP2C9 specific activity (4-OH-TBU formation rate), (**B**) M2 relative formation and CYP3A specific activity (1-OH-MDZ formation rate), (**C**) M4 relative formation and CYP3A specific activity, (**D**) M3 relative formation and CYP3A specific activity and (**E**) M3 relative peak area and CYP2C19 specific activity (4-OH-MPH formation rate) are shown. (**F**) Lack of correlation between M2 relative formation and CYP2C19 specific activity is depicted. (**H**) Multiple linear regression of M3 relative formation with CYP3A and CYP2C19 specific activities, both as predictors, is shown plotted from two different angles (left panel and right panel). The correlations were significant (*p-value* < 0.01) between metabolite formation and CYP isoform specific activity in panels A-E and H. CYP2C9 and CYP3A specific activities were also found to be correlated (*p-value* < 0.01). Figure courtesy of Yue Wen.

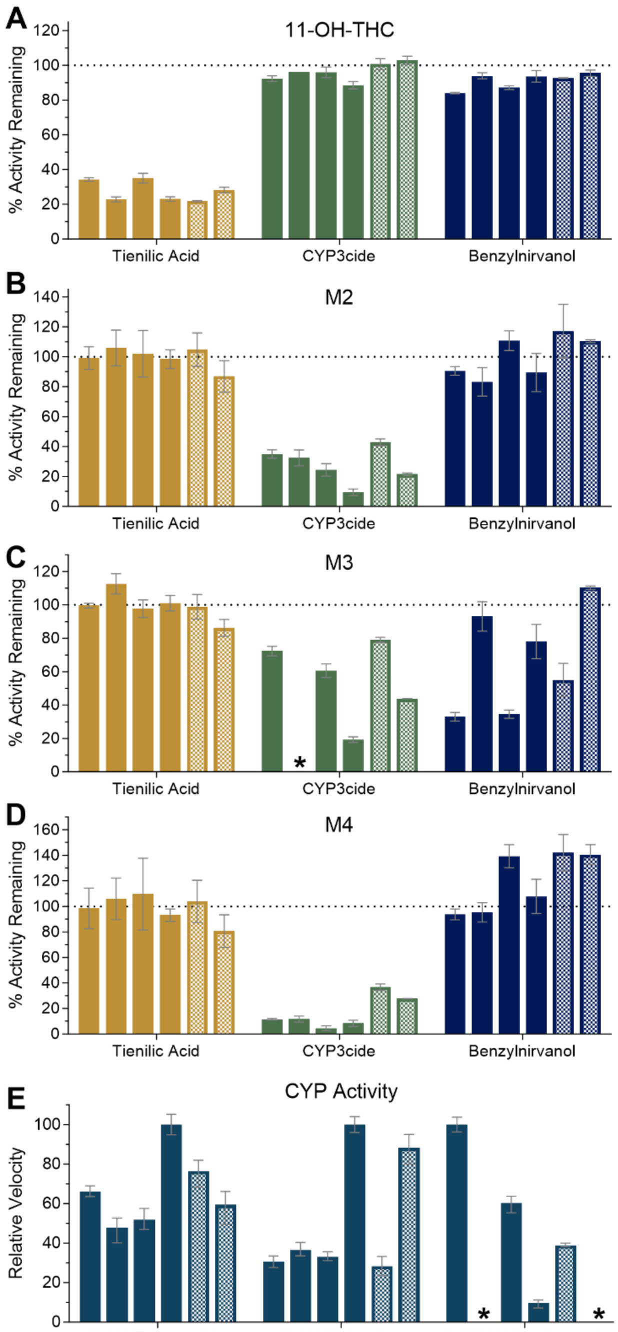

F

Genotypes	HL-105	HL-109	HL-114	HL-134	HL-108	HL-158
CYP2C9	*1/*1	*1/*3	*1/*3	*1/*1	*1/*1	*1/*3
CYP3A5	*3/*3	*3/*3	*3/*3	*3/*3	*1/*3	*1/*3
CYP2C19	*17/*17	*1/*2	*1/*17	*1/*2	*1/*17	*1/*1

Figure 4.6. Inhibition of THC metabolism in human liver microsomes (HLMs) from six individual liver donors.

The formation of (**A**) 11-OH-THC, (**B**) M2, (**C**) M3 and (**D**) M4 in HLMs in the presence of selective inhibitors is shown as the % activity remaining compared to no inhibitor controls. Inhibition by tienilic acid (CYP2C9), CYP3cide (CYP3A4) and (+)-N-3-benzyl-nirvanol (CYP2C19) are shown in gold, green and blue, respectively. (**E**) Specific activity of CYP2C9, CYP3A and CYP2C19 enzymes in the six livers as measured using the indicated probe substrates. The order of the six livers from left to right for each dataset is HL-105, HL-109, HL-114, HL-134, HL-108, and HL-158. Shaded bars represent livers with CYP3A5 expression. Metabolite formation below limit of quantification is indicated by asterisks. (**F**) CYP2C9, CYP3A5 and CYP2C19 genotypes for the six individual livers included.

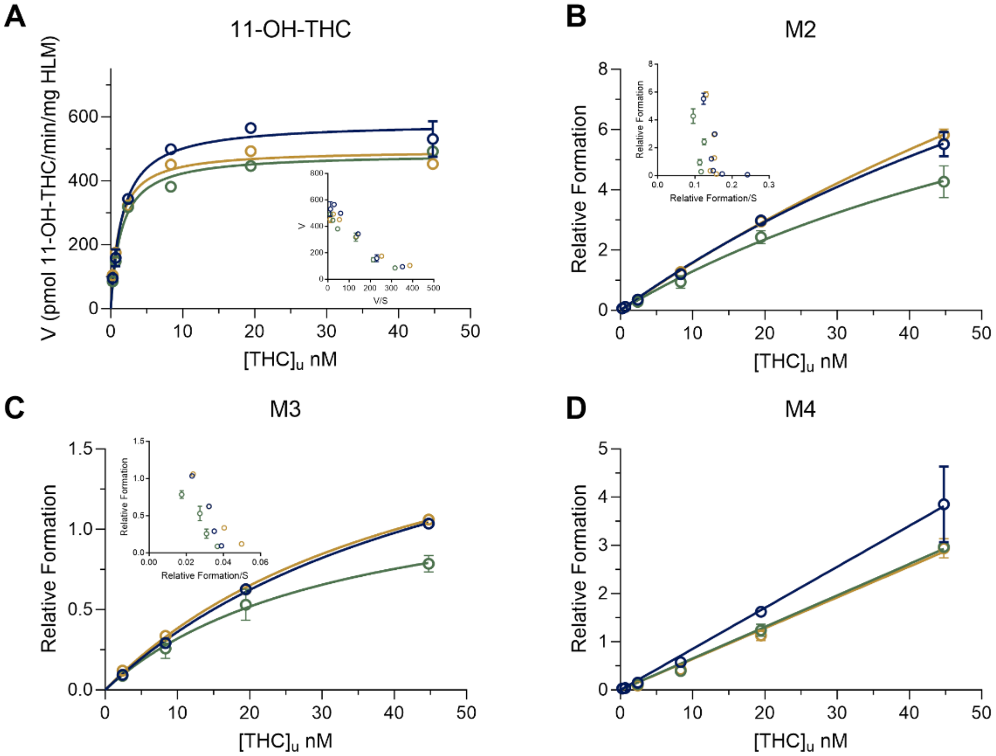

Figure 4.7. Kinetics of 11-OH-THC, M2, M3 and M4 formation in human liver microsomes (HLMs).

Formation of (**A**) 11-OH-THC, (**B**) M2, (**C**) M3 and (**D**) M4 metabolites in HLMs as a function of free THC concentration is plotted. The Michaelis-Menten equation (11-OH-THC, M2 and M3 formation data, A-C, solid lines) or linear regression model (M4 formation data D, solid lines) was fit to the data and model fits are shown as solid lines. Eadie-Hofstee plots are shown as insets. Replicate experiments performed on separate days are shown in dark blue, green and gold symbols and lines.

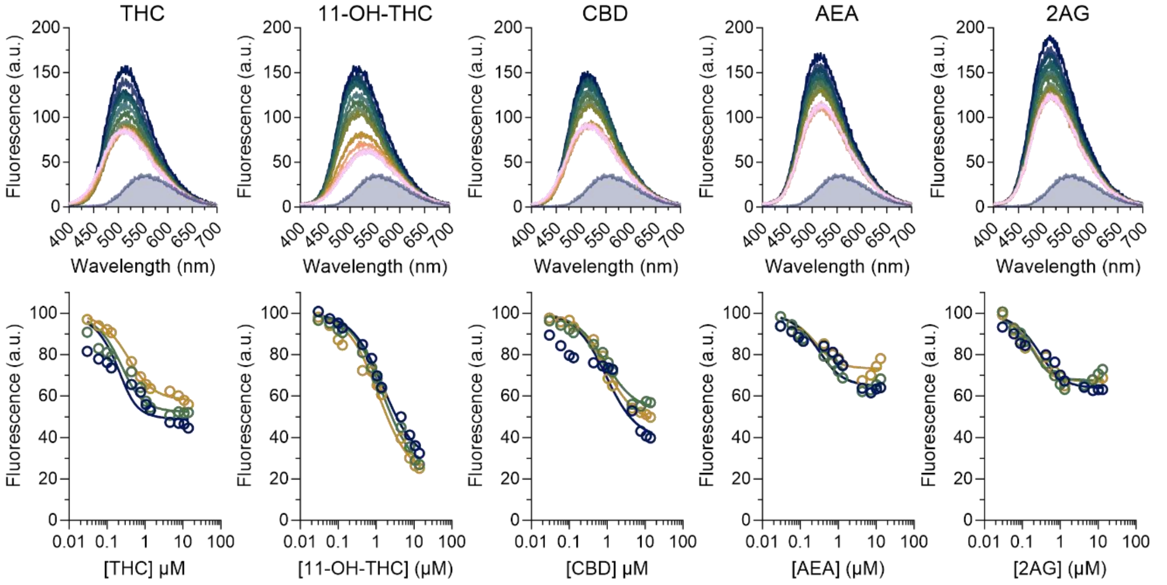

Figure 4.8. Binding of cannabinoids to FABP1.
Top panels show fluorescence emission spectra of titrations with THC, 11-OH-THC, cannabidiol (CBD) and the endogenous cannabinoids anandamide (AEA) and 2-arachidonoylglycerol (2AG) from DAUDA displacement assays. The top dark blue spectra represent the spectra of DAUDA bound with FABP1 (DAUDA-FABP1) in the absence of a cannabinoid and each subsequent spectrum represents increasing concentrations of cannabinoids to saturation (pink spectra). The shaded gray spectrum represents the spectrum of DAUDA in solution in the absence of FABP1. Bottom panels show the change in the specific fluorescence of DAUDA-FABP1 based on singular value decomposition analysis of titration spectra. Dark blue, gold, and green open circles show replicate experiments done on three separate days and the corresponding solid lines show COPASI fits of a ternary complex binding model to the data.

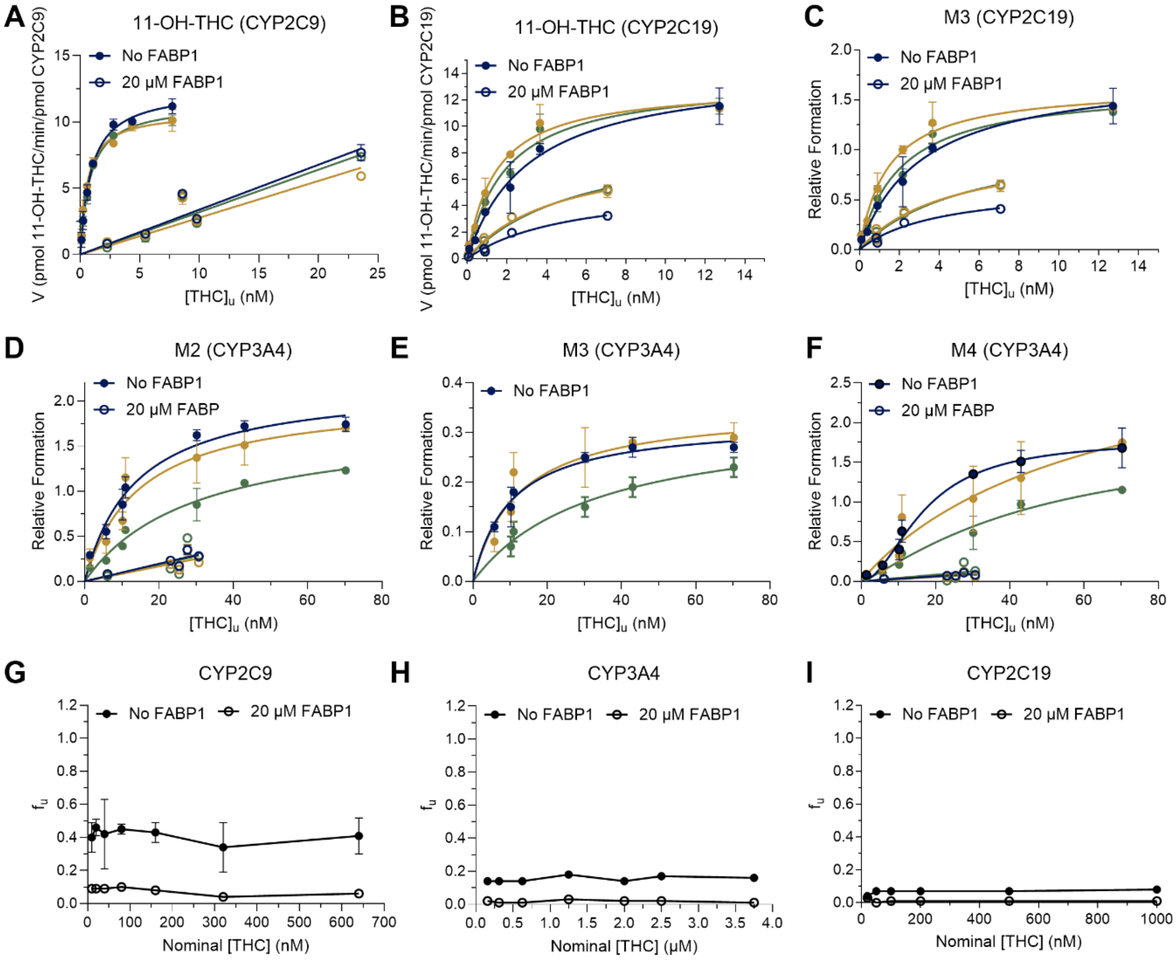

Figure 4.9. Kinetics of THC metabolism by recombinant cytochrome P450 (CYP) enzymes CYP2C9, CYP3A4 and CYP2C19 in the presence and absence of FABP1.

The velocities of 11-OH-THC formation by (**A**) CYP2C9 and (**B**) CYP2C19 are plotted as a function of free THC concentration. The relative rates of (**C**) M3 formation by CYP2C19, (**D**) M2 formation by CYP3A4, (**E**) M3 formation by CYP3A4 and (**F**) M4 formation by CYP3A4, are plotted as a function of free THC concentrations. The formation of metabolites in the absence and presence of FABP1 is indicated by solid and open circles, respectively. The solid lines show the Michaelis-Menten model fit to the 11-OH-THC, M2 and M3 formation data in the absence of FABP1 **(A-E)**, the allosteric model fit to the M4 formation data in the absence of FABP1 (**F**), the Michaelis-Menten model fit to the 11-OH-THC and M3 formation data by CYP2C19 data in the presence of FABP1 (**B,C**), a linear regression model fit to the 11-OH-THC and M2 and M4 formation data for CYP2C9 and CYP3A4, respectively (**A, D,F**). Replicate experiments performed on separate days are shown in dark blue and gold. The unbound fraction of THC (**G-I**) in the absence (closed circles) and presence (open circles) of 20 µM FABP1 is shown for all nominal THC concentrations used in kinetic experiments with CYP2C9 (**G**), CYP3A4 (**H**) and CYP2C19 (**I**).

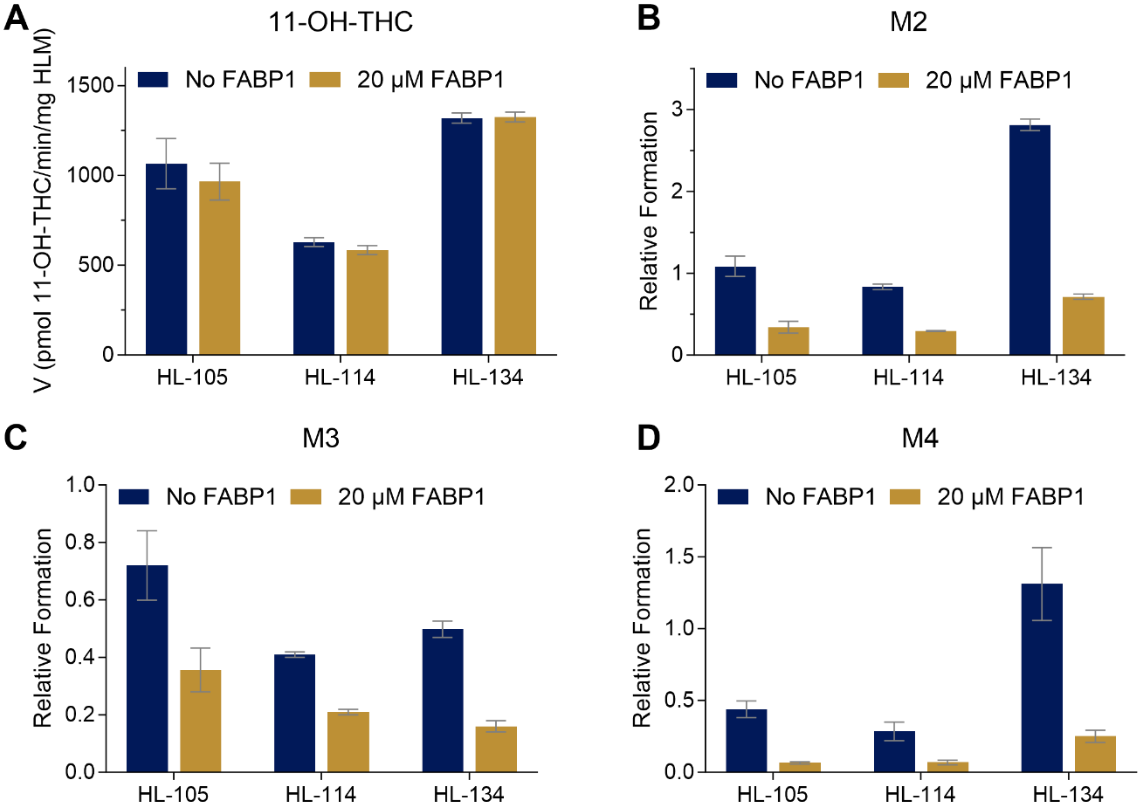

Figure 4.10. The effect of FABP1 on THC metabolite formation in human liver microsomes (HLMs).

The panels show (**A**) 11-OH-THC, (**B**) M2, (**C**) M3 and (**D**) M4 metabolite formation in the absence (dark blue) and presence (gold) of 20 μM FABP1 in HLMs from three individual donors with no CYP3A5 expression.

Table 4.1. Correlations between cytochrome P450 (CYP) specific activities and THC metabolite formation in human liver microsomes (HLMs) from the panel of individual liver donors (n=23).

Absolute p-values for the regression models are shown. Multiple R-squared (R^2) is reported for the simple linear regression models. Table courtesy of Yue Wen.

Model Used	Activity	11-OH-THC Formation	M2 Relative Formation	M3 Relative Formation	M4 Relative Formation
Simple linear regression	CYP2C9	$p=0.000000301$ $R^2=0.721$	$p=0.000000347$ $R^2=0.7172$	$p=0.0000197$ $R^2=0.5881$	$p=0.000000578$ $R^2=0.7034$
	CYP3A	$p=0.000113$ $R^2= 0.5159$	$p=0.000000000000305$ $R^2=0.9242$	$p=0.0000569$ $R^2=0.5456$	$p=0.0000000000000595$ $R^2=0.9351$
	CYP2C19	$p=0.253$ $R^2=0.06175$	$p=0.68555$ $R^2=0.007963$	$p=0.005432$ $R^2=0.3138$	$p=0.577067$ $R^2=0.01505$
Multiple linear regression	CYP2C9 + CYP3A + CYP2C19	2C9: $p=0.00493$ 3A: $p=0.60454$ 2C19: $p=0.11172$	2C9: $p=0.4196$ 3A: $p=0.00000127$ 2C19: $p=0.9654$	2C9: $p=0.344$ 3A: $p=0.000000222$ 2C19: $p=0.0000000000909$	2C9: $p=0.5315$ 3A: $p=0.000000311$ 2C19: $p=0.6904$

Table 4.2. Stepwise linear regression analysis of cytochrome P450 (CYP) activities as measured by specific metabolite formation from probe substrates and THC metabolite formation.

Y ~ X indicates the linear regression with Y as a response variable and X as the predictor. Added predictor as indicated was included to the linear regression one at a time to determine whether it improves the goodness of fit. The absolute *p-value* from the analysis of variance (ANOVA) test is shown. Table courtesy of Yue Wen.

Linear Regression	Added Predictor	*P-value*
11-OH-THC ~ CYP2C9	CYP3A	0.949
	CYP2C19	0.122
M2 ~ CYP3A	CYP2C9	0.369
	CYP2C19	0.728
M3 ~ CYP3A	CYP2C9	0.0721
	CYP2C19	0.00000000000880
M3 ~ CYP3A + CYP2C19	CYP2C9	0.344
M4 ~ CYP3A	CYP2C9	0.594
	CYP2C19	0.844

Table 4.3. Kinetic parameter estimates of THC metabolite formation in pooled human liver microsomes.

The data are reported as means ± standard deviation from experiments done on 3 separate days. N.D. Not determined due to lack of saturation of the metabolite formation.

	11-OH-THC	M2	M3	M4
$K_{m,unbound}$ (nM)	1.4 ± 0.2	> 45	> 45	> 45
V_{max} (pmol/min/mg HLM)	521 ± 53	N.D.	N.D.	N.D.

Table 4.4. The binding affinities of the tested cannabinoids with FABP1.
Ligand binding was determined via DAUDA displacement assay. The K_d value was determined from the COPASI fit of the ternary binding model to the DAUDA displacement data while EC_{50} and E_{min} were determined from fit of a three parameter dose response curve to the data. All parameter estimates are reported as means ± standard deviation from three replicate experiments performed on separate days. The ligands tested included THC, 11-OH-THC, cannabidiol (CBD) and the endogenous cannabinoids anandamide (AEA) and 2-arachidonoylglycerol (2AG).

	K_d (μM)	**EC_{50} (μM)**	**E_{min} (% fluorescence remaining)**
THC	0.30 ± 0.34	0.22 ± 0.13	52 ± 4.0
11-OH-THC	0.86 ± 0.15	1.5 ± 0.23	23 ± 3.8
CBD	0.57 ± 0.006	0.92 ± 0.07	46 ± 6.1
2AG	0.06 ± 0.04	0.18 ± 0.02	65 ± 1.3
AEA	0.19 ± 0.12	0.31 ± 0.14	66 ± 5.7

Table 4.5. Kinetic parameter estimates of THC metabolite formation by recombinant cytochrome P450 (CYP) enzymes CYP2C9, CYP2C19 and CYP3A4 in the presence and absence of 20 µM FABP1.

All the data except M4 formation are reported for the fits of the Michaelis Menten model to the metabolite formation data as a function of unbound THC concentration. The allosteric model was fit for M4 formation and the $K_{0.5,u}$ and hill slope (h) are reported. N.D. Not determined due to lack of detection of the metabolite in the presence of FABP1 (M3, CYP3A4), or lack of saturation of the metabolite formation in the presence of FABP1.

	$K_{m,u}$ -FABP1 (nM)	**$K_{m,u}$ +FABP1 (nM)**	**k_{cat} -FABP1 (min^{-1})**	**k_{cat} +FABP1 (min^{-1})**
11-OH-THC				
CYP2C9	0.77 ± 0.16	> 20	12 ± 0.87	N.D
CYP2C19	2.2 ± 0.87	5.2 ± 0.64	14 ± 0.68	8.0 ± 2.0
M2				
CYP3A4	29 ± 19	> 20	N.D	N.D
M3				
CYP2C19	2.2 ± 0.85	4.7 ± 0.72	N.D	N.D
CYP3A4	18 ± 13	N.D.	N.D.	N.D
M4				
CYP3A4	43 ± 25 (h = 1.4 ± 0.5)	> 20	N.D	N.D

Chapter 5. CONCLUSIONS

Intracellular lipid binding proteins (iLBPs) have been shown to impact rates of uptake and metabolism of endogenous ligands in cells, yet the role of iLBPs in xenobiotic disposition is unknown. Cellular retinoid binding proteins have served as a model for how iLBPs may impact ligand metabolism through substrate channeling and protein-protein interactions with metabolic enzymes. Specifically, cellular retinoic acid binding proteins, CRABP1 and CRABP2, have been shown to alter the metabolism of *all-trans*-retinoic acid (*at*RA) by CYP26 enzymes, the major family of CYP enzymes involved in the clearance of *at*RA. Liver fatty acid binding protein (FABP1) is a prominent member of the iLBP family that is highly expressed in the liver and has been previously reported to bind xenobiotics. However, whether FABP1 impacts the metabolism of xenobiotic ligands by CYPs in a similar manner to CRABPs is not known. The overarching hypothesis of this thesis was that iLBPs bind xenobiotics and facilitate the metabolism of xenobiotics by CYP enzymes in an enzyme specific manner. This thesis aimed to elucidate the impact of cellular retinoic acid binding proteins (CRABP1 and CRABP2) and liver fatty acid binding protein (FABP1) on the metabolism of their ligands by cytochrome P450 enzymes in the liver.

In chapter 2 of this thesis, I hypothesized that CRABP1 and CRABP2 interacted with CYP26A1 to modulate *at*RA metabolism in the liver. The aim of this project was to establish these interactions by defining the impact of CRABP1 and CRABP2 on 4-OH-*at*RA formation CYP26A1. The work in chapter 2 showed that *at*RA bound to CRABP1 and CRABP2 with high affinity (K_d = 4.7 and 7.6 nM, respectively) based on stopped-flow experiments. In kinetic experiments with recombinant CYP26A1, the presence of CRABP1 and CRABP2 had little effect on the unbound K_m ($K_{m,u}$) of 4-OH-*at*RA formation, but both CRABPs decreased the k_{cat} of

CYP26A1 by ~30%. In addition, 4-OH-*at*RA formation decreased with increasing concentrations of apo-CRABP1 and apo-CRABP2. Kinetic analysis of the 4-OH-*at*RA formation shows that both apo-CRABP1 and apo-CRABP2 inhibit CYP26A1 (K_i = 0.39 nM and 0.53 nM, respectively) and that holo-CRABP1 and CRABP2 directly deliver *at*RA to CYP26A1 for metabolism. Collectively, these results suggest that in the cell, when *at*RA concentrations are scarce and apo-CRABP concentration is high, apo-CRABP is likely to inhibit CYP26A1 to prevent further metabolism of *at*RA. In contrast, when *at*RA concentrations are high, higher fraction of the cellular CRABP is present as the holo-CRABP facilitating the clearance of *at*RA in the cell by relieving inhibition of CYP26A1 by apo-CRABP and by directly channeling *at*RA for metabolism by CYP26A1. The findings in this chapter shed light on the mechanisms by which CRABP1 and CRABP2 may fine tune cellular concentrations of *at*RA.

In chapter 3, I hypothesized that drugs bind to human (h)FABP1 and hFABP1 forms ternary complexes with drugs. The aims of this project were to determine 1) drug binding affinities with hFABP1 using DAUDA fluorescence displacement assay, and 2) the effect of hFABP1 binding on the metabolism of diclofenac by CYP2C9. I showed that DAUDA, a fluorescent fatty acid analogue, bound to hFABP1 at a high ($K_{d,1}$ = 0.2 µM) and low affinity ($K_{d,2}$ >10 µM) binding site. Though these findings are consistent with what has been previously reported for fatty acid (palmitate and oleate) binding to hFABP1, this was the first study to report two binding sites for DAUDA with hFABP1. Based on DAUDA fluorescence displacement assay, drugs also formed ternary complexes with hFABP1 and DAUDA. The binding affinities ranged from 1to 20 µM. DAUDA-FABP1-DAUDA and diclofenac-DAUDA-FABP1 ternary complex formation was verified using native protein MS. The findings in this chapter suggest that drugs are likely bound to hFABP1 *in vivo* and may occupy a separate binding site apart from a putative fatty acid binding site. In diclofenac incubations with recombinant CYP2C9, hFABP1 decreased the $K_{m,u}$ and k_{cat} of 4'-OH-diclofenac formation suggesting that hFABP1 directly interacts with CYP2C9 to modulate diclofenac metabolism.

In chapter 4, I hypothesized that hFABP1 could alter the metabolism of Δ-9-tetrahydrocannabinol (THC) by CYPs in an enzyme specific manner. The aims of this project were to 1) determine the CYP enzymes that formed the major primary metabolites of THC in the human liver and 2) characterize the impact of hFABP1 on the metabolism of THC by CYPs. THC was metabolized to four primary metabolites in human liver microsomes (HLMs) – 11-OH-THC and M2-M4 metabolites. CYP2C9 was the major contributor to 11-OH-THC formation, while CYP3A enzymes were mainly responsible for the formation of M2 and M4 metabolites. Both CYP2C19 and CYP3A4 contributed to the formation of M3. These findings suggest that CYP2C19 and CYP3A4 contribute to THC metabolic clearance consistent with *in vivo* and early *in vitro* findings. However, these results challenge more recent *in vitro* findings suggesting that THC metabolism is > 90% mediated by CYP2C9 with minor contribution from CYP2D6 (< 10%). In THC incubations with recombinant CYPs, hFABP1 had a profound impact on THC metabolism by CYP enzymes. The formation of 11-OH-THC, M2, M3 and M4 metabolites by recombinant CYP2C9, CYP2C19 and CYP3A4 was significantly decreased in the presence of hFABP1. In HLMs, hFABP1 significantly decreased M2, M3 and M4 formation but had little effect on the formation of 11-OH-THC. The findings from this chapter suggest that hFABP1 has the largest impact on CYP3A4 activity likely leading to an increase in the relative contribution of CYP2C9 and CYP2C19 to THC clearance *in vivo*.

In conclusion, CRABPs and hFABP1 had a profound impact on the metabolism of their ligands by CYP enzymes. The impact of CRABPs on *at*RA metabolism by CYP26A1 was consistent with a substrate channeling model described by protein-protein interactions. Similarly, hFABP1 altered the metabolism of diclofenac and THC by CYPs though the effect was enzyme specific. In addition, the data presented in this thesis show that drugs bind to hFABP1 with micromolar affinities. Given the high expression of FABP1 in the liver, these drugs are likely bound to FABP1 in the human liver *in vivo* and changes in FABP1 expression or binding may alter partitioning of drugs into the liver. Taken together, these findings suggest that FABP1 may be a determinant of drug disposition for FABP1 ligands *in vivo*.

BIBLIOGRAPHY

Agellon LB, Toth MJ, and Thomson ABR (2002) Intracellular lipid binding proteins of the small intestine, in *Cellular Lipid Binding Proteins* (Glatz JFC ed) pp 79–82, Springer US, Boston, MA.

Agurell S, Halldin M, Lindgren JE, Ohlsson A, Widman M, Gillespie H, and Hollister L (1986) Pharmacokinetics and metabolism of delta 1-tetrahydrocannabinol and other cannabinoids with emphasis on man. *Pharmacol Rev* 38:21–43, American Society for Pharmacology and Experimental Therapeutics.

Alpers DH, Bass NM, Engle MJ, and DeSchryver-Kecskemeti K (2000) Intestinal fatty acid binding protein may favor differential apical fatty acid binding in the intestine. *Biochimica et Biophysica Acta* 1483:352–362.

Amory JK, Muller CH, Shimshoni JA, Isoherranen N, Paik J, Moreb JS, Amory DW, Evanoff R, Goldstein AS, and Griswold MD (2011) Suppression of spermatogenesis by bisdichloroacetyldiamines is mediated by inhibition of testicular retinoic acid biosynthesis. *J Androl* 32:111–119.

Arnold WR, Weigle AT, and Das A (2018) Cross-talk of cannabinoid and endocannabinoid metabolism is mediated via human cardiac CYP2J2. *Journal of Inorganic Biochemistry* 184:88–99.

Atshaves BP, Martin GG, Hostetler HA, McIntosh AL, Kier AB, and Schroeder F (2010) Liver Fatty Acid Binding Protein and Obesity. *J Nutr Biochem* 21:1015–1032.

Babin PJ (2009) *Molecular evolution of vertebrate fatty-acid binding proteins*, Transworld Research Network.

Bashor MM, Toft DO, and Chytil F (1973) In Vitro Binding of Retinol to Rat-Tissue Components. *Proceedings of the National Academy of Sciences* 70:3483–3487, Proceedings of the National Academy of Sciences.

Bass NM, Barker ME, Manning JA, Jones AL, and Ockner RK (1989) Acinar heterogeneity of fatty acid binding protein expression in the livers of male, female and clofibrate-treated rats. *Hepatology* 9:12–21.

Beers JL, Authement AK, Isoherranen N, and Jackson KD (2023) Cytosolic Enzymes Generate Cannabinoid Metabolites 7-Carboxycannabidiol and 11-Nor-9-carboxytetrahydrocannabinol. *ACS Med Chem Lett* 14:614–620, American Chemical Society.

Berger WT, Ralph BP, Kaczocha M, Sun J, Balius TE, Rizzo RC, Haj-Dahmane S, Ojima I, and Deutsch DG (2012) Targeting Fatty Acid Binding Protein (FABP) Anandamide Transporters – A Novel Strategy for Development of Anti-Inflammatory and Anti-Nociceptive Drugs. *PLOS ONE* 7:e50968, Public Library of Science.

Bernlohr DA, Simpson MA, Hertzel AV, and Banaszak LJ (1997) Intracellular Lipid-Binding Proteins and Their Genes. *Annual Review of Nutrition* 17:277–303.

Besnard P, Niot I, Poirier H, Clément L, and Bernard A (2002) New insights into the fatty acid-binding protein (FABP) family in the small intestine. *Mol Cell Biochem* 239:139–147.

Bland TM, Haining RL, Tracy TS, and Callery PS (2005) CYP2C-catalyzed delta(9)-tetrahydrocannabinol metabolism: Kinetics, pharmacogenetics and interaction with phenytoin. *Biochemical Pharmacology* 70:1096–1103.

Blaner WS (2019) Vitamin A signaling and homeostasis in obesity, diabetes, and metabolic disorders. *Pharmacology & Therapeutics* 197:153–178.

Bornheim LM, and Correia MA (1991) Purification and characterization of the major hepatic cannabinoid hydroxylase in the mouse: a possible member of the cytochrome P-450IIC subfamily. *Mol Pharmacol* 40:228–234, American Society for Pharmacology and Experimental Therapeutics.

Bornheim LM, Lasker JM, and Raucy JL (1992) Human hepatic microsomal metabolism of delta 1-tetrahydrocannabinol. *Drug Metab Dispos* 20:241–246.

Budhu A, Gillilan R, and Noy N (2001) Localization of the RAR interaction domain of cellular retinoic acid binding protein-II. *Journal of Molecular Biology* 305:939–949.

Cai J, Lücke C, Chen Z, Qiao Y, Klimtchuk E, and Hamilton JA (2012) Solution Structure and Backbone Dynamics of Human Liver Fatty Acid Binding Protein: Fatty Acid Binding Revisited. *Biophysical Journal* 102:2585–2594.

Centers for Disease Control and Prevention (2022) Data and Statistics.

Chen LX, Zhang Z, Scafonas A, Cavalli RC, Gabriel JL, Soprano KJ, and Soprano DR (1995) Arginine 132 of Cellular Retinoic Acid-binding Protein (Type II) Is Important for Binding of Retinoic Acid (∗). *Journal of Biological Chemistry* 270:4518–4525.

Chen Q, and Ross AC (2004) Retinoic acid regulates cell cycle progression and cell differentiation in human monocytic THP-1 cells. *Experimental Cell Research* 297:68–81.

Chuang S, Velkov T, Horne J, Porter CJH, and Scanlon MJ (2008) Characterization of the Drug Binding Specificity of Rat Liver Fatty Acid Binding Protein. *J Med Chem* 51:3755–3764, American Chemical Society.

Chuang S, Velkov T, Horne J, Wielens J, Chalmers DK, Porter CJH, and Scanlon MJ (2009) Probing the Fibrate Binding Specificity of Rat Liver Fatty Acid Binding Protein. *J Med Chem* 52:5344–5355, American Chemical Society.

Chute JP, Muramoto GG, Whitesides J, Colvin M, Safi R, Chao NJ, and McDonnell DP (2006) Inhibition of aldehyde dehydrogenase and retinoid signaling induces the expansion of human hematopoietic stem cells. *Proceedings of the National Academy of Sciences* 103:11707–11712, Proceedings of the National Academy of Sciences.

Corsico B, Cistola DP, Frieden C, and Storch J (1998) The helical domain of intestinal fatty acid binding protein is critical for collisional transfer of fatty acids to phospholipid membranes. *Proc Natl Acad Sci U S A* 95:12174–12178.

Davidson KL, Oberreit DR, Hogan CJ, and Bush MF (2017) Nonspecific aggregation in native electrokinetic nanoelectrospray ionization. *International Journal of Mass Spectrometry* 420:35–42.

Davies JK, Hagan RM, and Wilton DC (2002) Effect of Charge Reversal Mutations on the Ligand- and Membrane-binding Properties of Liver Fatty Acid-binding Protein*. *Journal of Biological Chemistry* 277:48395–48402.

Dinis-Oliveira RJ (2016) Metabolomics of Δ-9-tetrahydrocannabinol: implications in toxicity. *Drug Metabolism Reviews* 48:80–87.

Dong D, Ruuska SE, Levinthal DJ, and Noy N (1999) Distinct Roles for Cellular Retinoic Acid-binding Proteins I and II in Regulating Signaling by Retinoic Acid. *Journal of Biological Chemistry* 274:23695–23698.

E X, Zhang L, Lu J, Tso P, Blaner WS, Levin MS, and Li E (2002) Increased Neonatal Mortality in Mice Lacking Cellular Retinol-binding Protein II*. *Journal of Biological Chemistry* 277:36617–36623.

Elmes MW, Kaczocha M, Berger WT, Leung K, Ralph BP, Wang L, Sweeney JM, Miyauchi JT, Tsirka SE, Ojima I, and Deutsch DG (2015) Fatty Acid-binding Proteins (FABPs) Are Intracellular Carriers for Δ9-Tetrahydrocannabinol (THC) and Cannabidiol (CBD)*. *Journal of Biological Chemistry* 290:8711–8721.

Elmes MW, Prentis LE, McGoldrick LL, Giuliano CJ, Sweeney JM, Joseph OM, Che J, Carbonetti GS, Studholme K, Deutsch DG, Rizzo RC, Glynn SE, and Kaczocha M (2019) FABP1 controls hepatic transport and biotransformation of Δ9-THC. *Sci Rep* 9:7588, Nature Publishing Group.

Falomir-Lockhart LJ, Laborde L, Kahn PC, Storch J, and Córsico B (2006) Protein-Membrane Interaction and Fatty Acid Transfer from Intestinal Fatty Acid-binding Protein to Membranes: SUPPORT FOR A MULTISTEP PROCESS*. *Journal of Biological Chemistry* 281:13979–13989.

Favretto F, Santambrogio C, D'Onofrio M, Molinari H, Grandori R, and Assfalg M (2015) Bile salt recognition by human liver fatty acid binding protein. *The FEBS Journal* 282:1271–1288.

Ferreira R, Napoli J, Enver T, Bernardino L, and Ferreira L (2020) Advances and challenges in retinoid delivery systems in regenerative and therapeutic medicine. *Nat Commun* 11:4265.

Ferrolino MC, Zhuravleva A, Budyak IL, Krishnan B, and Gierasch LM (2013) Delicate Balance between Functionally Required Flexibility and Aggregation Risk in a β-Rich Protein. *Biochemistry* 52:8843–8854.

Fiorella PD, Giguère V, and Napoli JL (1993) Expression of cellular retinoic acid-binding protein (type II) in Escherichia coli. Characterization and comparison to cellular retinoic acid-binding protein (type I). *Journal of Biological Chemistry* 268:21545–21552.

Fiorella PD, and Napoli JL (1991) Expression of cellular retinoic acid binding protein (CRABP) in Escherichia coli. Characterization and evidence that holo-CRABP is a substrate in retinoic acid metabolism. *Journal of Biological Chemistry* 266:16572–16579.

Fiorella PD, and Napoli JL (1994) Microsomal retinoic acid metabolism. Effects of cellular retinoic acid-binding protein (type I) and C18-hydroxylation as an initial step. *Journal of Biological Chemistry* 269:10538–10544.

Floresta G, Pistarà V, Amata E, Dichiara M, Marrazzo A, Prezzavento O, and Rescifina A (2017) Adipocyte fatty acid binding protein 4 (FABP4) inhibitors. A comprehensive systematic review. *European Journal of Medicinal Chemistry* 138:854–873.

Flower DR, North ACT, and Sansom CE (2000) The lipocalin protein family: structural and sequence overview. *Biochimica et Biophysica Acta (BBA) - Protein Structure and Molecular Enzymology* 1482:9–24.

Fogh K, Voorhees JJ, and Aström A (1993) Expression, purification, and binding properties of human cellular retinoic acid-binding protein type I and type II. *Arch Biochem Biophys* 300:751–755.

Folli C, Calderone V, Ottonello S, Bolchi A, Zanotti G, Stoppini M, and Berni R (2001) Identification, Retinoid Binding, and X-Ray Analysis of a Human Retinol-Binding Protein. *Proceedings of the National Academy of Sciences of the United States of America* 98:3710–3715, National Academy of Sciences.

Folli C, Calderone V, Ramazzina I, Zanotti G, and Berni R (2002) Ligand Binding and Structural Analysis of a Human Putative Cellular Retinol-binding Protein*. *Journal of Biological Chemistry* 277:41970–41977.

Foucaud L, Niot I, Kanda T, and Besnard P (1998) Indirect dexamethasone down-regulation of the liver fatty acid-binding protein expression in rat liver. *Biochimica et Biophysica Acta (BBA) - Lipids and Lipid Metabolism* 1391:204–212.

Furuhashi M (2019) Fatty Acid-Binding Protein 4 in Cardiovascular and Metabolic Diseases. *Journal of Atherosclerosis and Thrombosis* 26:216–232.

Furuhashi M, and Hotamisligil GS (2008) Fatty acid-binding proteins: role in metabolic diseases and potential as drug targets. *Nat Rev Drug Discov* 7:489–503, Nature Publishing Group.

Furuhashi M, Saitoh S, Shimamoto K, and Miura T (2015) Fatty Acid-Binding Protein 4 (FABP4): Pathophysiological Insights and Potent Clinical Biomarker of Metabolic and Cardiovascular Diseases. *Clin Med Insights Cardiol* 8:23–33.

Gajda AM, and Storch J (2015) Enterocyte fatty acid-binding proteins (FABPs): Different functions of liver and intestinal FABPs in the intestine. *Prostaglandins, Leukotrienes and Essential Fatty Acids* 93:9–16, Elsevier.

Gasse A, Pfeiffer H, Köhler H, and Schürenkamp J (2018) 8β-OH-THC and 8β,11-diOH-THC—minor metabolites with major informative value? *Int J Legal Med* 132:157–164.

Gasteiger E, Hoogland C, Gattiker A, Duvaud S, Wilkins MR, Appel RD, and Bairoch A (2005) Protein Identification and Analysis Tools on the ExPASy Server, in *The Proteomics Protocols Handbook* (Walker JM ed) pp 571–607, Humana Press, Totowa, NJ.

Gerstner JR, Bremer QZ, Vander Heyden WM, Lavaute TM, Yin JC, and Landry CF (2008) Brain fatty acid binding protein (Fabp7) is diurnally regulated in astrocytes and hippocampal granule cell precursors in adult rodent brain. *PLoS One* 3:e1631.

Ghiaur G, Yegnasubramanian S, Perkins B, Gucwa JL, Gerber JM, and Jones RJ (2013) Regulation of human hematopoietic stem cell self-renewal by the microenvironment's control of retinoic acid signaling. *Proceedings of the National Academy of Sciences* 110:16121–16126, Proceedings of the National Academy of Sciences.

Giguère V, Lyn S, Yip P, Siu CH, and Amin S (1990) Molecular cloning of cDNA encoding a second cellular retinoic acid-binding protein. *Proc Natl Acad Sci U S A* 87:6233–6237.

Gillilan RE, Ayers SD, and Noy N (2007) Structural Basis for Activation of Fatty Acid Binding Protein 4. *J Mol Biol* 372:1246–1260.

Giroud C, Ménétrey A, Augsburger M, Buclin T, Sanchez-Mazas P, and Mangin P (2001) Δ9-THC, 11-OH-Δ9-THC and Δ9-THCCOOH plasma or serum to whole blood concentrations distribution ratios in blood samples taken from living and dead people. *Forensic Science International* 123:159–164.

Glass SM, and Guengerich FP (2021a) Cellular retinoid-binding proteins transfer retinoids to human cytochrome P450 27C1 for desaturation. *Journal of Biological Chemistry* 297, Elsevier.

Glass SM, and Guengerich FP (2021b) Cellular retinoid-binding proteins transfer retinoids to human cytochrome P450 27C1 for desaturation. *Journal of Biological Chemistry* 297, Elsevier.

Glatz JanFC, and Luiken JoostJFP (2018) Dynamic role of the transmembrane glycoprotein CD36 (SR-B2) in cellular fatty acid uptake and utilization. *Journal of Lipid Research* 59:1084–1093.

Glatz JFC, and Veerkamp JH (1983) A radiochemical procedure for the assay of fatty acid binding by proteins. *Analytical Biochemistry* 132:89–95.

Gong YZ, Everett ET, Schwartz DA, Norris JS, and Wilson FA (1994) Molecular cloning, tissue distribution, and expression of a 14-kDa bile acid-binding protein from rat ileal cytosol. *Proc Natl Acad Sci U S A* 91:4741–4745.

González JM, and Fisher SZ (2015) Structural analysis of ibuprofen binding to human adipocyte fatty-acid binding protein (FABP4). *Acta Crystallogr F Struct Biol Commun* 71:163–170.

Gudas LJ, and Wagner JA (2011) Retinoids regulate stem cell differentiation. *Journal of Cellular Physiology* 226:322–330.

Gurny O, Maynard DE, Pitcher RG, and Kierstead RW (1972) Metabolism of (-)- .DELTA.9- and (-)- .DELTA.8-tetrahydrocannabinol by monkey liver. *J Am Chem Soc* **94**:7928–7929, American Chemical Society.

Gyamfi J, Yeo JH, Kwon D, Min BS, Cha YJ, Koo JS, Jeong J, Lee J, and Choi J (2021) Interaction between CD36 and FABP4 modulates adipocyte-induced fatty acid import and metabolism in breast cancer. *npj Breast Cancer* 7:1–18, Nature Publishing Group.

Halldén G, and Aponte GW (1997) Evidence for a Role of the Gut Hormone PYY in the Regulation of Intestinal Fatty Acid-binding Protein Transcripts in Differentiated Subpopulations of Intestinal Epithelial Cell Hybrids*. *Journal of Biological Chemistry* 272:12591–12600.

Hanhoff T, Lücke C, and Spener F (2002) Insights into binding of fatty acids by fatty acid binding proteins. *Mol Cell Biochem* 239:45–54.

Haunerland NH, and Spener F (2004) Fatty acid-binding proteins – insights from genetic manipulations. *Progress in Lipid Research* 43:328–349.

He Y, Yang X, Wang H, Estephan R, Francis F, Kodukula S, Storch J, and Stark RE (2007) Solution-State Molecular Structure of Apo and Oleate-Liganded Liver Fatty Acid-Binding Protein. *Biochemistry* 46:12543–12556, American Chemical Society.

Hendler RW, and Shrager RI (1994) Deconvolutions based on singular value decomposition and the pseudoinverse: a guide for beginners. *Journal of Biochemical and Biophysical Methods* 28:1–33.

Herr FM, Li E, Weinberg RB, Cook VR, and Storch J (1999) Differential Mechanisms of Retinoid Transfer from Cellular Retinol Binding Proteins Types I and II to Phospholipid Membranes *. *Journal of Biological Chemistry* 274:9556–9563, Elsevier.

Hodsdon ME, and Cistola DP (1997a) Discrete Backbone Disorder in the Nuclear Magnetic Resonance Structure of Apo Intestinal Fatty Acid-Binding Protein: Implications for the Mechanism of Ligand Entry,. *Biochemistry* 36:1450–1460, American Chemical Society.

Hodsdon ME, and Cistola DP (1997b) Ligand Binding Alters the Backbone Mobility of Intestinal Fatty Acid-Binding Protein as Monitored by 15N NMR Relaxation and 1H Exchange. *Biochemistry* 36:2278–2290, American Chemical Society.

Hogarth CA, Arnold S, Kent T, Mitchell D, Isoherranen N, and Griswold MD (2015) Processive Pulses of Retinoic Acid Propel Asynchronous and Continuous Murine Sperm Production1. *Biology of Reproduction* 92:37, 1–11.

Hohoff C, Börchers T, Rüstow B, Spener F, and van Tilbeurgh H (1999) Expression, Purification, and Crystal Structure Determination of Recombinant Human Epidermal-Type Fatty Acid Binding Protein ’. *Biochemistry* 38:12229–12239.

Hoops S, Sahle S, Gauges R, Lee C, Pahle J, Simus N, Singhal M, Xu L, Mendes P, and Kummer U (2006) COPASI—a COmplex PAthway SImulator. *Bioinformatics* 22:3067–3074.

Horspool AM, Wang T, Scaringella Y-S, Taub ME, and Chan TS (2020) Human Liver Microsomes Immobilized on Magnetizable Beads: A Novel Approach to Study In Vitro Drug Metabolism. *Drug Metab Dispos* 48:645–654, American Society for Pharmacology and Experimental Therapeutics.

Hostetler HA, Lupas D, Tan Y, Dai J, Kelzer MS, Martin GG, Woldegiorgis G, Kier AB, and Schroeder F (2011) Acyl-CoA binding proteins interact with the acyl-CoA binding domain of mitochondrial carnitine palmitoyl transferase I. *Mol Cell Biochem* 355:135–148.

Hostetler HA, McIntosh AL, Atshaves BP, Storey SM, Payne HR, Kier AB, and Schroeder F (2009) L-FABP directly interacts with PPARα in cultured primary hepatocytes. *Journal of Lipid Research* 50:1663–1675.

Hotamisligil GS, and Bernlohr DA (2015) Metabolic functions of FABPs—mechanisms and therapeutic implications. *Nat Rev Endocrinol* 11:592–605, Nature Publishing Group.

Hotamisligil GS, Johnson RS, Distel RJ, Ellis R, Papaioannou VE, and Spiegelman BM (1996) Uncoupling of Obesity from Insulin Resistance Through a Targeted Mutation in aP2, the Adipocyte Fatty Acid Binding Protein. *Science* 274:1377–1379, American Association for the Advancement of Science.

Hsu K-T, and Storch J (1996) Fatty Acid Transfer from Liver and Intestinal Fatty Acid-binding Proteins to Membranes Occurs by Different Mechanisms *. *Journal of Biological Chemistry* 271:13317–13323, Elsevier.

Huang H, McIntosh AL, Martin GG, Dangott LJ, Kier AB, and Schroeder F (2018) Structural and Functional Interaction of Δ9-Tetrahydrocannabinol with Liver Fatty Acid Binding Protein (FABP1). *Biochemistry* 57:6027–6042, American Chemical Society.

Huang H, McIntosh AL, Martin GG, Landrock D, Chung S, Landrock KK, Dangott LJ, Li S, Kier AB, and Schroeder F (2016) FABP1: A Novel Hepatic Endocannabinoid and Cannabinoid Binding Protein. *Biochemistry* 55:5243–5255, American Chemical Society.

Huang H, McIntosh AL, Martin GG, Landrock KK, Landrock D, Gupta S, Atshaves BP, Kier AB, and Schroeder F (2014) Structural and functional interaction of fatty acids with human liver fatty acid-binding protein (L-FABP) T94A variant. *The FEBS Journal* 281:2266–2283.

Huang W, Czuba LC, Manuzak JA, Martin JN, Hunt PW, Klatt NR, and Isoherranen N (2022) Objective Identification of Cannabis Use Levels in Clinical Populations Is Critical for Detecting Pharmacological Outcomes. *Cannabis and Cannabinoid Research* 7:852–864, Mary Ann Liebert, Inc., publishers.

Huang X, Zhou Y, Sun Y, and Wang Q (2022) Intestinal fatty acid binding protein: A rising therapeutic target in lipid metabolism. *Progress in Lipid Research* 87:101178.

Huestis MA (2005) Pharmacokinetics and Metabolism ofthe Plant Cannabinoids, Δ9-Tetrahydrocannabinol, Cannabidiol and Cannabinol. *Handbook of Experimental Pharmacology* 657–690.

Hughes MLR, Liu B, Halls ML, Wagstaff KM, Patil R, Velkov T, Jans DA, Bunnett NW, Scanlon MJ, and Porter CJH (2015) Fatty Acid-binding Proteins 1 and 2 Differentially Modulate the Activation of Peroxisome Proliferator-activated Receptor α in a Ligand-selective Manner*. *Journal of Biological Chemistry* 290:13895–13906.

Hunault CC, Mensinga TT, de Vries I, Kelholt-Dijkman HH, Hoek J, Kruidenier M, Leenders MEC, and Meulenbelt J (2008) Delta-9-tetrahydrocannabinol (THC) serum concentrations and pharmacological effects in males after smoking a combination of tobacco and cannabis containing up to 69 mg THC. *Psychopharmacology* 201:171–181.

Hung DY, Burczynski FJ, Chang P, Lewis A, Masci PP, Siebert GA, Anissimov YG, and Roberts MS (2003) Fatty acid binding protein is a major determinant of hepatic pharmacokinetics of palmitate and its metabolites. *American Journal of Physiology-Gastrointestinal and Liver Physiology* 284:G423–G433, American Physiological Society.

Hunt CA, and Jones RT (1980) Tolerance and disposition of tetrahydrocannabinol in man. *J Pharmacol Exp Ther* 215:35–44, American Society for Pharmacology and Experimental Therapeutics.

Hutzler JM, Balogh LM, Zientek M, Kumar V, and Tracy TS (2009) Mechanism-Based Inactivation of Cytochrome P450 2C9 by Tienilic Acid and (±)-Suprofen: A Comparison of Kinetics and Probe Substrate Selection. *Drug Metab Dispos* 37:59–65, American Society for Pharmacology and Experimental Therapeutics.

Iglewicz B, and Hoaglin DC (1993) *How to detect and handle outliers*, ASQC Quality Press, Milwaukee, Wis.

Ishimura S, Furuhashi M, Watanabe Y, Hoshina K, Fuseya T, Mita T, Okazaki Y, Koyama M, Tanaka M, Akasaka H, Ohnishi H, Yoshida H, Saitoh S, and Miura T (2013) Circulating Levels of Fatty Acid-Binding Protein Family and Metabolic Phenotype in the General Population. *PLOS ONE* 8:e81318, Public Library of Science.

Isoherranen N, Yagen B, Woodhead JH, Spiegelstein O, Blotnik S, Wilcox KS, Finnell RH, Bennett GD, White HS, and Bialer M (2003) Characterization of the anticonvulsant profile and enantioselective pharmacokinetics of the chiral valproylamide propylisopropyl acetamide in rodents. *Br J Pharmacol* **138**:602–613.

Isoherranen N, and Zhong G (2019) Biochemical and physiological importance of the CYP26 retinoic acid hydroxylases. *Pharmacology & Therapeutics* 204:107400.

Jarmoskaite I, AlSadhan I, Vaidyanathan PP, and Herschlag D (2020) How to measure and evaluate binding affinities. *eLife* 9:e57264, eLife Sciences Publications, Ltd.

Jenkins AE, Hockenberry JA, Nguyen T, and Bernlohr DA (2002) Testing of the Portal Hypothesis: Analysis of a V32G, F57G, K58G Mutant of the Fatty Acid Binding Protein of the Murine Adipocyte. *Biochemistry* 41:2022–2027, American Chemical Society.

Jenkins-Kruchten AE, Bennaars-Eiden A, Ross JR, Shen W-J, Kraemer FB, and Bernlohr DA (2003) Fatty Acid-binding Protein-Hormone-sensitive Lipase Interaction: FATTY ACID DEPENDENCE ON BINDING *. *Journal of Biological Chemistry* 278:47636–47643, Elsevier.

Kaczocha M, Glaser ST, and Deutsch DG (2009) Identification of intracellular carriers for the endocannabinoid anandamide. *Proceedings of the National Academy of Sciences* 106:6375–6380, Proceedings of the National Academy of Sciences.

Kaczocha M, Vivieca S, Sun J, Glaser ST, and Deutsch DG (2012) Fatty Acid-binding Proteins Transport N-Acylethanolamines to Nuclear Receptors and Are Targets of Endocannabinoid Transport Inhibitors*. *Journal of Biological Chemistry* 287:3415–3424.

Kandel SE, and Lampe JN (2014) Role of Protein–Protein Interactions in Cytochrome P450-Mediated Drug Metabolism and Toxicity. *Chem Res Toxicol* 27:1474–1486, American Chemical Society.

Kane CD, and Bernlohr DA (1996) A Simple Assay for Intracellular Lipid-Binding Proteins Using Displacement of 1-Anilinonaphthalene 8-Sulfonic Acid. *Analytical Biochemistry* 233:197–204.

Kane MA, Bright FV, and Napoli JL (2011) Binding affinities of CRBPI and CRBPII for 9-cis-retinoids. *Biochimica et Biophysica Acta (BBA) - General Subjects* 1810:514–518.

Karkeni E, Bonnet L, Astier J, Couturier C, Dalifard J, Tourniaire F, and Landrier J-F (2017) All-trans-retinoic acid represses chemokine expression in adipocytes and adipose tissue by inhibiting NF-κB signaling. *The Journal of Nutritional Biochemistry* 42:101–107.

Kato M, Blaner WS, Mertz JR, Das K, Kato K, and Goodman DS (1985) Influence of retinoid nutritional status on cellular retinol- and cellular retinoic acid-binding protein concentrations in various rat tissues. *Journal of Biological Chemistry* 260:4832–4838.

Khan SH, and Sorof S (1990) Preferential binding of growth inhibitory prostaglandins by the target protein of a carcinogen. *Proceedings of the National Academy of Sciences* 87:9401–9405, Proceedings of the National Academy of Sciences.

Kim HK, and Storch J (1992) Mechanism of free fatty acid transfer from rat heart fatty acid-binding protein to phospholipid membranes. Evidence for a collisional process. *Journal of Biological Chemistry* 267:20051–20056.

Kim JH (2019) Multicollinearity and misleading statistical results. *Korean J Anesthesiol* 72:558–569, Korean Society of Anesthesiologists.

Kitova EN, El-Hawiet A, Schnier PD, and Klassen JS (2012) Reliable Determinations of Protein–Ligand Interactions by Direct ESI-MS Measurements. Are We There Yet? *J Am Soc Mass Spectrom* 23:431–441, American Society for Mass Spectrometry. Published by the American Chemical Society. All rights reserved.

Kleywegt GJ, Bergfors T, Senn H, Motte PL, Gsell B, Shud K, and Jones TA (1994) Crystal structures of cellular retinoic acid binding proteins I and II in complex with all-trans-retinoic acid and a synthetic retinoid. *Structure* 2:1241–1258.

Kumar V, Brundage RC, Oetting WS, Leppik IE, and Tracy TS (2008) Differential Genotype Dependent Inhibition of CYP2C9 in Humans. *Drug Metab Dispos* 36:1242–1248.

Kushlan MC, Gollan JL, Ma WL, and Ockner RK (1981) Sex differences in hepatic uptake of long chain fatty acids in single-pass perfused rat liver. *Journal of Lipid Research* 22:431–436.

Lai MP, Katz FS, Bernard C, Storch J, and Stark RE (2020) Two fatty acid-binding proteins expressed in the intestine interact differently with endocannabinoids. *Protein Science* 29:1606–1617.

LaLonde JM, Levenson MA, Roe JJ, Bernlohr DA, and Banaszak LJ (1994) Adipocyte lipid-binding protein complexed with arachidonic acid. Titration calorimetry and X-ray crystallographic studies. *Journal of Biological Chemistry* 269:25339–25347.

Lee GS, Kappler K, Porter CJH, Scanlon MJ, and Nicolazzo JA (2015) Fatty Acid Binding Proteins Expressed at the Human Blood–Brain Barrier Bind Drugs in an Isoform-Specific Manner. *Pharm Res* 32:3432–3446.

Lee GS, Pan Y, Scanlon MJ, Porter CJH, and Nicolazzo JA (2018) Fatty Acid–Binding Protein 5 Mediates the Uptake of Fatty Acids, but not Drugs, Into Human Brain Endothelial Cells. *Journal of Pharmaceutical Sciences* 107:1185–1193.

Lee S-A, Yang KJZ, Brun P-J, Silvaroli JA, Yuen JJ, Shmarakov I, Jiang H, Feranil JB, Li X, Lackey AI, Krężel W, Leibel RL, Libien J, Storch J, Golczak M, and Blaner WS (2020) Retinol-binding protein 2 (RBP2) binds monoacylglycerols and modulates gut endocrine signaling and body weight. *Science Advances* 6:eaay8937, American Association for the Advancement of Science.

Lemberger L, Martz R, and Rodda B (1973) Comparative Pharmacology of A-Tetrahydrocannabinol and its Metabolite, 11-OH-Δ9-Tetrahydrocannabinol. *Journal of Clinical Investigation* 2411–2417.

Lemberger L, Silberstein SD, Axelrod J, and Kopin IJ (1970) Marihuana: Studies on the Disposition and Metabolism of Delta-9-Tetrahydrocannabinol in Man. *Science* 170:1320–1322.

Lemberger, Louis, Crabtree RE, and Rowe HM (1972) 11-Hydroxy-Δ9-tetrahydrocannabinol: Pharmacology, Disposition, and Metabolism of a Major Metabolite of Marihuana in Man. *Science* 177:62–64.

Liu R-Z, Li X, and Godbout R (2008) A novel fatty acid-binding protein (FABP) gene resulting from tandem gene duplication in mammals: transcription in rat retina and testis. *Genomics* 92:436–445.

Lowe JB, Sacchettini JC, Laposata M, McQuillan JJ, and Gordon JI (1987) Expression of rat intestinal fatty acid-binding protein in Escherichia coli. Purification and comparison of ligand binding characteristics with that of Escherichia coli-derived rat liver fatty acid-binding protein. *Journal of Biological Chemistry* 262:5931–5937.

Lücke C, Zhang F, Hamilton JA, Sacchettini JC, and Rüterjans H (2000) Solution structure of ileal lipid binding protein in complex with glycocholate. *European Journal of Biochemistry* 267:2929–2938.

Luebker DJ, Hansen KJ, Bass NM, Butenhoff JL, and Seacat AM (2002a) Interactions of flurochemicals with rat liver fatty acid-binding protein. *Toxicology* 176:175–185.

Luebker DJ, Hansen KJ, Bass NM, Butenhoff JL, and Seacat AM (2002b) Interactions of flurochemicals with rat liver fatty acid-binding protein. *Toxicology* 176:175–185.

Lunn S, Diaz P, O'Hearn S, Cahill SP, Blake A, Narine K, and Dyck JRB (2019) Human Pharmacokinetic Parameters of Orally Administered Δ9-Tetrahydrocannabinol Capsules Are Altered by Fed Versus Fasted Conditions and Sex Differences. *Cannabis and Cannabinoid Research* 4:255–264, Mary Ann Liebert, Inc., publishers.

Lutz JD, Dixit V, Yeung CK, Dickmann LJ, Zelter A, Thatcher JE, Nelson WL, and Isoherranen N (2009) Expression and functional characterization of cytochrome P450 26A1, a retinoic acid hydroxylase. *Biochemical Pharmacology* 77:258–268.

Lutz JD, VandenBrink BM, Babu KN, Nelson WL, Kunze KL, and Isoherranen N (2013) Stereoselective Inhibition of CYP2C19 and CYP3A4 by Fluoxetine and Its Metabolite: Implications for Risk Assessment of Multiple Time-Dependent Inhibitor Systems. *Drug Metab Dispos* 41:2056–2065, American Society for Pharmacology and Experimental Therapeutics.

Luxon BA, and Weisiger RA (1993) Sex differences in intracellular fatty acid transport: role of cytoplasmic binding proteins. *American Journal of Physiology-Gastrointestinal and Liver Physiology* 265:G831–G841, American Physiological Society.

Maatman RG, Van Kuppevelt TH, and Veerkamp JH (1991) Two types of fatty acid-binding protein in human kidney. Isolation, characterization and localization. *Biochem J* 273:759–766.

MacDonald PN, and Ong DE (1987) Binding specificities of cellular retinol-binding protein and cellular retinol-binding protein, type II. *Journal of Biological Chemistry* 262:10550–10556.

Majumdar A, Petrescu AD, Xiong Y, and Noy N (2011) Nuclear translocation of cellular retinoic acid-binding protein II is regulated by retinoic acid-controlled SUMOylation. *J Biol Chem* 286:42749–42757.

Manuzak JA, Gott TM, Kirkwood JS, Coronado E, Hensley-McBain T, Miller C, Cheu RK, Collier AC, Funderburg NT, Martin JN, Wu MC, Isoherranen N, Hunt PW, and Klatt NR (2018)

Heavy Cannabis Use Associated With Reduction in Activated and Inflammatory Immune Cell Frequencies in Antiretroviral Therapy–Treated Human Immunodeficiency Virus–Infected Individuals. *Clinical Infectious Diseases* 66:1872–1882.

Martin GG, Atshaves BP, Mcintosh AL, Mackie JT, Kier AB, and Schroeder F (2005) Liver fatty-acid-binding protein (L-FABP) gene ablation alters liver bile acid metabolism in male mice. *Biochemical Journal* 391:549–560.

Martin GG, Danneberg H, Kumar LS, Atshaves BP, Erol E, Bader M, Schroeder F, and Binas B (2003) Decreased Liver Fatty Acid Binding Capacity and Altered Liver Lipid Distribution in Mice Lacking the Liver Fatty Acid-binding Protein Gene*. *Journal of Biological Chemistry* 278:21429–21438.

Martin GG, Huang H, Atshaves BP, Binas B, and Schroeder F (2003) Ablation of the Liver Fatty Acid Binding Protein Gene Decreases Fatty Acyl CoA Binding Capacity and Alters Fatty Acyl CoA Pool Distribution in Mouse Liver. *Biochemistry* 42:11520–11532, American Chemical Society.

Martin GG, McIntosh AL, Huang H, Gupta S, Atshaves BP, Landrock KK, Landrock D, Kier AB, and Schroeder F (2013) Human Liver Fatty Acid Binding Protein (L-FABP) T94A Variant Alters Structure, Stability, and Interaction with Fibrates. *Biochemistry* 52:9347–9357.

Matarese V, and Bernlohr DA (1988) Purification of murine adipocyte lipid-binding protein. Characterization as a fatty acid- and retinoic acid-binding protein. *Journal of Biological Chemistry* 263:14544–14551.

McKillop IH, Girardi CA, and Thompson KJ (2019) Role of fatty acid binding proteins (FABPs) in cancer development and progression. *Cellular Signalling* 62:109336.

Menozzi I, Vallese F, Polverini E, Folli C, Berni R, and Zanotti G (2017) Structural and molecular determinants affecting the interaction of retinol with human CRBP1. *Journal of Structural Biology* 197:330–339.

Naef M, Russmann S, Petersen-Felix S, and Brenneisen R (2004) Development and pharmacokinetic characterization of pulmonal and intravenous delta-9-tetrahydrocannabinol (THC) in humans. *Journal of Pharmaceutical Sciences* 93:1176–1184.

Nakamura K, Hirayama-Kurogi M, Ito S, Kuno T, Yoneyama T, Obuchi W, Terasaki T, and Ohtsuki S (2016) Large-scale multiplex absolute protein quantification of drug-metabolizing enzymes and transporters in human intestine, liver, and kidney microsomes by SWATH-MS: Comparison with MRM/SRM and HR-MRM/PRM. *PROTEOMICS* 16:2106–2117.

Napoli J, Posch K, FioreIIa P, and Boerman M (1991) Physiological occurrence, biosynthesis and metabolism of retinoic acid: evidence for roles of Cellular Retinol-Binding Protein (CRBP) and Cellular Retinoic Acid-Binding Protein (CRABP) in the pathway of retinoic acid homeostasis. *Biomed* 45:131–143.

Napoli JL (2017) Cellular retinoid binding-proteins, CRBP, CRABP, FABP5: Effects on retinoid metabolism, function and related diseases. *Pharmacology & Therapeutics* 173:19–33.

Napoli JL (2016) Functions of Intracellular Retinoid Binding-Proteins. *Subcell Biochem* 81:21–76.

Napoli JL (2012) Physiological insights into all-trans-retinoic acid biosynthesis. *Biochimica et Biophysica Acta (BBA) - Molecular and Cell Biology of Lipids* 1821:152–167.

Nath A, Fernández C, Lampe JN, and Atkins WM (2008) Spectral resolution of a second binding site for Nile Red on cytochrome P4503A4. *Archives of Biochemistry and Biophysics* 474:198–204.

National Institute on Drug Abuse (NIDA) (2022) Marijuana and hallucinogen use among young adults reached all time-high in 2021 | National Institute on Drug Abuse (NIDA).

Nelson CH, Peng C-C, Lutz JD, Yeung CK, Zelter A, and Isoherranen N (2016) Direct protein–protein interactions and substrate channeling between cellular retinoic acid binding proteins and CYP26B1. *FEBS Letters* 590:2527–2535.

Nemecz G, Hubbell T, Jefferson JR, Lowe JB, and Schroeder F (1991) Interaction of fatty acids with recombinant rat intestinal and liver fatty acid-binding proteins. *Archives of Biochemistry and Biophysics* 286:300–309.

Newberry EP, Xie Y, Kennedy S, Han X, Buhman KK, Luo J, Gross RW, and Davidson NO (2003) Decreased Hepatic Triglyceride Accumulation and Altered Fatty Acid Uptake in Mice with Deletion of the Liver Fatty Acid-binding Protein Gene *. *Journal of Biological Chemistry* 278:51664–51672, Elsevier.

Nilsson O, Isoherranen N, Guo MH, Lui JC, Jee YH, Guttmann-Bauman I, Acerini C, Lee W, Allikmets R, Yanovski JA, Dauber A, and Baron J (2016) Accelerated Skeletal Maturation in Disorders of Retinoic Acid Metabolism: A Case Report and Focused Review of the Literature. *Horm Metab Res* 48:737–744, © Georg Thieme Verlag KG.

Noiri E, Doi K, Negishi K, Tanaka T, Hamasaki Y, Fujita T, Portilla D, and Sugaya T (2009) Urinary fatty acid-binding protein 1: an early predictive biomarker of kidney injury. *Am J Physiol Renal Physiol* 296:F669–F679.

Norris Andrew W., Cheng L, Giguère V, Rosenberger M, and Li E (1994) Measurement of subnanomolar retinoic acid binding affinities for cellular retinoic acid binding proteins by fluorometric titration. *Biochimica et Biophysica Acta (BBA) - Protein Structure and Molecular Enzymology* 1209:10–18.

Norris A. W., Cheng L, Giguère V, Rosenberger M, and Li E (1994) Measurement of subnanomolar retinoic acid binding affinities for cellular retinoic acid binding proteins by fluorometric titration. *Biochim Biophys Acta* 1209:10–18.

Norris AW, and Spector AA (2002) Very long chain n-3 and n-6 polyunsaturated fatty acids bind strongly to liver fatty acid-binding protein. *Journal of Lipid Research* 43:646–653.

Nossoni Z, Assar Z, Yapici I, Nosrati M, Wang W, Berbasova T, Vasileiou C, Borhan B, and Geiger J (2014) Structures of holo wild-type human cellular retinol-binding protein II (hCRBPII) bound to retinol and retinal. *Acta Crystallogr D Biol Crystallogr* 70:3226–3232.

Noy N (2000) Retinoid-binding proteins: mediators of retinoid action. *Biochem J* 348:481–495.

Ockner RK, and Manning JA (1974) Fatty Acid-Binding Protein in Small Intestine IDENTIFICATION, ISOLATION, AND EVIDENCE FOR ITS ROLE IN CELLULAR FATTY ACID TRANSPORT. *J Clin Invest* 54:326–338, American Society for Clinical Investigation.

Omura T, and Sato R (1964) The Carbon Monoxide-binding Pigment of Liver Microsomes: I. EVIDENCE FOR ITS HEMOPROTEIN NATURE. *Journal of Biological Chemistry* 239:2370–2378.

Ong DE, Kakkad B, and MacDonald PN (1987) Acyl-CoA-independent esterification of retinol bound to cellular retinol-binding protein (type II) by microsomes from rat small intestine. *Journal of Biological Chemistry* 262:2729–2736.

Owada Y, Abdelwahab SA, Kitanaka N, Sakagami H, Takano H, Sugitani Y, Sugawara M, Kawashima H, Kiso Y, Mobarakeh JI, Yanai K, Kaneko K, Sasaki H, Kato H, Saino-Saito S, Matsumoto N, Akaike N, Noda T, and Kondo H (2006) Altered emotional behavioral responses in mice lacking brain-type fatty acid-binding protein gene. *European Journal of Neuroscience* 24:175–187.

Pan Y, Scanlon MJ, Owada Y, Yamamoto Y, Porter CJH, and Nicolazzo JA (2015) Fatty Acid-Binding Protein 5 Facilitates the Blood–Brain Barrier Transport of Docosahexaenoic Acid. *Mol Pharmaceutics* 12:4375–4385, American Chemical Society.

Pan Y, Short JL, Choy KHC, Zeng AX, Marriott PJ, Owada Y, Scanlon MJ, Porter CJH, and Nicolazzo JA (2016) Fatty Acid-Binding Protein 5 at the Blood–Brain Barrier Regulates Endogenous Brain Docosahexaenoic Acid Levels and Cognitive Function. *J Neurosci* 36:11755–11767, Society for Neuroscience.

Patil R, Laguerre A, Wielens J, Headey SJ, Williams ML, Hughes MLR, Mohanty B, Porter CJH, and Scanlon MJ (2014) Characterization of Two Distinct Modes of Drug Binding to Human Intestinal Fatty Acid Binding Protein. *ACS Chem Biol* 9:2526–2534, American Chemical Society.

Patil R, Mohanty B, Liu B, Chandrashekaran IR, Headey SJ, Williams ML, Clements CS, Ilyichova O, Doak BC, Genissel P, Weaver RJ, Vuillard L, Halls ML, Porter CJH, and Scanlon MJ (2019) A ligand-induced structural change in fatty acid–binding protein 1 is associated with potentiation of peroxisome proliferator–activated receptor α agonists. *Journal of Biological Chemistry* 294:3720–3734, Elsevier.

Patilea-Vrana GI, Anoshchenko O, and Unadkat JD (2019) Hepatic Enzymes Relevant to the Disposition of (−)-Δ9-Tetrahydrocannabinol (THC) and Its Psychoactive Metabolite, 11-OH-THC. *Drug Metab Dispos* 47:249–256, American Society for Pharmacology and Experimental Therapeutics.

Patilea-Vrana GI, and Unadkat JD (2019) Quantifying Hepatic Enzyme Kinetics of (-)-Δ9-Tetrahydrocannabinol (THC) and Its Psychoactive Metabolite, 11-OH-THC, through In Vitro Modeling. *Drug Metab Dispos* 47:743–752, American Society for Pharmacology and Experimental Therapeutics.

Paulussen RenéJA, van der Logt CPE, and Veerkamp JH (1988) Characterization and binding properties of fatty acid-binding proteins from human, pig, and rat heart. *Archives of Biochemistry and Biophysics* 264:533–545.

Paulussen RJ, van Moerkerk HT, and Veerkamp JH (1990) Immunochemical quantitation of fatty acid-binding proteins. Tissue distribution of liver and heart FABP types in human and porcine tissues. *Int J Biochem* 22:393–398.

Pelsers MMAL, Hermens WT, and Glatz JFC (2005) Fatty acid-binding proteins as plasma markers of tissue injury. *Clinica Chimica Acta* 352:15–35.

Pelsers MMAL, Namiot Z, Kisielewski W, Namiot A, Januszkiewicz M, Hermens WT, and Glatz JFC (2003) Intestinal-type and liver-type fatty acid-binding protein in the intestine. Tissue distribution and clinical utility. *Clinical Biochemistry* 36:529–535.

Pelton PD, Zhou L, Demarest KT, and Burris TP (1999) PPAR⫻ Activation Induces the Expression of the Adipocyte Fatty Acid Binding Protein Gene in Human Monocytes. *BIOCHEMICAL AND BIOPHYSICAL RESEARCH COMMUNICATIONS* 261.

Peng X-E, Wu Y-L, Lu Q-Q, Hu Z-J, and Lin X (2012) Two genetic variants in FABP1 and susceptibility to non-alcohol fatty liver disease in a Chinese population. *Gene* 500:54–58.

Penman SL, Roeder NM, Berthold EC, Senetra AS, Marion M, Richardson BJ, White O, Fearby NL, McCurdy CR, Hamilton J, Sharma A, and Thanos PK (2023) FABP5 is important for cognitive function and is an important regulator of the physiological effects and pharmacokinetics of acute Δ9 tetrahydrocannabinol inhalation in mice. *Pharmacology Biochemistry and Behavior* 231:173633.

Peterson PA, and Rask L (1971) Studies on the Fluorescence of the Human Vitamin A-transporting Plasma Protein Complex and Its Individual Components. *Journal of Biological Chemistry* 246:7544–7550.

Pettersen EF, Goddard TD, Huang CC, Couch GS, Greenblatt DM, Meng EC, and Ferrin TE (2004) UCSF Chimera—A visualization system for exploratory research and analysis. *Journal of Computational Chemistry* 25:1605–1612.

Poirier H, Braissant O, Niot I, Wahli W, and Besnard P (1997) 9-cis-Retinoic acid enhances fatty acid-induced expression of the liver fatty acid-binding protein gene. *FEBS Letters* 412:480–484.

Ragona L, Pagano K, Tomaselli S, Favretto F, Ceccon A, Zanzoni S, D’Onofrio M, Assfalg M, and Molinari H (2014) The role of dynamics in modulating ligand exchange in intracellular lipid binding proteins. *Biochimica et Biophysica Acta (BBA) - Proteins and Proteomics* 1844:1268–1278.

Raverdeau M, and Mills KHG (2014) Modulation of T Cell and Innate Immune Responses by Retinoic Acid. *The Journal of Immunology* 192:2953–2958, American Association of Immunologists.

Rezar R, Jirak P, Gschwandtner M, Derler R, Felder TK, Haslinger M, Kopp K, Seelmaier C, Granitz C, Hoppe UC, and Lichtenauer M (2020) Heart-Type Fatty Acid-Binding Protein (H-FABP) and Its Role as a Biomarker in Heart Failure: What Do We Know So Far? *J Clin Med* 9:164.

Rhinn M, and Dollé P (2012) Retinoic acid signalling during development. *Development* 139:843–858.

Richieri GV, Ogata RT, and Kleinfeld AM (1994) Equilibrium constants for the binding of fatty acids with fatty acid-binding proteins from adipocyte, intestine, heart, and liver measured with the fluorescent probe ADIFAB. *Journal of Biological Chemistry* 269:23918–23930.

Richieri GV, Ogata RT, and Kleinfeld AM (1996) Thermodynamic and Kinetic Properties of Fatty Acid Interactions with Rat Liver Fatty Acid-binding Protein *. *Journal of Biological Chemistry* 271:31068–31074, Elsevier.

Richieri GV, Ogata RT, and Kleinfeld AM (1995) Thermodynamics of Fatty Acid Binding to Fatty Acid-binding Proteins and Fatty Acid Partition between Water and Membranes Measured Using the Fluorescent Probe ADIFAB (∗). *Journal of Biological Chemistry* 270:15076–15084.

Rizvi SMohdD, Shakil S, and Haneef Mohd (2013) A simple click by click protocol to perform docking: AutoDock 4.2 made easy for non-bioinformaticians. *EXCLI J* 12:831–857.

Rolf B, Oudenampsen-Krüger E, Börchers T, Færgeman NJ, Knudsen J, Lezius A, and Spener F (1995) Analysis of the ligand binding properties of recombinant bovine liver-type fatty acid binding protein. *Biochimica et Biophysica Acta (BBA) - Lipids and Lipid Metabolism* 1259:245–253.

Rowland A, Elliot DJ, Knights KM, Mackenzie PI, and Miners JO (2008) The “Albumin Effect” and in Vitro-in Vivo Extrapolation: Sequestration of Long-Chain Unsaturated Fatty Acids Enhances Phenytoin Hydroxylation by Human Liver Microsomal and Recombinant Cytochrome P450 2C9. *Drug Metab Dispos* 36:870–877, American Society for Pharmacology and Experimental Therapeutics.

Rowland A, Hallifax D, Nussio MR, Shapter JG, Mackenzie PI, Brian Houston J, Knights KM, and Miners JO (2015) Characterization of the comparative drug binding to intra- (liver fatty acid binding protein) and extra- (human serum albumin) cellular proteins. *Xenobiotica* 45:847–857.

Rowland A, Knights KM, Mackenzie PI, and Miners JO (2009) Characterization of the Binding of Drugs to Human Intestinal Fatty Acid Binding Protein (IFABP): Potential Role of IFABP as an Alternative to Albumin for in Vitro-in Vivo Extrapolation of Drug Kinetic Parameters. *Drug Metab Dispos* 37:1395–1403, American Society for Pharmacology and Experimental Therapeutics.

Sacchettini JC, Hauft SM, Van Camp SL, Cistola DP, and Gordon JI (1990) Developmental and structural studies of an intracellular lipid binding protein expressed in the ileal epithelium. *Journal of Biological Chemistry* 265:19199–19207.

Sachse-Seeboth C, Pfeil J, Sehrt D, Meineke I, Tzvetkov M, Bruns E, Poser W, Vormfelde S, and Brockmöller J (2009) Interindividual Variation in the Pharmacokinetics of Δ9-Tetrahydrocannabinol as Related to Genetic Polymorphisms in CYP2C9. *Clinical Pharmacology & Therapeutics* 85:273–276.

Saito N, Furuhashi M, Koyama M, Higashiura Y, Akasaka H, Tanaka M, Moniwa N, Ohnishi H, Saitoh S, Ura N, Shimamoto K, and Miura T (2021) Elevated circulating FABP4 concentration predicts cardiovascular death in a general population: a 12-year prospective study. *Sci Rep* 11:4008, Nature Publishing Group.

Sanquer S, and Gilchrest BA (1994) Characterization of Human Cellular Retinoic Acid-Binding Protein-I and Protein-II: Ligand-Binding Affinities and Distribution in Skin. *Archives of Biochemistry and Biophysics* 311:86–94.

Santambrogio C, Favretto F, D’Onofrio M, Assfalg M, Grandori R, and Molinari H (2013) Mass spectrometry and NMR analysis of ligand binding by human liver fatty acid binding protein. *Journal of Mass Spectrometry* 48:895–903.

Schaap FG, Van der Vusse GJ, and Glatz JFC (2002) Evolution of the family of intracellular lipid binding proteins in vertebrates. *Mol Cell Biochem* 239:69–77.

Schmider J, Greenblatt DJ, Von Moltke LL, Karsov D, and Shader RI (1997) Inhibition of CYP2C9 by selective serotonin reuptake inhibitors in vitro: studies of phenytoin p-hydroxylation. *British Journal of Clinical Pharmacology* 44:495–498.

Schroeder F, Jolly CA, Cho T-H, and Frolov A (1998) Fatty acid binding protein isoforms: structure and function. *Chemistry and Physics of Lipids* 92:1–25.

Schroeder F, McIntosh AL, Martin GG, Huang H, Landrock D, Chung S, Landrock KK, Dangott LJ, Li S, Kaczocha M, Murphy EJ, Atshaves BP, and Kier AB (2016a) Fatty Acid Binding Protein-1 (FABP1) and the Human FABP1 T94A Variant: Roles in the Endocannabinoid System and Dyslipidemias. *Lipids* 51:655–676.

Schroeder F, McIntosh AL, Martin GG, Huang H, Landrock D, Chung S, Landrock KK, Dangott LJ, Li S, Kaczocha M, Murphy EJ, Atshaves BP, and Kier AB (2016b) Fatty Acid Binding Protein-1 (FABP1) and the Human FABP1 T94A Variant: Roles in the Endocannabinoid System and Dyslipidemias. *Lipids* 51:655–676.

Schug TT, Berry DC, Shaw NS, Travis SN, and Noy N (2007) Opposing Effects of Retinoic Acid on Cell Growth Result from Alternate Activation of Two Different Nuclear Receptors. *Cell* 129:723–733.

Sha RS, Kane CD, Xu Z, Banaszak LJ, and Bernlohr DA (1993) Modulation of ligand binding affinity of the adipocyte lipid-binding protein by selective mutation. Analysis in vitro and in situ. *Journal of Biological Chemistry* 268:7885–7892.

Sharma Ashwani, and Sharma Amit (2011) Fatty Acid Induced Remodeling within the Human Liver Fatty Acid-binding Protein *. *Journal of Biological Chemistry* 286:31924–31928, Elsevier.

Shen AL, Porter TD, Wilson TE, and Kasper CB (1989) Structural analysis of the FMN binding domain of NADPH-cytochrome P-450 oxidoreductase by site-directed mutagenesis. *J Biol Chem* 264:7584–7589.

Sheng N, Li J, Liu H, Zhang A, and Dai J (2016) Interaction of perfluoroalkyl acids with human liver fatty acid-binding protein. *Arch Toxicol* 90:217–227.

Shimizu F, Watanabe TK, Shinomiya H, Nakamura Y, and Fujiwara T (1997) Isolation and expression of a cDNA for human brain fatty acid-binding protein ž B-FABP/. 1354:24–28.

Shrestha S, Sunaga H, Hanaoka H, Yamaguchi A, Kuwahara S, Umbarawan Y, Nakajima K, Machida T, Murakami M, Saito A, Tsushima Y, Kurabayashi M, and Iso T (2018) Circulating FABP4 is eliminated by the kidney via glomerular filtration followed by megalin-mediated reabsorption. *Sci Rep* 8:16451, Nature Publishing Group.

Sievers F, Wilm A, Dineen D, Gibson TJ, Karplus K, Li W, Lopez R, McWilliam H, Remmert M, Söding J, Thompson JD, and Higgins DG (2011) Fast, scalable generation of high-quality protein multiple sequence alignments using Clustal Omega. *Molecular Systems Biology* 7:539, John Wiley & Sons, Ltd.

Silvaroli JA, Arne JM, Chelstowska S, Kiser PD, Banerjee S, and Golczak M (2016) Ligand Binding Induces Conformational Changes in Human Cellular Retinol-binding Protein 1 (CRBP1) Revealed by Atomic Resolution Crystal Structures. *Journal of Biological Chemistry* 291:8528–8540.

Smathers RL, and Petersen DR (2011) The human fatty acid-binding protein family: Evolutionary divergences and functions. *Human Genomics* 5:170.

Smith ER, and Storch J (1999) The Adipocyte Fatty Acid-binding Protein Binds to Membranes by Electrostatic Interactions*. *Journal of Biological Chemistry* 274:35325–35330.

Snyder JM, Zhong G, Hogarth C, Huang W, Topping T, LaFrance J, Palau L, Czuba LC, Griswold M, Ghiaur G, and Isoherranen N (2020) Knockout of Cyp26a1 and Cyp26b1 during postnatal life causes reduced lifespan, dermatitis, splenomegaly, and systemic inflammation in mice. *The FASEB Journal* 34:15788–15804.

Spitsberg VL, Matitashvili E, and Gorewit RC (1995) Association and Coexpression of Fatty-Acid-Binding Protein and Glycoprotein CD36 in the Bovine Mammary Gland. *European Journal of Biochemistry* 230:872–878.

Stevison F, Hogarth C, Tripathy S, Kent T, and Isoherranen N (2017) Inhibition of the all-trans Retinoic Acid (*at*RA) Hydroxylases CYP26A1 and CYP26B1 Results in Dynamic, Tissue-

Specific Changes in Endogenous *at*RA Signaling. *Drug Metab Dispos* 45:846–854, American Society for Pharmacology and Experimental Therapeutics.

Storch J, and Corsico B (2008) The Emerging Functions and Mechanisms of Mammalian Fatty Acid–Binding Proteins. *Annual Review of Nutrition* 28:73–95.

Storch J, and McDermott L (2009) Structural and functional analysis of fatty acid-binding proteins. *J Lipid Res* 50:S126–S131.

Storch J, and Thumser AE (2010) Tissue-specific Functions in the Fatty Acid-binding Protein Family*. *Journal of Biological Chemistry* 285:32679–32683.

Storch J, and Thumser AEA (2000) The fatty acid transport function of fatty acid-binding proteins. *Biochimica et Biophysica Acta (BBA) - Molecular and Cell Biology of Lipids* 1486:28–44.

Stott C, White L, Wright S, Wilbraham D, and Guy G (2013) A Phase I, open-label, randomized, crossover study in three parallel groups to evaluate the effect of Rifampicin, Ketoconazole, and Omeprazole on the pharmacokinetics of THC/CBD oromucosal spray in healthy volunteers. *SpringerPlus* 2:236.

Sulsky R, Magnin DR, Huang Y, Simpkins L, Taunk P, Patel M, Zhu Y, Stouch TR, Bassolino-Klimas D, Parker R, Harrity T, Stoffel R, Taylor DS, Lavoie TB, Kish K, Jacobson BL, Sheriff S, Adam LP, Ewing WR, and Robl JA (2007) Potent and selective biphenyl azole inhibitors of adipocyte fatty acid binding protein (aFABP). *Bioorganic & Medicinal Chemistry Letters* 17:3511–3515.

Sun J, Kitova EN, Wang W, and Klassen JS (2006) Method for Distinguishing Specific from Nonspecific Protein−Ligand Complexes in Nanoelectrospray Ionization Mass Spectrometry. *Anal Chem* 78:3010–3018, American Chemical Society.

Suzuki H, Kneller MB, Haining RL, Trager WF, and Rettie AE (2002) (+)-N-3-Benzyl-Nirvanol and (−)-N-3-Benzyl-Phenobarbital: New Potent and Selective in Vitro Inhibitors of CYP2C19. *Drug Metab Dispos* 30:235–239, American Society for Pharmacology and Experimental Therapeutics.

Tan N-S, Shaw NS, Vinckenbosch N, Liu P, Yasmin R, Desvergne B, Wahli W, and Noy N (2002) Selective Cooperation between Fatty Acid Binding Proteins and Peroxisome Proliferator-Activated Receptors in Regulating Transcription. *Mol Cell Biol* 22:5114–5127.

Tang X-H, and Gudas LJ (2011) Retinoids, Retinoic Acid Receptors, and Cancer. *Annual Review of Pathology: Mechanisms of Disease* 6:345–364.

Thatcher JE, Buttrick B, Shaffer SA, Shimshoni JA, Goodlett DR, Nelson WL, and Isoherranen N (2011) Substrate Specificity and Ligand Interactions of CYP26A1, the Human Liver Retinoic Acid Hydroxylase. *Mol Pharmacol* 80:228–239, American Society for Pharmacology and Experimental Therapeutics.

Thatcher JE, Zelter A, and Isoherranen N (2010) The relative importance of CYP26A1 in hepatic clearance of all-trans retinoic acid. *Biochemical Pharmacology* 80:903–912.

Thomas BF, Compton DR, and Martin BR (1990) Characterization of the lipophilicity of natural and synthetic analogs of delta 9-tetrahydrocannabinol and its relationship to pharmacological potency. *J Pharmacol Exp Ther* 255:624–630, American Society for Pharmacology and Experimental Therapeutics.

Thompson J, Winter N, Terwey D, Bratt J, and Banaszak L (1997) The Crystal Structure of the Liver Fatty Acid-binding Protein: A Complex Bound with Two Oleates*. *Journal of Biological Chemistry* 272:7140–7150.

Thumser AE, Voysey J, and Wilton DC (1996) Mutations of recombinant rat liver fatty acid-binding protein at residues 102 and 122 alter its structural integrity and affinity for physiological ligands. *Biochem J* 314:943–949.

Thumser AE, and Wilton DC (1994) Characterization of binding and structural properties of rat liver fatty-acid-binding protein using tryptophan mutants. *Biochem J* 300 (Pt 3):827–833.

Thumser AE, and Wilton DC (1996) The binding of cholesterol and bile salts to recombinant rat liver fatty acid-binding protein. *Biochem J* 320 (Pt 3):729–733.

Thumser AEA, and Storch J (2000) Liver and intestinal fatty acid-binding proteins obtain fatty acids from phospholipid membranes by different mechanisms. *Journal of Lipid Research* 41:647–656.

Topletz AR, Thatcher JE, Zelter A, Lutz JD, Tay S, Nelson WL, and Isoherranen N (2012) Comparison of the function and expression of CYP26A1 and CYP26B1, the two retinoic acid hydroxylases. *Biochemical Pharmacology* 83:149–163.

Tracy TS, Marra C, Wrighton SA, Gonzalez FJ, and Korzekwa KR (1996) Studies of Flurbiprofen 4′-Hydroxylation. *Biochemical Pharmacology* **52**:1305–1309.

Trevaskis NL, Nguyen G, Scanlon MJ, and Porter CJH (2011) Fatty Acid Binding Proteins: Potential Chaperones of Cytosolic Drug Transport in the Enterocyte? *Pharm Res* 28:2176–2190.

Utsey K, Gastonguay MS, Russell S, Freling R, Riggs MM, and Elmokadem A (2020) Quantification of the Impact of Partition Coefficient Prediction Methods on Physiologically Based Pharmacokinetic Model Output Using a Standardized Tissue Composition. *Drug Metab Dispos* 48:903–916.

Vaezeslami S, Mathes E, Vasileiou C, Borhan B, and Geiger JH (2006) The Structure of Apo-wild-type Cellular Retinoic Acid Binding Protein II at 1.4 Å and its Relationship to Ligand Binding and Nuclear Translocation. *Journal of Molecular Biology* 363:687–701.

Valizadeh M, Aghasizadeh M, Nemati M, Hashemi M, Aghaee-Bakhtiari SH, Zare-Feyzabadi R, Esmaily H, Ghazizdaeh H, Sahebi R, Ahangari N, Ferns GordonA, Pasdar A, and Ghayour-Mobarhan M (2021) The association between a Fatty Acid Binding Protein 1 (FABP1) gene polymorphism and serum lipid abnormalities in the MASHAD cohort study. *Prostaglandins, Leukotrienes and Essential Fatty Acids* 172:102324.

Veerkamp JH, and Maatman RGHJ (1995) Cytoplasmic fatty acid-binding proteins: Their structure and genes. *Progress in Lipid Research* 34:17–52.

Veerkamp JH, van Moerkerk HTB, Prinsen CFM, and van Kuppevelt TH (1999) Structural and functional studies on different human FABP types. *Mol Cell Biochem* 192:137–142.

Veerkamp JH, and Zimmerman AW (2001) Fatty Acid-Binding Proteins of Nervous Tissue. *JMN* 16:133–142.

Velkov T (2013) Interactions between Human Liver Fatty Acid Binding Protein and Peroxisome Proliferator Activated Receptor Selective Drugs. *PPAR Research* 2013:e938401, Hindawi.

Velkov T, Chuang S, Wielens J, Sakellaris H, Charman WN, Porter CJH, and Scanlon MJ (2005) The Interaction of Lipophilic Drugs with Intestinal Fatty Acid-binding Protein*. *Journal of Biological Chemistry* 280:17769–17776.

Velkov T, Horne J, Laguerre A, Jones E, Scanlon MJ, and Porter CJH (2007) Examination of the Role of Intestinal Fatty Acid-Binding Protein in Drug Absorption Using a Parallel Artificial Membrane Permeability Assay. *Chemistry & Biology* 14:453–465.

Velkov T, Lim MLR, Capuano B, and Prankerd R (2008) A protocol for the combined sub-fractionation and delipidation of lipid binding proteins using hydrophobic interaction chromatography. *Journal of Chromatography B* 867:238–246.

Velkov T, Lim MLR, Horne J, Simpson JS, Porter CJH, and Scanlon MJ (2009) Characterization of lipophilic drug binding to rat intestinal fatty acid binding protein. *Mol Cell Biochem* 326:87–95.

Villeneuve J, Bassaganyas L, Lepreux S, Chiritoiu M, Costet P, Ripoche J, Malhotra V, and Schekman R (2018) Unconventional secretion of FABP4 by endosomes and secretory lysosomes. *Journal of Cell Biology* 217:649–665.

Vogel S, Mendelsohn CL, Mertz JR, Piantedosi R, Waldburger C, Gottesman ME, and Blaner WS (2001) Characterization of a New Member of the Fatty Acid-binding Protein Family That Binds All-trans-retinol*. *Journal of Biological Chemistry* 276:1353–1360.

Vogler A (2015) Fluorescence of retinoic acid in the presence of metal salts. *Inorganic Chemistry Communications* 57:69–71.

Vork MM, Glatz JFC, and Surtel DAM (1990) Assay of the binding of fatty acids by proteins: evaluation of the Lipidex 1000 procedure. *Mol Cell Biochem* 98:111–117.

Walsky RL, Obach RS, Hyland R, Kang P, Zhou S, West M, Geoghegan KF, Helal CJ, Walker GS, Goosen TC, and Zientek MA (2012) Selective Mechanism-Based Inactivation of CYP3A4 by CYP3cide (PF-04981517) and Its Utility as an In Vitro Tool for Delineating the Relative

Roles of CYP3A4 versus CYP3A5 in the Metabolism of Drugs. *Drug Metab Dispos* 40:1686–1697, American Society for Pharmacology and Experimental Therapeutics.

Wang G, Bonkovsky HL, de Lemos A, and Burczynski FJ (2015) Recent insights into the biological functions of liver fatty acid binding protein 1. *J Lipid Res* 56:2238–2247.

Wang L, Li Y, and Yan H (1997) Structure-Function Relationships of Cellular Retinoic Acid-binding Proteins: Quantitative Analysis of the Ligand Binding Properties of the Wild-Type Proteins and Site-Directed Mutants *. *Journal of Biological Chemistry* 272:1541–1547, Elsevier.

Wang Q, Rizk S, Bernard C, Lai MP, Kam D, Storch J, and Stark RE (2017) Protocols and pitfalls in obtaining fatty acid-binding proteins for biophysical studies of ligand-protein and protein-protein interactions. *Biochemistry and Biophysics Reports* 10:318–324.

Wang Y, Law W-K, Hu J-S, Lin H-Q, Ip T-M, and Wan DC-C (2014) Discovery of FDA-Approved Drugs as Inhibitors of Fatty Acid Binding Protein 4 Using Molecular Docking Screening. *J Chem Inf Model* 54:3046–3050.

Wang Y-T, Liu C-H, and Zhu H-L (2016) Fatty acid binding protein (FABP) inhibitors: a patent review (2012-2015). *Expert Opinion on Therapeutic Patents* 26:767–776.

Watanabe K, Matsunaga T, Yamamoto I, Funae Y, and Yoshimura H (1995) Involvement of CYP2C in the Metabolism of Cannabinoids by Human Hepatic Microsomes from an Old Woman. *Biological & Pharmaceutical Bulletin* 18:1138–1141.

Watanabe K, Yamaori S, Funahashi T, Kimura T, and Yamamoto I (2007) Cytochrome P450 enzymes involved in the metabolism of tetrahydrocannabinols and cannabinol by human hepatic microsomes. *Life Sciences* 80:1415–1419.

Waterhouse AM, Procter JB, Martin DMA, Clamp M, and Barton GJ (2009) Jalview Version 2--a multiple sequence alignment editor and analysis workbench. *Bioinformatics* 25:1189–1191.

Widstrom RL, Norris AW, and Spector AA (2001) Binding of Cytochrome P450 Monooxygenase and Lipoxygenase Pathway Products by Heart Fatty Acid-Binding Protein. *Biochemistry* 40:1070–1076, American Chemical Society.

Wolfrum C, Borrmann CM, Börchers T, and Spener F (2001) Fatty acids and hypolipidemic drugs regulate peroxisome proliferator-activated receptors α- and γ-mediated gene expression via liver fatty acid binding protein: A signaling path to the nucleus. *Proceedings of the National Academy of Sciences* 98:2323–2328, Proceedings of the National Academy of Sciences.

Wolfrum C, Buhlmann C, Rolf B, Börchers T, and Spener F (1999) Variation of liver-type fatty acid binding protein content in the human hepatoma cell line HepG2 by peroxisome proliferators and antisense RNA affects the rate of fatty acid uptake. *Biochimica et Biophysica Acta (BBA) - Molecular and Cell Biology of Lipids* 1437:194–201.

Wootan MG, Bernlohr DA, and Storch J (1993) Mechanism of fluorescent fatty acid transfer from adipocyte fatty acid binding protein to membranes. *Biochemistry* 32:8622–8627, American Chemical Society.

Yabut KCB, and Isoherranen N (2022) CRABPs Alter all-trans-Retinoic Acid Metabolism by CYP26A1 via Protein-Protein Interactions. *Nutrients* 14:1784, Multidisciplinary Digital Publishing Institute.

Yabut KCB, and Isoherranen N (2023) Impact of Intracellular Lipid Binding Proteins on Endogenous and Xenobiotic Ligand Metabolism and Disposition. *Drug Metab Dispos* 51:700–717, American Society for Pharmacology and Experimental Therapeutics.

Yabut KCB, Martynova A, Nath A, Zercher BP, Bush MF, and Isoherranen N (2024) Drugs Form Ternary Complexes with Human Liver Fatty Acid Binding Protein (FABP1) and FABP1 Binding Alters Drug Metabolism, bioRxiv.

Yamamoto I, Narimatsu S, Shimonishi T, Watanabe K, and Yoshimura H (1984) Difference in Epoxides Formation and Their Further Metabolism Between Δ-9 and Δ-8 Tetrahydrocannabinols by Human Liver Microsomes. *Journal of Pharmacobio-Dynamics* 7:254–262.

Yu S, Levi L, Casadesus G, Kunos G, and Noy N (2014) Fatty Acid-binding Protein 5 (FABP5) Regulates Cognitive Function Both by Decreasing Anandamide Levels and by Activating the Nuclear Receptor Peroxisome Proliferator-activated Receptor β/δ (PPARβ/δ) in the Brain*♦. *Journal of Biological Chemistry* 289:12748–12758.

Zhang Y, Zhang J, Ren Y, Lu R, Yang L, and Nie G (2020) Tracing the evolution of fatty acid-binding proteins (FABPs) in organisms with a heterogeneous fat distribution. *FEBS Open Bio* 10:861–872.

Zhong G, Hogarth C, Snyder JM, Palau L, Topping T, Huang W, Czuba LC, LaFrance J, Ghiaur G, and Isoherranen N (2019) The retinoic acid hydroxylase Cyp26a1 has minor effects on postnatal vitamin A homeostasis, but is required for exogenous *at*RA clearance. *Journal of Biological Chemistry* 294:11166–11179.

Zhong G, Ortiz D, Zelter A, Nath A, and Isoherranen N (2018) CYP26C1 Is a Hydroxylase of Multiple Active Retinoids and Interacts with Cellular Retinoic Acid Binding Proteins. *Mol Pharmacol* 93:489–503.

Zhou Q, Matsumoto S, Ding LR, Fischer NE, and Inaba T (2004) The comparative interaction of human and bovine serum albumins with CYP2C9 in human liver microsomes. *Life Sciences* 75:2145–2155.

Zhou Y, Elmes MW, Sweeney JM, Joseph OM, Che J, Hsu H-C, Li H, Deutsch DG, Ojima I, Kaczocha M, and Rizzo RC (2019) Identification of Fatty Acid Binding Protein 5 Inhibitors Through Similarity-Based Screening. *Biochemistry* 58:4304–4316, American Chemical Society.

VITA

King Clyde was born in Quezon City, Philippines. He immigrated to the U.S. when he was three years old with his mother, four siblings, cousin, aunt and two uncles. He lived with his family in the city of Oxnard in Southern California until he was eight years old, then moved up to small town in northwest Oregon called St. Helens. It was in Oregon where King cultivated his love for biology aimlessly exploring the "vast" Oregon forests in his neighborhoods. King studied biology at Oregon State University where he did research in Dr. Robert Mason's laboratory on feeding behavior in garter snakes. In his undergraduate years, he committed part of his studies to learning Spanish as a second language. He spent time studying abroad in Granada, Spain and exploring Europe where he also met his partner MacKenzie. After obtaining his B.S. in Biology, he moved to Santiago, Chile to teach English. He then returned to the Pacific Northwest and worked for a short time as a research technician in the Basic Sciences Division at Fred Hutchinson Cancer Research Center in Seattle, Washington studying wound healing in fruit flies. He eventually transitioned to the University of Washington, first, in the Department of Biochemistry where he worked on microtubule nucleation in yeast in Dr. Trisha Davis's laboratory. He joined the Department of Pharmaceutics at the University of Washington where he completed his thesis work in Dr. Nina Isoherranen's laboratory studying the role of intracellular lipid binding proteins in xenobiotic and retinoid disposition.